FIRST-PRINCIPLES AND CLASSICAL ATOMISTIC STUDY OF INTERACTIONS BETWEEN METHANE AND OTHER SUBSTANCES

A THESIS SUBMITTED TO THE

CENTRAL DEPARTMENT OF PHYSICS

INSTITUTE OF SCIENCE AND TECHNOLOGY

TRIBHUVAN UNIVERSITY

NEPAL

FOR THE AWARD OF

DOCTOR OF PHILOSOPHY

IN PHYSICS

By

NURAPATI PANTHA

JANUARY 2017

FIRST-PRINCIPLES AND CLASSICAL ATOMISTIC STUDY OF INTERACTIONS BETWEEN METHANE AND OTHER SUBSTANCES

A THESIS SUBMITTED TO THE

CENTRAL DEPARTMENT OF PHYSICS

INSTITUTE OF SCIENCE AND TECHNOLOGY

TRIBHUVAN UNIVERSITY

NEPAL

FOR THE AWARD OF

DOCTOR OF PHILOSOPHY

IN PHYSICS

By

NURAPATI PANTHA

JANUARY 2017

DECLARATION

Thesis entitled **"First-principles and classical atomistic study of interactions between methane and other substances "** which is being submitted to the Central Department of Physics, Institute of Science and Technology (IOST), Tribhuvan University, Nepal, for the award of the degree of Doctor of Philosophy (Ph.D.), is a research work carried out by me under the supervision of Prof. Dr. Narayan Prasad Adhikari, Central Department of Physics, Tribhuvan University and co-supervision of Prof. Dr. Sandro Scandolo, The Abdus Salam International Centre For Theoretical Physics, Trieste, Italy.

This research is original and has not been submitted earlier in part or full in this or any other form to any university or institute, here or elsewhere, for the award of any degree.

Nurapati Pantha

RECOMMENDATION

This is to recommend that **Nurapati Pantha** has carried out research entitled **"First-principles and classical atomistic study of interactions between methane and other substances "** for the award of Doctor of Philosophy (Ph.D.) in **Physics** under our supervision. To our knowledge, this work has not been submitted for any other degree.

He has fulfilled all the requirements laid down by the Institute of Science and Technology (IOST), Tribhuvan University, Kirtipur for the submission of the thesis for the award of Ph.D. degree.

. . . . . .

Prof. Dr. Narayan Prasad Adhikari,
Supervisor
Central Department Of Physics,
Tribhuvan University,
Kirtipur, Kathmandu,
Nepal

. . . . . .

Prof. Dr. Sandro Scandolo,
Co-Supervisor
The Abdus Salam ICTP,
Trieste, Italy

January 2017

LETTER OF APPROVAL

[Date:30/01/2017]

On the recommendation of **Prof. Dr. Narayan Prasad Adhikari** of Central Department of Physics, Tribhuvan, University, Kirtipur, Kathmandu, Nepal, and **Prof. Dr. Sandro Scandolo** of The Abdus Salam International Centre For Theoretical Physics, Trieste, Italy, this Ph.D. thesis submitted by **Nurapati Pantha**, entitled "**First-principles and classical atomistic study of interactions between methane and other substances**" is forwarded by Central Department Research Committee (CDRC) to the Dean, IOST, TU.

.....

Dr. Binil Aryal

Professor and Head

Central Department Of Physics,

Tribhuvan University,

Kirtipur, Kathmandu,

Nepal

ACKNOWLEDGMENTS

Passing through a number of ups and downs, I have come to the stage of concluding my research activities conducted in last five years. There are many people and institutions to whom I am indebted for their moral, academic and economic support at the different stages during my journey of Ph.D. work. First of all I am thankful to all of you who supported me knowingly or unknowingly at different level and are not included in this document because of limitations in space.

On writing words of acknowledgment, my first and sincere appreciation goes to my supervisors Prof. Dr. Narayan Prasad Adhikari of Tribhuvan University (TU), Kirtipur, Kathmandu, Nepal and Prof. Dr. Sandro Scandolo, *The Abdus Salam* International Center for Theoretical Physics (ICTP), Trieste, Italy, for their patience, scientific guidance, support, friendship as well as parent-ship throughout my research work. You will be my role model in scientific and social activities during the days to come.

I am equally indebted to Professor Shobhana Narasimhan, Jawarlal Nehru Center for Advanced of Scientific Research (JNCASR), India, Dr. Ali Hassanani (ICTP) and Dr. Kanchan Ulman (ICTP), for their scientific guidance especially during my visit to JNCASR and ICTP, respectively. I would also like to thank STEP (Sandwich Training and Educational Program) program of ICTP, ICMS (International Center for Material Science) of JNCASR, TWAS (The World of Academy for Sciences) and NAST (Nepal Academy of Science and Technology) for their logistic and economic support during different stages of my work.

I am also thankful to my seniors Dr. Gopi Chandra Kaphle (TU), and Dr. A. Raji (ICTP) for their moral and academic support. I always found Dr. Kaphle as my elder brother who takes care of my sentiments and emotions during my difficult time, in addition to scientific instructions. I am grateful to Mr. Rajesh Kumar Bachchan for his generous help to arrange required format of the present thesis. My sincere thanks goes to my labmates Saran Lamichane, Sunil Pokhrel, Shyam Khanal, Rajendra Prasad Koirala and more than a dozen of master's students to whom I discussed about science and daily life.

I would like to thank Prof. Abhijit Mookerjee, Prof. Devendra Raj Mishra and Prof. Raju Khanal who encouraged me to jump for research activities in the field of my interest. I do not want to miss this opportunity to thank all the concerned staff members of ICTP and JNCASR

for their help and generosity whenever I encountered to them with this or that kind of problem.

Finally, I would like to thank Prof. Binil Aryal, Head of the Central Department of Physics, Prof. Lok Narayan Jha (former Head), and all the faculty members and the staffs of the Central Department of Physics (CDP) who helped me for varying nature of works without which my thesis work would not be of present shape.

At the last but not the least, I would like to thank my parents and family members for their support and encouragement. Special thank goes to Sushila, Sashwat and Sarbagya who patiently waited me when I was not available during their needy time.

Nurapati Pantha

January, 2017

ABSTRACT

Methane related compounds are frontier topics in research and industrial sectors because of their relevancy in energy to environment, geophysics to astronomy and physical chemistry to biological sciences. In addition to its dominant presence in traditional fossil fuels, methane (in the form of clathrates) is available at the continental slopes and permafrost regions of the earth. Because of its dominant presence in the earth, methane in unconventional (clathrates) form is supposed to be a major energy resource for near future. However, its safe and economical extraction, storage and transportation are the major challenges. As the simplest alkane molecule, methane-methane interactions in different solvent environments are supposed to be relevant model systems to understand hydrophobic interactions and phenomenon of protein folding. In the present work, we study geometrical and electronic properties of methane in clathrates, and modified graphene (with the adsorption of transition metal atoms) by using density-functional theory (incorporating van der Waals interactions) level of calculations in quantum ESPRESSO codes. We also use atomistic level of calculations to study the nature of methane-methane interactions in different liquid-media (water, methanol and acetonitrile).

Methane hydrates are stable in compressed states and thus relevant to the interior of giant icy planets and the earth. Earlier studies have indicated some controversial results regarding the stability of methane hydrates during the elevated pressure. Some studies have found that the compound is remarkably stable under extreme conditions like 1000 K of temperature and 86 GPa (Giga pascal) of pressure. However, a recent experiment has shown that the compound decomposes into its constituents, ice and methane, above 3 GPa. We use density-functional theory (DFT) level of calculations (with van der Waals interactions in relevant regions) and show that methane hydrate is thermodynamically unstable against decomposition above 4 GPa of pressure. The enthalpy difference between the compound and the constituents reaches a value of 0.45 eV per CH_4 molecule at 80 GPa, in favor of the constituents. Within the metastable region of methane hydrate, we also show that MH-III transforms into a high-pressure (HP) structure above 180 GPa. The new structure is characterized by a quasi one-dimensional arrangement of the methane molecules.

Two dimensional materials are relevant for the purpose of storing energy carrying gases like methane due to their (light) weight and large surface to volume ratio. We functionalize mono-layer graphene by single transition metal atoms to analyze the adsorption properties of methane molecule(s). Ten elements of 3d series in periodic table, Sc to Zn, are used to modify graphene. Metal-graphene complexes thus formed are useful to study their interactions towards tetrahedral methane molecule(s). Non-polar methane molecule(s), in the most symmetric configurations (straddle, tripod-towards and tripod-away), have been adsorbed on the most preferred geometries of such metal-graphene complexes. In addition to the adsorption energy of methane, various physical and electronic/magnetic properties of

the metal-adatom graphene (with and with out methane(s)) like: geometries, density of states, magnetic moment, redistribution of charge density have been calculated. The metal atoms whose 3d orbitals are partially filled (Sc, Ti, V, Fe, Co and Ni) have been found chemically bound (with binding energy higher than 0.8 eV). Atoms with half or completely filled 3d-orbitals: Cr, Mn, Cu, Zn have been found weakly bound (with binding energy lower than 0.6 eV), and follow the physisorbed properties. Our findings for metal-adatom systems agree with the previous studies. Unlike isolated metal atoms and graphene, adatom-graphenes develop their unique properties to hold methane within a wide range of adsorption energy, 0.04 eV to 0.91 eV per methane, depending up on the chemistry of metal species. On increasing the methane concentration (by double) on Sc, Ti, V, Fe, Co and Ni -adatom graphene, the adsorption energy per methane remains almost intact for the first group of three atoms (Sc, Ti and V) where as the quantity decreases almost by half for the next group of atoms (Fe, Co, and Ni). The values of average adsorption energy per methane molecule (when methane-dimer are adsorbed) have been estimated in between 0.35 eV to 0.56 eV.

The study of interactions between two methane molecules in different solvent environments can be a model research in understanding hydrophobic effects, and biological processes like protein folding and its denaturation. Based on MD simulations, our study has shown that the potential of mean force (PMF) between two methane molecules in liquid media (water, methanol and acetonitrile) is characterized by the deeper contact minimum (at around 0.38 nm to 0.40 nm) and shallower solvent separated minimum (in between 0.72 nm to 0.78 nm). Our results in water (as liquid media) agree with the previous studies. Our study implies that long-range interactions due to molecular dipoles of liquid media around the hydrophobes (methane) in combination with Lennard-Jones potential causes solvent separated minimum. The position of the contact minimum (of PMF) seems to be independent to the solvent environment. The position of solvent separated minimum, however, changes with the solvent-size, and found to be at 0.72 nm, 0.77 nm and 0.78 nm in water, methanol and acetonitrile, respectively. Furthermore, the desolvation barrier with reference to contact minimum have been estimated as 3.40 kJ/mol, 2.75 kJ/mol and 2.94 kJ/mol respectively. The binding energies at second minimum seems to be slightly varying with respect to their solvent media (values lie in between 0.31 kJ/mol to 0.28 kJ/mol). The analysis of the present study shows that the methane-methane interactions in methanol and acetonitrile is softer and long-ranged comparing to that in water. The results also imply that the presence of competitive methyl group methanol and acetonitrile might have caused for softer methane-methane interactions.

LIST OF ACRONYMS AND ABBREVIATIONS

AFM	Anti-ferromagnetic
AIM	Atoms In Molecules
B. E.	Binding Energy
BCP	Bond Critical Point
BOA	Born-Oppenheimer Approximation
BP	Bond-Path
CNG	Condensed Natural Gases
CNT	Carbon Nanotube
CP	Critical Point
CS-I	Cubic Structure-I
CS-II	Cubic Structure-II
DFT	Density Functional Theory
DFT-D2	Density Functional Theory - D2
DOE, US	Department Of Energy, United States
DOS	Density of States
ELF	Electron Localization Function
ESPRESSO	opEn-Source Package for Research in Electronic Structure, 3cm Simulation, and Optimization
eV	Electron Volt
FIIhs	Filled Ice Structure
FM	Ferromagnetic
GGA	Generalized Gradient Approximation
GPa	Giga Pascal
GROMACS	GROningen MAchine for Chemical Simulations
h-BN	hexagonal-Boron Nitride
h-BNC	hexagonal-Boron Nitrogen Carbon
H-K	Hohenberg - Kohn
HEG	Homogeneous Electron Gas

HF	Hartree-Fock
HP	High Pressure
HPZGNRs	Hydrogen Passivated Zig-zag Nano Ribbons
HSCoE	Hydrogen Sorption Center of Excellence
HSECE	Hydrogen Storage Engineering Center of Excellence
ICTP	Abdul Salam International Center For Theoretical Physics
K-S	Kohn - Sham
K. E.	Kinetic Energy
GGA	Generalized Gradient Approximation
LDA	Local Density Approximation
LJ	Lennard Jones
LNG	Liquefied Natural Gases
M/G	Metal on Graphene
MAGs	Metal Adatom Graphenes
MD	Molecular Dynamics
MH-I	Methane Hydrates-I
MH-II	Methane Hydrates-II
MH-III	Methane Hydrates-III
MOFs	Metal Organic Frameworks
NBO	Natural Bonding Orbitals
NETL	National Energy Technology Laboratory
NMR	Nuclear Magnetic Resonance
PBE	PerdewĂŞ Burke ĂŞErnzerhof
PBC	Periodic Boundary Condition
PDOS	Projected Density Of States
PMF	Potential of Mean Force
PW92	Perdew-Wang
PZ81	Perdew-Zunger
QE	Quantum ESPRESSO
RSAS	The Royal Swedish Academy of Sciences

Ry	Rydberg
S	Straddle
SCF	Self Consistent Field
sH	structure Hexagonal
sI	structure I
sII	structure II
STM	Scanning Tunneling Microscopy
SWCNTs	Single-Walled carbon NanoTubes
SWM	Scanning Tunneling Microscopy
TU	Tribhuvan University
TA	Tripod-Away
TDOS	Total Density Of States
TEM	Transmission Electron Microscopy
TFD	Thomas-Fermi-Dirac
TM	Transition Metal
TMOs	Transition Metal Oxides
TT	Tripod-Towards
TWAS	Third World Academy of Science
vdW	van der Waals
VWN	Vosko-Wilk-Nusair
WHAM	Weighted Histogram Analysis Method
XC	Exchange Correlation
XRD	X-ray Diffraction

LIST OF TABLES

LIST OF FIGURES

TABLE OF CONTENTS

CHAPTER 1

INTRODUCTION

Every part of the world is competing for the exploitation of currently available energy resources, mainly fossil fuels like coal, petroleum oils and gases for their daily needs and development activities (Chong et al., 2016; Makogon et al., 2007). The fossil fuels, so called conventional sources of energy, however, are going to be over in near future (Makogon et al., 2007). Also it has been understood that the excessive emission of carbon and other green house gases on the cost of exploitation of fossil fuels for luxury and material development has adversely affected the environment (Eslamimanesh et al., 2012). Green house gases are supposed to be the main cause of *global warming* (the continuous increases in temperature of the earth) which has endangered natural creation and human life. In this context, the search of environment friendly, or less pollutant sources of energy is more than compulsory. Methane in natural gas-resources like clathrate hydrates has been considered widely available unconventional source of energy, if their extraction becomes technically and economically viable (Mahajan & Mansoori, 2007). Methane clathrate structures are ice like solids which enclose the methane molecules inside them. Even though extraction of methane from its natural resources is one of the major challenges, its extraction, effective storage and transportation as an energy fuel is another hurdle for practical applications like vehicular transportation. Absorptive storage in light materials like porous carbon materials are supposed to be one of the options for such purpose (Menon & Komarneni, 1998; Wood et al., 2012). On the other hand, methane is the simplest alkane molecule and can be a model structure to understand the process in protein folding and its denaturation (Hummer et al., 1998). In this context, understanding methane in different environments like, methane hydrates, porous carbon materials and liquid media, is the first step for methane related multidimensional practical applications. In the present work, we will introduce methane-methane and methane-host interactions in clathrates, functionalized graphene and solvent environments.

1.1 Methane hydrates

The natural reserve of methane occurs within the clathrate structure of methane hydrates (CH_4-H_2O). As we discussed before, methane hydrates, including other gas hydrates, are mainly ice like cages (however different from the ordinary ices structures), where the gaseous molecules are encapsulated and compressed within the cages (Sloan Jr & Koh, 2007; Tulk et al., 2012). The cage structure is stable due to two factors (i) hydrophobic (repulsive) interaction in between the host (water cages) and guest (methane) molecules, and (ii) an attractive interaction in between water molecules in the cages (Sloan et al., 1998). These ice-like hydrates burn in contact with fire, upon release of methane, and are known as *fiery ice* meant for *burning ice* [Figure 1]. The empty cages are also unstable and get collapsed due to lack in balance of forces (Belosludov et al., 2002). Since the methane hydrates are stable only within the limited region of P-T diagram, mainly at high pressure and low temperature, they are unstable either on lowering the pressure or increasing the temperature (Eslamimanesh et al., 2012).

Figure 1: Methane hydrate, in contact with fire, burns upon release of methane. (`https://soundwaves.usgs.gov/2012/06/` dated: Jan 12, 2016.)

The first discovery of gas hydrate clathrates starts 200 hundred years ago (Davy, 1811; Loveday & Nelmes, 2008). Many small non-polar small gas molecules like H_2, CO_2, NH_3, CH_4 and some large polar molecules (tetrahydrafuran) have been investigated as the guest molecules in clathrate hydrates (Sloan et al., 1998; Loveday & Nelmes, 2008). The natural occurrence of gas hydrates is available at the particular conditions of temperature and pressure (Jeffrey, 1996; Petrenko & Whitworth, 1999), and methane hydrates in particular are found at the moderate compression and low temperature (300 bar at 22 °C, and 50 bar at 4 °C, the latter being typical conditions in the ocean floor) (Sloan Jr & Koh, 2007) as shown in Figure 2. The dissociation/decomposition of the gas hydrates release the gaseous molecules and water, and do not make chemical bonding in between them. Since methane gas causes a heavy green house effect, dozens of times more than CO_2 (Parry et al., 2007), its unwanted release from the

natural resources promotes cyclic effect of global warming (Dickens et al., 1995). Atomistic level of understanding of the physical, thermodynamic and structural properties of multiple hydrates helps to know the undergoing phenomena at different environmental conditions, and carries multi-dimensional applications like clearance of pipeline blockage (Sloan Jr & Koh, 2007; Sloan, 2003), understanding global warming phenomenon in academia (Dickens et al., 1995), enhancing academic thought for clathrate solids (Loveday & Nelmes, 2008), stability of sea floor (Kvenvolden, 1993) and potential of unconventional source of energy (Kvenvolden, 1988; Chong et al., 2016). The basic understanding of methane hydrate is also important for the separation (Kang & Lee, 2000), storage and transportation of energy carrying gases (Yevi et al., 1996; Eslamimanesh et al., 2012).

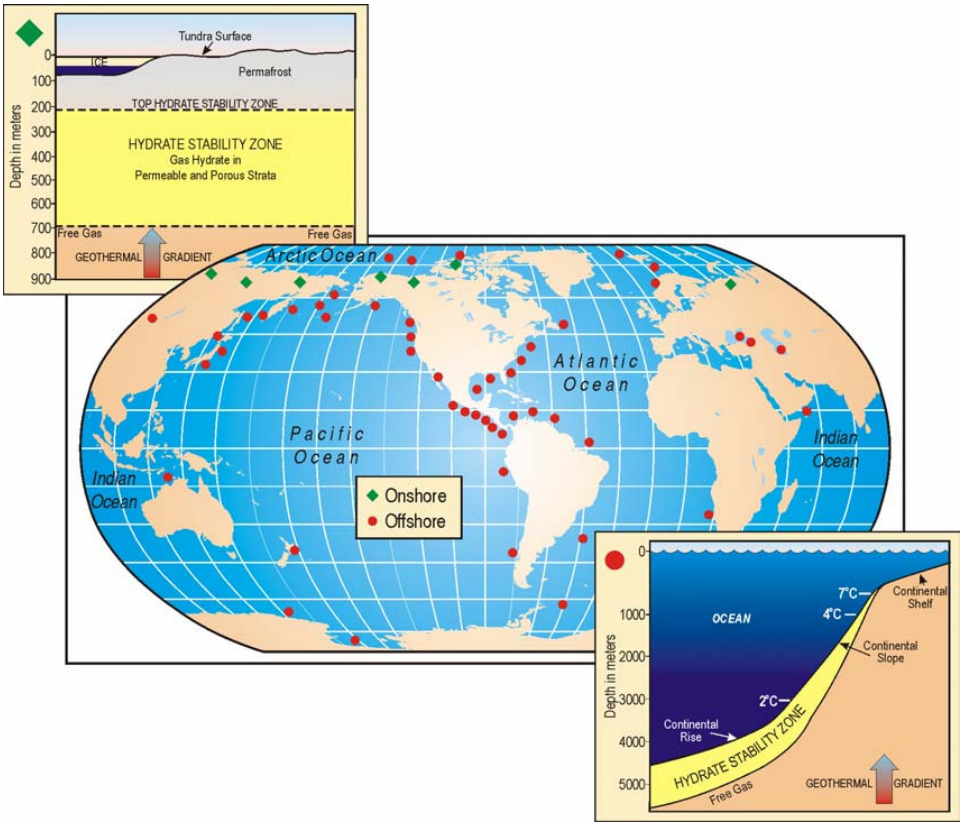

Figure 2: Worldwide locations of gas hydrate. Continental margins and permafrost regions are the rich area for gas hydrate (Brewer et al., 2002).

Since the methane hydrate is one of the major components of the interior of the outer planets and their moons like Uranus, Neptune, and Titan, its relevancy extends to the planetary science, and also to the outer Solar system, where they are supposed to be composed of methane-water mixture (Alibert et al., 2006; S.-i. Machida et al., 2006). On the earth, it is available at the conditions of permafrost regions in between 200-700 m and on the ocean floor in between 2000-4000 m as shown in Figure 2 (Sloan et al., 1998). The location and the

thickness of the hydrate slab are affected by the temperature, pressure, availability of methane gas itself, and other geological factors. The source of natural methane is supposed to be either from the biological activities at the level of ocean sediments or geological phenomenon in the deep of the earth (Brewer et al., 2002).

It is believed that carbon in methane hydrates is more than twice of the carbon available in currently exploited fossil fuel: conventional gas, oil and coal combined (Booth et al. (1996); Shu et al. (2011)). The United States, department of energy (DOE), has predicted a huge storage of natural methane in hydrates, and has reported that its partial extraction can fulfill the total national demand of energy for more than eight decades (Mahajan & Mansoori, 2007). Since methane emits less carbon on burning comparing to larger hydrocarbon systems, it is supposed to be cleaner source of energy. In addition to the abundant source of methane, methane-rich compounds are widely distributed in all around the world (Figure 2). This diversity in distribution is favorable to access methane hydrates at wider parts of the world and encourage more and more authorities to be involved in methane extraction process. Some of the countries like Japan and South Korea, whose increasing national demand of energy are being fulfilled with exporting their huge economy, have prioritized gas hydrate related research and industrial activities (Makogon et al., 2007).

Methane hydrates (MH) are also found to be present on man made pipelines carrying petroleum gas and oil, particularly to those which pass though the cold temperatures (Sloan et al., 1998). The formation of solid hydrates in pipelines is concerned to the flow (blockage of the pipeline) and safety issues of transportation of petroleum products. The knowledge of environmental conditions and inhibitors for the formation and decomposition of methane hydrates may help to get assurance of pipeline flow. Gas hydrates, on the other hand, can be the useful media for industrial sectors if they are used in proper way. They are applicable for the segregation, sequestration and storage of useful (like CH_4) and unwanted (like CO_2) gas molecules (Chatti et al., 2005). The process helps to reduce the green house gases in the environment (Rackley, 2009; Hester & Harrison, 2010). The knowledge of in/stability of gas hydrates is the fundamental requirement for the segregation of energy carrying gases like methane in natural hydrate stores (Makal et al., 2012). Since methane is compressed in hydrate structure, the volume of methane is 160 times the volume of ice at normal temperature and pressure (Mahajan & Mansoori, 2007), gas hydrates are the obvious choice for the effective storage and transportation of methane like gases (Ganji et al., 2007; S. Thomas & Dawe, 2003). The effects of surfactants and techniques to study the hydrate formation kinetics are

also the subject of interest (Daimaru et al., 2007; Rogers et al., 2007).

As we discussed in last paragraphs, the relevancy of gas hydrates in energy and industrial sectors is highly dependent on its structural stability. Figure 2 shows the stability zone of methane hydrates, and reveals that its clathrate structures are usually stable at the conditions of natural occupancy of hydrates, low temperature and high pressure (Sloan Jr & Koh, 2007). The clathrates at high pressure have thus attracted a large number of research activities from the academicians and industrial sectors to understand the formation, dissociation and changes in structural properties of gas hydrates (Loveday, Nelmes, Guthrie, Klug, & Tse, 2001; Hirai et al., 2004). They have reported some controversial results regarding its stability (Loveday & Nelmes, 2008) and dissociation (Shu et al., 2011) into its constituents during the elevated pressure. MH-III structure, also known as the filled-ice structure (FIIhS), is the highest pressure structure known till date (S.-i. Machida et al., 2006). It is supposed to be consistent to the interior of some of the icy planets and has been the subject of great interest for further study. Experiments have their limitations due to huge expenses, and unaccessible (extreme pressure and temperature) laboratory requirements. The computational facilities on the other hand, are being developed historically in the fastest rate which make larger systems accessible (Pakin & Lang, 2013) for simulations in extreme conditions.

Since methane is the major component of conventional energy resources and natural gas hydrates, its dominance in energy related territories in present and near future is understandable. Its extraction (from the natural stores), effective storage and transportation for practical applications are prime issues of methane related research and technology. The carbon nanomaterials with the selected functional groups as porous media are considered as potential candidates for light, safe and economic storage of natural gases.

1.2 Methane on Functionalized graphene

Adsorption properties of methane on two dimensional materials, including carbon nano compounds, are discussed under this section. We introduce the changes in properties of monolayer graphene as two dimensional material upon adsorption of impurity atoms (metal atoms) which are important to increase the reactivity of the substrates. Since graphene has light mass and high surface to volume ratio, increase in reactivity of such materials have additional advantage to store non-polar gases like methane with the desired range of binding strength (Carrillo et al., 2009). We will introduce implications of change in geometric,

electronic and magnetic properties of such materials upon adsorption of single metal atoms and small gaseous molecules like molecular methane and hydrogen.

Carbon combine to itself in varied ways and different hybridizaions to form many allotropes. They can be listed as nanotubes, nanoribbons, nanohorns, fullerenes and other newly developed carbon nano-families (Figure 3). Among the allotropes, diamond and graphite with sp^3 hybridization, are 3-dimensional materials (Geim & Novoselov, 2007). Carbon nanotube, on the other hand, is 1-dimensional material because of its (long) length comparing to other dimensionalities (X. Li et al., 2008). Fullerene is 0-dimentional material whose structure look like a football and is made up of 60 carbon atoms (C60) with 20 hexagons and 12 pentagons (Kroto et al., 1985).

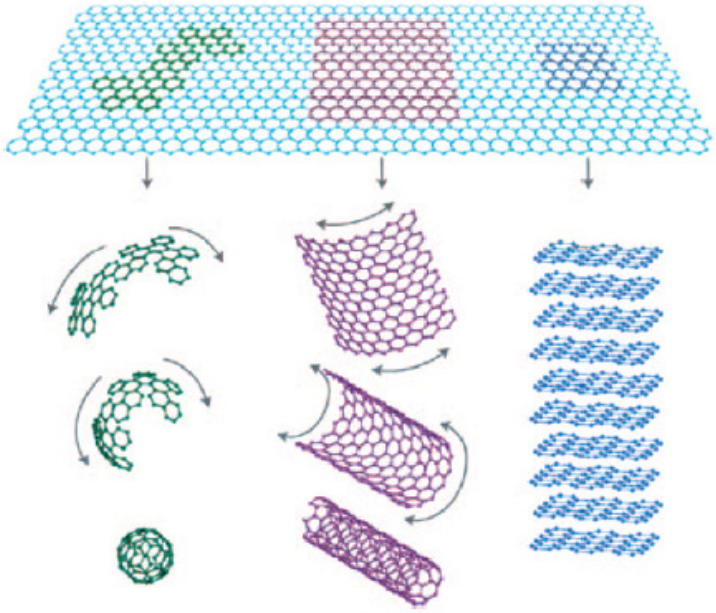

Figure 3: Graphene and its allotropes (Geim & Novoselov, 2007).

Graphene, an atom thick two dimensional honeycomb lattice, has a series of special electronic and physical properties. In addition, as a carbon material it is cheap, widely distributed and abundant in nature. Its exceptional physical strength, large surface area, high electrical and thermal conductivities, low noise effect and many more other interesting properties explore multiple possible applications (Novoselov et al., 2005; Schedin et al., 2007). Graphene with its high sensitivity towards external charge, magnetic field and mechanical strain, has controllably tunable band structure which deserves its application for industrial sectors like electronics (Han et al., 2014), spintronics (Hu et al., 2014) and chemical and gas sensors (Basu & Bhattacharyya, 2012).

Because of tunable graphene bands and well-developed experimental techniques at nano level, doped graphene including other carbon nanomaterials are becoming interesting areas for material scientists (K. T. Chan et al., 2008). Alkali-metal-doped carbon materials to fabricate the electronic devices (Radosavljević et al., 2004), and heavily doped Ti-adatom-graphene to adsorb CO_2 and CH_4 (Carrillo et al., 2009) have been tested with useful results. The adsorption of gaseous particles like molecular hydrogens in modified graphene with vacancies (Fair et al., 2013), and adatoms (Pantha, Belbase, & Adhikari, 2015) have also been studied for the purpose of storage and transportation of energy carrying gases. The results remark that modified graphene are superior over pure graphene for the adsorption of non-polar molecules (say molecular hydrogen) at operating temperature. Graphene has also been studied as a component of bilayer material (graphene-MoS_2 bilayer for an example) for the adsorption of molecular gases (Lamichhane et al., 2016). The comparison of adsorption properties of molecular hydrogen and helogens on bilayer structure show that two sides of heterostructure behave differently towards the gaseous molecules (Paudyal et al., 2015).

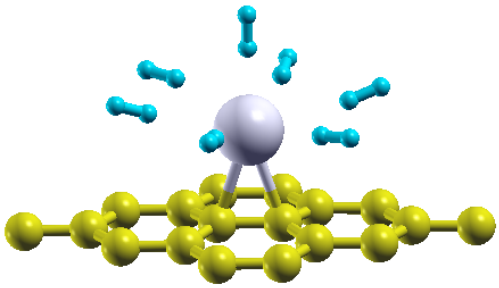

Figure 4: Adsorption of molecular hydrogen on Pd adatom graphene (Pantha, Khaniya, & Adhikari, 2015).

As discussed in previous paragraphs, methane is one of the widely used natural sources of energy. Besides its dominant presence in nature, methane is superior over conventional petroleum oil and fossil fuels mainly due to two main reasons. First; methane carries more energy due to its higher hydrogen to carbon ratio and the second; it is more environment friendly as methane emits less carbon on burning (Black et al., 2010; Ma & Zhou, 2010). However, the traditional methods of its storage and transportation; compressed natural gases (CNG) and liquefied natural gases (LNG), are always the subject of debate due to space, weight and safety related issues especially for vehicular (fuel) applications at operating conditions (Mason et al., 2015; Casco et al., 2015). Adsorption of methane in suitable

substrates like two dimensional light materials such as modified (by functional groups) graphitic materials with right order of binding has been considered as one of the options for reversible storage (Wood et al., 2012; Kandagal et al., 2012). Modification of pure graphitic substrates with metal atoms also improves the reactivity of such materials and increases the binding strength towards the nonpolar adsorbates (Lamichhane et al., 2014). A wide range of transition metal atoms in graphene and nanotube surfaces have shown that most of the metal adatoms are useful for improving the binding strength towards molecular hydrogens (Valencia et al., 2015; Pantha, Khaniya, & Adhikari, 2015). Note that reversible storage of energy carrying gases requires moderate range of adsorption energy (eg. in the order of 0.2 eV for hydrogen and methane), where very high adsorption energy requires extra energy to release and very small adsorption energy does not hold the gases at high (room) temperature (Bhatia & Myers, 2006). Because of their incomplete inner shells, transition metal atoms have tunable properties during their interaction with other materials and considered them in metal clusters for metal organic frameworks (MOFs). MOFs are being designed as porous materials to store energy carrying gases (Ma et al., 2008).

Adsorption of methane by graphene-oxide systems have been recently studied by Chouhan et al. (Chouhan et al., 2015). The authors have noticed significant increment of adsorption energy (up to 50 %) due to modification with oxides where the vdW interactions are shown to be crucial. We incorporate London dispersion forces as vdW interactions to study the effects of transition metal adatoms from 3d series (Sc to Zn) on graphene for binding of molecular methane(s).

1.3 Methane-dimer in solvent environment

Hydrophobicity of non-polar molecules in water is characterized by low solubility of solutes and strong like-molecular attractive interactions (Sharp et al., 1991; Scheraga, 1998). It can also be defined by the aggregating property of hydrocarbons in water/aqueous-solutions where the water molecules are excluded by the hydrophobes (McNaught & Wilkinson, 1997). Hydrophobicity mainly includes two aspects of the interactions; (i) the effect of solute particles on surrounding solvent molecules, defined by hydrophobic hydration, and (ii) the tendency of solute particles to aggregate, defined by hydrophobic interaction (Raschke et al., 2001). Because of hydrophobic hydration, water molecules make a spherical shell around the nonpolar solutes (methane for an example). On the other hand, solute particles and

nonpolar residues in proteins aggregate to expose less surface area to water, which is related to hydrophilic interaction. Solvent perturbation in solute-solute (hydrophobic) interaction is one of the model systems of biological processes in protein- (or/and protein like molecules) structure, folding, functions and denaturation (Gekko et al., 1998; Hwang et al., 2011). It has also been observed that the strength and magnitude of hydrophobic properties are affected by the size and nature of the solute particles, and also the temperature and pressure of the solvent environment (Makowski et al., 2009).

Hydrocarbons are the major components of biological molecules (including proteins) and are widely considered to study hydrophobic processes. Proteins are made up of a long chain of amino acids with side-chain residues in different arrangements (Leach, 2001). The interior of natural proteins is found to be occupied by the non-polar hydrophobic groups, which usually govern their structural stability. The surfaces, on the other hand, are covered by (charged) polar molecules, and play an important role in the formation/breaking of hydrogen bonding, a common process of solvent-solute interactions in hydrophobic effect. The hydrophobicity is also influenced by the variation in surrounding pressure - on increasing pressure water molecules are forced into the hydrophobic core and favor to denaturation (Hummer et al., 1998). Solvent induced interactions are noted in wider physical processes like surfactant coagulation, complexation, detergency and the formation of gas clathrates (Sobolewski et al., 2007).

The effect of temperature has been noted in protein structures. On rising temperature, the hidden nonpolar amino acids at the interior of proteins are exposed to water upon their unfolding/denaturation due to rising temperature (Dill, 1990). The enthalpic and entropic parameters are the indicators of hydrophobic effect, and thus finally play a vital role for protein folding and denaturation. Nearby room temperature, temperature effects are mainly driven by the entropic contributions (Privalov & Gill, 1988). For folded amino acids in water, where protein residues are more ordered with less exposed surface area, the entropic change is negative and the structure is favorable comparing to the removal of those molecules from water (Scott & Hildebrand, 1950). Dispersion interactions and point charge electrostatics are also important to identify the structural stability of side chains in aminoacids, and the same help to determine the nature of folding (Raschke et al., 2001). As the simplest hydrocarbon, methane is considered to model organic molecules within the solvent environment, which is important in biochemical processes (Dang, 1994).

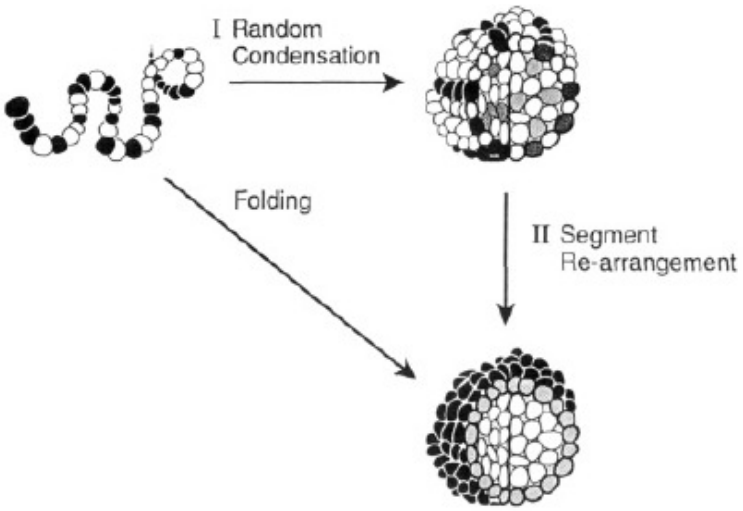

Figure 5: Process I represents random compactness of the chain and the process II represents the rearrangement to more stable configuration, where the nonpolar groups move into the core (Dill, 1990).

Solvent induced solute-solute interactions, where hydrophobicity is the primary concern, can be described in terms of changes in free energy as the function of reaction co-ordinates (separation between the solute molecules). This is equivalent to the potential of mean force (PMF) in between solute particles in aqueous solution (Hotta et al., 2005; J.-L. Li et al., 2007). PMF is generally characterized by the nature of contact minimum, desolvation barrier and solvent separated minimum which are controlled by the molecular size of solvent medium in addition to the inherent interactions in between the solutes (Sobolewski et al., 2007; Leach, 2001). Also the dynamics of the system due to modulating effect of solvents through collision and viscus drag force can be expressed in terms of PMF.

Experiments lack the microscopic details to study the atomistic level of interactions. For example: X-rays diffraction requires the crystal environment and can not observe the disordered conformations (Hwang et al., 2011). Nuclear magnetic resonance (NMR) can identify intermolecular interactions, however, lacks high resolution of molecular parameters, their dynamics and the process of governing protein structure. The details, on the other hand, can be achieved through computational simulations like molecular dynamics (Allen & Tildesley, 1989). Computer modeling can thus be a source of information for the prediction of ongoing process in any system which can be verified by the following experiments (Raschke et al., 2001). Furthermore, limitations of computer simulations have been addressed in later modifications. Umbrella sampling simulation is a technique accommodated in GROMACS (*GROningen MAchine for Chemical Simulations*, a popular software for the method of molecular dynamics) which insists to visit every part of the energy landscape in PMF with the

help of biasing potential. This is specially preferred for the rarely visited configurations in normal molecular dynamics (Kästner, 2011). We use this technique as an enhanced sampling approach to study methane-methane interactions in different solvent environments.

1.4 Rationale of the study

Methane in hydrates are important because of their dominant occupancy in nature. As a major component of natural gases, and less pollutant hydrocarbon than conventional sources like petrolium oil and gases, stability of methane in the conditions of natural occurrence is important. For the practical purpose like for on-board applications, on the other hand, effective storage media are demanding. Since methane-methane interactions are affected by the environment where they sit on, similar to proteins in human body, the perturbation of liquid media on methane-methane interactions are to be understood.

There are controversial reports regarding the stability of methane hydrate (CH_4-H_2O) compounds. Some of the reports show stable high pressure phases of methane hydrates like FIIhS (MH-III) and post-FIIhS structures, up to 86 GPa of pressure and 1000 K of temperature. However, a recent experiment indicates the decomposition of methane hydrate into its constituents above few GPa of pressure. In this context, detail study of the stability of methane hydrates at high pressure (up to hundreds of GPa) including possibility of its decomposition or/and transition of MH-III structure into another (high pressure) structure by using any reliable method is one of the frontier research topics.

Molecular distortions are difficult to see experimentally, because they involve hydrogen (H), which is a low X-ray scatterer. Hydrogen can only be seen with neutrons, but the sample size limitations do not allow to push neutron studies above $(10 - 20)$ GPa. The structural features of methane hydrate up to high pressure (say few hundreds GPa of pressure), relevant to the geo-planetary regime, can be calculated with the help of computational methods. Computational methods are highly useful to attain clathrate like compounds at extreme conditions where the experiments have limitations due to high expenses and technological barrier. Ab-initio calculations predict interesting (and so far unexplained) structural features and thermodynamic properties of methane hydrates with reference to its constituents at high-pressure. The properties can be considered important indicators to study the structural preferences and possible changes in phase. The results from the computation are expected to be verified by experiments in near future with the development of new technologies.

Besides the dominant presence of methane in nature, it is beneficial over the conventional petroleum oil and fossil fuels because of its higher energy density and less emission of carbon on burning. The conventional techniques of storing natural gases as well as other energy carrying gases need either very high pressure or very low temperature. The techniques are not efficient due to space, safety and economy related perspectives. On the other hand, adsorption of methane on porous solid media like carbon nanomaterials are being heavily searched as alternatives since last few decades. Pure graphene and graphitic materials are unfit for the purpose of reversible storage of methane for practical applications due to their low temperature desorption properties. The recent scientific works, therefore, are trying to find different forms of carbon-metal combinations so that they show a good performance for storing methane at operating conditions. Use of TM atoms (of 3d series in periodic table) to functionalize graphene and study their optimized geometries, electronic properties and charge redistribution to check their usefulness for adsorbing methane with appropriate strength. One can find the right proportion of methane on functionalized monolayer graphene for its optimal storage.

Methane-methane interactions in different liquid media can be a model research to understand the hydrophobic interaction in atomistic level. Understanding of such interactions is important in biological processes including protein folding and its denaturation. Previous reports, based on MD simulations, have shown that the potential of mean force (PMF) between two methane molecules is characterized by the deeper contact minima (at around 4 angstrom) and shallower solvent separated minima (at around 7.3 angstrom). It has been reported that the solvent molecules, like water, induce dipoles around the surface of (hydrophobic) methane molecules, and the dipole-dipole interaction in combination with Lennard-Jones potential, creates an effective potential. This effective potential incorporates long-range interaction which is responsible for the solvent separated minima. Our aim is to probe the effect of different solvent environment like water, methanol and acetonitrile on methane-methane interaction as a function of distance. We use enhanced sampling simulations like umbrella sampling in GROMACS. The comparison of PMF between two methane molecules with the available results will check the reliability of our method. Similar calculations, in methanol and acetonitrile will show the effect of different liquid molecules on methane-methane interactions.

1.5 Objectives of the study

Present work studies the interactions of methane molecules within themselves and host materials in different environmental conditions. The main objectives of this thesis are summarized as follows.

(i) We aim to study the changes in geometrical parameters and thermodynamic stability of methane hydrates as a function of pressure up to hundreds of GPa. First-principles study of methane hydrates has an advatage of meeting extreme conditions, like very high pressure, which are not possible in real experiments due to economic and technological barriers.

(ii) We use TM atoms (of 3d series in periodic table) to functionalize graphene and study their optimized geometries, electronic properties and charge redistribution to check their usefulness adsorbing methane (one of the major energy carrying gases) with appropriate strength. Since pure graphene and graphitic materials are unfit for the purpose of reversible storage of methane at operating conditions due to their low temperature desorption properties, we aim to find the appropriate metal atom(s) to enhance adsorption energy of methane in light two-dimensional substrates.

(iii) We aim to probe the effect of different solvent environments like water, methanol and acetonitrile on methane-methane interactions as a function of distance. Umbrella sampling in GROMACS helps to calculate the potential of mean force (PMF) between two methane molecules in different solvents.

1.6 Organization of the thesis

The structure of this thesis is organized as follows:

(i) In chapter 2, we shall discuss the available literature related to the present work. The chapter is named as Literature Review, which aims to prepare the required background and justify the objectives of the current work.

(ii) We present the theoretical background, necessary formulas and algorithm that we have used during the entire work in Materials and Methods (Chapter 3). Basic introduction of density-functional theory and molecular dynamics with some special features including the systems under study are discussed in the chapter.

(iii) Chapter 4 presents and discusses the main findings of the present work. Section 4.1 introduces the background for the whole chapter. Section 4.2 deals with the structural and thermodynamic stability of methane hydrate (MH-III) against its constituents (solid methane and ice) during the elevated pressure up to 300 GPa. In section 4.3, we present the adsorption properties of methane on pure and functionalized (by metal atoms) graphene. We have checked the changes in reactivity of monolayer graphene towards the non-polar gases like methane and hydrogen upon its functionalization with single metal atoms, and we report changes in adsorption properties of methane on such modified graphene. Methane-methane interactions in different solvent media is an important model reaction for biological systems and we include water, methanol and acetonitrile as solvents in the present work. This part of results are discussed in section 4.4.

(iv) The conclusions and possible extension of the present work are discussed in Chapter 5. The chapter is named as "Conclusions and Recommendations". "Summary" is mentioned in chapter 6. Finally the references are listed before closing this document.

CHAPTER 2

LITERATURE REVIEW

We present the review of relevant literature in this chapter. We go through the literature related to methane in clthrates, and functionalized graphene. The graphene could be functionalized by sigle metal atom, dimers or any functional groups. We also discuss the effect of solvents on methane-methane interactions.

2.1 Methane in clathrate structures

The clathrate structures of gas hydrates have been noticed since more than two centuries. Even though there are few reports regarding the experiment performed by Joseph Priestley in 1778 who observed ice like structure impregnated with alkaline air (NH_3), there are no evidences that the observed structure was hydrate (Sloan Jr & Koh, 2007). The well-accepted credit for the pioneer work on clathrates of gas hydrates goes to Sir Humprey Davy, who discovered chlorine hydrate clathrates in 1810 (Davy, 1811). After his discovery, the progress of research activities in natural gas hydrates has been descried mainly in three phases. The first phase of development discusses gas hydrates as the matter of scientific curiosity which went through more than a century for their structure/composition in scientific laboratories. The second phase is related to the recognition of gas hydrates in petroleum pipelines as a hindrance due to blockage of proper flow of oil and gases passing through the freezing temperature. In this way, almost for thirty years starting from the middle-thirties of twentieth century, gas hydrates were the subject of industrial interest in addition to the scientific curiosity (Hammerschmidt, 1934). The gases as guest molecules in the clathrate were methane, ethane, propane and isobutane. From the mid-sixties of twentieth century till the date (the third/latest stage) gas hydrates have been observed at natural occupancies by being recognized in multidisciplinary applications like planetary science and alternative source of energy (Arora & Cameotra, 2015). The recent

works have also revealed the techniques to exploit methane from their natural occupancies for energy resources (Chong et al., 2016). Hence beginning from the prediction/recognition of gas hydrates, the development passes through finding their stability regions, structural changes with environmental conditions, and finally to the establishing prerequisites for extracting methane from remote resources.

Because of the increasing area of interest and method of investigations, the subjects related to gas hydrates have attracted scientific and industrial communities especially since last two decades. The popularity could be understood on the basis of number of publications, eg: the publications related to gas hydrates crossed 400 during 2005 alone comparing to the total 40 publications during more than one century just after its first discovery in 1811 (Sloan, 2004). Google scholar shows this number more than 15000 in 2015 only (dated: 26 August, 2016). At the beginning time of gas hydrate era, research activities were focused to identify the compounds forming hydrate structure and their quantitative composition. They were mainly carried out with the direct method of measurement (usually through chromatography). However, the exact measurement of water to gas ratio in hydrates (called hydration number n) via such method was challenging due to excess water in hydrate mass (Sloan Jr & Koh, 2007). Indirect methods developed in later time, where the information of heat of formation above and below the ice point, were used to be crucial. In the modern time, both the approaches (direct and indirect methods) are used with the latest technology in which hydration number can be achieved through X-rays and neutron diffraction (Udachin et al., 2001), and also via Raman (Sum et al., 1997) and NMR (Davidson et al., 1983) spectroscopy.

Professor D. L. Katz and his group with the information of experimental study, found two different methods to predict the hydrate formation conditions for the given composition of gases. One of them is based on the distribution coefficient of gas hydrates (Wilcox et al., 1941), and another one is related to the hydrate formation pressure with reference to the gravity of gases (ratio of molecular wt. of gases to air) (Katz et al., 1945). The techniques were also useful to calculate the hydrate formation conditions for the mixture of gases without costly and time consuming experiments, which leaves positive impact in industrial sectors (Stackelberg & Müller, 1951).

The equilibrium (time-independent) properties of gas hydrate could be studied by using the thermodynamic parameters. However, they do not explain the kinetic and transport properties which are relevant to the pipeline flow of petroleum products. We need time-dependent prop-

erties to understand the dynamics of such a system which controls the structure and stability of hydrate plugs. Hence the technique shifts from hydrate avoidance (thermodynamic conditions avoiding hydrate stability zone) to hydrate risk management. The hydrate risk management is related to the prevention of hydrate particles from nucleations. Time-dependent research activities started during mid-1990s and developed through size-dependent observations like macroscopic (Nerheim et al., 1994), mesoscale (Staykova et al., 2003) and microscopic measurements (Koh et al., 1996).

Stackelberg and his colleagues concluded two cubic type hydrate structures on the ground of two decade-long experiments (Stackelberg & Müller, 1951). The authors classify the structure I (sI) and structure II (sII) for small gas molecules (Cl_2, SO_2, Br_2 etc.) and larger molecules (CH_2Cl_2, $CHCl_3$ etc.), respectively. With more examples of small and larger gas molecules, McMullan and coworkers verified those two crystal unit cells ubiquitous in hydrates (Mak & McMullan, 1965; McMullan & Jeffrey, 1965). Two decades later, Ripmeester et al. discovered hexagonal hydrate structure (sH), which requires both the small and large gas molecules for stability (Ripmeester et al., 1987). Hence the common gas clathrates (Lattin word which means *in cage*) were defined in three structures, sI, sII and sH, mainly on the basis of size of guest (gas) molecules.

Dyadin et al. were the pioneer group to study methane hydrates at high pressure (Dyadin et al., 1997). The authors showed structural change of methane hydrates from sI type to the denser sII structure, during the elevated pressure up to 6 kbr. They also showed temperature and pressure dependent dissociation properties of methane hydrates into ice/water and methane, where the dissociation temperature increases for denser structure s-II. The phase diagram describing the structural stability with respect to its constituents and other high pressure structures were revealed in the later works (Hirai et al., 2001; Loveday & Nelmes, 2008). In addition, multiple gas molecules in the larger cages were also realized during the late 1990 and early 2000 (Kuhs et al., 1997).

The common cubic structures of gas hydrates, sI and sII, are also known as cubic structure I (CS-I) and cubic structure II (CS-II). At lower pressure regions, majority of gas hydrates remain in either of these two common cubic structures (Stackelberg & Müller, 1951; Loveday & Nelmes, 2008). Methane hydrates, in particular, are usually found in CS-I, also known as methane hydrate I (MH-I), at low pressures. The unit cell of MH-I is made up of two type of cages, two small and six large, with the space group of $Pm3n$. The small and large cages are

composed of pentagons and the combination of pentagons and hexagons of hydrogen bonded water molecules, respectively. With a single methane molecule at each cage and 46 water molecules, water to methane ratio becomes 5.75:1 (Stackelberg & Müller, 1951). Loveday et al. (Loveday, Nelmes, Guthrie, Belmonte, et al., 2001) and Shimizu et al. (Shimizu et al., 2002) with the help of X-rays diffraction study and Raman spectroscopy, discovered that MH-I structure changes to methane hydrate II (MH-II) structure, which is usually consistent to CS-II structure, at around 1GPa. Chou et al. (Chou et al., 2000), however, showed the possibility of hexagonal structure for MH-II clathrates. Since MH-II is denser for methane with water to methane ratio of around 3.6:1, ice-VI is produced as a byproduct during this transformation. Further compression of MH-II may also follow one of the two possible options, (i) changes to new phase of methane hydrates, known as MH-III or (ii) dissociates into methane and ice VII (Loveday, Nelmes, Guthrie, Belmonte, et al., 2001). Quick compression of MH-II dissociates into its constituents, however, the gradual compression of MH-II changes to MH-III above 2 GPa (Loveday, Nelmes, Guthrie, Klug, & Tse, 2001; Hirai et al., 2004). The unit cell of MH-III is orthorhombic in structure, closely related to that of ice-I*h*, and also known as filled ice structure (FIIhS). The rate dependent phenomenon of Mh-II as the function of increasing pressure shows that methane and ice are only metastable against MH-III and the formation of MH-III is kinetically hindered due to the large energy barrier.

As discussed in last paragraph, using a combination of X-rays and neutron diffraction experiments, Loveday et al. (Loveday, Nelmes, Guthrie, Klug, & Tse, 2001; Loveday, Nelmes, Guthrie, Belmonte, et al., 2001) solved the structure of MH-III up to few GPa of pressure. MH-III was found to be richer in methane, comparing to MH-I and MH-II structure, with water to methane ratio 2:1. Methane hydrates do not retain the cage structure in MH-III anymore, rather, the guest (methane) molecules reside into the hydrogen bonded ice channels. The experimental study of gas hydrates under very high pressure have their own limitations especially because of two reasons: (i) it is difficult to achieve the extreme conditions (high pressure) in laboratory due to technological barrier, (ii) the experimental set up is very expensive. For example: neutron experiments, performed by Loveday and his coworkers, were limited to a maximum pressure of 10 GPa and the hydrogen positions could not be refined with precision. Hirai et al. (Hirai et al., 2003, 2004) with the help of X-rays diffraction and optical observations claimed that filled ice Ih structure (FIIIhS) of methane hydrates survives until 42 GPa with the anisotropic compression of the sample. The unit cell volume of the structure was found to be compressed by 40 % at 40 GPa comparing to that at 3 GPa. Machida

et al. (S.-i. Machida et al., 2006; S.-I. Machida et al., 2007), using a combination of X-rays diffraction and Raman spectroscopy, reported evidence for a phase transition at 40 GPa. The authors (S.-i. Machida et al., 2006), however, ruled out the possibility of decomposition of methane hydrates into its constituents (methane and ice) up to 86 GPa and 1000 K. Based on oxygen-oxygen distances, Hirai and coworkers, on the other hand, reported that the phase change observed in X-rays diffraction pattern at around 40 GPa could be related to the symmetrization of hydrogen-bonds (Hirai et al., 2003; Tanaka et al., 2013). Theoretical studies based on density-functional theory confirmed the structural data for MH-III and pointed out that hydrogen-bond symmetrization takes place in methane hydrates at lower pressure than in pure ice (Iitaka & Ebisuzaki, 2003).

Lee and Scandolo (J. Y. Lee et al., 2011) carried out density-functional theory based molecular dynamics calculations for a liquid mixture of methane and water at the conditions relevant to the interiors of giant planets like Uranus and Neptune (hundreds of giga-pascal of pressure and thousands kelvin of temperature), and suggested that repulsive interactions in between methane and water is reduced due to their ionization at extreme conditions. The consequences of ionization could be felt with a pressure-induced enhancement of the two species to mix. Differing with most of the above reports, an experiment performed by Shu et al. found that methane hydrate decomposes into its constituents, water and methane, at pressures as low as 3 GPa (Shu et al., 2011). Thermodynamic stability of a compound can in principle be determined theoretically by evaluating the enthalpy of formation. In the particular case of methane hydrates the task is simplified by the knowledge of the crystal structure of MH-III, solid methane and ice upon the compression until 300 GPa.

Even though clathrates of gas hydrates themselves are supposed to be a good medium to store and transport energy carrying natural gases like methane, traditional methods of storage, i e., liquefied gases at very low temperature (LNG) and compressed gases at very high pressure are still in practice. However, the traditional methods have limitations due to space, cost and safety related issues, and scientists have been involved to find an alternative media like two dimensional graphitic materials for such purpose. Consistent to all these alternative systems, we study the single metal atom adsorbed monolayer graphene for adsorptive storage of methane.

2.2 Methane on pure and functionalized graphene

Graphite is made up of multiple graphene layers which are coupled weakly by vdW interactions. The compound is one of the early known materials (around 1564) with the invention of pencil as an instrument for writing (Petroski, 1992). Few layer of graphene stacks might be generated while writing by a pencil in a paper, and somewhere a single layer could have also been unknowingly produced hundreds of years prior to the formal isolation of graphene in 2004 (Novoselov et al., 2004). Professors A. Geim and K. Novoselov were the first who formally isolated a single graphene layer in laboratory and were awarded by the Nobel Prize in physics in 2010 for their 'ground breaking experiment' (Norrby, 2010; Geim, 2011). The scientists duo with their co-workers noticed one atom thick carbon layer among few-layer flakes of graphene peeled off from a bulk graphite (Novoselov et al., 2004). The phenomenon was observed with an ordinary optical microscope on the top of 300 nm thick silicon wafer (SiO_2) (Abergel et al., 2007), in addition to the sophisticated instruments like atomic force microscopy (AFM), transmission electron microscopy (TEM), scanning tunneling microscopy (STM) etc. (Rao et al., 2009).

P. R. Wallace was the first person studying band structure of graphene, not as a stable two dimensional substrate that is widely discussed in the present time, but as a building block of graphite (Wallace, 1947). It is because the existence and stability of 2D materials including single graphene layer was out of thought. Graphite, on the other hand, was assumed to be an important material for the nuclear reactors. Its electronic structure along with the structural arrangement was a matter of interest for a number of studies during the following years (Neto et al., 2009). Slonczewski, Weiss and McClure developed SWM (Slonczewski-Weiss-McClure) model to describe the band structure of graphite with its two-dimensional lattice structure using tight binding calculations (McClure, 1957; Slonczewski & Weiss, 1958). During their study, the authors found a meeting point in between valence and conduction bands, calculated the concentration of charge carriers (holes and electrons), and successfully described experimental data (McClure, 1958). Graphite was then considered a material composed of two-dimensional stacks of carbon layers, however, the model was unable to describe vdW interactions in between the adjacent layers. It was revisited during the early years of twenty-first century with the help of many body problems which was out of practice during the early SWM studies (Rydberg et al., 2003). Once the stable existence of monolayer graphene was revealed in 2004, its relevancy has been geometrically expanding on the search

of interesting properties of graphene and other two dimensional materials for various potential applications (Restrepo et al., 2014).

The basic structure of graphene and its series of special physical/electronic properties have been reviewed by a number of authors (Rao et al., 2009; Neto et al., 2009; Liu et al., 2013). The basic structure includes its composition (composed of carbon atoms in two dimensional honeycomb lattice), sp^2 hybridization between the s and p orbitals of carbon atoms that leads to the formation of planar structure of graphene, C-C bond length (1.42 Å) and its strength (due to the σ bonding in between sp^2 hybridized orbitals) at minimum energy structure, in addition to the other properties which are not mentioned here (Neto et al., 2009). The band structures, on the other hand, are related to the electronic properties which are mainly determined by the p_z-orbitals (perpendicular to the plane). P_z orbitals do not participate in hybridization of the orbitals and cause for the half-filled π band. The band structure further reveals that π and π^* bands of graphene meet at a single point of the Fermi level, where the electrons behave as mass-less Dirac particles with exceptional properties like linear dispersion relation, the foundation for potential applications (Liu et al., 2013). Because of growing allotropes, and tunable thermal, electronic and mechanical properties through appropriate modifications, graphene has recently become a leading section of solid state physics and material science.

Modifications of graphene and graphitic materials have shown potential of various applications in multiple areas and are being searched by thousands of researchers. Substitution of some of the carbons in graphene with the suitable number of borons and nitrogens, forms a wonderful hybrid material composed of carbon, boron and nitrogen (h-BNC). The properties of h-BNC are different from those of doped graphene and hexagonal boron-nitrides (h-BN), basically because of their band gap engineering. The new materials are shown to be applicable in electronics and optics (Ci et al., 2010; Mukherjee & Kaloni, 2012; N. Singh et al., 2013). Different level of vacancies and oxidized monovacancies on graphene were considered by Singh et al. (N. Singh et al., 2013) to study optical spectrum of the modified compound comparing to that of bare graphene. Spintronic and nanoelectronic applications are also revealed by Kaloni et al. (T. P. Kaloni et al., 2011) with their study on multilayer graphene in different type of stacking and other graphitic arrangements with intercalated transition metal atoms. The authors showed changing band structure and magnetism in some of the combinations which could be the foundations for further development of materials.

Substitution of carbons (in graphene) by boron and nitrogen impurities does not break its hexagonal symmetry due to their comparable size and atomic weights. Also the process of doping of these atoms is similar to the p- and n-type impurities in silicon semiconductor, where a small proportion of impurities heavily change conductivity and band gap of new materials. The use of impurities thus make materials possible using in semiconductor applications. A number of studies have been devoted to see band structure properties of doped graphene so that the corresponding silicon devices for a wide range of conductivity could be replaced with carbon nanostructures (Mukherjee & Kaloni, 2012; T. Kaloni et al., 2014). Doped graphene properties are highly dependent to the impurity atoms, like doping of Li metalize the graphene ribbons (Ataca et al., 2008) dissimilar to doping of boron and nitrogen which aim to replace silicon semiconductors. Li-doped graphene is also observed as a good adsorbate for hydrogen storage device. Tunning of magnetic and other properties of graphitic materials have been observed through a number of techniques like: via vacancies (Ugeda et al., 2010; T. P. Kaloni et al., 2012), atomic/molecular doping (Saha et al., 2009; R. Thapa et al., 2011), functionalization (Wood et al., 2012), irradiation (Esquinazi et al., 2003) and external fields (Park & Louie, 2010). These modifications have shown their relevancy in the filed of electronics (Geim, 2009), spintronics (Palacios et al., 2008; J. Ding et al., 2011), chemical sensors (Saha et al., 2009), and energy storage (Pumera, 2011; Dai et al., 2012).

Adsorption of metal atoms on graphene and other carbon nanomaterials have been studied by a number of authors to find modified material properties (Duffy & Blackman, 1998; K. T. Chan et al., 2008; Valencia et al., 2010; Longo et al., 2011). Duffy et al. performed spin polarized calculations to study 3d series of TM atoms on planar graphite surfaces, showed the stable geometries and site dependent magnetic behavior of adatoms. Chan et al. by using DFT level of calculations studied adsorption of 12 different metal atoms from groups I-III of the Periodic Table on monolayer graphene to see multiple properties like adsorption energy, density of states (DOS), magnetic moment, work function and charge transfer in between the constituents of final geometries. The authors also predict the nature of bonding in between the metal and carbon atoms on the basis of magnitude of charge trnsfer. Longo et al. (Longo et al., 2011) have also performed a first-principles study of adsorption of few metal atoms and their dimers from transition group (3d, 4d, and 5d) elements in hydrogen-passivated zig-zag nanoribbons (HPZGNRs). The authors find the most stable adsorption sites, geometries and changing magnetic behaviour of metal atoms due to hybridization in between metal d-orbitals and carbon 2p orbitals. Valencia et al., on the other hand, performed similar calculations

for nine metal atoms of 3d series (Sc-Cu) on monolayer graphene and single-walled carbon nanotubes (SWCNTs). The results of their work analyze the energy level of individual orbitals and nature of hybridization in between metal and carbon atoms. The authors reveal the reasons behind the physisorption and chemisorption of metal atoms on the substrate, and show a chevron curve for binding energy of metal atoms while moving from left towards right in the periodic table with the explanation using Pauli's principle. The interlayer separation in between graphene planes was maintained as 20 $\mathring{A}$ by keeping possibility of H_2 adsorption for energy storage in mind, which is recently published by the authors (Valencia et al., 2015).

Hydrogen, either in gaseous form or as a component of abundant compounds like water and hydrocarbons, is widely available energy resource in the Earth and extra-terrestrial planets. As hydrogen releases only the water vapour when it burns, it is considered as one of the clean and green source of energy. Because of larger proportion of hydrogen (comparing to other hydrocarbons) and availability of related compounds in the Earth, methane is considered to be an easy resource of hydrogen in addition to molecular hydrogen itself. In spite of being a potential gas for future energy carrier, user friendly storage and transportation has become one of the major challenges. There are a number of traditional techniques which have been in practice to store natural gases and hydrogen; like in tanks under high pressure (Compressed natural gases, CNG) (Burchell & Rogers, 2000; Düren et al., 2004) and in cryogenic vessels at low temperature (Liquefied natural Gases, LNGs) (Nakanishi & Reid, 1971) and in the form of chemical hydrides (Orimo et al., 2007). The techniques, however, are not user-friendly due to weight, space and economy concerned perspectives and also they display the risk of leakage and explosion (Chen et al., 1999). Adsorption of hydrogen, methane and other hydrocarbons in different porous materials: carbon nanomaterials including activated carbons (Menon & Komarneni, 1998), metallacarborane (A. K. Singh et al., 2010), metal-organic frameworks (Ma & Zhou, 2010), and graphitic materials with metal atoms (Carrillo et al., 2009) are some of the highly searched areas. For industrial interest, eg: on-board applications of energy carrying gases, one has to consider the economic and technological challenges. *Hydrogen Storage Engineering Center of Excellence* (HSECE) has declared volumetric and gravimetric content of hydrogen in adsorbing media as targets to mitigate such challenges, an interim target of 0.040 Kg L^{-1} and 5.5 wt.% for the year of 2011 and the ultimate target as 0.070 Kg L^{-1} and 7.5 wt.% for 2017 (Kaiser et al., 2013). For methane the storage target has been set to 180 V/V meant the volume of stored methane per unit volume of storing media (Bhatia & Myers, 2006). The targets usually require light-weight

adsorbing media with large surfaces, and also moderate binding strength of the gases on the substrates. The United State's department of energy (US, DOE) has set such energy range in between 0.1 eV to 0.4 eV (Kaiser et al., 2013; Simpson & Director, 2009). Lower than 0.1 eV requires low temperature storage in combination with the high pressure, where as higher than 0.4 eV requires high desorbing temperature (above the room temperature). The interactions in between the unsaturated metal atoms and molecular hydrogens, defined by Kubas interactions, has shown this intermediate range of binding strength towards hydrogen (Kubas et al., 1984; N. Singh et al., 2013). This is expected due to the exchange (donation and back-donation) of electronic charge in between the interacting atoms.

Metal organic frameworks (MOFs) are made up of metal-involved clusters connected by organic linkers, which are being immensely studied with experimental (Ma et al., 2008) and theoretical (Eddaoudi et al., 2002) methods for the purpose of storing gaseous fuel (N. Singh et al., 2013). MOFs as the new porous materials are found to have better performance over the traditional materials (Casco et al., 2015). A series of 3d transition metal elements have been used in those metal oxide units where the metal atoms are usually the primary sites for holding adsorbed gases (Makal et al., 2012; H. Wu et al., 2009). Redistribution of electronic charge density during the interactions between metallic clusters and carbon materials induces the system for developing the polarity. The polarity causes increasing reactivity towards the gases of our interest and favors the process of adsorption (Durgun et al., 2004). Existing improvements on MOFs have met (in principle) the threshold level for practical applications set by united states department of energy (US, DOE) (H. Wu et al., 2009; Guo et al., 2011; Ma et al., 2008), however, in our best knowledge, economically competing systems at operating conditions are yet to develop for industrial purpose.

In addition to the applications of metal atoms in MOFs, single atoms, metal dimers and also the clusters of metal atoms have been used to enhance the binding energy of hydrogen and methane in graphitic materials (Pantha, Khaniya, & Adhikari, 2015; Ramos-Castillo et al., 2015). Let us discuss some of the previous studies about alkali metal atoms and transition elements in the context of their use for adsorption of energy carrying gases. Mechanical strain produced by metal atoms on substrate has found to enhance the reactivity of the substrate (Zhou et al., 2010). Because of the modified properties of metal adsorbed graphene with reference to both the constituents, fundamental knowledge of their properties is prerequisite to study the potential of gaseous storage in such materials. Being as electron donor atoms, alkali metal atoms donate electronic charge towards the carbon nanomaterials, which is an advantage

in the context of positive relation in between charge transfer and binding strength (Bora & Singh, 2013). Liu et al. (Liu et al., 2011, 2012) have studied various properties (like: adsorption energy, diffusion barrier, dipole moment) of MAGs including the charge transfer from ten different metal atoms towards the graphene layer. The charge transfer has been observed in the order of one electron for alkali metal atoms (Li, Na and K) and higher for some of the transition (3d) metal atoms (like Fe, Ni etc.). Lithium in particular is the lightest alkali metal atom, which metalize graphene, and enhances hydrogen storage capacity up to 12.8 wt% (Ataca et al., 2008). In the previous work, we have performed DFT level of calculations for the adsorption of molecular hydrogens in bare and Na (alkali metal) atom adsorbed graphene (Pantha, Belbase, & Adhikari, 2015). The results show that molecular hydrogens are physisorbed (adsorption energy in the order of 0.06 eV) in pure graphene where as the adsorption energy increase up to 0.192 eV in Na-adatom graphene. The increased values lie within the window of optimum adsorption energy (Kaiser et al., 2013; Bora & Singh, 2013) in Na-adsorbed graphene. Transition metal atoms, on the other hand, have partially filled inner shells and readily modify their electronic structure while communicating to the molecules encounter nearby to them. Also the most of the transition metal atoms are strongly bound in the graphitic materials (Lamichhane et al., 2014) and avoid aggregation of metal atoms themselves (A. K. Singh et al., 2010). The phenomenon supports for the spillover effect of hydrogen for moderate binding in metal atoms and organic linkers. The authors have shown that the optimum storage capacity of the compounds are dependent to the number of vacant d-orbitals, i.e. higher the number of vacant d-orbitals higher the concentration of adsorbed hydrogens.

Carrillo et al. (Carrillo et al., 2009) studied heavily doped titanium (Ti) adatom-graphene at finite temperatures for the purpose of adsorbing CO_2 and CH_4 by using DFT and molecular dynamics level of calculations. The results of the study show that CO_2 dissociates into O and CO during adsorbtion above the upper Ti layer. Adsorption of dissociated constituents is obviously stronger than that of corresponding molecular adsorption. Methane (CH_4) on the other hand is adsorbed with the adsorption energy 0.176 eV/CH_4 at 300 K without any dissociation. The authors also noticed that the initial orientation of methane does not alter the optimized structure of methane on Ti-graphene. By using DFT based ab initio method of calculations, Wood et al. (Wood et al., 2012) have also studied the adsorption properties and geometries of the same gases (CH_4 and CO_2) on pure and functionalized graphene nanoribbons with different functional groups. The authors have used two type of functional

groups, electron donors (OH, NH_2, CH_3) and acceptors (NO_2, COOH, H_2PO_3), on hydrogen passivated graphene nanoribbons. Among the functional groups attached nearby edge of zig-zag graphene nanoribbons, the polar groups COOH, NH_2, NO_2, and H_2PO_3 are found to enhance the binding strength towards both the gases comparing to pure nanoribbons. Consistent to the previous study (Carrillo et al., 2009), CO_2 is bound more strongly (almost by factor of two) comparing to that of methane. The authors have incorporated few models of vdW interactions which are found to be important for binding non-polar gaseous molecules. For the similar functional groups, Kandagal et al. (Kandagal et al., 2012) used ab initio and Monte Carlo simulations to study molecular adsorption of methane on functionalized benzene and edge-functionalized bilayer graphene nanoribbons. The results find that both the adsorption energy and mass (content) of methane enhanced (comparing to that on pure nanomaterials) at operating conditions (40 bar and 298 K). The maximum enhancement of adsorption energy and mass uptake are found to be around 0.1 eV/methane and 44.5 % respectively, comparing to that in hydrogen terminated nanoribbons.

Adsorption of methane on graphite and carbon nanomaterials are searched by many other groups as well. Yang et al. (Yang et al., 2006) by using DFT level of study have found the adsorption energy of methane 0.118 eV/methane at 3.21 Å above the graphite layer. Methane shows tripod down configuration in its most favorable geometry. Similar calculations in graphite (Albesa et al., 2008), and carbon nanotubes (Adisa et al., 2011) have been performed by many groups and some of them will be discussed in upcoming chapters. In the following section, we review methane-methane interactions in liquid media.

2.3 Methane-dimer in solvent environment

Hydrophobicity can be understood in terms of disaffinity of oil with water (Southall et al., 2002). This simple physical observation, however, carries a significant meaning in chemical and biological processes. Protein folding, ligand-protein and protein-protein binding, membrane and micelles formation are some of the examples where the hydrophobic effect plays a key role. Protein folding, a familiar biological process, is the consequence of complex combination of forces/contributions, few of which are electrostatic, hydrogen bonding, van der Waals interactions and some other intrinsic properties (Dill, 1990). Folded proteins at room temperature are marginally stable, and thus even a small change in any contributing factor/s may alter their structure and stability (Dill, 1990). Because of its significance in

a number of research areas, more importantly in chemical, biological and pharmaceutical sciences (Djikaev & Ruckenstein, 2016), hydrophobicity in aqueous medium has been the subject of curiosity for researchers of diverse field via experiments (Crovetto et al., 1982), theoretical analysis (Pratt & Chandler, 1980) and computer simulations (Guillot & Guissani, 1993), since more than two centuries.

An experiment performed by Benjamin Franklin has been considered as the first reported work of hydrophobicity (in 1773) where a drop of oil was poured into water (Tanford, 2004). Rayleigh almost a century later estimated the size of a molecule by assuming single layer of oil film above water based on the property of disaffinity in between two liquids (Tanford, 2004). In case of biological molecules like proteins, made up of a large number of aminio acids and side chains, the native structure is found in folded state (Tanford, 1997; Alberts et al., 2002). The role of hydrophobicity in protein folding was introduced by Kauzmann at the time when details of protein structure and mathematical algorithms were not developed (Kauzmann, 1959). The author further introduced about the primary, secondary and tertiary protein structures. The amphiphilic properties of proteins and soaps, where the hydrophobic and hydrophilic groups are available in the same molecule, were however already recognized (Tanford, 1997). The precise study (with numerics) of oil and surfactants on water were studied by Langmuir in 1917 (Langmuir, 1917). In amphiphilic molecule, the hydrophobic (non-polar) groups of hydrocarbon (which are hidden in the native protein structure) were found to be exposed to water upon their denaturation in 1941 (Bull, 2009). The prediction was later verified by X-rays experiments in micelles and proteins, and observed that polar and nonpolar groups were aggregated at the surfaces and interior of the structures respectively.

As we discussed before, the disaffinity of water for oil is controlled through various interactions. Surprisingly, no repulsive interactions in between two liquids exist in such disaffinity, rather the attractive forces in between like molecules, water with water and oil with oil, have been noticed (Southall et al., 2002). Among the attractive interactions (hydrogen bonding and dispersion interactions), hydrogen bonding in between water molecules is stronger and dominant over the dispersion interactions in oil (Pauling, 1960). Because of the dipolar and nonpolar groups, and helix-coil transitions in proteins, electrostatic and intrinsic molecular interactions are important in their conformational changes and ion-pairing interactions (Anufrieva et al., 1967). The electrostatic interactions are the function of ionic-strength, their positions and dynamics, and PH value (total charge) of the total system (Gitlin et al., 2006). The effect of changes in acidity and basicity (changes in charge concentration) has

been described in terms of non-specific electrostatic repulsion which is dominant at higher concentration and helps to destabilize the folded protein (Tanford et al., 1961). The ion-paring interactions (where a charge is shielded by oppositely charged aminoacids), on the other hand, are effective at lower ionic concentration and support for protein stability (Dill, 1990). Comparing these two contradictory effects, the ionic shielding gets saturated beyond certain concentration and the pairing (specific charge) interaction becomes less important.

The distance dependent interactions (in between interacting units), which were first introduced during the middle of twentieth century (Hill, 1960), are categorized as long-ranged and short-ranged. The interaction is long-ranged if the total energy varies with r^{-p}, for $p \leq 3$. It is said to be short-ranged if $p > 3$. The ion-ion/ion-dipole type, and Lennard-Jones type of interactions are the examples of long-ranged and short ranged interactions respectively. Go and Taketomi in 1978 (Go & Taketomi, 1978), by using Monte-Carlo simulations, further explained the particular role of distance dependent interactions: (i) long-ranged for stabilization and (ii) short-ranged for rate of folding and unfolding during the changes in protein conformations. Local and non-local were also categorized depending upon whether the units are topologically near or far-positioned (Go & Taketomi, 1979; Abkevich et al., 1995).

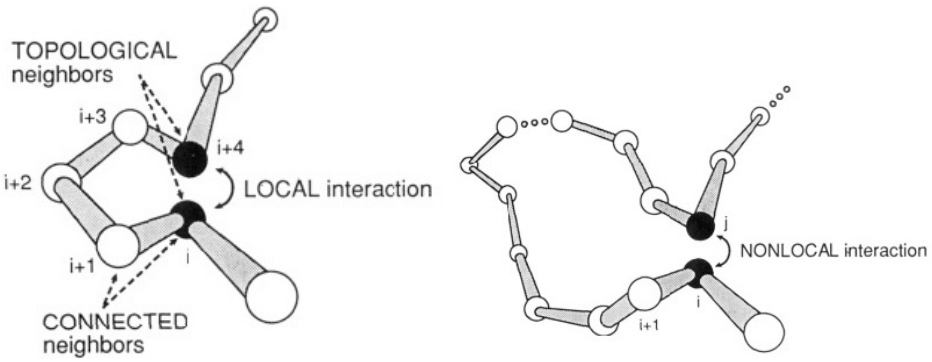

Figure 6: Local and non-local interactions. Polymer residues and their interactions are defined as local and non-local depending upon immediate and topological neighbors, respectively (Dill, 1990).

Protein stability and their configurations may change with the variation in temperature, pressure and composition of solvent-constituents (salt and other organic solvents) around them (Djikaev & Ruckenstein, 2016). The stability, in general, decreases with increasing temperature due to increase in entropy and free energy, which however, might be decreasing with decreasing temperature in some cases. This unexpected phenomenon is recognized as *cold denaturation* (Privalov & Gill, 1988; Southall et al., 2002). Proteins are thus marginally stable for a certain range of temperature and, unstable elsewhere. Furthermore, hydrophobicity is driven by entropy at low temperature and enthalpy at high temperature (Southall et al.,

2002).

In biological creatures, protein activities are affected by their solvent environment. The effect of aqueous solution in model protein systems are thus important to understand in atomistic level. For a nonpolar solute in water, it is noticed that water forms a clathrate-like shell and does not waste its hydrogen bonding by pointing towards solutes on the cost of strong (hydrogen) bonding with another water. Frank and Evens introduced this concept as *iceberg model* (Frank & Evans, 1945), where the ordered water structure surround protein keeping nonpolar amino acids at the inner part so that they do not directly meet water. The nonpolar residues come up to the surface only after protein denaturation (Dill, 1990).

The size and nature of interacting particles are also found to be important in hydrophobicity, and the stability of protein structure (Djikaev & Ruckenstein, 2016). The effect of molecular-size of both the solute and solvents on hydrophobicity have been discussed by using the concept of free energy and other thermodynamic parameters. Lucas computed the changes in free energy due to transfer of nonpolar solutes from gaseous states to water and other solvents as a function of solvent's molecular dimension (Lucas, 1976). The author and the later works (B. Lee, 1985) proposed that the increase in free energy due to insertion of nonpolar molecules into water was because of requirement of appropriate cavity to adjust the solute particles. Larger the molecular size of solvents create larger the cavity, and easier to adjust the solutes in the cost of small changes in free energy. Since the water molecules are among the smallest solvent molecules, it can be predicted that the solubility of nonpolar solutes in water is low (indicating higher hydrophobicity). The size-effect of solute particles has also been searched on the basis of solvation energy (H. S. Chan & Dill, 1991; McAuliffe, 1963). Although there are some controversial views for selecting more precise parameter, whether molar volume or solvent-accessible surface area of solute to calculate the solubility of hydrocarbons in water (Parker, 1963; Franks, 1966; Reynolds et al., 1974), it could be appreciated that free energy of solvation increases with the solute dimension (due to the requirement of larger cavity in solvent). The correct formulation for the proportionality, however, requires molecular shape and geometry (Lazaridis & Karplus, 2000).

More examples of organic solvents to study their response on protein conformations, denaturation, stabilization and crystallization through hydrophobic effect have been searched. Addition of methanol in aqueous solution of peptide BBA5 has been found to increase the size of the hydrophobic core and weaken the hydrophobic effect (Hwang et al., 2011). Similar effect of

acetoitrile (AN), where the OH group of methanol is replaced by CN group, is seen in case of lysozome (protein) immersed water-AN mixture. When the concentration of AN crosses 40 % (by weight), hydrophobic effect weakens on the cost of increasing peptide-peptide hydrogen bonds (Gekko et al., 1998). The order of solubility of small non-polar side chains increases from AN towards methanol and then ethanol. Urea and guanidium chloride (GdmCl), on the other hand, have little effect in hydrophobic association for the denaturation of protein molecules (O'Brien et al., 2007).

Hydrophobic interaction in between two solutes can be a model study for pair-wise addition, which is usually described in terms of PMF (J. Wu & Prausnitz, 2008). Sobolewski et al. (Sobolewski et al., 2007) have discussed solute-size dependent PMF of solute-solute interactions for a series of alkane molecules. Their calculations show that positions of the maxima and minima in PMF shift towards larger values for larger solutes. The authors have also described the arrangement of water molecules, molecular surface area and hydrogen bonding around the solutes, which characterize the nature of hydrophobic interactions. The solvent-effect in solute-solute interactions has been predicted with the help of difference in PMFs in water and vacuum. Similar study for the larger solutes (nanoscale limit) was performed by Makowski et al. in 2010 (Makowski et al., 2009). The pairs of neopantane, bicyclooctane, adamantane and fullerene were considered for such purpose.

Hummer et al., by using computational method, estimated the effect of surrounding pressure on stability of model system for protein structure (Hummer et al., 1998). Unlike the usual convention of transfer of solute particles in water, the authors proposed that the water molecules enter into the protein interior due to increasing pressure which leads to the denaturation of protein structure. The results show decreasing methane-methane (contact) interactions and increasing desolvation barrier during the elevated pressure. At higher pressure, the energy cost of forming cavity increases, and destabilize the contact configurations with respect to solvent separated configurations. The role of structure making and structure breaking around the ion-cores in different solvents was studied by Ding et al. (Y. Ding et al., 2014). In this context, a comparative study of solvent-effects will be meaningful for the better understanding of biochemical processes in living beings. We consider methane-methane interactions in water, methanol and acetoitrile to model stability of protein structure in different solvents.

We use method of classical molecular dynamics as the computational technique whose history starts from the fifties of twentieth century (Alder & Wainwright, 1957). Assuming

the particles as hard spheres with elastic collision between them, Alder and Wainwright studied the dynamics of liquid molecules during late fifties (Allen & Tildesley, 1989) by using the techniques of computer simulations. The development of MD passes through the Lennard Jones model in 1964 (Rahman, 1964) and then towards the dynamics of larger molecules (Kremer, 2003) upon the development of digital computers. In the present work, we use GROMACS (GROningen MAchine for Chemical Simulations) as the computing software (Lindahl et al., 2010) whose detail will be discussed in section 3.

CHAPTER 3

MATERIALS AND METHODS

3.1 Introduction

Materials are mainly found in three phases; solids, liquids and gases. In gaseous phase, the molecules are at long distance and arranged in random manner. Thus the material density and intermolecular interaction is low at the normal temperature and pressure (Frenkel & Smit, 2002). The molecules in liquid phase have only short-range order and density is larger than that in gaseous phase. The interatomic/molecular interactions in liquids is stronger than to those in gaseous phases. In solids, the atoms or/and molecules have long-range order/arrangement with the highest atomic packing. This causes the highest density and the strongest interaction in between the constituent particles. Based on these properties, it is understood that the arrangement of the particles and nature of their interaction differ from one phase to another (Hansen & McDonald, 2006). Also the properties of interest are shape and size dependent (Rao et al., 2009). In this context, one can consider the atomistic level of study to understand the microscopic properties of a material where the separate identity of electrons is neglected. For nanostructures, however, diagnosis of electronic properties is essential to understand their basic physics and chemistry. Hence the fundamental techniques to study their properties differ on the basis of their atomic/molecular arrangement and properties of interest.

In the present work, we study the interactions of methane with other materials in solid and liquid phases. We first consider electronic structure calculations within DFT to understand the methane-water hydrophobic interactions in methane hydrates at high pressure, and methane-graphene interactions within two dimensional nanostructures. In addition, the atomistic level of calculations by incorporating empirical potentials are considered to study the perturbation of liquid media (like water, methanol and acetonitrile) on methane-methane interactions. In

this chapter, we begin our discussion from the theoretical background and then move into the systems considered for the present work.

(a) Electronic structure of a material determines important physical and chemical properties. Electrons and nuclei are treated as interacting many body particles by using Schrödinger equation.

(b) Born-Oppenheimer approximation separates nuclear and electronic equations including external potentials wherever necessary.

(c) Interacting many-body problem can be converted into non-interacting single particle problem in both the wave-function and density-functional theory methods of calculations.

(d) DFT, functional of electron density instead of many body wave-functions, is superior in many perspectives.

(e) Classical molecular dynamics uses empirical potentials to treat the particles in atomistic level. The method solves Newton's equations of motion and draws static as well as dynamic properties of the materials. This technique is more usual for the materials in liquid and gaseous phases.

A material is made up of a large number of atoms and/or molecules, where an atom (the smallest building block of a material) contains a positively charged nucleus at the center and light electrons in the shells around the nucleus. The number, distribution, and the interactions in between electrons and also with the nucleus in addition to the inter-atomic/molecular bonding determine the electronic properties of a material. The electronic structure of a material consisting of many interacting nuclei and electrons can thus be described by the quantum mechanical treatment of many body Schrönger equation (Martin, 2004).

3.2 The many-body Schrödinger equation

The Schrödinger equation for a system of many electrons and nuclei can be written as:

$$\begin{aligned}\hat{\mathbf{H}} = -\frac{\hbar^2}{2m_e}\sum_{i=1}^{N}\nabla_i^2 \quad &+ \quad \frac{1}{2}\sum_{i\neq j}\frac{e^2}{|r_i - r_j|} - \frac{1}{2}\sum_{i,I}\frac{Z_I e^2}{|r_i - R_I|} \\ &- \quad \sum_{I}^{N_c}\frac{\hbar^2\nabla_I^2}{2M_I} + \frac{1}{2}\sum_{I\neq J}\frac{Z_I Z_J e^2}{|R_I - R_J|}\end{aligned} \tag{3.1}$$

Here, i, j and I, J run over the electrons and nuclei respectively. The masses m_e and M_I refer the masses of electrons and nuclei. In short notation,

$$\hat{\mathbf{H}} = \hat{\mathbf{T}}_e + \hat{\mathbf{V}}_{\text{int}} + \hat{\mathbf{V}}_{\text{ext}} + \hat{\mathbf{T}}_N + \hat{\mathbf{V}}_{II}, \tag{3.2}$$

where,

$$\hat{\mathbf{T}}_e = -\frac{\hbar^2}{2m_e}\sum_{i=1}^{N}\nabla_i^2 \qquad \text{K. E. of electrons}$$

$$\hat{\mathbf{V}}_{\text{int}} = \frac{1}{2}\sum_{i\neq j}\frac{e^2}{|\mathbf{r}_i - \mathbf{r}_j|} \qquad \text{Electron-electron Coulomb repulsion energy}$$

$$\hat{\mathbf{V}}_{\text{ext}} = -\frac{1}{2}\sum_{i,I}\frac{Z_I e^2}{|\mathbf{r}_i - \mathbf{R}_I|} \qquad \text{Electron-nuclei Coulomb attraction energy}$$

$$\hat{\mathbf{T}}_N = -\sum_{I}^{N_c}\frac{\hbar^2\nabla_I^2}{2M_I} \qquad \text{K. E of nuclei}$$

$$\hat{\mathbf{V}}_{II} = \frac{1}{2}\sum_{I\neq J}\frac{Z_I Z_J e^2}{|\mathbf{R}_I - \mathbf{R}_J|} \qquad \text{Nuclei-Nuclei Coulomb repulsion energy}$$

If $\Psi(\{\mathbf{R}_I\},\{\mathbf{r}_I\})$ is the total wave-function of the system, Schrödinger equation becomes

$$\hat{\mathrm{H}}\Psi(\{\mathbf{R}_I\},\{\mathbf{r}_I\}) = \mathrm{E}\Psi(\{\mathbf{R}_I\},\{\mathbf{r}_I\}) \tag{3.3}$$

The equation is exact and the solution of this equation, in-principle, gives every required information. However, the exact solution of the Schrödinger equation even for small systems is practically impossible because of the requirement of huge computational cost. To reduce this complexity, one can consider the time scales of the movement of the nuclei and electrons. Since a nucleus is much more heavier than that of an electron (the lightest nucleus is 1837 times heavier than an electron), its motion is much more slower. It means a nuclei remains instantaneously at rest in the time scale of the electronic motion, and their motion can be separated from each other. This principle was separately proposed by Born and Oppenheimer in 1927, and is referred as Born-Oppenheimer approximation (BOA) (Born & Oppenheimer, 1927).

3.2.1 Born-Oppenheimer Approximation (BOA)

Because of heavy mass, nuclear velocities are small comparing to that of electrons. The nuclei are then instantaneously at rest in the time scale of the motion of electrons, and the instantaneous ground-states for electrons can be determined by using time independent

Schrödinger equation. The positions of nuclei thus provide an external potential. Separating the nuclear and electronic parts of the wave-function we write,

$$\Psi(\{\mathbf{R}_I\},\mathbf{r}_I\}) = \chi(\{\mathbf{R}_I\}).\phi(\{\mathbf{R}_I\},\{\mathbf{r}_I\}) \tag{3.4}$$

where, $\chi(\{\mathbf{R}_I\})$ describes the nuclei and $\phi(\{\mathbf{R}_I\},\{\mathbf{r}_I\})$ describes the electrons. The electronic part of Hamiltonian that incorporates interacting electrons under the influence of static external (nuclear) potential becomes,

$$\hat{\mathbf{H}}_e = -\frac{\hbar^2}{2m_e}\sum_{i=1}^{N}\nabla_i^2 - \frac{1}{2}\sum_{i,I}\frac{Z_I e^2}{|\mathbf{r}_i - \mathbf{R}_I|} + \frac{1}{2}\sum_{i\neq j}\frac{e^2}{|\mathbf{r}_i - \mathbf{r}_j|}. \tag{3.5}$$

Hence the Schrödinger equations for the electronic and nuclear part of Hamiltonians respectively can be written as follows:

$$\left[-\frac{\hbar^2}{2m_e}\sum_{i=1}\nabla_i^2 - \frac{1}{2}\sum_{i,I}\frac{Z_I e^2}{|r_i - R_I|} + \frac{1}{2}\sum_{i\neq j}\frac{e^2}{r_i - r_j}\right]\phi(\{\mathbf{R}_I\},\{\mathbf{r}_I\})$$
$$= V(\{\mathbf{R}_I\})\Phi(\{\mathbf{R}_I\};\{\mathbf{r}_I\}) \tag{3.6}$$

$$\left[-\sum_I \frac{\hbar^2\nabla_I^2}{2M_I} + V(\{\mathbf{R}_I\})\right]\chi(\{\mathbf{R}_I\}) = \mathrm{E}'\chi(\{\mathbf{R}_I\}) \tag{3.7}$$

The eigen-values of energy $\mathrm{V}(\{\mathbf{R}_I\})$ parametrically depend on the nuclear positions, and can be found after solving equation (3.6). The values of $\mathrm{V}(\{\mathbf{R}_I\})$ from the solution of equation (3.6) can further be used in equation (3.7) to solve nuclear motion. Once the electronic and nuclear equations are solved, the total energy of the system can be obtained from the information of these solutions.

3.3 Single-Particle Approximation

Although BOA reduces the complexity of the Schrödinger equation by separating it into the electronic and nuclear parts of Hamiltonian, the solutions are still complicated due to unknown electron-electron interactions. This problem can be further resolved by replacing interacting electrons into a system of non-interacting electrons where every electron moves under the influence of effective potential created by nuclei and the remaining electrons. This leads to a single particle picture and also called independent electron/particle approximation. There are mainly two approaches for using independent particle approximation instead of many body problem; (a) the wave-function method and (b) density-functional theory method.

3.4 Wave function Approach

We discuss Hartree (Hartree, 1928) and Hartree-Fock (Fock, 1930) approximations within wavefunction approach.

3.4.1 Hartree Approximation

D. R. Hartree was the first person to introduce independent electron approximation where the electrons are uncorrelated to each other except obeying the Pauli-exclusion principle (Hartree, 1928). According to this model, every electron moves under the effective potential of average Coulomb interactions, and the total wave-function of electrons is the product of N one-electron wave-functions. The many-body wave function can be written as,

$$\Psi(r_1, r_2, \ldots, r_n) = \phi_1(r_1)\phi_2(r_2)\ldots\phi_n(r_n). \tag{3.8}$$

The total energy will be in the form,

$$\mathbf{H}\Psi(r_1, r_2, \cdots, r_n) = \mathrm{E}\Psi(r_1, r_2, \cdots, r_n).$$

The solutions are accessed through self-consistent variational method. Although the Hartree's principle helps to reduce the complexity of interacting many electron approach, it ignores the antisymmetric electronic wave-functions, and does not account the exchange and correlation energies.

3.4.2 Hartree-Fock Approximation

The anti-symmetric nature of electronic wave function is introduced in Hartree-Fock theory (Fock, 1930), where the wave functions are expressed in terms of single Slater (Slater, 1937) determinant of N spin-orbitals.

$$\Psi_{\mathrm{HF}} = \frac{1}{\sqrt{N!}} \begin{vmatrix} \phi_1(r_1, s_1) & \phi_2(r_1, s_2) & \cdots & \phi_n(r_1, s_n) \\ \phi_2(r_2, s_1) & \phi_2(r_2, s_2) & \cdots & \phi_n(r_n, s_n) \\ \vdots & \vdots & & \vdots \\ \phi_n(r_n, s_1) & \phi_n(r_n, s_2) & \cdots & \phi_n(r_n, s_n) \end{vmatrix} \tag{3.9}$$

Hence the Hamiltonian in the form of $\phi_i(r)$ becomes (in Hartree units),

$$\left(-\frac{\nabla^2}{2} + \mathrm{V_{ext}}\right) + \int \mathrm{d}^3 r' \frac{1}{(|r - r'|)} \sum_{j \neq i} \phi_j^*(r')\phi_j(r')\phi_i(r) - \sum_{j \neq i} \phi_j^*(r')\phi_i(r')\phi_j(r)\delta_{s_i s_j} = \varepsilon_i \phi_i(r).$$

(3.10)

This Hamiltonian incorporates exchange potential (which is absent in Hartree equations) and is defined by

$$\mathrm{V}_x = -\sum_{j\neq i} \frac{1}{|r-r'|}\phi_j^*(r')\phi_i(r')\phi_j(r).$$

With the inclusion of Hartree and exchange terms in screening potential, the Hartree-Fock approximation appears as

$$\left(-\frac{\nabla^2}{2} + \mathrm{V}_{(\mathrm{ext})} + \mathrm{V}_{\mathrm{sc}}\right)\phi_i = \varepsilon_i\phi_i$$

where

$$\mathrm{V}_{\mathrm{sc}} = \mathrm{V}_H + \mathrm{V}_X.$$

The first and second terms of equation (3.10) represent the kinetic energy of electrons and the electron-ion interaction energy. The third term represents the electrostatic interactions in between the electrons which includes the self-interaction term (when $j = i$). The self-interaction term is not physical and is excluded through the exchange term. This obeys the law of Pauli-exclusion principle where the like-spin avoid to each other. The correlation between the electrons, which is important in real systems, is still missing in the expression and can be understood as the difference between the exact ground state energy of many body system and Hartree-Fock energy ($\mathrm{E}^0_{\mathrm{exact}} - \mathrm{E}^0_{\mathrm{HF}}$).

Although Hartree and Hartree-Fock approximations are useful methods to solve many body problems, we need to solve a large number variables ($3N$ degrees of freedom for N-body problem), and requires high computational resources. Also the Hartree-Fock approximation does not include the correlation term and may not be able to find the exact ground state wave-function. Density-functional theory (DFT) is a widely accepted alternative method in this regard. In DFT, instead of solving many-electron wave-functions, a single variable of electronic density can be used to extract all the information of electronic wave-functions. This technique is based on Thomas-Fermi model and was proposed during the early second quarter of twentieth century. After the important developments made by Hohenberg-Kohn theorems and Kohn-Sham equations during the sixties of twentieth century, the algorithm has been further simplified by many authors to make popular in first-principles study of the periodic systems.

3.5 Density-Functional Theory (DFT)

Density-functional theory assumes the ground state density $n_0(\mathrm{r})$ as a single variable to describe many body interacting particles. The functional of electron density can describe all the ground state and excited state electronic properties of solids, molecules and other finite systems. The electronic density contains all the information of many-body wavefunctions and reduces the degree of freedom. For an example, a single DFT based Schrödinger equation solves N-electron system, instead of $3N$ degrees of freedom in case of wavefunctions method. The fundamental concept of DFT was first introduced by Thomas and Fermi in 1927 (L. H. Thomas, 1927; Fermi, 1928). Later, the exchange and correlation terms were introduced by Dirac (Dirac, 1930) and the approximation is named as Thomas-Fermi-Dirac (TFD) approximation. However, it has been in practice after the breakthrough of Hohenberg-Kohn theorems and Kohn-Sham ansatz.

3.5.1 Thomas-Fermi-Dirac Approximation

Thomas and Fermi used electron density as a basic variable to solve a system of interacting particles instead of wavefunctions (L. H. Thomas, 1927; Fermi, 1928). By using their model, the total energy of a system can be written as the functional of electron density $n(\mathbf{r})$ under the influence of external potential $V_{\mathrm{ext}}(\mathbf{r})$.

$$\mathrm{E_{TF}}[n(\mathbf{r})] = C_1 \int \mathrm{d}^3 r\, n(\mathbf{r})^{5/3} + \int \mathrm{d}^3 r\, \mathrm{V_{ext}}(\mathbf{r}) n(\mathbf{r})^{5/3} + \frac{1}{2} \int\int \frac{n(\mathbf{r}) n(\mathbf{r}')}{r_i - r_j} \mathrm{d}^3(\mathbf{r}) \mathrm{d}^3(\mathbf{r}') \quad (3.11)$$

The first term in right hand side is the kinetic energy of non-interacting electrons in homogeneous electron gas (HEG) with $C_1 = \frac{3}{10}(3\pi^2)^{2/3}$ in atomic units ($m_e = e = \hbar = \frac{4\pi}{\epsilon_0} = 1$). The second term represents the Coulomb electrostatic interaction in between nuclei and the electrons. The third term is the electrostatic Coulomb repulsion energy in between the electrons, known as Hartree energy.

The kinetic energy of HEG can be calculated from the information of kinetic energy density through adding up all of the free-electron energy states $\epsilon_k = \frac{k^2}{2}$ up to the Fermi wavevector $k_{\mathrm{F}} = [3\pi^2 n(\mathbf{r})]^{1/3}$ as:

$$\mathrm{T_0}[n(\mathbf{r})] = \frac{2}{(2\pi)^3} \int 4\pi k^2 \mathrm{d}k = C_1 n(\mathbf{r})^{5/3}$$

The exchange and correlation among the electrons were neglected in Thomos-Fermi model. Later in 1930, Dirac extended the local exchange term $C_2 \int n(\mathbf{r})^{4/3} \mathrm{d}^3\mathbf{r}$, with $C_2 = -\frac{3}{4}(\frac{3}{\pi})^{1/3}$.

Here the Thomas-Fermi-Dirac (TFD) equation becomes

$$\mathrm{E_{TFD}}[n(\mathbf{r})] = C_1 \int \mathrm{d}^3\mathbf{r}\, n(\mathbf{r})^{5/3} + \int \mathrm{d}^3\mathbf{r}\, \mathrm{V_{ext}}(\mathbf{r}) n(\mathbf{r})^{5/3} + \frac{1}{2}\int\int \frac{n(\mathbf{r})n(\mathbf{r}')}{r_i - r_j}\mathrm{d}^3\mathbf{r}\, \mathrm{d}^3\mathbf{r}' + C_2 \int n(\mathbf{r})^{4/3}\mathrm{d}^3\mathbf{r} \tag{3.12}$$

Minimizing the energy functional (from 3.12) for all the possible $n(\mathbf{r}')$ with $\int n(\mathbf{r}')\mathrm{d}\mathbf{r}' = N$ (N: total number of electrons) may obtain the ground state density and energy. By using the method of Lagrange multiplier, minimization of the functional gives

$$\delta[\mathrm{E_{TFD}}[n(\mathbf{r})] - \mu\left(\int n(\mathbf{r})\mathrm{d}^3\mathbf{r} - N\right)] = 0\,, \tag{3.13}$$

where μ is the Lagrange multiplier, named as chemical potential. It is equal to Fermi energy at 0 K. Following the stationary functional, the TFD equation leads to,

$$\frac{5}{3}C_1 n(\mathbf{r})^{2/3} + \mathrm{V_{ext}}(\mathbf{r}) + \int \frac{n(\mathbf{r}')}{r_i - r_j}\mathrm{d}^3\mathbf{r}' + \frac{4}{3}C_2 n(\mathbf{r})^{1/3} - \mu = 0. \tag{3.14}$$

This can be solved to find ground state density. Although Fermi-Dirac model gets credit of pioneer concept on density-functional theory, it lacks the information of shell structure of atoms and binding of molecules. In this situation, it fails to describe the electrons in solids.

3.5.2 Hohenberg-Kohn Theorems

The Hohenberg-Kohn (H-K) Theorems (Hohenberg & Kohn, 1964) are the basic foundations of modern DFT. The theorems established the density as the basic variable, and the concept is applicable to any system of interacting particles under an external potential. There are two H-K theorems which are discussed below.

Theorem I : *The ground state particle density $n_0(\mathbf{r})$ of any system of interacting particles in an external potential $V_{\mathrm{ext}}(\mathbf{r})$ uniquely determines the potential $V_{\mathrm{ext}}(\mathbf{r})$, except for a constant.* This implies that all the properties of the system could be determined if the ground state (particle) density $n_0(\mathbf{r})$ is known.

The proof of the theorem is simple. We consider two external potentials $\mathrm{V_1}(\mathbf{r})$ and $\mathrm{V_2}(\mathbf{r})$ which differ by more than a additive constant are associated to the same ground state density of N-electron systems. The different external potentials lead to different Hamiltonians ($\mathrm{H_1}$ and $\mathrm{H_2}$),

$$\mathrm{H_1} = \mathrm{T} + \mathrm{U} + \sum_i \mathrm{V_1}(r_i); \quad \mathrm{H_2} = \mathrm{T} + \mathrm{U} + \sum_i \mathrm{V_2}(r_i)$$

where

$$\mathrm{T} = -\frac{1}{2}\sum_{i}^{N} \nabla_i^2 \quad \text{and} \quad \mathrm{U} = \frac{1}{2}\sum_{i\neq j} \frac{1}{|\mathbf{r}_i - \mathbf{r}_j|}\ .$$

The corresponding Schrödinger equations for two Hamiltonians are, $\mathrm{H}_1\psi_1 = \mathrm{E}_1\psi_1$; $\mathrm{H}_2\psi_2 = \mathrm{E}_2\psi_2$. They are associated to two wave functions ψ_1 and ψ_2, say ψ_2 is not ground state of H_1, yield the same electron density as

$$\rho(\mathbf{r}) = N \int \psi^*_{1|2}(\mathbf{r}_1, \mathbf{r}_2, \ldots, \mathbf{r}_N)\psi_{1|2}(\mathbf{r}, \mathbf{r}_2, \ldots \mathbf{r}_N)\, \mathrm{d}\mathbf{r}_2\mathrm{d}\mathbf{r}_3 \ldots \mathrm{d}\mathbf{r}_N \tag{3.15}$$

Now,

$$\begin{aligned} \mathrm{E}_1 &= \langle\Psi_1|H_1|\Psi_1\rangle \leq \langle\Psi_2|H_1|\Psi_2\rangle \\ &\leq \langle\Psi_2|H_2|\Psi_2\rangle + \langle\Psi_2|H_1 - H_2|\Psi_2\rangle \\ &\leq \mathrm{E}_2 + \int \mathrm{d}r\ \rho(r)[V_1(\mathbf{r}) - V_2(\mathbf{r})]. \end{aligned} \tag{3.16}$$

Similar mathematics leads to,

$$\mathrm{E}_2 \leq \mathrm{E}_1 + \int \mathrm{d}r\ \rho(r)[\mathrm{V}_2(\mathbf{r}) - \mathrm{V}_1(\mathbf{r})]. \tag{3.17}$$

The addition of above two inequalities leads to the contradiction

$$\mathrm{E}_1 + \mathrm{E}_2 \leq \mathrm{E}_2 + \mathrm{E}_1. \tag{3.18}$$

The inequality implies that the same ground state density $n_0(\mathbf{r})$ can not be determined from two different external potentials $\mathrm{V}_{\mathrm{ext}}(\mathbf{r})$. Instead, there is a unique external potential corresponding to the given ground state density. Here the external potential $\mathrm{V}_{(\mathbf{r})}$ fixes the Hamiltonian and its wave function by solving the Schrödinger equation. Since the wave function is a functional of density, the ground state density determines the ground state wavefunction and the energy functional $\mathrm{E}_v[\rho]$, for a given external potential $\mathrm{V}_{\mathrm{ext}}(\mathbf{r})$.

Theorem II: *The universal functional for the energy E[n] in terms of the density n(***r***) can be defined, valid for any external potential* $V_{\mathrm{ext}}(\mathbf{r})$*. For any particular potential the exact ground state energy of the system is the global minimum value of this functional, and the density that minimizes the functional is the exact ground state density.*

This means when the total energy functional is known, it is enough to determine the ground state energy and the density for a given external potential.

The Hohenberg-Kohn energy functional (excluding nuclear interaction energy) can be expressed as,

$$\mathrm{E}^{(\mathrm{HK})}[n(\mathbf{r}); \mathrm{V}_{\mathrm{ext}}] = \mathrm{T}[n(\mathbf{r})] + \mathrm{E}_{\mathrm{int}}[n(\mathbf{r})] + \int V_{\mathrm{ext}}(r) n(\mathbf{r}) \mathrm{d}r \tag{3.19}$$

The first and second terms at the right hand side represent the kinetic energy and Coulomb potential energy of interacting electrons. They are independent to any external potential and can be defined by a universal functional of density F[n**(r)**],

$$\mathrm{F}[n(\mathbf{r})] = \mathrm{T}[n(\mathbf{r})] + \mathrm{E}_{\mathrm{int}}[n(\mathbf{r})]. \tag{3.20}$$

The third term, on the other hand, carries the information of electron-nuclei interactions and specific to the given system. It is a linear functional of electron density. With the definition of universal energy functional F[n**(r)**], equation 3.19 becomes

$$\mathrm{E}^{(\mathrm{HK})}[n(\mathbf{r}); \mathrm{V}_{\mathrm{ext}}] = \mathrm{F}[n(\mathbf{r})] + \int V_{\mathrm{ext}}(r) n(\mathbf{r}) \mathrm{d}r \tag{3.21}$$

The second H-K theorem says; the density which minimizes the energy functional is the exact ground state density. Hence minimization of the equation (3.21) with the variations of electron density gives the exact ground state energy and density which, in principle, calculate all the ground state properties. However, the exact energy functional is not known in reality. The kinetic energy of the electrons which is one of the major contributors of F[n**(r)**], involves the gradient of electronic positions and is difficult to find as a functional of electron density. Further, the functional of electron-electron interaction term $\mathrm{E}_{\mathrm{int}}[n(\mathbf{r})]$ is also not known. Based on the foundation of H-K theorems, Kohn and Sham developed an algorithm to solve real problems which are defined by Kohn-Sham equations (Kohn & Sham, 1965).

3.5.3 Kohn-Sham Equations

Based on the philosophy of H-K theorems, Kohn and Sham proposed a mathematical model, called Kohn-Sham (K-S) ansatz (Kohn & Sham, 1965) to study the electronic structure calculations. The Khon-Sham equations consider auxiliary non-interacting particle approximation instead of interacting many body problem, which in principle gives the exact ground state density as given by original interacting system. Further, all the problems in many-body interacting system are taken care of with the exchange-correlation functional. DFT itself is therefore an exact method. In practice, however, the exchange-correlation functional is not known, and one has to consider some approximations to find the energy functional of

density. The accuracy of the calculations depends solely on the approximations made in exchange-correlation functionals. After Kohn-Sham equations made public in 1965, many useful advancements have been released to study the properties of condensed matter and large molecular systems. The local density approximation (LDA) and various generalized-gradient approximations (GGA) are supposed to be the basic exchange-correlation functionals, which are surprisingly accurate for most of the wide-band systems (like semiconductors), some metals (Na, Al), insulators (diamond, NaCl), and the molecular systems having covalent and/or ionic bonding (Martin, 2004). Hybrid systems (Becke, 1993; Adamo & Barone, 1999) and other developments like inclusion of van der Waals effect for long-range interactions (Klimeš & Michaelides, 2012) have been added in the traditional DFTs to overcome their shortcomings in special situations.

KS ansatz replaces the original ground state density by an equivalent ground state density of a fictitious system of non-interacting particles. This is called 'non-interacting-V-representability'. The electrons move under the effective Kohn-Sham single-particle potential $V_{\mathrm{KS}}(\mathbf{r})$ instead of the potential of original system (interacting particles).

For an auxiliary independent particle system, Hamiltonian (in atomic units) can be written as

$$\hat{\mathrm{H}}_{\mathrm{KS}} = -\frac{1}{2}\nabla_i^2 + V_{\mathrm{KS}}(\mathbf{r}). \tag{3.22}$$

For N-independent electrons we get N Schrödinger equations,

$$\left[-\frac{1}{2}\,\nabla_i^2 + V_{\mathrm{KS}}(\mathbf{r})\right]\psi_i = \epsilon_i\psi_i \tag{3.23}$$

and the ground state energy densities can be obtained by solving them. Each of the electron will occupy the orbitals of lowest possible eigen values ϵ_i. The density of the auxiliary system is

$$n(\mathbf{r}) = \sum_{i=1}^{N} |\psi_i|^2 \tag{3.24}$$

with conserved number of electrons. For a system of independent-particles the universal energy functional is

$$\mathrm{F}[n(\mathbf{r})] = \mathrm{T}_s[n(\mathbf{r})] + \mathrm{E}_{\mathrm{H}}[n(\mathbf{r})] + \mathrm{E}_{\mathrm{XC}}[n(\mathbf{r})].$$

Here the first term at right hand side is (independent-particle) kinetic energy ($\mathrm{T}_s[n(\mathbf{r})] = \sum_i^N \int \psi*(\mathbf{r})\,\nabla^2\,\psi(\mathbf{r})$), the second term is classical electrostatic energy (Hartree energy) of the electrons, and the third term is exchange correlation (XC) energy. The XC energy is unknown

and needs approximations for self-consistent solution. This term contains (i) the difference in exact kinetic energy and non-interacting kinetic energy assumed in Kohn-Sham approach, and (ii) all the remaining many body interactions in between the electrons like exchange and correlation energies which are not included in Hartree term. Hence the ground state energy functional for many-body interacting system using KS model becomes

$$\mathrm{E}[n(\mathbf{r})] = \mathrm{T}_s[n(\mathbf{r})] + \mathrm{E}_\mathrm{H}[n(\mathbf{r})] + \mathrm{E}_\mathrm{XC}[n(\mathbf{r})] + \mathrm{V}_\mathrm{ext}(r)n(\mathbf{r})\mathrm{d}r$$

The last term represents the external field, if any, and the potential due to nuclei. The ground state of the energy functional can be found by minimizing the equation with respect to electron density by keeping number of electrons conserved. With this process, the corresponding Kohn-Sham one-particle potential can be calculated.

$$\begin{aligned}\mathrm{V}[_\mathrm{KS}(\mathbf{r})] &= \mathrm{V}_\mathrm{ext}(\mathbf{r}) + \mathrm{V}_\mathrm{H}(\mathbf{r}) + \mathrm{V}_\mathrm{XC}(\mathbf{r}) \\ &= \mathrm{V}_\mathrm{ext}(\mathbf{r}) + \frac{\partial \mathrm{E}_\mathrm{H}[n(\mathbf{r})]}{\partial n(\mathbf{r})} + \frac{\partial \mathrm{E}_\mathrm{XC}[n(\mathbf{r})]}{\partial n(\mathbf{r})}\end{aligned} \tag{3.25}$$

Here $\mathrm{V}_\mathrm{XC} = \frac{\partial \mathrm{E}_\mathrm{XC}[n(\mathbf{r})]}{\partial n(\mathbf{r})}$ is the functional derivative of XC energy, and is called XC potential. Similarly, $\mathrm{V}_\mathrm{H} = \frac{\partial \mathrm{E}_\mathrm{H}[n(\mathbf{r})]}{\partial n(\mathbf{r})}$ is the Hartree potential.

The equations (3.23), (3.24) and (3.25) together are called Kohn-Sham equations, and can be solved self-consistently. It is because, the Kohn-Sham potential V_KS depends on electron density and the same potential is used to solve KS equations to find electron density. As we discussed above, the XC term is the crucial quantity to control the accuracy of the calculations and good approximations are required to solve KS density-functional theory. In this way, Kohn-Sham approach relies on some empirical quantities in addition to the universal energy functional which is independent to the material under study.

3.6 Exchange-Corelation Functional

After developing an auxiliary system and independent particle equations for a system of many body interacting particles, one needs to search for the independent-particle kinetic energy, Hartree energy and exchange correlation energy terms. Since they are the functionals of density, calculation of charge density as a basic variable is an important task in Kohn-Sham ansatz. The charge density could be found by solving self consistent method, which however requires KS potential. The KS potential, on the other hand, is composed of different ingredients (as mentioned before) among which the exchange-correlation term is very complex

and requires approximations. We first include the simple and most widely used approximations for exchange-correlation functionals; local density approximation (LDA) and generalized gradient approximation (GGA). The required additions like London dispersion interactions have been considered according to their relevancy in the present work.

3.6.1 The Local density approximation (LDA)

The local density approximation assumes a uniform distribution of electron density, where the exchange-correlation term obeys the law of homogeneous electron gas (HEG). LDA works well for a system of slowly varying density, and covers a wide range of systems where either the electronic system is not too strongly correlated or the electrons in the system feel constant external potential. It is one of the popular traditional methods for geometrical optimization and electronic structure calculations in case of the systems, where the XC energy is local in nature.

The concept of uniform electron density (in LDA) is consistent with Thomas-Fermi model (Fermi, 1928), and the Hohenberg-Kohn theorems (Hohenberg & Kohn, 1964), where the electrons are treated as homogeneous electron gas. In case of inhomogeneous system, LDA approximates XC functional as an integral over space with a local function of the charge density at each point. Because of cancellation of errors in exchange and correlation terms, LDA is successful to carry very good results than generally expected.

For a system of HEG, the total exchange-correlation functional ($[n(\mathbf{r})]$) can be written as

$$\mathrm{E}_{\mathrm{XC}}^{\mathrm{LDA}}[n] \;=\; \int n(\mathbf{r})\varepsilon_{\mathrm{XC}}[n(\mathbf{r})]\mathrm{d}\mathbf{r}\,, \tag{3.26}$$

where $\varepsilon_{\mathrm{XC}}[n(\mathbf{r})]$ is exchange-correlation energy per electron in a HEG with electron density $n(\mathbf{r})$.

The exchange ($\mathrm{E_X}[n]$) and correction $\mathrm{E_C}[n]$ terms in XC functional $\mathrm{E_{XC}}$ are written as

$$\mathrm{E_{XC}}[n] = \mathrm{E_X}[n] + \mathrm{E_C}[n]. \tag{3.27}$$

The analytical expression of exchange energy functional (Dirac, 1930) is

$$\mathrm{E}_{\mathrm{X}}^{\mathrm{LDA}}[n] = \int n(\mathbf{r})\varepsilon_{\mathrm{X}}[n(\mathbf{r})]\mathrm{d}\mathbf{r} \tag{3.28}$$

with

$$\varepsilon_{\mathrm{X}}[n] = -\frac{3}{4}\left(\frac{3}{\pi}\right)^{1/3}[n(\mathbf{r})]^{1/3}. \tag{3.29}$$

On the other hand, the analytical expression of correlation energy density for HEG is very complicated, and known only for high and low density limits. At low density limit, correlation energy becomes simply the electrostatic energy of point charges, and dominates over the exchange energy. Reversely, at the high density regime, correlation energy becomes less relevant over the exchange energy.

The correlation energy of homogeneous electron gas, at the moderate density, has been accurately calculated from quantum Monte-Carlo (QMC) simulations (Ceperley & Alder, 1980). Interpolated values from these simulations are used in later development of LDAs like Vosko-Wilk-Nusair (VWN) (Vosko et al., 1980), Perdew-Zunger (PZ81) (Perdew & Zunger, 1981), Cole-Perdew (CP) (Cole & Perdew, 1982), and Perdew-Wang (PW92) (Perdew & Wang, 1992).

Real systems are far from the assumptions of homogeneous electron density and hence the fundamental approximation of LDA is not correct. Accurate description for many real systems could be understood by (i) systematic cancellation of error: under-estimated E_c and over-estimated E_x (Levine et al., 2009; Parr & Weitao, 1994), and (ii) spherical description of averaged pair density.

3.6.2 The Generalized Gradient Approximation (GGA)

LDA assumption of homogeneous electron gas is far from the reality and can not cover the inhomogeneous electron density of real systems. This limitation is addressed by generalized gradient approximation (GGA) where its exchange-correlation functional E_{XC} incorporates density gradient corrections in addition to the HEG approximation made by LDA.

The E_{XC} in GGA is written as:

$$E_{XC}^{GGA}[n(\mathbf{r})] = \int f[n(\mathbf{r}), \nabla n(\mathbf{r})]d\mathbf{r}. \tag{3.30}$$

The symbol 'f' is some functional of '$n(\mathbf{r})$' and it's gradient '$\nabla n(\mathbf{r})$'.

Similar to LDA, the exchange-correlation energy E_{XC}^{GGA} of GGA contains exchange (E_X^{GGA}) and correlation (E_C^{GGA}) parts. It can be expressed as;

$$E_{XC}^{GGA} = E_X^{GGA} + E_C^{GGA}. \tag{3.31}$$

Different methods of construction for obtaining f[$n(\mathbf{r})$, $\nabla n(\mathbf{r})$] (exchange correlation functionals) are developed by a number of groups of authors. Some of the popular functionals among

them are proposed by Perdew and Wang (PW91) (Perdew & Wang, 1992), and by Perdew, Burke and Ernzerhof (PBE) (Perdew et al., 1996). Further, Becke's formula (Becke, 1988) for the exchange part was combined with Perdew's formula (Perdew, 1986) of correlation and also with the correlation functional of Lee, Yang and Parr (C. Lee et al., 1988) to give BP88 and BLYP type of GGA functionals. All these functionals generally work well for the materials having chemical bonding like covalent, ionic, metallic or hydrogen. For van der Waals interactions, however, either we need to adopt some hybrid functionals or add some semi-empirical terms in standard GGA functionals.

3.7 London dispersion Interactions

The widely used exchange correlation functionals, LDA and/or GGA, within the frame work of density-functional theory(DFT) address many condensed matter physics and quantum chemistry problems with reasonable accuracy. However, these traditional functionals are short-sighted and do not include non-local interactions between the electrons, which are especially important in case of bio-molecular systems, atomic packing of crystals, host-guest interactions in gaseous bindings and some other cases where the chemical bonding is absent. These non-local interactions are defined by van der Waals (vdW) interactions. Van der Waals interactions include three different terms known as Keesom, Debye and London interactions (Ulman et al., 2014). The Keesom term includes the interactions between the permanent dipoles, the Debye term includes the interaction between permanent dipoles and the induced dipoles in the system, and the London dispersion term includes the interactions between instantaneously induced dipoles in the system. Among the three different type of interactions, London dispersion interactions is found to be the major contributor of vdW interactions in binding of gaseous molecules, which is one of the prime concerns of the present work.

The London dispersion interactions are caused by the effect of charge fluctuations at one region of the system to the electrons residing anywhere on the system. They are weak, attractive and long-ranged. Some of the models to incorporate the dispersion forces (Grimme, 2006; Klimeš & Michaelides, 2012) are still underway to find more effective and cheap algorithms.

The effect of dispersion interactions in standard DFT calculations can be achieved either by inclusion of semi-empirical terms which are responsible for the long-range interactions

into the standard exchange-correlation functionals or by using the new-functionals which themselves incorporate the non-local electronic interactions. The first type are primary in the context of accuracy ladder, where as the second type are still under development to find cheaper algorithms.

Methods to treat van der Waals interactions is one of the popular areas in last decade. Grimme's model of DFT-D is well tested (Grimme, 2004) with high accuracy in different applications (Piacenza & Grimme, 2005; Parac et al., 2005). This method has an additional term ($-1/r^6$, 'r' is the inter-particle distance) in standard DFT where it takes care of asymptotic behavior of interactions in between the particles at larger separation. Note that the cases for smaller r are accounted by the normal DFT. Hence the total energy (E_{tot}) of a system is given by

$$E_{tot} = E_{KS\text{-}DFT} + E_{disp}. \tag{3.32}$$

In equation 3.32, $E_{KS\text{-}DFT}$ is the KS-DFT energy with approximated XC functional and E_{disp} is the empirical dispersion energy term. The dispersion energy term (E_{disp}) in DFT-D2 approach (Grimme, 2006) is given by

$$E_{disp} = -s_6 \sum_{i}^{N_{at}-1} \sum_{j>i}^{N_{at}} \frac{c^{ij}}{r_{ij}^6} f_{damp}(r_{ij}). \tag{3.33}$$

In equation 3.33, N_{at} is the number of atoms in the system, c^{ij} is dispersion coefficient for atom pair *ij* and calculated from a relation coupling ionization potentials and static polarizabilities of isolated atoms. Similarly, 's' is a global scaling factor for the kind of DFT we use and $f_{damp}(r_{ij})$ is the damping function to avoid singularities at samller distances r_{ij}. The damping factor is given as;

$$f_{damp}(r_{ij}) = \frac{1}{1 + e^{-d(r_{ij}/r_s - 1)}} \tag{3.34}$$

with r_s as the sum of atomic vdW radii.

DFT-D2 approach considers the pairwise dispersion terms and gives total dispersion due to all pairs of particles. This approach is widely used because of its simplicity and low computational cost. However, the method has some limitations like: it only considers the leading dipole-dipole interaction term, and neglects the many body correlations. Previous studies reveal that the level of accuracy with DFT-D2 calculations is high comparing to traditional DFT approaches (Joshi & Ghosh, 2013). We use DFT-D2 method (i) to study the binding behavior of methane on pure and functionalized graphene, and (ii) to check the

effect of vdW interactions in case of guest-host interactions of methane hydrate clathrate at comparatively low pressure regime.

3.8 Solution of KS-equation

The Kohn-Sham ansatz is based on the self-consistent iterative process. It removes one type of problem by an another type by replacing real interacting electrons with a system of non-interacting electrons. The KS equations are solved self-consistently by using the relationship in between ground state energy/density and KS potential V_{KS}. The process begins with the initial choice of electron density, based on superposition of electron density of individual atoms, which uniquely determine the KS potential and solves KS equations with this potential. The self-consistent condition/s of the system are checked upon finding this new density, where we compare the new and old density/energy or forces by subtracting the new values from the corresponding old ones. Once the difference is smaller than some defined threshhold, the system is said to be conversed and the desired properties can be extracted. On the other hand, if the difference is above the threshhold value, the density from the previous iteration is mixed with the new ones, and go through the repeated process until satisfying the conditions of convergence.

In the present work, we use pseudo-potential method along with plane wave basis as implemented in Quantum ESPRESSO (stands for opEn-Source Package for Research in Electronic Structure, Simulation, and Optimization) (Giannozzi et al., 2009) codes to study the high pressure methane hydrate clathrate and functionalized graphene structures within the framework of periodic systems.

3.8.1 Pseudo-potentials and Plane waves

A basis set is a set of basis functions that are combined, generally in linear combinations, to create molecular orbitals. Atomic orbitals are a type of basis functions. A basis set which is composed of the minimum number of basis functions and represent all of the electrons on each atom, is called minimal basis set. Depending up on the choice of basis functions, a number of basis sets are available for the expansion of Kohn Sham orbitals in Kohn Sham ansatz. We use orthogonalized plane wave basis sets within the pseudopotential scheme, which are popular in the systems where the periodic boundary conditions are applicable.

Other frequently used basis sets in material calculations are gaussians (Frisch et al., 2004), Augmented plane waves (Loucks & Slater, 1967), Localized atomic orbitals (Soler et al., 2002) etc.

For a periodic system, the solution of Schrödinger equation satisfies the fundamental property of the Bloch's theorem and can be written in the form of,

$$\Psi_k(\mathbf{r}) = u_k(r)e^{i\mathbf{k}.\mathbf{r}}. \tag{3.35}$$

Here $u_k(\mathbf{r})$ is the periodic potential which is consistent with the period of the unit cell. In this case, the Schrödinger equation can be solved independently for each value of $\mathbf{k}$. The functions $e^{i\mathbf{k}.\mathbf{r}}$ are called plane waves, and k's are the reciprocal vectors. The plane waves are the obvious choice as basis sets for the expansion of wave functions in the periodic systems, especially when the external potential of nuclei are replaced by pseudopotentials (will be discussed in the following paragraphs). Plane waves are orthonormal and independent to the atomic positions and energy. In DFT calculations, they convert the Kohn-Sham equation to a simple matrix eigenvalue problem for the expansion of coefficients. The plane waves are able to perform the exact variational calculations based on a discrete numerical grid.

Ideally the electronic wave functions in a periodic system require infinite sum of plane waves which however is not practical for the purpose of actual computations. In the real calculations, the wave function should be described by plane waves within a certain energy cut-off E_{cut}. Caution should be taken while defining the value of E_{cut} so that the wave function be smooth, and the parameters of interest like total energy are well converged. Selection of E_{cut}, in principle, is the compromise in between the accuracy and computational resources.

In all electron DFT calculations, we need to take wave functions for each of the electrons (both core and valence) and solve a large number of basis functions. The core electrons are localized, oscillatory and include high Fourier components. On the other hand, the valence wave functions are smooth at the outer region i. e. at the chemically important bonding area, but have a lot of wiggles (nodal structure) near the nuclei. Although, these nodal structures of the valence electron wave functions are helpful for the requirement of orthogonality to the wave functions (oscillatory core electrons and wiggles of valence electrons near the nuclei), they (the nodal structures) include the high Fourier components. The high Fourier components require larger plane wave cut-off and a large number of plane waves for their solution. This ultimately requires a huge computational cost and practically impossible to address the real materials. One of the effective solutions for this problem could be (i) not to solve the core

electrons and (ii) remove the wiggles of the valence wave functions near the nuclei.

We have a logical justification for not to solve the core electrons. It is because the valence electrons are responsible for most of the physical and chemical properties of materials, and participate in bonding between the atoms. During the formation of inter-atomic bonds, their wave functions change significantly. The core electrons, on the other hand, have nothing to do in bonding and their wave functions are only slightly affected during the interatomic interactions. In this case, the core electrons can be neglected if their screening effect is included in some effective potential. One can consider a virtual potential, known as *pseudopotential*, by freezing core electrons with the nuclei due to which separate wave functions for core electrons are not required. Assumption of virtual potential is also useful to remove the wiggles of the valence wavefunctions. It is because the valence electrons see a weaker potential when the inner electrons are combined with the nuclei comparing to the full coulomb potential. In summary, a pseudopotential replaces the all electron Coulomb potential by a weaker virtual potential which behaves correctly at the region of interest and removes the Coulomb singularity at the origin. Since the wiggles of the valence wave functions near the nuclei are removed, the number of wave functions, the sizes of the basis sets, and the size of the matrices to diagonalize are also reduced.

As we discussed in recent paragraphs, pseudopotentials replace the strong electrostatic potential of nuclei and core electrons. This gives the same wave function outside the core as given by the true wave function to accustom the real properties. Further, it is nodeless and goes smoothly near to nuclei instead of the nodal structures in the real systems. It means pseudopotentials simplify the problems by retaining the properties of interest. However, because of the challenges in choice psedopotentials, which are neither exact nor unique, the idea of pseudopotentials is not errorless. One of the major challenges during the construction of pseudopotential is to differentiate the core and valence electrons. One can define a cutoff radius (r_c) on the basis of justifiable principle, to isolate the core and the valence electrons. The electrons inner and outer regions to the cutoff radius are called core and valence electrons respectively. As the core electrons are frozen to the nuclei, the potentials with small r_c are hard pseudopotentials and with large r_c are called soft pseudopotentials. Although none of the pseudopotentials are exact, a good pseudopotential should be soft and transferable (Vanderbilt, 1990). Because of larger r_c, a soft pseudopotential has a less number of valence electrons and requires less number of plane waves. To be transferable, a pseudopotential should work considerably well in different chemical environments and the harder pseudopotentials are

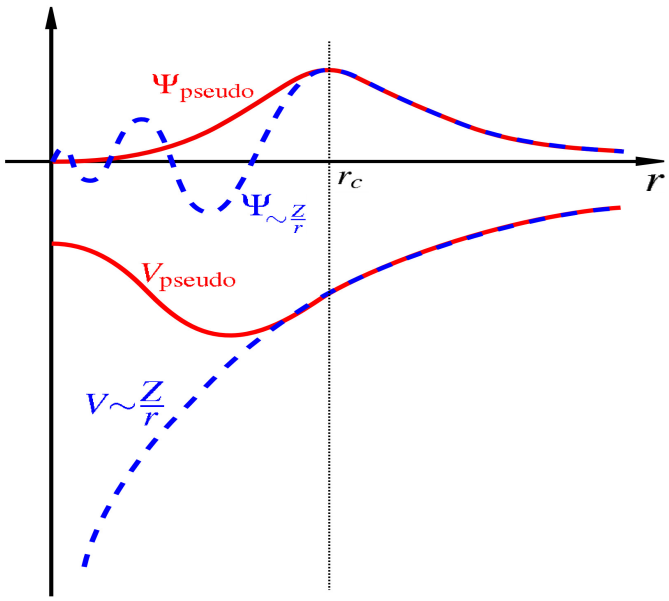

Figure 7: The model of pseudo-potential. The dashed lines show the singularity of the Coulomb potential and wiggles of the corresponding wave functions near the nuclei. The solid lines, on the other hand, show the pseudopotential and the pseudo wavefunction. The pseudopotential and pseudo wavefunction are consistent with the real system outside the cutoff radius (r_c), where as they exclude the hurdles of the real system like; the singularity in potential and wiggles at the wavefunctions near to nuclei (`https://en.wikipedia.org/wiki/Pseudopotential`, dated: Jan 12, 2016).

accurate in this sense.

A pseudopotential that conserves the electronic charge with respect to the real system is called norm-conserving pseudopotential (Hamann et al., 1979). Since the conservation of charge ensures correct description of scattering properties, norm-conserving pseudopotentials are transferable. However, they require a significant computational cost. The requirement of the computational cost can be reduced by using ultrasoft pseudopotentials (Vanderbilt, 1990). One has to use different cutoffs for charge density and kinetic energy for the wave function for these pseudopotentials. The choice of pseudopotential is thus a tricky job and needs care to retain desirable properties using low computational cost.

3.8.2 Hellman-Feynman Forces

The nomenclature "Hellman-Feynman theorem" acknowledges Hans Hellmann (Hellmann, 1939) and Richard Feynman (Feynman, 1939). This theorem helps to find the forces acting on atoms by using the information of expectation values of Hamiltonian, instead of finite difference of total energy values which is too expensive due to the requirement of a large

number of atomic configurations. The forces are important to find the optimized geometry of a system.

The common relation refers forces as the first derivative of the total energy with respect to the atomic positions,

$$\mathrm{F}_I = -\frac{\partial \mathrm{E}}{\partial \mathrm{R}_I}. \tag{3.36}$$

By using first order perturbation theory, the position derivative of total energy becomes,

$$-\frac{\partial \mathrm{E}}{\partial \mathrm{R}_I} = -\langle\Psi|\frac{\partial \mathrm{H}}{\partial \mathrm{R}_I}|\Psi\rangle - \langle\frac{\partial \Psi}{\partial \mathrm{R}_I}|\mathrm{H}\Psi\rangle - \langle\Psi|H|\frac{\partial \Psi}{\partial \mathrm{R}_I}\rangle \tag{3.37}$$

where the last two terms at the right hand side vanish due to the fact that exact ground state solution needs total energy minimum with respect to all the possible variations in wavefunction. Hence only the term which is explicitly atomic/nuclear position dependent is non-zero.

$$-\frac{\partial \mathrm{E}}{\partial \mathrm{R}_I} = -\langle\Psi|\frac{\partial \mathrm{H}}{\partial \mathrm{R}_I}|\Psi\rangle \tag{3.38}$$

Here the derivative of the total energy is equal to the expectation value of derivative of Hamiltonian. This depends only on electronic density and the external potential through the following relation,

$$\mathrm{F}_I = -\frac{\partial \mathrm{E}}{\partial \mathrm{R}_I} = -\langle\Psi|\frac{\partial \mathrm{H}}{\partial \mathrm{R}_I}|\Psi\rangle = \int \frac{\partial \mathrm{V}_{\mathrm{ext}}(r)}{\partial \mathrm{R}_I} n(\mathbf{r})\mathrm{d}^3 r\,. \tag{3.39}$$

The forces on the atomic positions can be calculated by using only one configurations of atomic positions. This saves a lot of time and resources. However, the force theorem assumes that the electronic wave functions are the exact eigenstates (electronic calculations are well converged), and needs care if the basis is not complete or state is approximated.

3.9 Molecular Dynamics

Molecular dynamics (MD) is a computer simulation technique where the time evolution of movement of particles is numerically calculated by solving their equations of motion (Allen & Tildesley, 1989; Frenkel & Smit, 2002). The movement of particles includes their linear, to and fro, twisting and turning type of motion and occurs in all the phases of a materials, although the nature and magnitude differ in solids, liquids and gases. The motion of every particle is affected by its surroundings i.e. due to interactions with other particles and also

possibly with their container (Haile, 1992). Hence, the (MD) simulation process describes the changes in positions, velocities and orientations of the particles present in the model system. We can trace the trajectories of all the constituent atoms (molecules), analyze them correctly and hence estimate their static and dynamic properties of the system by identifying microstates.

Molecular dynamics is broadly classified as classical and quantum molecular dynamics. In case of classical MD, molecules are treated as classical particles and Newton's laws of motion are applicable to describe their dynamics. The classical systems are usually described by using empirical force-field parameters. Quantum mechanical MD, on the other hand, models valence electrons in terms of electron density assuming them as quantum particles and the dynamics of ions (nuclei and their core electrons) classically (Car & Parrinello, 1985; Marx & Hutter, 2009; Barnett & Landman, 1993). The simulation starts from the first-principles incorporating inherent complexity of the system, and is limited to small systems because of the requirement of heavy computational resources. In the present work, we are interested to model-systems of biological molecules (usually large molecules) and use classical MD as implemented in GROMACS (Lindahl et al., 2010).

As the atoms in molecules or any systems are held via interactions in between them, force acting on every atom/particle can be described by using potential energy of the system which is ultimately the function of positions [U($\mathbf{r_1}, \mathbf{r_2} \ldots \mathbf{r_N}$)]. The force acting on i^{th} atom of mass m_i can be expressed as,

$$m_i \frac{\partial^2 \mathbf{r_i}}{\partial t^2} = -\nabla_i \mathrm{U}(\mathbf{r_1}, \mathbf{r_2} \ldots \mathbf{r_N}) = \mathbf{F_i} \tag{3.40}$$

where $i = 1, 2, \ldots, N$. The atomic positions are the determining factors of force acting on each of the atoms through equation (3.40). Knowledge of positions at any time 't' helps to predict their motion for the prescribed step of time. The co-ordinates and velocities of particles are the function of time and hence trace trajectories of each particle throughout the simulations. Once the system is simulated until it reaches to equilibrium, we can calculate all its static and transport properties by using their trajectories (Frenkel & Smit, 2002). Since the movement of a single particle is affected by the collective dynamics of the system, observation of single-particle or pair of particles under the influence of larger number of moving particles can probe the stability of the total system. MD simulation thus obviously shows its relevancy in the wider field of research from gaseous diffusion (Poudyal & Adhikari, 2014; Pokharel et al., 2016) to biological simulations (Shimizu et al., 2002).

In molecular dynamics, the structures, interactions and dynamics of each of the particle is guided by input information in stepwise process that occurs at outside world. The major steps in the process are as follows (Lindahl et al., 2010).

- *Modeling a system*
- *Initialization*
- *Calculation of force and movement of the particles*
- *Analysis of results*

3.9.1 Modeling a system

The process of computer simulation starts from the designation of *model system* which is equivalent to the real experimental set up. In molecular dynamics, we first need to test proper force field parameters, atomic mass, charge, van der Waals constants etc. which guide the particle movements in a particular way. Since the missing of a factor or small deviation in parameter(s) may cause large fluctuations in the result, choice of right parameters is one of the important steps to be taken with care. We start discussing force field parameters which are based on structural properties of the system of interest and tested before (Lindahl et al., 2010).

In classical molecular dynamics, the forces acting on atoms are derived from the information of empirical potentials (called force fields). Each of the atoms in the system is supposed to be spherically symmetric, which communicates with other atoms via bonded (intra-molecular) and non-bonded (inter-molecular) interactions (Balbuena & Seminario, 1999). The bonded interactions include the potentials due to bond stretching U_{bond}, bond angle bending U_{angle}, dihedral angle potential U_{dihed}, and improper (out- of - plane distortions) U_{impr} potential. The non-bonded interactions, on the other hand, are represented by van der Waals potential U_{vdW} and the coulomb potential $U_{coulomb}$. The total potential is the sum of bonded and non-bonded potentials (Rapoport, 1997), and may be expressed as,

$$U_{total} = U_{bond} + U_{angle} + U_{dihed} + U_{impr} + U_{non-bonded} \tag{3.41}$$

where $U_{non-bonded} = U_{vdW} + U_{coulomb}$.

Bond Stretching: The bond stretching between two bonded atoms *i* and *j* is represented by harmonic potential,

$$U_b(r_{ij}) = \frac{1}{2}\, k_{ij}^b\, (r_{ij} - b_{ij})^2 \tag{3.42}$$

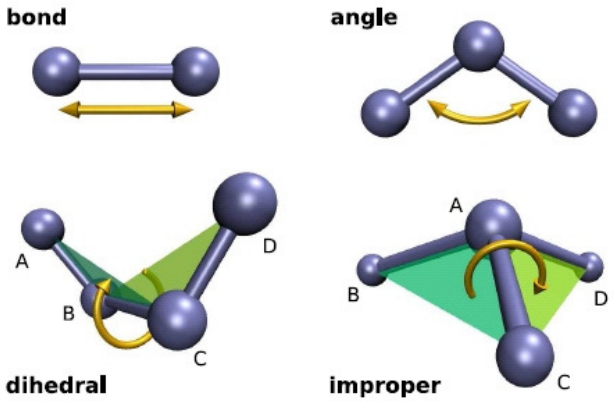

Figure 8: The various bonding between atoms and atomic planes in a molecule (Bergethon, 1998).

where b_{ij} is the bond length between two atoms and k_{ij}^{b} is the force constant.

Bond-angle vibration: The change in angle between three consecutive bonded atoms (say *i, j, k*) from its equilibrium value causes vibrational motion and this type of vibration is defined by angular harmonic potential. Mathematically, the expression can be written as

$$\mathrm{U}_{\mathrm{angle}}(\Theta_{ijk}) = \frac{1}{2} k_{ijk}^{\Theta}(\Theta_{ijk} - \Theta_{ijk}^{0})^2. \tag{3.43}$$

Here k_{ijk}^{Θ} and Θ_{ijk}^{0} are the angular force constant and equilibrium bond angle respectively. Since the both, bond stretching and bond-angle vibration, are represented by harmonic potential their curvature seems to be similar.

Proper dihedral: Dihedral angle is based on four-body interactions. Proper dihedral is the angle between two planes made up of four consecutive atoms which constrain the rotation around a bond. In Figure 8, two planes are formed by A-B-C and B-C-D. The periodic dihedral potential can be written as, in the form of equation 3.44,

$$\mathrm{U}_{\mathrm{dihed}} = k_{\phi}(1 + \cos(n\phi - \phi_s)), \tag{3.44}$$

where k_{ϕ} is force constant, n is multiplicity number, ϕ is proper dihedral angle and ϕ_s is the angle at which the potential attains its minimum value. The multiplicity (n) represents the number of minima when bond is rotated through 2π.

Improper dihedral: Improper dihedral potential forces atoms to remain in a plane or to prevent from transition to its mirror image. Improper dihedral is also the angle between two planes formed by ABC and ACD (Figure 8), however, the atom A remains at the center rather than end of the one of planes in proper dihedral. The harmonic form of improper potential

can be represented as,

$$U_{impr} = \frac{1}{2} k_\xi (\xi - \xi_0)^2 \tag{3.45}$$

where k_ξ is force constant, ξ is improper dihedral angle and ξ_0 is equilibrium improper dihedral angle.

Non- Bonded Interaction: Beside the bonded interactions, there are few non-bonded interactions in between the particles. Two of the main non-bonded type are Coulomb and van der Waals (vdW) interactions. In case of non-polar molecules like methane and closed shell atoms like Ar, Kr etc, usually the coulomb interaction is not present. In such a situation, potential energy of a system is composed of short-ranged repulsive term because of overlapping electron clouds and long-ranged attractive term because of the vdW interactions. The most popular potential which incorporates these terms is called Lennard-Jones (LJ) potential (Kittel, 2005). LJ potential is also known as 12-6 potential and represented by,

$$U_{\mathrm{LJ}}(r_{ij}) = 4\epsilon_{ij} \left[\left(\frac{\sigma_{ij}}{r_{ij}} \right)^{12} - \left(\frac{\sigma_{ij}}{r_{ij}} \right)^{6} \right]. \tag{3.46}$$

In equation (3.46), σ and ϵ are the Lennard-Jones constant, which are usually chosen via empirical methods (Ercolessi, 1997). In GROMACS package, these constants are already available for many atoms/systems for further applications. For the structures conducted in the present work, we have chosen force-field parameters from GROMACS itself.

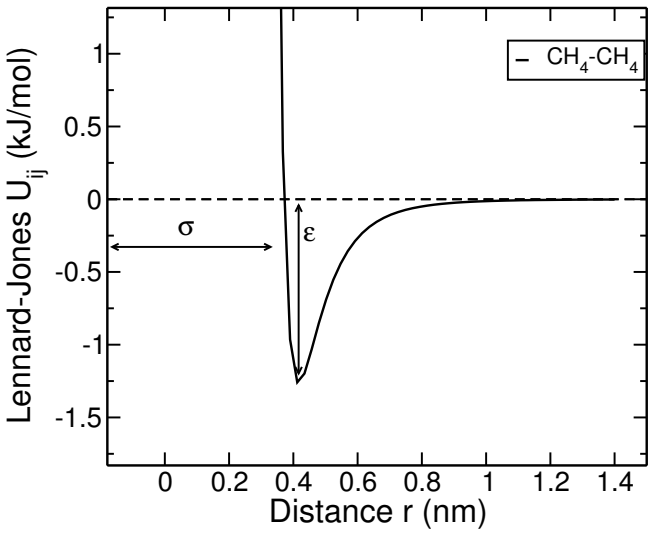

Figure 9: Lennard-Jones potential for methane dimer. Data are taken from the GROMOS force field parameters. The symbols σ and ϵ represent the repulsive region and the minimum potential at equilibrium state, respectively.

When two atoms are brought very close to each other, their electron cloud starts overlapping and causes partial promotion of electrons to unoccupied higher energy orbitals (Kittel, 2005).

Hence the energy of the system increases, and the interaction becomes repulsive. This phenomenon is described by Pauli-exclusion principle. In equation 3.46, the repulsive term is represented by the first term $(1/r_{ij})^{12}$ which is obviously dominant at short distances. The second term $(1/r_{ij})^{6}$, on the other hand, constitutes the attractive part and is dominant at large distances. As we discussed above, this is because of vdW interactions which are originated due to interactions in between electric-dipoles. The vdW interactions are the non-local type of interactions and are the consequences of three different contributions. The contributions from the interactions in between polar molecules or permanent dipoles are referred as Keesom interactions. On the other hand, the vdw interactions in between permanent dipoles and induced dipoles are related to Debye interactions (Stone, 1996; Ulman et al., 2014). The most common type of non-local interactions, originated from instantaneous dipole and induced-dipole interactions where the fluctuation of electron density at one region induces dipole into another region of the system, are called London dispersion interactions (Klimeš & Michaelides, 2012). The London dispersion interactions (proportional to $(1/r_{ij})^{6}$) is incorporated in LJ potential. Although vdW is a weak and long-ranged potential, it is important in the systems with spherical valence shells (where other dominant interactions are absent) (Leach, 2001).

The LJ potential can also be expressed in new parameters, ($C_{ij}{}^{(12)}$ and $C_{ij}{}^{(6)}$) with $C_{ij}{}^{(12)} = 4\epsilon_{ij}\sigma_{ij}^{12}$ and $C_{ij}{}^{(6)} = 4\epsilon_{ij}\sigma_{ij}^{6}$. Hence equation 3.46 becomes

$$U_{\mathrm{LJ}}(r_{ij}) = \left[\frac{C_{ij}^{(12)}}{r_{ij}^{12}} - \frac{C_{ij}^{(6)}}{r_{ij}^{6}}\right] \tag{3.47}$$

One can use proper combination rules to calculate the parameters of molecules with different values of atomic LJ constants (Lindahl et al., 2010).

Coulomb Interaction: Coulomb interaction may exist in between the point charges of same or different molecules. For any two point charges q_i and q_j separated by distance r_{ij}, the coulomb term can be expressed as:

$$\mathrm{U}_{\mathrm{coulomb}} = \frac{q_i q_j}{4\pi\epsilon\epsilon_o r_{ij}} \tag{3.48}$$

In equation (3.48), ϵ and $\epsilon_\circ$ represent the dielectric constant and the permittivity of free space, respectively. Coulomb potential has very important role in case of ionic system, and sometimes may exist in non-ionic systems when electron density in valence shells shifts due to unequal values of electronegativity of atoms.

Periodic Boundary Conditions (PBCs): Particles at/near to the surface feel different forces than that of the particles deep inside the surface(boundary) (Allen & Tildesley, 1989). Ideal

infinite-systems have no surface atoms, however, the real systems are different from this hypothesis. For an example, in case of 1000 atoms in a cubical box (arranged by $10 \times 10 \times 10$), more than 488 atoms appear at the surface of the cube (Allen & Tildesley, 1989). In larger (macroscopic) systems, only a small fraction of atoms are close enough to the surface of the container to realize the surface effects (an effect due to presence of surface or wall of the container which provide rigid boundary for atoms while trying to escape during the simulation).

The system-size of usual molecular dynamics is limited to few thousands of atoms because of complexity in structure and computational limitations. The smaller systems are dominated by surface effects, and one of the easiest ways to minimize the surface effect is to consider the periodic boundary condition where the system is surrounded by the copies of its images (Frenkel & Smit, 2002). It means the box containing N number of atoms (to be simulated) is assumed to be a primitive cell which is propagated through out the space to construct an infinite system. Hence the boundary of the central box has been removed and the particles feel no surface effects. During the course of simulation, when one particle leaves the box from one side, its nearby image enters into the box from another side keeping the number density of the system fixed (Hansen & McDonald, 2006). Another consequence of PBC is *minimum image*

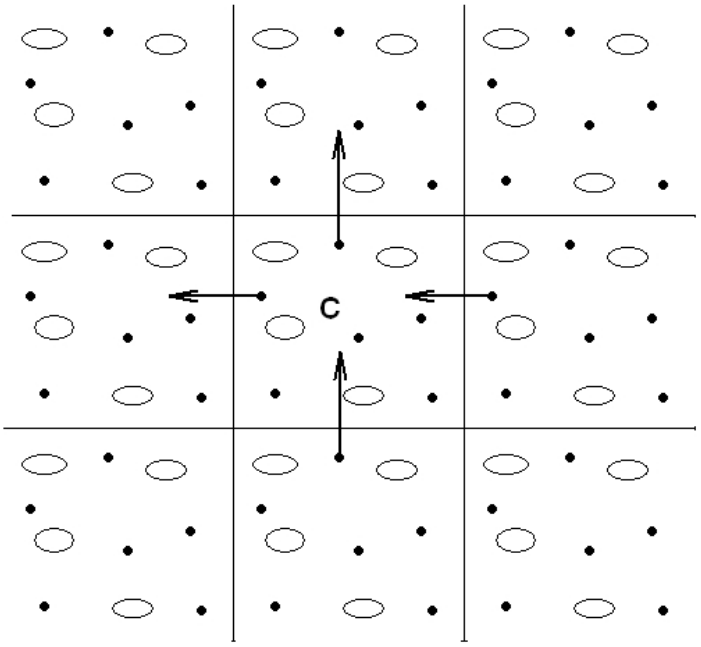

Figure 10: Schematic representation of periodic boundary conditions (Lindahl et al., 2010).

criterion which is applicable to limit the interaction between the particles. That is among N number of particles, each atom interacts with the closest images of other $N - 1$ particles and ignores all remaining images (Allen & Tildesley, 1989). Since the potential is considered

through pairwise addition of the interactions, the total potential involves $N(N-1)/2$ terms, which is still high and can be reduced further (for short range interactions) by using spherical cut-off. To avoid the images from double counting, the value of cutoff (say R_c) should not be greater than half of the box size (Ercolessi, 1997). For long range interactions (like for ionic systems), however, truncation of potential at small R_c can not include the interactions at longer distances and causes a serious problem. This problem can be minimized by using the method of Ewald, where short-range potential is summed in real space with appropriate truncation, and the long-range summation is taken over the reciprocal lattice vectors (Hansen & McDonald, 2006).

Although the size effect is minimized by using PBC, it is not the absolute solution. Its magnitude depends up on the kind of the system and the properties of interest. One can check varying size samples to estimate the size effect and possible error due to chosen size (Poudyal & Adhikari, 2014).

3.9.2 Initialization

Initialization is the step to assign the initial co-ordinates and velocities which should be compatible to the structures. One has to exclude the overlap of atomic cores while choosing positions in this stage. The velocities are attributed by using Maxwell-Boltzmann distribution and scaled to adjust the mean kinetic energy to the desired values (Lindahl et al., 2010). The relationship of velocity with temperature in thermal equilibrium is given by (Frenkel & Smit, 2002),

$$\langle v_\alpha^2 \rangle = \frac{k_B T}{m}. \tag{3.49}$$

Here v_α is the $\alpha(x, y, z)$ component of the velocity, m is the mass of a given particle, T is the temperature and k_B is Boltzmann's constant.

3.9.3 Force Calculation

The main step of MD simulations after *initialization* of a system, is the calculation of forces acting on each of the particles. This process includes the estimation of forces on a particle i due to all its neighbors (Ercolessi, 1997). By using the relation of potential, which is pairwise addition of interacting particles $U(r_i)$, the force can be calculated by

$$\mathbf{F_i} = -\nabla_i U(\mathbf{r}_i). \tag{3.50}$$

Calculation of forces should include all the interacting particles within the range of defined cutoff and excludes all the remaining ones. The procedure follows the *minimum image convention* where particle *i* interacts with the nearest image of *j* (Frenkel & Smit, 2002; Ercolessi, 1997).

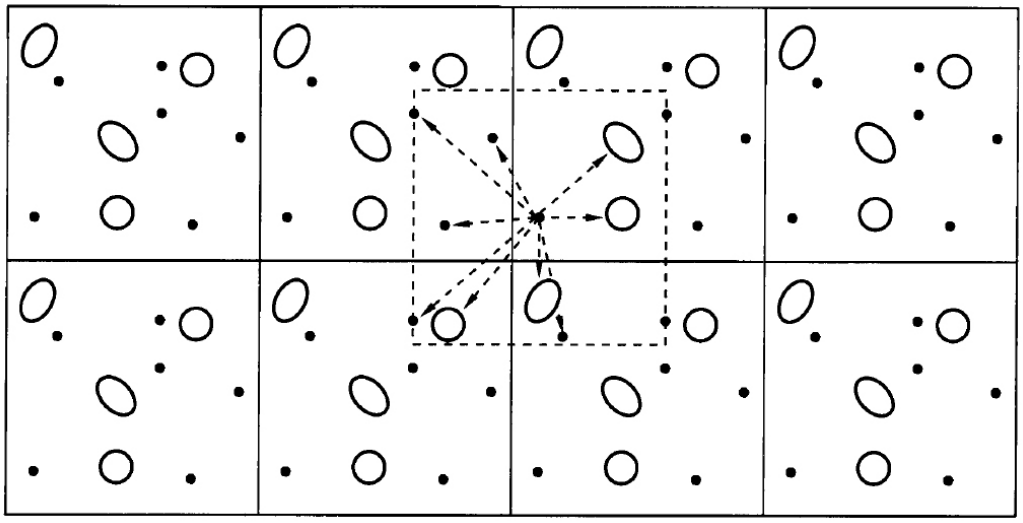

Figure 11: Use of cut-off and near-image convention for periodic boundary condition (Frenkel & Smit, 2002).

The value of cutoff R_c can not be large enough due the limitations on the size of the simulating box (R_c should not be greater than half of the box-size). For long range interactions, however, the interaction beyond R_c could be significant and needs correction. One of corrections is based on mean field approximation where the field beyond R_c is constant (S. Thapa & Adhikari, 2013). Another usual method for the correction includes Ewald summation in which all interactions between the particle *i* in the central cell and its (unit cells) replica surrounding the central one are integrated (Lindahl et al., 2010).

3.9.4 Integration of Equation of Motion

The calculations of new coordinates for position and components of velocities of particles by using their initial (known) information is related to the solution of equations of motion. The forces are position dependent through potentials, and mathematical algorithms are able to predict the new coordinates by using the available information. Hence the phase space coordinates generate their trajectories. There are many methods to trace these trajectories, and the methods with higher precision and the least possible computational cost are supposed to be the most preferred ones. The precision and computational cost are contradictory for a simulation, and requires compromise in between their perfect conditions(Allen & Tildesley,

1989). In case of MD simulations, the length of time step is one of the major determining factors for computational cost (the higher the time step, the lesser the computational cost) and accuracy (the smaller the time step, the higher the accuracy).

3.9.5 Verlet Algorithm

One of the popular methods for integrating the equations of motion is Verlet algorithm where the positions $\mathbf{r}(t)$, and accelerations $\mathbf{a}(t)$ are found from the previous steps (Frenkel & Smit, 2002). The relations for Verlet algorithm are based on Taylor series expansion, where for time step δt we get

$$\mathbf{r}(t+\delta t) = \mathbf{r}(t) + \mathbf{v}(t)\delta t + \frac{\mathbf{F}(t)}{2m}\delta t^2 + \frac{\delta t^3}{3!}\frac{d^3r}{dt^3} + O(\delta t^4) \tag{3.51}$$

$$\mathbf{r}(t-\delta t) = \mathbf{r}(t) - \mathbf{v}(t)\delta t + \frac{\mathbf{F}(t)}{2m}\delta t^2 - \frac{\delta t^3}{3!}\frac{d^3r}{dt^3} + O(\delta t^4) \tag{3.52}$$

Now adding equations (3.51) and (3.52) we get

$$\mathbf{r}(t+\delta t) + \mathbf{r}(t-\delta t) = 2\mathbf{r}(t) + \frac{\mathbf{F}(t)}{m}\delta t^2 + O(\delta t^4) \tag{3.53}$$

$$\mathbf{r}(t+\delta t) = 2\mathbf{r}(t) - \mathbf{r}(t-\delta t) + \frac{\mathbf{F}(t)}{m}\delta t^2 + O(\delta t^4) \tag{3.54}$$

Equation (3.54) shows that error in position is in the order of δt^4. Velocities are importat to estimate the kinetic energy (however are absent in position trajectories), and can be obtained by using equations (3.52) and (3.51).

$$\mathbf{r}(t+\delta t) - \mathbf{r}(t-\delta t) = 2\mathbf{v}(t)\delta t + O(\delta t^3) \tag{3.55}$$

$$\mathbf{v}(t) = \frac{\mathbf{r}(t+\delta t) - \mathbf{r}(t-\delta t)}{2\delta t} - O(\delta t^2) \tag{3.56}$$

Since the error of velocity is in the order of δt^2 (comparing to δt^4 in positions), accuracy is expected to be lower in velocity. Furthermore, velocity and positions could not be calculated simultaneously, that is velocity at time t needs the coordinates at $t + \delta t$.

3.9.6 Leap frog Algorithm

Leap frog algorithm is an equivalent scheme to Verlet algorithm. It is named for half-integer time steps of velocities with respect to positions (and acceleration), and uses these velocities to compute the new positions. It means that velocities leap over the position coordinates to

give the next mid step values (Figure 12) (Frenkel & Smit, 2002). If $(t - \delta t/2)$ and $(t + \delta t/2)$ are the mid-integer time steps, the corresponding velocities are defined by

$$\mathbf{v}\left(t - \frac{\delta t}{2}\right) \equiv \frac{\mathbf{r}(t) - \mathbf{r}(t - \delta t)}{\delta t} \tag{3.57}$$

and

$$\mathbf{v}\left(t + \frac{\delta t}{2}\right) \equiv \frac{\mathbf{r}(t + \delta t) - \mathbf{r}(t)}{\delta t} \,. \tag{3.58}$$

The new positions can be calculated from the old positions and velocities.

$$\mathbf{r}(t + \delta t) = \mathbf{r}(t) + \mathbf{v}\left(t + \frac{\delta t}{2}\right)\delta t \tag{3.59}$$

By using the Taylor series expansion on velocity about t, we get the Verlet type relations as

$$\mathbf{v}\left(t + \frac{\delta t}{2}\right) = \mathbf{v}(t) + \frac{\mathbf{F}(t)}{2m}\delta t \,. \tag{3.60}$$

Again,

$$\mathbf{v}\left(t - \frac{\delta t}{2}\right) = \mathbf{v}(t) - \frac{\mathbf{F}(t)}{2m}\delta t \,. \tag{3.61}$$

Solving the above two equations we get

$$\mathbf{v}\left(t + \frac{\delta t}{2}\right) = \mathbf{v}\left(t - \frac{\delta t}{2}\right) + \frac{\mathbf{F}(t)}{m}\delta t \,. \tag{3.62}$$

Since the velocities and positions are defined at different time, potential energy and kinetic energies can not be defined simultaneously. It means the total energy can not be calculated directly from the above equations. However, the trajectories for the position and velocities are similar (Ercolessi, 1997; Bergethon, 1998). The schematic representation of Leap frog algorithm is shown in Figure 12.

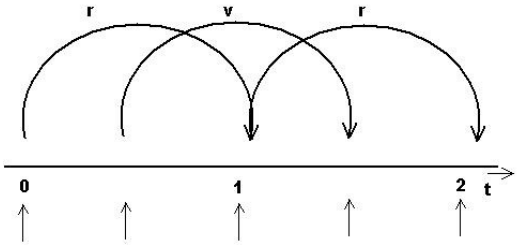

Figure 12: Schematic representation of leap-frog algorithm (Frenkel & Smit, 2002).

Time reversibility is one of the major applications of leapfrog integration. It means integration for n steps forward, and then n steps backwards bring the system at the starting (same) position (Allen & Tildesley, 1989). The velocities at current time t can also be calculated via indirect method (by using equations 3.57 and 3.58),

$$\mathbf{v}(t) = \frac{1}{2}\left(\mathbf{v}\left(t + \frac{1}{2}\delta t\right) + \mathbf{v}\left(t - \frac{1}{2}\delta t\right)\right) \,. \tag{3.63}$$

3.9.7 Constraint Dynamics

The non-polar spherical atoms can be treated with the LJ potential which used to be the obvious choices in early MD simulations (Harp & Berne, 1968, 1970). In molecular systems, however, the fundamental particles interact with intra- and intermolecular forces which are accounted by bond vibrations and changes in relative orientation etc. Some of these vibrations are very fast and require extremely short time step. This complexity in simulations can be replaced by constraint dynamics where the intra-molecular bonds and angles are supposed to be fixed. The magnitude of vibrations are small comparing to their molecular dimensions, and this assumption is near to the reality. For such a purpose, we need a constraint to force the system into required rigidities (Leach, 2001). SHAKE and LINCS are two popular constraints available in GROMACS package. In the present work, we have used SHAKE as constraint algorithm where a set of unconstrained co-ordinates are changed to another set that are constrained with distances (Lindahl et al., 2010).

3.10 Statistical Ensembles in Molecular Dynamics

The dynamical state of any system (having N number of particles) is defined by $3N$ position and $3N$ momentum coordinates. A set of these $6N$ variables define a micro-state in $6N$ dimensional phase space which is called phase point. We introduce *ensemble* to explain the probability distribution of the microscopically defined states of a system in terms of imaginary collections of the system. Each of these collections is the replica of real systems with same macroscopic properties. The concept of such ensembles realize the physical observables in terms of their average values (Pathria, 1996).

Depending up on the variables kept fixed in the systems, ensembles are classified as micro-canonical (NVE), canonical (NVT), isothermal-isobaric (NPT) and grandcanonical (μVT) ensembles. The symbols refer to the number of particles (N), volume (V), energy (E), pressure (P), temperature (T) and the combination of these variables define the type of ensemble. Constant temperature, and constant pressure experiments respectively, are relevant to NVT and NPT ensembles. Furthermore, microcanonical (NVE) ensembles are very common in MD simulations. Upon having enough lapse of time in MD simulations time average of desired properties like: total energy, can be replaced by ensemble averages (average property of large number of replications of systems at a time) which simplifies calculating the properties of

interest. Such a condition where the time average of an observable in a system is equivalent to the ensemble average, is called ergodic (Leach, 2001).

In MD simulations, pressure and temperature vary a lot. To fix them, some regulatory mechanisms are required (Leach, 2001). For the purpose of controlling temperature (T) and pressure (P), we have different coupling systems, and some of them are described in the following paragraphs.

3.10.1 Temperature Calculation and Control

The initial particle velocities in a system are defined by Maxwell-Boltzmann distribution as described in section 3.9.2. During the course of simulation, however, the velocity distribution changes to new values. Since the velocities are correlated with the temperature of the system, they need to be rescaled according to the target temperature which is the requirement for constant temperature ensembles. The ensembles with constant temperature are either NVT or NPT. The constant temperature condition is also the fundamental requirement for correct ensemble averages to study the properties of the system as a function of temperature like folding and unfolding of proteins (Leach, 2001). The temperature-controlled simulations are also important in order to systematically increase or decrease the temperature of the system like for simulated annealing. The correct temperature, within reasonable fluctuations, is maintained by using different types of temperature-control mechanisms like rescaling the velocities or by external heat baths (thermostats) (Frenkel & Smit, 2002). The choice of the thermostat depends on the nature of system and the properties of interest. Berendsen thermostat is useful for the cases of weak coupling scheme (Berendsen et al., 1984) and the extended-ensemble approach is attained by Nose-Hoover thermostat (Nosé, 1984; Hoover, 1985). We have used velocity-rescale (v-rescale) type of thermostat for such purpose. Velocity-rescale thermostat is basically identical with the Berendsen thermostat except few extra terms which ensure a correct kinetic energy distribution (Lindahl et al., 2010).

Rescaling velocities to control the temperature are related through the time average kinetic energy of the system, $\langle \text{K.E.} \rangle = \frac{3}{2} k_{\text{B}} T$, with some rescaling factor, $\lambda = [\text{T}_{\text{new}}/\text{T}(t))^{1/2}]$. Here T_{new} and $\text{T}(t)$ are new temperature after rescaling velocities and temperature at time t respectively.

Heat baths, on the other hand, exchange heat with the system to attain the target temperature.

$$\frac{d\mathrm{T}(t)}{dt} = \frac{1}{\tau}(\mathrm{T}_{\mathrm{bath}} - \mathrm{T}(t)), \tag{3.64}$$

where τ, $\mathrm{T}_{\mathrm{bath}}$ and $\mathrm{T}(t)$ represent the coupling constant, target (bath) temperature and the temperature at time t respectively.

In the microcanonical ensemble (constant NVE), temperature is defined by making use of the equipartition principle which states that the average kinetic energy per degree of freedom is $\frac{k_{\mathrm{B}}\mathrm{T}}{2}$. The instantaneous temperature in such a system becomes

$$\mathrm{T}(t) = \frac{2}{(3N - N_{\mathrm{c}})k_{\mathrm{B}}} \sum_{j}^{N} \frac{1}{2} m_i v_i^2(t) \tag{3.65}$$

Here N and N_{c} represent the number of particles and number of constraints on the system, respectively. Similarly, m_i and k_{B} represent mass of the i^{th} particle and Boltzmann's constant respectively.

3.10.2 Pressure calculation and control

As similar to the constant temperature, constant pressure simulations are important in many practical cases. The experiments at constant pressure are very common and computational work at similar condition is relevant for the purpose of estimation and comparison with the experiments. At fixed temperature (see subsection 3.10.1), NPT ensemble is characterized by constant pressure and number of particles. In practice, constant pressure simulations are important to study the system-properties as a function of pressure such as pressure induced phase transitions (Leach, 2001).

Since the constant pressure is usually maintained by changing volume, the observation of fluctuations in volume are important. NPT system is related to isothermal compressibility with the relation

$$\kappa = -\frac{1}{V}\frac{\partial \mathrm{V}}{\partial \mathrm{P}}. \tag{3.66}$$

This indicates that the easily compressible substance has larger changes/fluctuations in volume, comparing to the incompressible substances. In the reverse way, less compressible substance has larger fluctuations in pressure at constant volume. As similar to the control in temperature, there are various schemes to control pressure. They could be either by scaling the volume or

by using pressure bath (barostats) (Lindahl et al., 2010),

$$\frac{\mathrm{dP}(t)}{\mathrm{d}t} = \frac{1}{\tau_p}(\mathrm{P_{bath}} - \mathrm{P}(t)). \tag{3.67}$$

In the equation (3.67), τ_p, $\mathrm{P_{bath}}$ and $\mathrm{P}(t)$ represent the coupling constant, target (bath) pressure and the pressure at time t respectively. Pressure is felt by the momentum carried out by the particles while they cross the boundary and the force of interaction in between the particles at different surfaces. There are different types of barostats to control the pressure inside a simulation box, which are described in available literature (Parrinello & Rahman, 1981; Melchionna et al., 1993; Andersen, 1980). In the present work, we have used Parrinello-Rahman type of barostat for such a purpose. In Parrinello-Rahman Barostat, box-vectors follow an equation of motion where the equation of motion of the particles are also changeable. This type of barostat can also be applied in varying shapes of simulation cells (Parrinello & Rahman, 1981).

3.10.3 Umbrella Sampling

Thermally favorable microstates of a system are more frequently visited by the simulation trajectories in normal computational techniques (Boltzmann-like weights). There are some states, which are hindered by energy barriers, are either rarely sampled or not visited at all (Allen & Tildesley, 1989). For a number of properties, such as free energy difference which is especially important in biological systems (Kästner, 2011), are difficult to calculate via such direct simulation techniques due to the requirement of very high computational resources and length of time. However, few techniques with non-Boltzmann sampling are available to weight different energy states differently which encourages the system to visit the regions of the phase space not usually sampled by the direct approach. The usual techniques in use are umbrella sampling, thermodynamic integration, slow growth, steered MD etc (Frenkel & Smit, 2002; Kästner, 2011). *Umbrella Sampling* which literally means bridging the gap (umbrella) between two or more states, is an enhanced molecular dynamics where the potential is biased along the reaction coordinates and shifts a system from one thermodynamic state to another. Any type of potential, in principle, can be used as biasing potential, however harmonic potential is one of the frequently used schemes to overcome the effect of energy barrier in Boltzmann distribution. The algorithm introduces different windows against the reaction co-ordinates to sample the system throughout the regions of its energy landscape.

The information from the different windows are then combined via appropriate method to calculate the required parameter. In the present work, we have used weighted histogram analysis method (WHAM) for such a purpose (Kumar et al., 1992). WHAM is one of the popular methods to extract PMF which is useful to find the free energy difference against the reaction coordinates. The process uses the information of output files obtained from umbrella sampling simulations.

The technique of umbrella sampling was first suggested in 1977 by (G. M. Torrie & Valleau, 1977). The later developments were introduced to study the liquid mixture (G. Torrie & Valleau, 1977), to calculate the excess surface energy of a water model (C. Lee & Scott, 1980) and chemical potential of a particle in a fluid (Shing & Gubbins, 1981). We use the technique of potential of mean force (PMF), defined as the potential that is obtained by integrating the mean force from ensemble of configurations, by using the method of umbrella sampling simulations (Lindahl et al., 2010).

Potential of mean force: Solute-solute interactions is the primary concern of the present work. However, the average solvent-effects is important factor to be incorporated in many fields of research. Potential of mean force is an approach to observe changes in free energy with respect to some particular coordinates like separation between the solute particles (Leach, 2001). The method of PMF enables to study the modulating effect of solvents on the dynamics of the system through collision and viscus drag force.

PMF is the free energy surface along the chosen co-ordinates. The highest energy point of the surface thus represents the transition state of different phenomenon. Mathematically, PMF can be obtained by using the information of radial distribution function (RDF). Hence the Helmholtz free energy can obtained from PMF with the expression,

$$\mathrm{F}(r) = -k_{\mathrm{B}}\mathrm{T}\ln[g(r)] + \text{constant}. \tag{3.68}$$

With relation 3.68, small change in free energy causes a change in $g(r)$ from its most likely value which are not sampled by usual MD simulations. The method of biased simulations like umbrella sampling becomes relevant in such cases.

The usual potential is modified with the addition of some suitable type of potential which helps to sample unfavorable states sufficiently. The biased potential thus becomes,

$$\mathrm{V}'(r^N) = \mathrm{V}(r^N) + \mathrm{W}(r^N) \tag{3.69}$$

where $V(r^N)$ and $W(r^N)$ are the unbiased potential and weighing function. The weighing function is usually quadratic in nature. The general expression thus becomes

$$W(r^N) = k_W(r^N - r_0^N). \tag{3.70}$$

In equation 3.70, $(r^N - r_0^N)$ measures how far the system is from the equilibrium state r_0^N. The weighting function ($W(r^N)$) is large for the configurations which are far from the equilibrium state. The resulting distribution is non-Boltzmann type where the Boltzmann distribution for them can be extracted as per method suggested by Torrie and Valleau (G. M. Torrie & Valleau, 1977). For a quantity A, the average value is defined as,

$$\langle A \rangle = \frac{\langle A(r^N) \exp[+W(r^N)/k_B T] \rangle_W}{\langle \exp[+W(r^N)] \rangle_W}. \tag{3.71}$$

The average value, based on probability $P_W(r^N)$ and determined via modified potential $V'(r^N)$, is represented by subscript (W). In case of umbrella sampling simulations, a series of appropriate biasing potentials are generally applied with the caution that very large values of biasing for some of the windows may cause controlling the result by a few configurations. Insufficient biasing, on the other hand, is incapable to constrain the system at the target region of the phase space.

The method of simulation for *umbrella sampling* is not very different than usual MD. The initial configurations are prepared for a series of reaction coordinates. For an example: when the free energy surface (PMF) for the interactions between two solute molecules in solvent environment is to be determined against the distance between them (as reaction coordinates), a series of windows with varying distance are prepared. The simulating potential is biased with additional harmonic potential (say) for each configuration with appropriate overlapping in between the nearest windows. The biasing potential for each window which aims to constrain the system within certain region of the phase space, can be varied depending upon the nature and range of interactions.

Flow chart (Figure 13) shows that the construction of correct topology file is the first step of the simulation process. This can be done by using the coordinate file of the system via proper GROMACS executable (pdb2gmx). The choice of right size of the box and the number of solvent molecules are the next steps of the simulation which need care of nature of interactions and minimum image criteria. According to this convention, the separation between the molecules can not be greater than the half of the box size. In the process of minimization, the system finds its structure and configurations corresponding to local minimum searched by

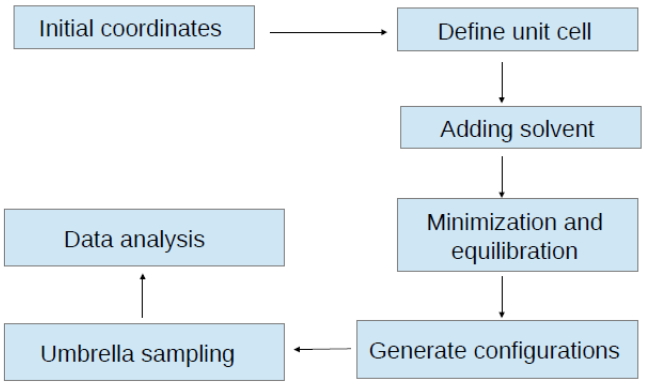

Figure 13: Flow chart representation of umbrella sampling simulations.

the appropriate algorithm (gradient of potential is zero in such points) (Lindahl et al., 2010). Minimization removes the bad contacts caused by the improper position of the atoms and avoids being far from the equilibrium configuration. A series of windows are then generated to run the separate simulations as shown in Figure (14).

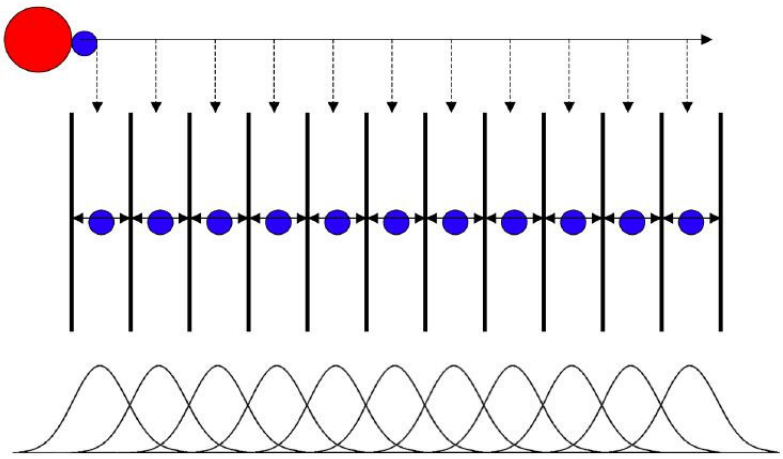

Figure 14: Schematic representation of a series of windows prepared for umbrella sampling simulations. The reaction coordinates are taken as the separation between two atoms (red large and small blue atoms). (Retrieved from: `http://www.gromacs.org/@api/deki/files/205/=pmf_tutorial_online.pdf`, dated: June 6, 2016).

The first row in Figure (14) represents the pulling simulation which helps to construct many windows against the reaction co-ordinates (shown in second row with respect to red large atom). The strength of biasing potential and separation between the windows are correlated and taken into care on the ground of adequate overlapping between the nearest windows. *Pull code* defines the distance between the center of masses of the interacting molecules or groups and takes care of correlation between the windows (Lindahl et al., 2010). Each of the windows

are then simulated for the appropriate time step. The biased information thus collected is made unbiased and analyzed by different methods. We use WHAM to calculate free energy surfaces, binding energy and also the solvent perturbation in solute-solute interactions.

3.11 Systems under study

In the present work, interactions of methane with other like and unlike atoms are studied. Methanes are considered in methane hydrates, functionalized graphene and methane dipoles at liquid environments.

3.11.1 Methane hydrate

The methane-rich clathrates are the high pressure compounds and have multiple structures with reference to varying environmental conditions (Sloan Jr & Koh, 2007). We have considered methane hydrate III (MH-III) as a sample where four methane molecules (in each unit cell) are encapsulated within the ice channels of eight water molecules (Figure 15). The initial structure of MH-III was constructed at 10 GPa where the internal coordinates and the lattice parameters were taken from experimental data (Loveday, Nelmes, Guthrie, Klug, & Tse, 2001). Since the authors used X-rays diffraction method to retrieve the experimental data, only the atomic coordinates of the heavier atoms, carbon and oxygen, are available. The positions of hydrogens for the water molecules were chosen to satisfy the ice rules. There are multiple ways to satisfy the ice rule, the structures with vanishing (anti-ferroelectric) and non-vanishing (ferroelectric) dipole moments were considered in the present calculations. The ferroelectric structure was basically assumed at some representative pressures, including extreme and moderate values, for the purpose of checking the effect of structural arrangement on stability/enthalpies. The initial orientations of the methane molecules were fixed arbitrarily and also the effect of different orientations were checked by using three configurations of methane as definition used by Wood et al. (Wood et al., 2012). The configurations based on their orientation are defined by Straddle (S), Tripod Towards (TT) and Tripod Away (TA) with reference to a particular direction. All the parameters (lattice and internal) were relaxed at zero temperature and fixed pressure values, from 10 GPa to 300 GPa, in steps of 10 GPa. Pressure was varying in both the directions, increasing from minimum (10 Gpa) towards the maximum (300 GPa) and vice-versa, during the simulations.

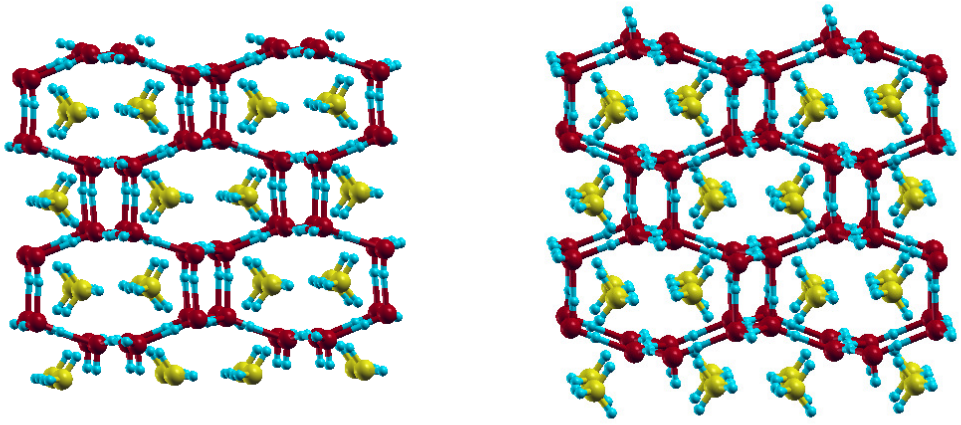

(a) Ferroelectric (b) Anti-ferroelectric

Figure 15: Ferroelectric (a) and antiferroelectric (b) arrangement of water channels enclosing methane molecules in $2 \times 2 \times 2$ supercell of MH-III structure of methane hydrates at 10 GPa.

The density-functional theory based first-principles calculations were performed to model the sample structures as implemented in quantum espresso codes (Giannozzi et al., 2009; Scandolo et al., 2005). Ultrasoft pseudopotentials were mainly used to account the ion-electron interactions. However, the calculations were checked with norm-conserving pseudopotentials at higher pressures where the effect of semi-core electrons could be significant. The exchange and correlation part of electron-electron interactions were taken into account by generalized-gradient approximation (GGA) (Perdew et al., 1996). Calculations with and without London dispersion interactions were performed at lower pressure regime (up to 60 GPa) to check the effect of van der Waals (vdW) interactions. It is because vdW interactions are important in determining structural parameters and phase transitions (Santra et al., 2011), at low pressure. They were included with pairwise addition method in standard DFT as per approximations suggested by Grimme (Grimme, 2004). At higher pressure, however, repulsive part of interaction becomes dominant and vdWs becomes less relevant.

Separate calculations for solid methane and ice, which are the constituent compounds of methane hydrates, were performed by using the similar level of approximations as discussed above for MH-III. This consistency is required in order to calculate the enthalpy of formation. The structure of ice was modeled in ice VIII-X phases by using initial structure from the experimental data (Yamawaki et al., 2004). Every unit cell of the structure contains eight molecules of water bonded in a specific way. The detail of this structure is described in the

following paragraphs. The structure of solid methane, on the other hand, was assumed as orthorhombic (space group $P2_12_12_1$) where the every unit cell contains four formula units of tetrahedral methane molecules (Gao et al., 2010; Pantha et al., 2014).

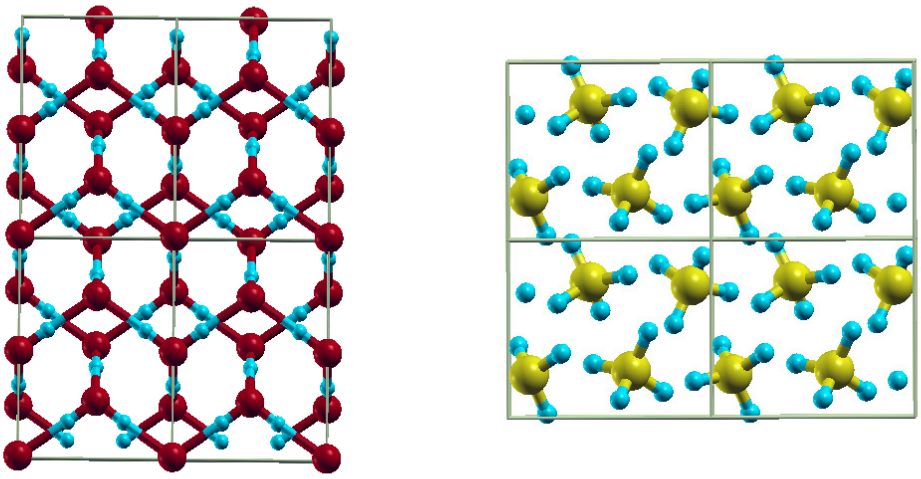

(a) Ice-VIII (b) Solid methane

Figure 16: Side-view of ice-VIII and solid methane structures in $2 \times 2 \times 2$ supercells. (a) Ice-VIII is the combination of two inter-penetrating cubic ice I_c structures. (b) Solid methane is in orthorhombic structure with space group of $P2_12_12_1$.

Among the multiple phases of ice, ice-VII, ice-VIII and ice-X are supposed to be the high pressure structures. Above 2 GPa of pressure, the structures in general fluctuate in between ice VII and VIII depending up on the temperature (Wolanin et al., 1997), where ice-VIII is recognized as low temperature structure (Yamawaki et al., 2004). This low temperature ice-VIII is tetragonal containing eight molecules per unit cell. Ice-VIII can also be understood by two inter-penetrating cubic ice lattices (Ic) which are arranged in such a way that the dipole moments of them are equal and opposite. The combined structure is therefore anti-ferroelectric (Goncharov et al., 1996) with each oxygen atom bonded to four other oxygens (among the eight nearest oxygens). Each of the oxygens then receives (donates) two protons from (to) its bonded neighbors following the *ice rule* (Fig 16). During the process, proton in between the oxygens fluctuates within two minima near to every oxygen at low pressure and comes exactly at the mid point at elevated pressure, above 65 GPa. This new structure is ice - X and also known as symmetric ice (Loubeyre et al., 1999).

X-rays diffraction experiment is a frequently used technique to find structural information of crystals. This can also be performed in virtual lab by using computational techniques. In the present work, a photon of wavelength 0.6128 Å was used to compute X-rays diffraction

spectra for the purpose of comparison with previous experiment (S.-i. Machida et al., 2006).

3.11.2 Adsorption of methane in functionalized graphene

Spin polarized density functional theory (DFT) calculations (Hohenberg & Kohn, 1964; Kohn & Sham, 1965) have been performed with PWscf code of the Quantum Espresso package (Giannozzi et al., 2009) to study the adsorption properties of metal atoms and molecular methane(s) in monolayer graphene and modified graphene respectively. The code uses ultrasoft psedopotentials to describe the interactions between ion cores and valence electrons. A plane-wave basis set, with cutoff values of 40 Ry and 400 Ry for wave functions and charge densities respectively, was used. Exchange and correlation interactions were taken into account by the Perdew-Burke-Ernzerhof (PBE) (Perdew et al., 1996) form of the generalized gradient approximation (GGA). London dispersion contributions, which are especially important for weakly bound gases, were described through the semi-empirical DFT-D2 treatment suggested by Grimme (Grimme, 2004, 2006).

Self-consistent field (scf) and geometry optimization calculations were performed with Monkhorst-Pack k-point meshes commensurate with a $12 \times 12 \times 1$ sampling of the primitive (1×1) cell of graphene. Convergence was aided by using Marzari-Vanderbilt smearing with a broadening of 0.001 Ry, except for isolated metal atoms, where fixed occupations (and no smearing) was used, to ensure that we obtained correct atomic ground state. In order to study metal adatoms on graphene, as well as adsorption of single (double) methane molecule on such systems, we used a 3×3 supercell (4×4 supercell) of the graphene substrate. A vacuum separation of 20 Å was used along the z-direction (perpendicular to the graphene sheet) to minimize the interaction between periodic images. All the atoms were allowed to relax until the forces in each direction were less than 10^{-3} Ry/Bohr. The calculations on the isolated metal atoms were performed using a cubical box of side 20 Å.

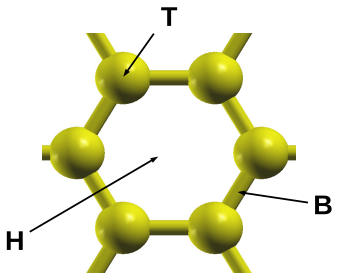

Figure 17: The high symmetry sites i) hollow (H), ii) bridge (B) and iii) top (T) of a graphene sheet.

Three high symmetry positions: the hollow (H, center of one of the hexagons), the bridge (B, midpoint of C-C bond), and the atop (T, directly above a carbon atom); were considered (Figure 17) for the adsorption of the metal adatoms on graphene. In order to sample various geometries, three possible initial orientations of the methane molecule with respect to substrate (functionalized graphene by metal atom) were allowed to relax. The geometries (say configurations) are defined by (i) Straddle (S), where two CH bonds point toward the substrate layer (ii) tripod towards (TT) with three CH bonds pointing toward the substrate and (iii) tripod away (TA) with three CH bonds pointing away from the substrate (Figure 18).

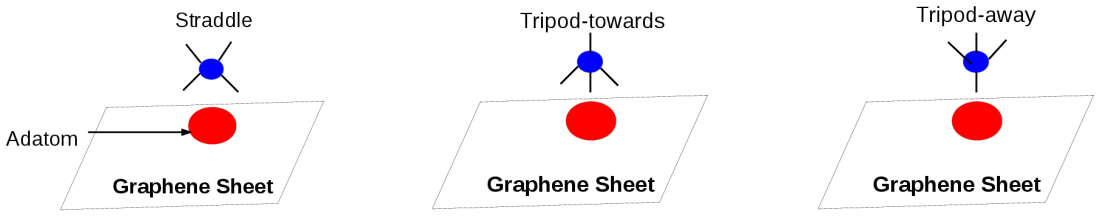

(a) Straddle (b) Tripod-towards (c) Tripod-away

Figure 18: Three different configurations Straddle (S), Tripod-towards (TT) and Tripod-away (TA) of methane are shown in substrate (metal adatom-graphene). The solid lines in methane represent covalent bonding of carbon with hydrogens to from its tetrahedral structures. Hydrogen atoms have been omitted for clarity.

Among the three initial orientations of methane, TA is the least stable configuration on graphene (will be discussed in Results section). Two equally preferable geometries, S and TT configurations separately, were used to study their adsorption properties on the most preferable metal adsorbed graphene (functionalized graphene) structures. In order to increase the gaseous (methane) concentration on functionalized graphene, five different initial configurations/combinations (on the basis of orientation and position) of two methanes on single metal atom added 4×4 supercell were considered. Their initial configurations are shown in Figure 19.

3.11.3 Methane-dimer in liquid media

Isolated methane molecules are non-polar and interactions between them is accounted by Lennard-Jones potential. When the methane molecules are kept within the liquid media the nature of interactions changes. In order to study the effect of liquid environment on methane-methane interactions, we have used water (H-O-H), methanol (CH_3-O-H) and acetonitrile (CH_3-C-N) around the methane-dimer.

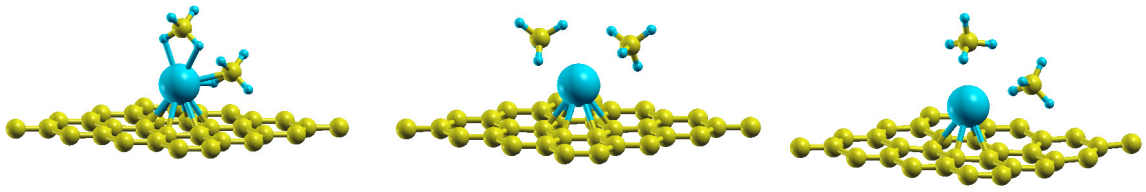

(a) Config-1 (b) Config-2 (c) Config-3

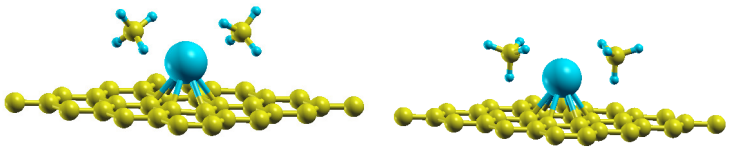

(d) Config-4 (e) Config-5

Figure 19: Initial configurations of two-methane molecules in functionalized (by metal atom) graphene. The configurations are named by Config-1, Config-2, Config-3, Config-4, Config-5 respectively.

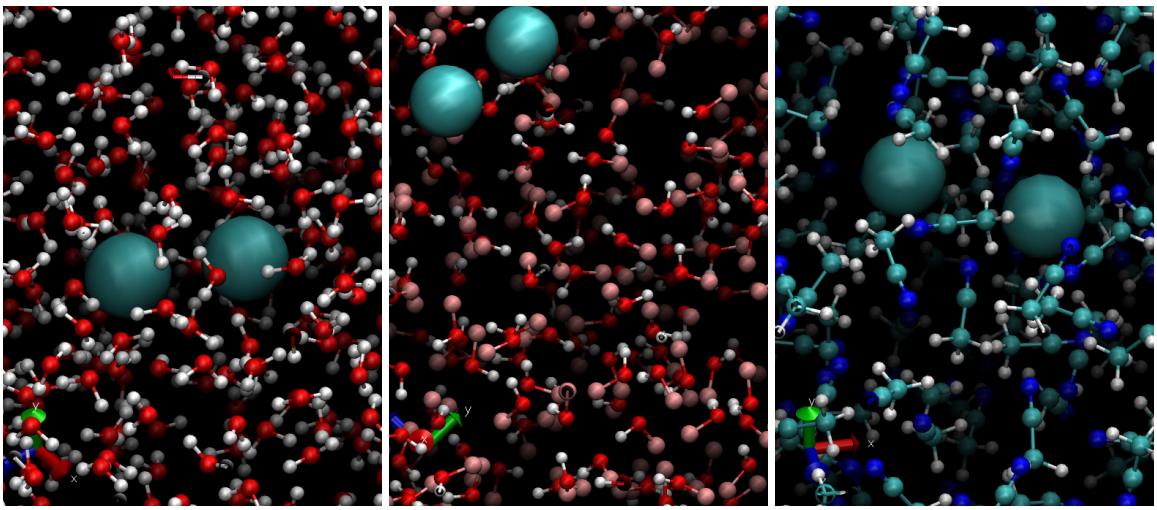

(a) Water (b) Methanol (c) Acetonitrile

Figure 20: Methane dimer is placed in different liquid media, a) water (H-O-H) (b) methanol (CH_3-O-H) (c) acetonitrile (CH_3-C-N).

The shape of the box was always cubic, however, its size for the particular liquid was chosen upon the requirement of molecular size by keeping possible interaction range and minimum image criteria in mind. The box size was 25 nm for water and 35 nm for methanol and acetonitrile. Based on their standard density at the normal conditions, the systems were having 507, 669 and 396 molecules of water, methanol and acetonitrile respectively.

Two methane molecules separated by varying distance, so-called methane-dimer are repre-

sented by united atom. In united atoms model, a methane molecule is a single sphere, like big spheres in Figure 20. The force field parameters for methene-methane interactions are inbuilt in GROMACS, and the same are used in present simulation.

Present work uses umbrella sampling within the molecular dynamics simulations to calculate the potential of mean force (PMF) in between two methane molecules placed in different solvent environments. The dimer of two methane molecules was immersed in three different solvents, water, methanol and acetonitrile in the cubic boxes of size 25 Å, 35 Å and 35 Å respectively. Overlapping between the solvent molecules were removed, and the number of solvent molecules were adjusted depending upon the box-size, molecular size of solvent molecules and their average density at room temperature (300 K) and atmospheric pressure.

Energy of each of the systems was minimized and then equilibrated in NPT (constant number of particles, pressure and temperature), where the temperature and pressure were controlled at 300 K and 1 atmosphere via velocity-rescale (v-rescale) and parrinello-Rahman barostat, respectively. The equilibrated systems were simulated in NVT ensemble for 10 ns (longer period) for each of the windows which are characterized by constraint methane-methane separation. The windows were defined with the regular interval (0.2 Å) of reaction co-ordinates (methane-methane separation). The integration time step was set as 1 fs and simulation was saved in every 200 steps, equivalent to 0.2 ps and 50000 number of configurations in each window.

The cutoff values of non-bonded interactions were defined by keeping their range of interactions and size of simulating boxes in mind. The values for van der Waals interactions and electrostatic interactions were set as 1.2 nm in water and 1.4 nm in case of methanol and acetonitrile. The constrain in methane-methane separation was maintained by using additional harmonic potentials at suitable positions in addition to the standard potentials defined for the simulations.

$$V_d = k(d - d_0)^2 \tag{3.72}$$

In equation [3.72], k is force constant (whose value is set to 1000 kJ mol^{-1} nm^{-2} for all the positions), d_0 is the equilibrium separation and d is the separation between the solute molecules. As defined in previous paragraphs, methane-methane separation defines the windows of simulation varying from 4.0 Å to 9.5 Å in case of water and 4.0 Å to 15 Å in case of methanol and acetonitrile respectively. The method of WHAM was used to calculate PMF between the solute molecules.

CHAPTER 4

RESULTS AND DISCUSSION

4.1 Introduction

In this chapter we present, discuss, and analyze the main findings of our work. Our work describes first-principles study of interactions of methane with itself and other molecules in different environmental conditions. It consists of DFT level of calculations to study molecular methane in methane hydrates and metal-adatom graphene structures, and also the atomistic simulations of methane-dimer in liquid environment. The findings of the present work will cover the following topics.

1. Clathrate structure of methane hydrate is supposed to be affected by the hydrophobic interactions in between methane and water molecules, where the surrounding pressure plays a key role for their geometry and stability. Here, we discuss the structural compression and thermodynamical and mechanical stability of the material as a function of pressure (up to 300 GPa).

2. Molecular methane(s) interacts differently with functionalized (with metal atoms) nanostructures comparing to their corresponding bare two-dimensional materials. The present study discusses the adsorption properties of single and two molecular methanes in metal-adatom graphene structures. It is relevant to the effective storage of energy-carrying gases (like methane) in light two-dimensional nanomaterials.

3. Biological processes like protein folding and their denaturation is controlled mainly by the hydrophobic interactions in between their amino acids, side-chain residues and surrounding solvent environment. Assuming methane as the simplest alkane molecule, we study methane-methane interactions in water, methanol and acetonitrile by using the method of molecular dynamics.

We go through methane hydrates, functionalized graphene and varying solvent media to study their response to molecular methanes in the sections 4.2, 4.3 and 4.4, respectively.

4.2 Methane hydrate clathrate (CH_4-H_2O)

Methane hydrates are ice like cages within which the molecular methanes are encapsulated and compressed (Sloan Jr & Koh, 2007). The properties of methane hydrate (MH-III) have been studied by using DFT level of calculations where the exchange and correlation part of electron-electron interactions were taken into account by PBE-type generalized-gradient Approximations (GGA) (Perdew et al., 1996) (Section 3.11.1). Also the vdW interactions, at least towards the lower pressure regime (within 90 GPa), have been considered to study their effect in the structural and thermodynamic properties.

4.2.1 Structural changes upon compression

The unit cell size and lattice parameters of most of the materials get compressed during the elevation of applied pressure. We first discuss the structural changes due to compression of MH-III by fixed (hydrostatic) pressure values starting from 10 GPa up to 300 GPa, in the steps of 10 GPa. The initial structure was constructed by using experimental data (X-rays diffraction) conducted at around 3 GPa (Loveday, Nelmes, Guthrie, Klug, & Tse, 2001) and then both the external and the internal parameters were relaxed. Similar level of calculations have been performed for its constituent compounds (solid methane and ice-VIII(X)). The structural symmetry of optimized MH-III was analyzed by using the the techniques suggested by Stokes and Hatch (Stokes & Hatch, 2005). Our finding shows that the general structure of MH-III as of space group *Pnma*, and upon removal of the hydrogen atoms the structure attains the higher symmetry (space group *Imma*). This result is in agreement with the previous experiment (Loveday, Nelmes, Guthrie, Klug, & Tse, 2001). As the X-rays diffraction experiments are limited to the heavier atoms of the compound, we get only the coordinates of carbon and oxygens, and the comparison with the computed structure is possible after removal of hydrogens. The crystal structure of MH-III is characterized by two different-sized channels, where the larger channels are running along the *a* axis and smaller channels are running along the *c* axis (Fig. 21). Furthermore, four-membered ring could also be observed along the *a* axis (Hirai et al., 2003). The compression is faster at the lower pressure values

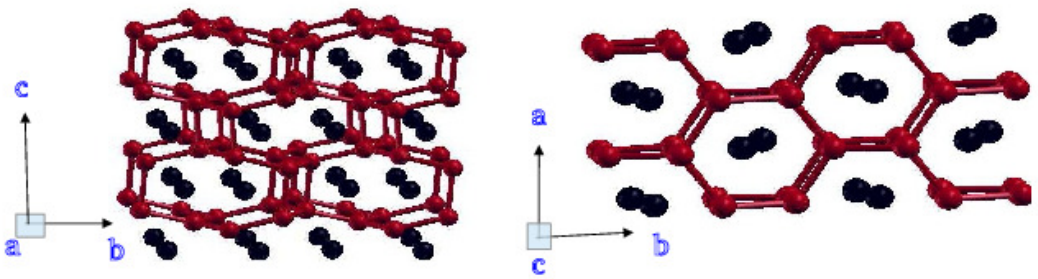

Figure 21: MH-III structure with the channels running along the *a* axis (left) and along the *c* axis (right) in $2 \times 2 \times 2$ supercells. Red (black) spheres are oxygen (carbon) atoms. For clarity, hydrogen atoms have been removed and oxygen atoms connected along hydrogen bonds.

and decreases continuously towards the higher pressure (until 180 GPa). For the hydrostatic compression of the compound, structural variation causes anisotropic changes along three different crystal directions. This anisotropy could be realized in terms of varying slopes of cell parameters and intermolecular separations as a function of applied pressure (Figures 22 and 25). The larger hollow spheres in Figure 22(a) represent the experimental values (Hirai et al., 2003) and show a good agreement with the present calculations. Note that the authors have provided the experimental values only for the lower pressure values (upto 42 GPa).

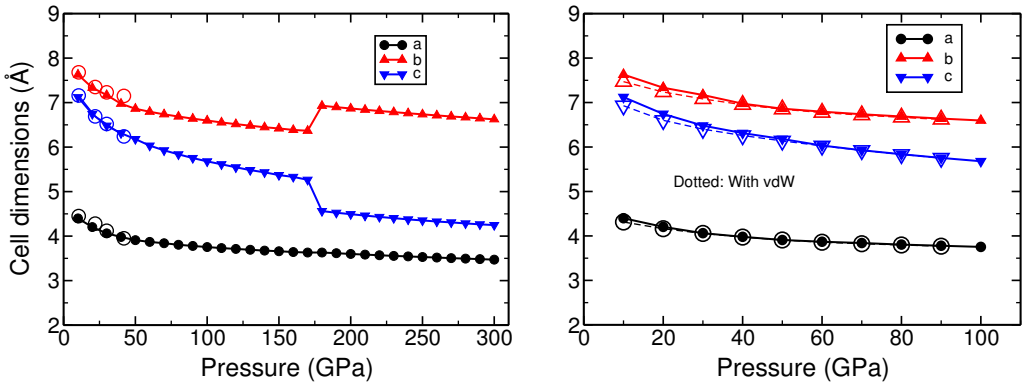

(a) Without vdW (b) With vdW

Figure 22: Pressure dependence of the cell parameters in methane hydrate clathrates, MH-III up to 170 GPa and HP structure afterwards (calculated without vdWs). The larger-hollow symbols in Figure (a) represent the experimental values (Hirai et al., 2003). In Figure (b), solid and hollow symbols represent the values calculated without and with vdW interactions.

Figure 22(a) shows that *c* axis decreases faster (with elevated pressure) than other lattice parameters. The rate of compression is moderate for *b* axis and the slowest for *a* axis. The jumps on the curves along *b* and *c* directions at 180 GPa is due to phase transition (structural

change) of the compound, the details will be discussed in section (4.2.3). For MH-III structure, the faster (slower) rate of decrease in lattice parameter along c (a) direction could be understood with the help of its geometry. As shown in Figure 21, the large channels run perpendicular to c axis, which is comparable to ice-Ih in the sense that six-membered hexagonal ring runs along c axis in both the structures. In MH-III, adjacent three water molecules in the ring are connected to upper layer and next three to the lower layer unlike to the alternate connection of water molecules in ice Ih (Hirai et al., 2003). This favors to create larger voids perpendicular to the c-axis and are more vulnerable to shrink faster along its shorter diameter. On the other hand, there are four-membered rings along a axis where the water molecules are closely packed. The denser arrangement of water molecules causes the compression harder along a axis. Above 180 GPa of pressure, the structure mechanically collapses along the c direction and elongated along the b direction. We label this structure as High Pressure (HP) structure (Figure 31).

The orientational ordering of guest molecules may also play a role in anisotropic compression of clathrate type materials. At low pressure, in particular, the guest molecules are orientationally disordered and the pressure dependent changes including anisotropic compression on geometry is guided by the process of ordering of the molecules. This effect is pronounced in the larger channels where the guest molecules are in the state of free rotation (Tanaka et al., 2013). Once the molecules start getting ordered during the elevated pressure, the rotational motion of the guest molecules goes down. As the consequence of reducing the state of free rotation, both the compressibility and anisotropy are reduced. On further increasing the pressure, the repulsive interaction between the guest-guest and also the host-guest molecules increases (Tanaka et al., 2013; Hirai et al., 2003) which ultimately leads the axes to the nearly incompressible state.

Figure 22(b) shows the comparison of lattice parameters calculated in absence and presence of vdW interactions. Here, van der Waals interactions incorporate the induced dipole-dipole interactions caused by London dispersion forces, and the inclusion of such forces increase the attractive forces between the molecules. Increasing attractive forces obviously helps to decrease the cell sides. The effect of vdW interactions is larger at the lower pressure values and decreases on increasing the pressure. For example: the percentage difference between the lattice parameters (in presence and absence of vdW) with respect to without vdW are (1.83 %, 1.64 % and 2.76 %) along a, b and c axes at 10 GPa, whereas these values at 60 GPa are (0.3 %, 0.18 % and 0.25 %), respectively. At higher pressures, the repulsive part is dominant

due to partial overlapping of electron cloud and thus the effect of vdW becomes negligible. The phenomenon is taken care by the damping factor towards the shorter distances in DFT-D2 method (Grimme, 2006).

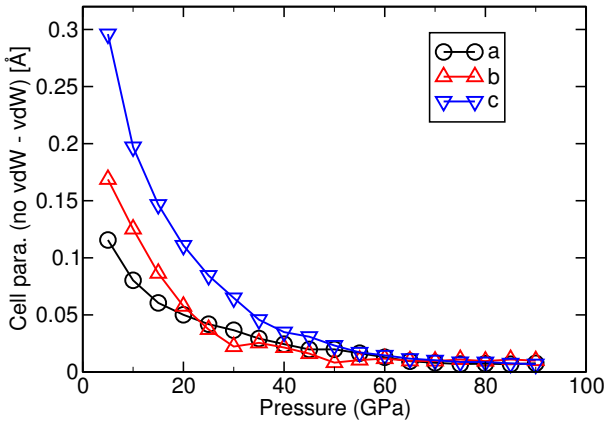

Figure 23: Difference in cell parameters without and with vdW interactions, as a function of pressure. Black circles, up-triangles and down-triangles represent the differences along a, b and c axes respectively.

The magnitude of difference in corresponding cell parameters (between without and with vdW interactions) is shown in Figure (23). The figure reveals that the role of vdW in the compression of lattice parameters is larger at low pressures and reduces significantly after 40 GPa. Beyond 60 GPa, the difference is negligible. The magnitudes of the difference is consistent with the actual cell sizes, larger the length of cell parameters larger the vdW corrections.

Because of change in geometrical structure (phase transition) at 180 GPa, an abrupt change in slopes of cell parameters is observed [Figure 22(a)]. However, it is insignificant along '*a*' direction, and noticeable along *b* and *c* directions. The geometrical structure (Figure 31) and magnitudes of cell parameters at 180 GPa imply that the structure is collapsed along *c* axis forming a quasi-one dimensional structure along *b* axis.

As a consequence of anisotropic compression of the compound, distance between the molecules filling the channels decreases differently along *a*, *b* and *c* directions. In order to recognize the magnitudes of intermolecular separation in different directions, we assign nominations for carbons and oxygens as shown in Figure 24. In the figure, the oxygens in the larger channels are named from O_1 to O_8 in clockwise order. The nearest carbon atoms from the reference carbon C along the channel running through *b* axis (*c* axis) are labeled C_+ and C_- (C' and C'') respectively.

The compression of (representative) intermolecular separation during the elevated pressure

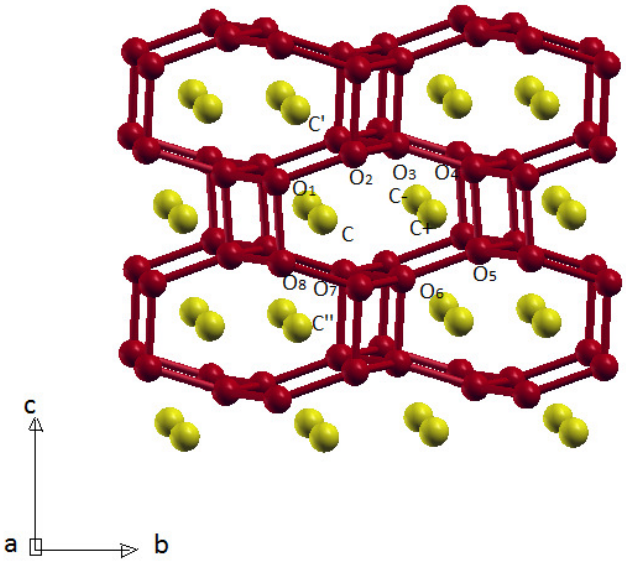

Figure 24: View of the MH-III methane hydrate structure along the *a* axis. Red (yellow) spheres are oxygen (carbon) atoms. Oxygen atoms are labeled O_1 to O_8 in clockwise order. The nearest carbon atoms from the reference carbon C along the channel running through *b* axis (*c* **axis**) are labeled C_+ and C_- (C' and C") respectively. For clarity, hydrogen atoms have been removed and oxygen atoms connected along hydrogen bonds (Pantha, Adhikari, & Scandolo, 2015).

is shown in Figure 25. As similar to the lattice parameters, the decrease in carbon-carbon separation as a function of pressure is direction dependent (anisotropic). It decreases faster along the smaller channel (*c* direction), where the carbon-carbon distance reaches a value of 3.0 Å at 80 GPa (Figure 25), than along the larger channel of value 3.3 Å (*b* direction). The distances along *c* and *b* directions, respectively, are represented by C - C′ and C - C_+ in Figure 25. The pressure of 80 GPa has been considered with reference to the highest pressure achieved experimentally (S.-i. Machida et al., 2006). For the purpose of comparison, the shortest carbon-carbon distance in solid methane at 80 GPa is 2.6 Å.

Water-methane in host-guest arrangement and water-water molecules in host channels come closer during the compression. Except at very low pressure, the compression of carbon-oxygen and oxygen-oxygen separation is almost identical along all the directions of MH-III unit cell (Figure 25). At low pressures, however, the carbon-oxygen separations are compressed differently most likely in the search of their stable relative positions. The shortest carbon-oxygen distance reaches a value of 2.52 Å at 80 GPa. The compression of water-water separation seems to depend on the relative positions rather than the particular direction. Starting from the identical water-water distances at 10 GPa, the bond length is larger for O_1 - O_8 than O_1 - O_2 separation. The nature of bonding reveals that O_1 - O_8 and O_4 - O_5 bonds

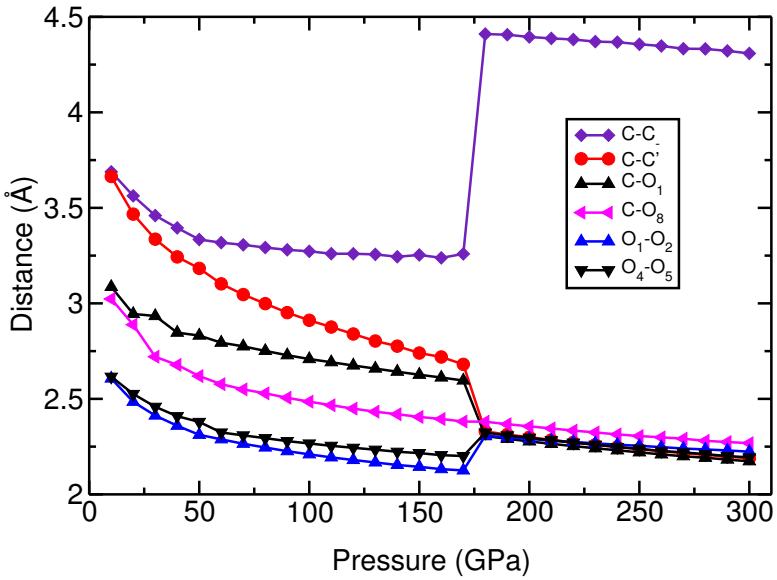

Figure 25: Pressure dependence of the distances between selected atoms in MH-III (below 180 GPa) and in the HP structure (above 180 GPa). Atoms are labeled according to Figure 24. Notice that the distance between methane molecules in MH-III decreases faster along the smaller channel (along the *c*-axis) than along the larger channel (along the *b*-axis).

are parallel to one of the cell parameters (*c* axis) while other bonds are arranged in zig-zag way to complete the channel which runs parallel to *a* axis in a unit cell. The combination of zig-zag bonds is less resistive during the elevated pressure, and vulnerable for larger compression. Water-water distances in MH-III decrease at a faster rate than their pure-ice counterpart and reach values between 2.24 Å and 2.29 Å at 80 GPa. For comparison, the shortest oxygen-oxygen distance in ice X at 80 GPa is 2.32 Å. As a consequence, hydrogen-bond symmetrization takes place at lower pressures in MH-III than in ice, as noted in previous work (Iitaka & Ebisuzaki, 2003).

We consider two inequivalent O-O distances (O_1 - O_2 and O_1 - O_8) to study the symmetrization behaviour of MH-III (Figure 26). At low pressure, hydrogen remains at one of the two potential minima along O-H...O bonds, where O-H represents the covalent bond and H...O represents the hydrogen bond in between two nearest oxygens (Iitaka & Ebisuzaki, 2003; Sugimura et al., 2008). On increasing pressure, H...O bond compresses more rapidly than the covalent bond, and the potential barrier between two minima decreases. Towards the moderate pressure, hydrogen starts tunneling this barrier which causes slight rearrangement in electron distribution. The neutral atoms are now slightly ionized (like O^- and H^+) which define the *ionization state*. On further increasing the pressure, hydrogen distribution becomes unimodal keeping H at the center of the oxygen-oxygen separation (from the bimodal distribution at

low pressures). This process is called symmetrization of H-bond. When two minima exist at the potential, even after unimodal distribution of H, the distribution is called dynamic symmetrization (Sugimura et al., 2008). The symmetrization becomes static (centering of H-bond) with the single potential minimum at the center of O-O bonding which is obtained due to further elevation of applied pressure. In practice, ionization and centering have been observed on the basis of threshold separations between the O-O atoms, eg. 2.40 Å and 2.30 Å for ionization and symmetrization, respectively (Benoit et al., 2002). As we already have noticed that O-O separation compresses faster in MH-III in comparison to ice, ionization and centering may occur at lower pressures in case of MH-III (S.-i. Machida et al., 2006).

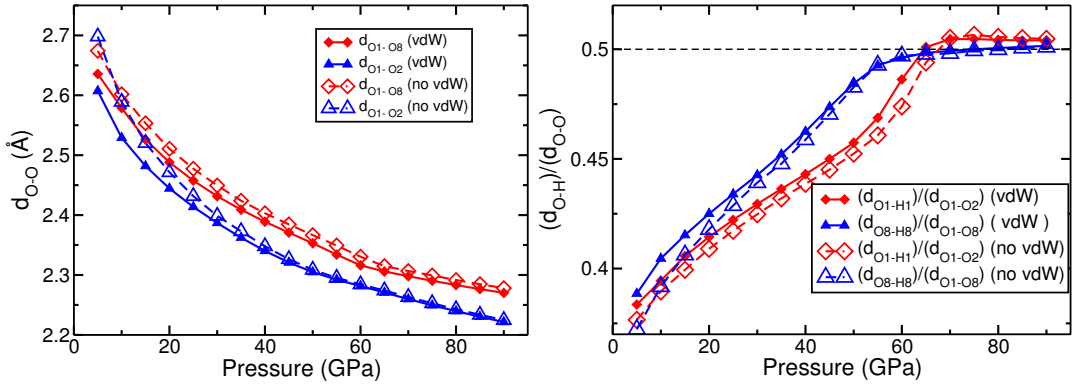

(a) (b)

Figure 26: (a) Variation of oxygen-oxygen separation along two symmetrically inequivalent directions. (b) Pressure dependence of the ratio of distance of hydrogen from its bonded oxygens to the oxygen-oxygen distance joined by the same hydrogen. H_1 connects oxygen atoms O_1 and O_2 along the *b* axis and H_8 connects oxygen atoms O_1 and O_8 along the *c* axis (Figure 24). Solid and hollow symbols represent the calculations in presence and absence of vdW interactions.

Figure 26 shows the variation of oxygen-oxygen separation (a) and the ratio of hydrogen-oxygen to oxygen-oxygen separation (b) as a function of elevated pressure. The solid symbols represent the values calculated in presence of vdW interactions whereas the corresponding hollow symbols represent them in absence of vdW interactions. As similar to the cell parameters, inter-atomic separation is smaller in presence of vdW comparing to that in absence of vdW at low pressures. This could be because of attractive contributions of vdw interactions. At higher pressures, however, the repulsive force becomes dominant and the effect of vdW is neglected. This is clearly visible in the figure. The interatomic separation (O-O), at the same pressure values, is different for two symmetrically inequivalent oxygen-oxygen bondings.

If the ionization and centering of H-bonds are considered on the basis of O-O separation, they occur at around (35-40) GPa and (65-70) GPa with distances 2.3 Å and 2.4 Å, in presence of vdW interactions, respectively. The values are slightly less than those in absence of vdW interactions (40 GPa and 70 GPa) and consistent with the previous study (Iitaka & Ebisuzaki, 2003). Similar phenomenon in pure ice counterpart, ionization and centering occur at higher pressures, around 55 GPa and 100 GPa, respectively (Benoit et al., 2002; Pantha & Adhikari, 2015). Note that the values are calculated (in the present work) within the limit of classical nuclei and zero temperature. Inclusion of quantum effects at finite temperature may lower the symmetrization pressure to 40-50 GPa. Figure 26(b), shows the variation of $(d_{\text{O-H}})/(d_{\text{O-O}})$ as a function of pressure where the ratio increases on increasing pressure. It is because, the numerator $d_{\text{O-H}}$ represents covalent (O-H) bond (smaller) distance, which is less compressible comparing to the sum of H...O and O-H bond (O-O bond). It means the ratio is less than 0.5 at lower pressures and reaches to 0.5 around (65-70) GPa, the condition for centering (H-bond symmetrization). There is not significant difference of symmetrization pressure in presence and absence of vdW interactions. In case of ionization, however, vdW seems to compress $d_{\text{O-H}}$ more rather than $d_{\text{O-O}}$.

In Figure 27 we show the calculated and corresponding experimental X-ray diffraction spectrum, at two representative pressures, 20 GPa and 60 GPa, respectively. Since X-rays diffraction experiment is limited to heavier atoms, hydrogens are removed in our calculations. The agreement between calculations and the experimental data of the Machida et al. (S.-i. Machida et al., 2006) is excellent at 20 GPa. At 60 GPa the calculations indicates the persistence of a doublet at a value of 2θ of about 15 degrees. The experimental data show a single peak in that range of 2θ. The transformation of the doublet into a single peak was interpreted as one of the main evidences for a phase transition that would occur around 40 GPa (S.-i. Machida et al., 2006). We do not find any evidence of phase transition at these pressures, with the exception of the symmetrization of the hydrogen bond, which however takes place in a continuous fashion and without changes in the symmetry of the structure in our calculations.

After discussion of structural changes in methane hydrates, we now present thermodynamic properties of the material.

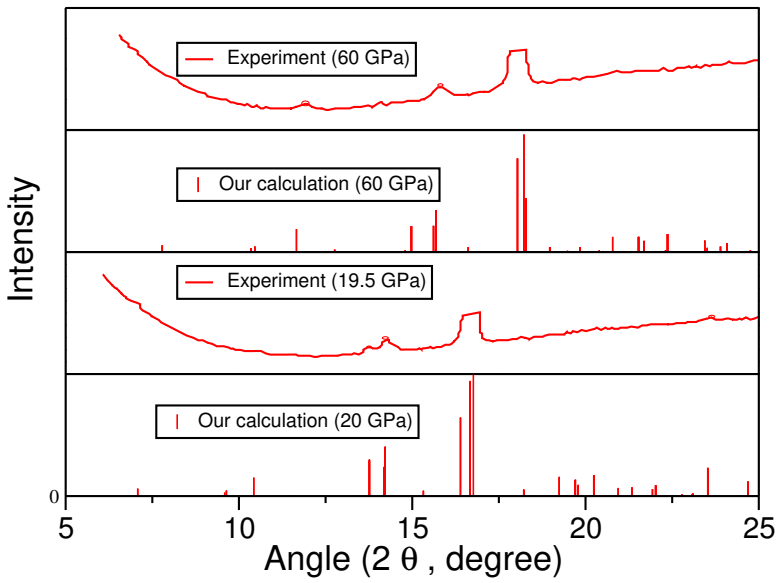

Figure 27: Calculated X-ray diffraction patterns and corresponding experimental spectrum of methane hydrate clathrate at 20 GPa (lower panel) and 60 GPa (upper panel). The experimental values are taken from the reference (S.-i. Machida et al., 2006) and simulated values are already published (Pantha, Adhikari, & Scandolo, 2015).

4.2.2 Thermodynamic stability of MH-III

The information of enthalpy of formation gives an idea of the relative (thermodynamic) stability. The line with up-triangles of Figure 28 (a) shows the calculated difference between the enthalpy of MH-III and that of its constituents, ice and solid methane, above 10 GPa. With the exception of a narrow range at very low pressure (10-12 GPa), we find that the enthalpy of the constituents is systematically lower than that of MH-III, and that the difference grows with pressure. At 80 GPa, the highest pressure at which MH-III has been observed in experiments (S.-i. Machida et al., 2006), the enthalpy difference reaches a value of 1.8 eV per MH-III unit cell, equivalent to 0.45 eV per CH_4 molecule and this value is too large to be overcome by entropic contributions at room temperature. Hence we remark that MH-III is only metastable at high pressure and room temperature. The line with down-triangles, on the other hand, shows the difference in enthalpy between the new structure, defined by high pressure (HP) structure, and MH III structure. The figure reveals that within the regime of metastability, HP structure is (thermodynamically) more stable over MH III beyond 180 GPa. The difference in enthalpy (with HP structure) also increases with pressure. The findings regarding the stability of MH-III is consistent with recent observations of a much more limited range of stability for MH-III (Shu et al., 2011), where the authors suggest that MH III decomposes to its constituents above 3 GPa. Note that these results are based on the

calculations which do not incorporate the vdW interactions. Since the vdWs are important to determine the phase diagram of ice like materials (Santra et al., 2011), we incorporated dispersion interactions in further calculations. We also see the enthalpy of formation at lower pressures (both in presence and absence of vdW interactions) for the purpose of comparison with the reference (Shu et al., 2011).

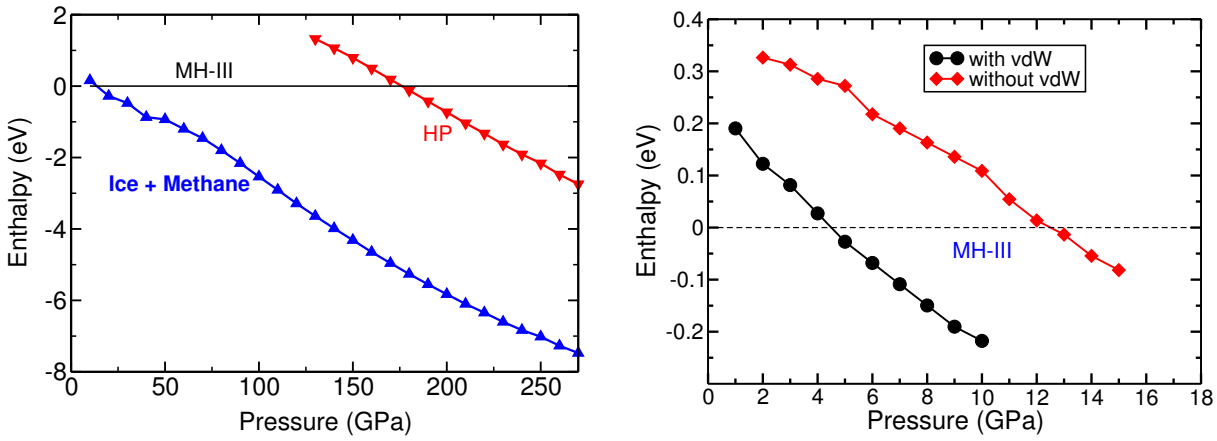

(a) (b)

Figure 28: (a) Relative enthalpies as a function of pressure for MH-III, HP structure (down-triangles), and for the constituents, ice and methane (down-triangles). (b) Relative enthalpies for constituents, ice and methane, with vdW (circles) and without vdW (squares). The reference enthalpy is that of MH-III.

Figure 28 (b) shows the relative stability of MH-III with respect to its constituents at lower pressure regime. The line with squares shows the calculations without vdW interactions in smaller interval of pressure, which reveals that constituents are thermodynamically more stable above 12 GPa. The line with circles on the same figure shows the similar calculations by taking vdW interactions into account, which lowers the stability region of MH III from 12 GPa to 4 GPa. The later result is nearer to the experiment where the authors find decomposition of methane hydrates above 3 GPa.

Figure 29 shows the experimental and calculated volume-vs-pressure curves for the methane hydrate and its constituents. Both experimental and calculated data (within the metastable regime of MH III) show that the volume of MH-III is systematically larger than that of the sum of the two constituents. Enthalpy (H) is related to volume (V) by the relation (H = E + PV) (where E is internal energy, and P is pressure), which means larger the volume contributes to higher (less negative) the enthalpy and lesser the stability. Again, the volume is the derivative of the enthalpy with respect to pressure, a larger volume implies a growing enthalpy difference between methane hydrate and its constituents, in favor of the constituents. This strengthen the

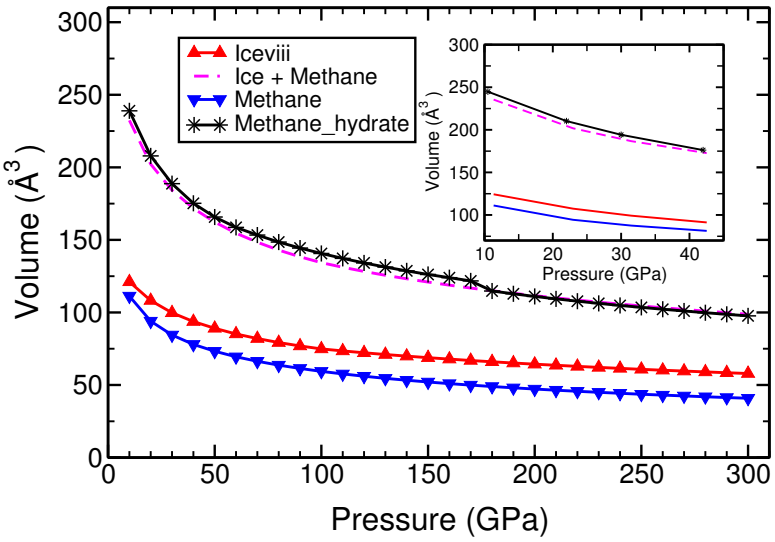

Figure 29: Pressure dependence of the calculated unit-cell volume of MH-III (below 180 GPa), of the HP structure (above 180 GPa), and of an equal molar amount of ice and methane (dashed line). The inset show the unit-cell volume of MH-III, and of an equal molar amount of ice and methane extracted from available experimental data for MH-III (Hirai et al., 2003), ice (Loubeyre et al., 1999), and methane (Sun et al., 2009), respectively. The sum of volumes for the constituent compounds is represented by the dashed line in inset figure.

idea revealed by enthalpy of formation, where the constituents are more stable over MH-III. The inset figure of experimental values (extracted with the help of equation of states) shows the similar trend with the present calculations. It means the current work is consistent with reference to the experiment.

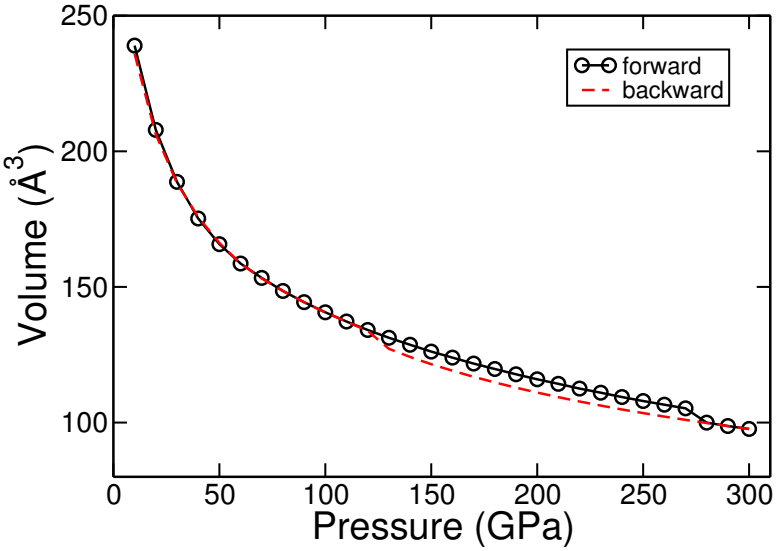

Figure 30: Pressure dependence of the calculated unit-cell volume of MH-III during increasing (black line) and decreasing (red dotted line) pressure, from 10 GPa to 300 GPa and vice-versa.

We show changes of unit cell volume on increasing pressure from 10 GPa to 300 GPa and on decreasing pressure from 300 GPa to 10 GPa (in the interval of 10 GPa in both the cases)

in Figure 30. Figure (30) represents continuous compression of the unit cell on increasing pressure (so called forward direction) until 270 GPa. When the pressure reaches to 280 GPa, the volume curve shows a jump indicating that the mechanical stability of MH III is lost beyond this pressure (will be discussed in section 4.2.3). The structure changes to more compact structure, defined by HP structure. On decreasing pressure, on the other hand, the unit cell volume of HP structure decreases monotonically via different path until 130 GPa. When the pressure is further decreased below 130 GPa, HP structure comes back to MH III structure. It means the structure is reversible as a function of pressure with some hysteresis as shown by closed loop in the figure. Based on the discussion made so far, we remark that thermodynamic stability of MH III is limited to 180 GPa while the mechanical stability remains until 280 GPa.

4.2.3 Structural transition at 180 GPa

Further compression of the MH-III structure in the multi-megabar range eventually leads to the collapse of the structure into a more compact structure which we label as 'HP'(Figure 31). The structural collapse takes place in our calculations at 280 GPa, indicating that the MH-III structure reaches its mechanical stability limit at this pressure.

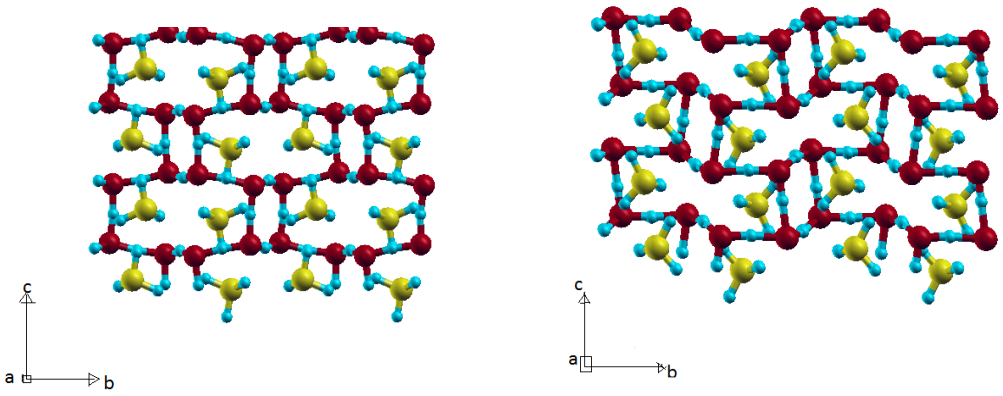

(a) MH III structure (b) HP structure

Figure 31: View of the MH III (a) and HP structure (b) at pressure 180 GPa, parallel to *a* axis.

Neglecting the possibility of a dissociation into its constituents, a comparison of the enthalpies of the MH-III and of the HP structure (Figure 28) indicates that the thermodynamic limit for the stability of the MH-III structure is 180 GPa, above which the HP structure becomes

energetically favored. The HP structure is characterized by the same space group symmetry as MH-III but by a sizable change of the internal and lattice parameters. However, the decrease in volume at 180 GPa is only 4 %. Furthermore, the difference in volume of the HP structure (beyond 180 GPa) and that of the sum of the constituents, ice and methane, is insignificant (Figure 29). The transition is characterized by an elongation of the shortest oxygen-oxygen distances from 2.1 Å at 170 GPa in MH-III to 2.3 Å in the HP structure at 180 GPa (Figure 25). It is also characterized by a dramatic reduction of the shortest carbon-carbon distance along the *c* axis. The collapse of the C-C distance along the *c* axis implies the formation of a quasi-one-dimensional chain of methane molecules in the HP structure.

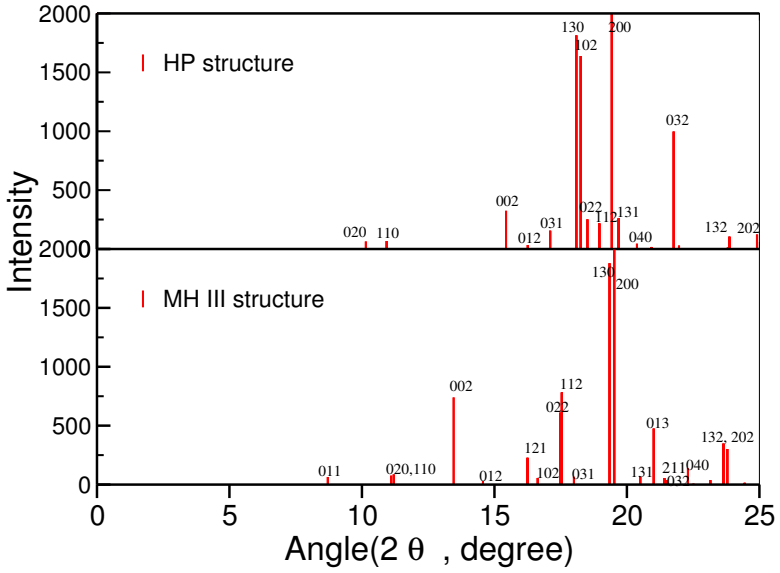

Figure 32: Comparison between the calculated X-ray diffraction spectra for MH-III (lower panel) and the HP structure (upper panel), at the coexistence pressure of 180 GPa (Pantha, Adhikari, & Scandolo, 2015).

The X-ray diffraction spectrum of the HP structure is compared to that of MH-III at the transition pressure of 180 GPa (Figure 32). Differences between the two spectra are noticeable and considerably more evident than the subtle changes reported in experiments at 40 GPa (Hirai et al., 2003; S.-i. Machida et al., 2006). In addition, our HP structure reverts back spontaneously to MH-III due to a mechanical instability when pressure is reduced below 130 GPa. We therefore do not see the possibility that the HP structure could be related to the new structure observed in those experiments.

4.3 Adsorption of methane in pure and functionalized graphene

In this section, we first study the adsorption of metal atom (of ten different species) on pristine graphene, to understand the structural, electronic and magnetic properties of metal-adatom garphene systems. Among the number of structures, we use the most stable/suitable geometries of metal-adatom graphene, defined as functinalized-graphenes, as the substrate materials. The section will be followed by the adsorption process of molecular methane(s), their adsorption energies, and the nature of interactions with the functinalized-graphenes.

4.3.1 Metal adatom-graphene

Ten metal (M) species, Sc to Zn of 3d transition elements in periodic table, are considered to adsorb an adatom on monolayer graphene which counts M to C (metal to carbon) ratio as 1:18 and 1:32 for (3×3) and (4×4) supercells, respectively. We first notice optimized geometries, calculate the binding energy, total magnetic moment of the compounds, and compare the results with the previously reported data. Furthermore, we discuss the electronic density of states and charge transfer calculations from metal adatom towards the monolayer graphene (and vice-versa if any) before moving into another section.

Binding energy (E_b) and geometries

The binding energy (E_b) of metal adatoms on graphene is defined by the following equation:

$$E_b = E_a + E_g - E_{ag}, \tag{4.1}$$

where, E_a, E_g and E_{ag} represent the total energy of an isolated metal adatom, monolayer graphene (3×3 supercell containing 18 carbon atoms except otherwise stated), and adatom-graphene, respectively. Positive values from this equation indicate favorable binding of metal atoms on graphene. The higher binding energy of an atom is an indicator of the higher stability. The diffusion barrier (E_{diff}), on the other hand, is defined as difference in binding energy in between the most stable site and the other high symmetry sites.

The metal atoms have been allowed to be adsorbed at three high symmetry (H, B and T) sites (Figure 17). For each adsorption site, the adatom and C atoms on graphene are relaxed along all possible directions. The adsorption geometry is obtained from the positions of the atoms after relaxation. The adatom height (h) is defned as the difference in z coordinate of the adatom and the average of the z coordinates of the carbon atoms in the graphene layer.

Table 1: Structural and energetic properties of transition metal atoms at different adsorption sites (H, B, T) of monolayer graphene containing 18 number of carbon atoms. The highest binding energies are boxed to get them noticed.

Adatoms	Adsorption site	E_b (eV)	E_{diff} (eV)	$\mu_{MG}(\mu_B)$	h (Å)	d_{MC} (Å)	$r_M + r_C$ (Å)	d_{GC} (10^{-1} Å)
Sc	H	**1.695** (1.51)		2.63 (2.24)	1.927 (1.927)	2.418 (2.435)	2.41	0.33
	B	1.165	0.530	1.09				2.4
	T	1.172	0.523	0.87				2.1
Ti	H	**2.002** (1.74)		3.33 (3.32)	1.819 (1.791)	2.346 (2.331)	2.23	0.26
	B	1.549	0.453	3.75				0.56
	T	1.494	0.508	3.0				0.50
V	H	**1.864** (1.09)		4.75 (4.41)	1.856 (1.791)	2.353 (2.331)	2.12	0.24
	B	1.748	0.116	4.75				0.58
	T	1.704	0.160	4.75				0.63
Cr	H	0.405 (0.18)	0.083	5.75 (5.55)	2.212 (2.045)	2.630 (2.518)	2.05	0.44
	B	**0.488**		5.75	2.406	2.434		0.70
	T	0.473	0.015	5.75		2.423		0.70
Mn	H	0.290 (0.13)	0.008	5.25 (5.40)	2.04 (2.022)	2.491 (2.511)	2.03	0.24
	B	0.273	0.025	5.25				0.96
	T	**0.298**		5.25	2.204	2.204		0.5
Fe	H	**0.870** (1.21)		2.0 (2.00)	1.564 (1.489)	2.125 (2.105)	2.04	0.07
	B	0.538	0.332	4.25				0.9
	T	0.240	0.630	2.25				0.8
Co	H	**1.254** (1.59)		1.25 (1.03)	1.503 (1.490)	2.091 (2.102)	2.02	0.17
	B	0.857	0.397	1.12				0.07
	T	0.836	0.418	2.80				0.77
Ni	H	**1.753** (1.55)		0.00 (0.00)	1.533 (1.510)	2.110 (2.117)	2.02	0.13
	B	1.539	0.214	0.0				0.26
	T	1.490	0.263	0.0				0.31
Cu	H	0.367 (0.24)	.203	0.75 (0.87)	1.978 (2.044)	2.432 (2.513)	2.05	0.13
	B	0.567	0.003	0.75				0.62
	T	**0.570**		0.75	2.068	2.068		0.43
Zn	H	**0.179**	-	0.25 (-)	3.069	3.390 (-)	2.16	0.12
	B	0.165	0.014	0.0				0.85
	T	0.167	0.012	0.02				0.15

Note: The properties listed in the table are binding energy (E_b), diffusion barrier (E_{diff}, difference in binding energy between the most stable site and the other high symmetry sites), the nearest metal to carbon distance (d_{MC}), magnetic moment of metal adatom-graphene (μ_{MG}), adatom height from graphene plane (h), and distortion in the graphene plane (d_{GC}). The diffusion barrier has been calculated by taking difference of binding energy in between the most stable geometry and that at other high symmetry sites. The magnetic and geometrical parameters for M/G are also tabulated.

The distance between the adatom and its nearest carbon atom has also been observed, and represented by (d_{AC}). The adsorption of metal atoms on graphene produces distortion which is quantified by computing the maximum deviation in the z direction of the C atoms in the graphene layer with respect to their initial positions.

Table 1 shows the geometrical, electronic, and magnetic properties of metal adatom graphenes. The binding energy values and their comparison with references have also been displayed in

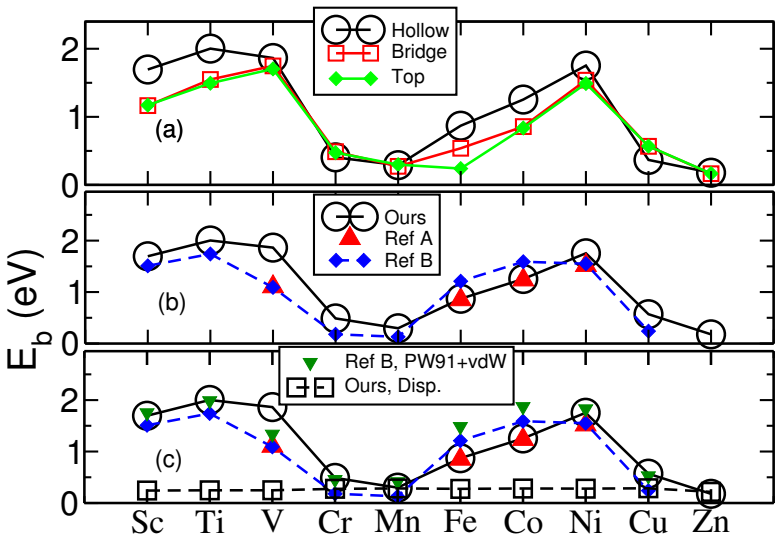

Figure 33: Binding energies of metal-adatoms on monolayer graphene sheet. (a) Binding energies of metal-adatoms at H, B and T sites of the graphene sheet, where all the strongly bound atoms (Sc-V, Fe-Ni) prefer hollow site for their adsorption. (b) The black line with circles represent the binding energy of metal-adatoms at the most favorable sites of graphene sheet. The red up-triangles (Ref.A) and the blue dotted line with diamonds (Ref.B) represent the values from the references, Liu et al. (Liu et al., 2011) and Valencia et al., (Valencia et al., 2010) respectively. (c) The additional black dotted line with squares represents the dispersion contributions and the green down-triangles in dotted line represent the Ref. B when our calculations for dispersion corrections are added to them.

Figure [33]. Table [1] and Figure [33] reveal that the most of the metal atoms under this study (except Cr, Mn, and Cu) prefer to be adsorbed at the hollow site of graphene. Chromium (Cr) prefers B site, and Mn and Cu prefer T site for their adsorption (Paudel et al., 2016). These results for the favorable adsorption site are consistent with the previous studies (Chai & Head-Gordon, 2008; Valencia et al., 2010; Yagi et al., 2004; Liu et al., 2011). The analysis of their electronic configurations follows Hund's rule which implies that metal atoms with partially filled 3d shell prefer H site of graphene for their adsorption. Also the magnitude of the binding energy of the adatoms is noticeably higher at H-site (except Zn) comparing to that at the remaining (B and T) sites. The adatoms having half-filled and totally filled 3d-orbitals (Cr-Mn and Cu-Zn), on the other hand, show low and comparable binding energies at all the tested sites. This implies that the adatoms are not localized in a particular site, and diffuse throughout the graphene layer. If we minutely see the magnitudes, Cr at B site, Mn and Cu at T site and Zn at H site are adsorbed within a difference of 15 meV with respect to their nearby favorable sites. Because of this low difference in binding energy and weak interaction between the adatoms and graphene, it is difficult to confirm the particular adsorption site for metal atom on graphene. For example: different studies find different positions (T site (M. Wu

et al., 2009; Liu et al., 2012) and B site (Cao et al., 2010)) as favorable sites for Cu. Our study (for Cu) shows almost equal binding energies, 0.570 eV and 0.567 eV for top and bridge sites respectively, and implies that the top site is more stable even though the difference is negligible in the context of present calculations. The holistic properties indicate that the metal atoms with low binding energy may favor to form metallic cluster on the cost of weakening metal to graphene interactions.

Let us consider the most stable systems to discuss/compare the binding energy of 3d-metal adatoms on graphene. The binding energy (E_b) of the adatoms generally increases on both the sides of Cr/Mn (Figure 33 (b)). Cu and Zn, lying at the right most of the 3d series, have their 3d shell filled and are less reactive towards the graphene layer. Comparing E_b with the reference (Liu et al., 2011), Vanadium is underestimated in the reference, whereas that of Fe, Co and Ni agree well with the present calculations. Liu et al. have included only four metal atoms (V, Fe, Co and Ni) by using PBE type GGA exchange-correlation functionals, which are consistent with the exchange-correlation functionals used by the present calculations (except the vdW interactions). Valencia et al. (Valencia et al., 2010), on the other hand, have calculated the binding energy values of Sc-Cu on graphene and shown that the magnitudes follow a special pattern. The curve following the pattern is defined as chevron shaped (V-shaped) curve. Present calculations follow the same trend with some differences in magnitude. In their calculations V is underestimated, and Fe and Co are overestimated. Valencia et al., have used different type of exchange correlation functional (PW91). It should also be noted that present calculations have incorporated van der Waal's (vdW) interaction through Grimme model (Grimme, 2006), which is absent in the references [Liu2011, Valencia2010], and thus could be understood that incorporation of vdW interactions in references can improve some of the lower values (like V) in the references (Figure 33 (c)). The differences for Fe and Co, however, increases in this situation, and needs further analysis to describe these few anomalies. The dispersion corrections calculated for binding energy by the present work have been noted in the order of 0.25 eV.

If the diffusion pathway is assumed through the high symmetry sites, difference in binding energy between the most stable and the other high symmetry sites gives the diffusion barrier (E_{diff}) (K. T. Chan et al., 2008). Present calculations find the values in between 0.30 eV to 0.55 eV for strongly bound atoms (except for V and Ni), and less than 0.1 eV for the weakly bound atoms. The smallest E_{diff} of V and Ni have been found to be 0.141 eV and 0.214 eV, respectively (Table 1). Chan et al. (K. T. Chan et al., 2008) have quantified

E_{diff} in between the most stable site and the second most stable site in the order of 0.5 eV for Ti and Fe, and the present calculations agree well for Ti. For Fe the difference is smaller in the present calculations (0.332 eV). The authors do not have considered other atoms which are concerned to our calculations. The overall trend of the present calculations agrees with the results obtained by Valencia et al. (Valencia et al., 2010). Summarizing all results, we can understand that the higher the value of E_{diff} the higher the possibility of getting adatom localized. The binding energy values of metal atoms and their stability can also be justified from the distances of metal atoms from the graphene plane.

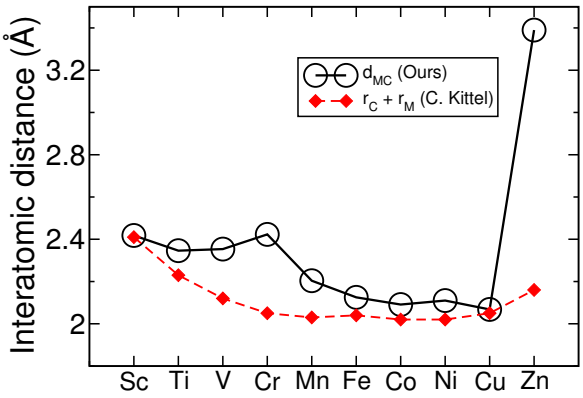

Figure 34: Distance of metal adatoms from the nearest C atom/s using present calculations (black circles) and sum of nearest atom radii (covalent radii of carbon and ionic radii of metal atoms) from the reference (Kittel, 2005).

Figure 34 shows the distance of adsorbed metal atoms (at most stable sites of graphene) from the nearest carbon atom(s). It is generally correlated with the binding energy in such a way that the higher the binding energy the smaller the metal to carbon distance (details will be discussed in next paragraph). We can classify the interactions between the metal atom and the nearest carbon atom(s) in two classes on the basis of distance between them (d_{MC}) (Valencia et al., 2010). The first class of interactions incorporate the chemically bound atoms, where (d_{MC}) falls in the order of (within 10%, except for V) of the sum of covalent radii of the metal and carbon atoms ($r_M + r_C$). In case of V, the difference in d_{MC} and $r_M + r_C$ is around 11 %. The chemicaly bound atoms are thus supposed to be bound with covalent bonding. On the other hand, the physisorbed atoms (except Cu) lie far from the sum of the covalent radii of the corresponding atoms. We assume the distance d_{MC} in these cases are rather near to the sum of van der Waals radii of the corresponding atoms. The exceptional case of Cu can be justified with two reasons. They are (i) the binding energy of Cu lies in the upper boundary region of physisorption, and (ii) Cu has low co-ordination number, that is Cu at the top site has only

one nearest neighbor to interact. In this case, Cu does not have to share its binding strength to many C-atoms. Hence it can be understood that changing the adsorption site changes the co-ordination number and affects the binding strength.

In present calculations, the strongly bound atoms are favorably adsorbed at the hollow site (co-ordination number 6). Among the weakly bound atoms, Mn and Cu prefer the top site (co-ordination number 1), Cr prefers the bridge site (co-ordination number 2) and Zn prefers the hollow site (co-ordination number 6). At the H site, strongly bound atoms follow the properties of covalent bonding with nearby six carbons. Zinc is very weekly bound at large distance, and does not have significance of binding site due to very small difference between all the tested sites. It is clear that Zn is held via weak van der Waals interactions, in absence of which it would not be bound. Cr is equally shared in between two carbon atoms of the most stable Cr/G structure (Cr at the B site). Consistent with its low binding energy and its geometry (slanting distance with carbons), Cr is remarkably far from the covalent distance $r_M + r_C$. Cu and Mn, however, are connected directly to only one carbon atom, have no slating path and the interaction is not shared with the other atoms. Further, Cu lies at the upper boundary region of physisorption energy (as mentioned above) and its d_{MC} remain near to ($r_M + r_C$). Even though the binding energy of Mn is quite low, it lies relatively near to C of graphene comparing to that for Cr due to one to one Cr-C interactions. It has been tested (not shown here) that for the same adsorption site (say H-site), the distance rule (the larger distance weaker the interaction) works very well. It has been found that present calculations agree well (within 3 %) with the previous results (Valencia et al., 2010), which are shown in (Table 1).

Magnetic properties and charge transfer

Unpaired (electrons) spins of an isolated atom posses non-zero value of total spin, and cause finite magnetic moment (Kittel, 2005). The transition metal atoms have inner electronic shells partially occupied and this occupancy determine their magnetism, on the basis of electronic configurations. In 3d series of transition elements (from Sc-Zn), the magnetic moment changes due to exchange of electronic occupancy mainly in 3d orbitals with 4s and others (Table 3). Figure 35(a) shows magnetic properties of isolated atoms and most stable most stable configurations of metal-adatom graphene. From Sc to V, their 4s shells are filled, and electron occupancy in d-shell increases continuously from 1 to 3. Hence the magnetic moment changes from 1 μ_B to 3 μ_B. Mn has half filled 3d-orbitals with 5 unpaired

electrons. From Fe to Zn, 3d orbitals start getting doubly filled, as every orbital already has one electron. It means magnetic moment decreases continuously from 5 μ_B towards zero while going through Mn to Zn. In case of Cr, however, both the 4s and 3d shells are half filled and posses six unpaired electrons. Similar case happens in Cu, where 4s shell is half filled with one unpaired electron on the cost of occupied 3d shell. This phenomenon is reflected in Figure 37.

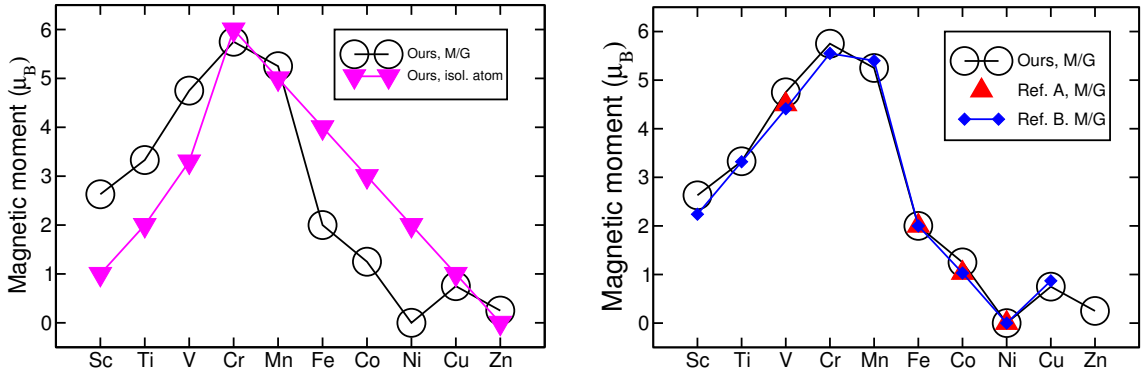

(a) Our-calculation (b) Comparison with Ref.

Figure 35: Figures display magnetic moments of isolated metal atoms and metal-adatom-graphene (M/G). The down-triangles and circles in Figure (a) represent present calculations for isolated atoms and M/G respectively. In Figure (b), the line with open circles displays present calculations for magnetic moments of M/G whereas up-triangles and the line with diamonds represent these values from the Liu et al. (Liu et al., 2011) (Ref. A) and Valencia et al., (Valencia et al., 2010) (Ref. B) respectively.

Figure [35] shows that the total magnetic moment of M/G ($\mu_{\mathrm{M/G}}$) decreases in the order of 2 μ_B for Fe, Co and Ni with respect to that of isolated metal atoms ($\mu_{\mathrm{Iso.}}$). In the periodic table these atoms are just right of Cr/Mn of 3d series, where the d-orbitals are already half filled. On the other hand, ($\mu_{\mathrm{M/G}}$) increases in the order of (1-2) μ_B for Sc, Ti and V. The atoms are at the left of the Cr/Mn in the periodic table, and their d-orbitals are yet to be singly filled. The chemically inactive and loosely bound metal atoms Cr, Mn, Cu and Zn do not show significant change in magnetic moment up on their adsorption in pure graphene sheet. Table 1 and Figure 35 (b) show that the present calculations for total magnetic moment agree well with the previous studies (Liu et al., 2011; Valencia et al., 2010; Yagi et al., 2004). Graphene itself is non-magnetic. Yagi et al. (Yagi et al., 2004) and the references therein state that π-bonded carbon p_z orbitals hybridize strongly with the metal d-orbitals, and the promotion of 4s electron to 3d orbital during hybridization causes the change in electron occupancies in the metal atoms adsorbed in graphene comparing to that of free atom. Present calculations show that not only the promotion of 4s electron to 3d orbitals but also the promotion of fractional

electronic charge to 4p orbitals and rearrangement in spin polarization within the orbitals cause change in electronic occupancy (Table 2). This causes change in spin polarization and magnetic properties of metal atoms on graphene. Since the metal atoms before and after Cr/Mn in the periodic table have different occupancies in 3d shell, they have different attitude towards the donation and back donation of the electronic charge from/to the carbon atom(s) of graphene. This variety in redistribution of electronic charge at the carbon p_z orbitals and the orbitals (4s, 3p and 3d) of partially filled metal adatoms during hybridization determine the change of magnetic properties of the adatom-graphene, and accordingly increases or decreases the magnetic moment (Liu et al., 2011).

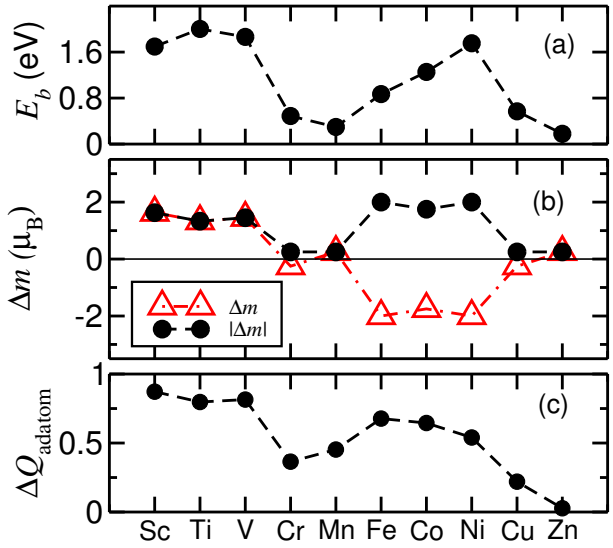

Figure 36: (a) Binding energy (E_b) of metal-adatoms at the most favorable sites of graphene sheet, (b) difference in magnetic moment of M/G (metal-graphene) and isolated metal (Δm) and the quantity in modulous form ($|\Delta m|$) (c) charge transfer from metal adatoms towards the graphene sheet by using Bader method of analysis. The graphs show a good correlation between the binding energy (E_b), difference in magnetic moment and charge transfer.

Figure 36 and Table 2 show the relationship in between binding energy (E_b), change in magnetic moment of metal adsorbed graphene with reference to that of isolated metal atom (Δm) and the charge transfer from metal adatom to graphene (ΔQ) calculated by using Bader's charge analysis method (Bader, 1990; Henkelman et al., 2006) (details will be discussed in the later sections). In general, the quantities E_b, Δm and ΔQ are related. Figure [36] reveals that higher the charge transfer causes the stronger interaction in between metal atom and the nearest carbon atom(s) of graphene layer. During the process of hybridization in between carbon p_z orbitals and available metal orbitals, there is not only transfer of charge from metal atom to carbon(s) but also the rearrangement of (valence) electronic charge within

Table 2: Electronic and magnetic properties of transition metal atoms at the most stable occupation sites of monolayer graphene containing 18 number of carbon atoms.

Adatoms	Adsorption site	E_b (eV)	Δm (μ_B)	ΔQ (e)	Δq_t (e)	Δq_s (e)	Δq_p (e)	Δq_d (e)
Sc	H	1.695	1.63	0.872	-0.58	-0.98	-0.008	0.41
Ti	H	1.781	1.29	0.797	-0.34	-1.49	0.39	0.76
V	H	1.823	1.75	0.815	-0.39	-1.22	0.39	0.44
Cr	B	0.488	-0.25	0.365	-0.03	-0.13	0.25	-0.17
Mn	T	0.298	0.25	0.453	-0.28	-1.0	0.33	0.34
Fe	H	0.870	-2.0	0.677	-0.34	-1.26	0.40	0.54
Co	H	1.254	-1.75	0.645	-0.57	-1.17	0.0	0.60
Ni	H	1.753	-2.0	0.540	-0.22	-0.96	0.48	0.26
Cu	T	0.570	-0.25	0.220	0.11	-0.02	0.30	0.17
Zn	H	0.179	0.25	0.027	0.05	-0.01	0.0	0.0

Note: The properties listed in the table are binding energy (E_b), change in magnetic moment of metal atom in graphene with reference to that of isolated atom (Δm), charge transfer from the metal atoms towards the graphene layer by Bader's charge analysis method (ΔQ). The decrease/increase in total charge at metal atom before and after its adsorption on graphene, and the quantities separately at s , p and d occupancies (Δq_s, Δq_p and Δq_d respectively) are also listed. Increase in charge is denoted by +ve sign and decrease in charge is denoted by -ve sign.

the different orbitals of the metal atom. This changes the occupancy of the electronic orbitals spin orientations.

Table 2 presents the quantitative data for the electronic charge transfer from metal atom towards the graphene surface (ΔQ) by Bader's charge analysis method (Bader, 1990), decreases in electronic charge at metal atom (Δq_t) and the rearrangement of electronic charge within the orbitals of metal adatoms before and after the adsorption on graphene by Löwdin charge analysis method (Sanchez-Portal et al., 1995). The values ΔQ and Δq_t are basically the same parameter (charge transfer) calculated through two methods of analysis. Although they follow a trend, the magnitudes differ a lot. It implies that the numerics of charge transfer calculations may not correctly represent absolute values, rather they compare the trend from one atom to another. Löwdin method of analysis shows that there is a promotion of electronic charge from s-orbital to p and d-orbitals in the order of one electron in case of strongly bound atoms. In spite of low binding energy, promotion of s-electron is remarkably high for Mn, which is the reason for higher charge transfer (Figure 36. The table also presents the change in electronic occupancy at p and d-orbitals which shows the origin of changing magnetism after

the adsorption of metal atom on graphene with respect to the quantity when it was isolated.

Table 3: The total magnetic moment of isolated metal atom $m_{Iso.}$ and that of M/G ($m_{M/G}$) are listed in the table. The table also reveals the contributions of individual orbitals (m_s, m_p and m_d) in both the cases. The values are measured in μ_B.

Adatoms	Adsorption site	Iso. metal ($m_{Iso.}$)				M/G			
		Total mag.	m_s	m_p	m_d	Total mag.	m_s	m_p	m_d
Sc	H	1.0	0.0623	0.0	0.94	2.63	0.78	0.0	0.91
Ti	H	2.0	0.002	0.0	1.998	3.29	0.42	0.18	2.14
V	H	3.3	0.036	0.0	3.27	4.75	0.33	0.18	3.38
Cr	B	6.0	1.0	0.0	5.0	5.75	0.82	0.11	4.69
Mn	T	5.0	0.0	0.0	5.0	5.25	0.76	0.16	4.53
Fe	H	4.01	0.53	0.0	3.48	2.0	0.0	0.11	2.11
Co	H	3.0	0.67	0.0	2.32	1.25	0.0	0.0	1.09
Ni	H	2.0	0.83	0.0	1.17	0.0	0.0	0.0	0.0
Cu	T	-1.0	-0.99	0.0	0.01	0.75	0.72	0.12	0.01
Zn	H	0.0	0.0	0.0	0.0	0.25	0.0	0.0	0.0

Table 3 compares the magnetic moments of isolated metal atoms and metal adatom-graphene including their sources. As shown in Figure 36 and discussed in previous paragraphs, magnetic moment of isolated metal atom is different with the quantity when it is adsorbed in graphene. In case of isolated metal atoms, total magnetism is due to the sum of s and d orbital's contributions. The magnetic moment arises due to the polarized charge of electronic occupancy in the corresponding orbitals. In case of metal adatom-graphene, there is transfer of charge from metal atom to graphene. Also change in occupancy of electronic charge in different orbitals occurs due to hybridization between the p_z orbital of C and metal atom orbitals. The table reveals that p orbitals of metal atoms are also affected during the interactions and contribute on total magnetism. The sum of m_s, m_p and m_d gives the major contribution of magnetism at M/G. However, the sum of contributions does not meet the value of total magnetism. The difference is supposed to be supplimented from the C atoms (nearby the metal atom) of graphene, which are not shown in table. Although total magnetic moment is predicted by the electronic occupancy in different orbitals, d-band filling can also determine the major factor contributing on magnetism and nature of interactions.

Figure 37 shows the d-band filling of the metal atom when it is isolated, and adsorbed on graphene. The figure reveals the fact that spin up are filled in increasing order from Sc to Mn by the magnitude of unity (except for Cr) while moving from left to right in the periodic table.

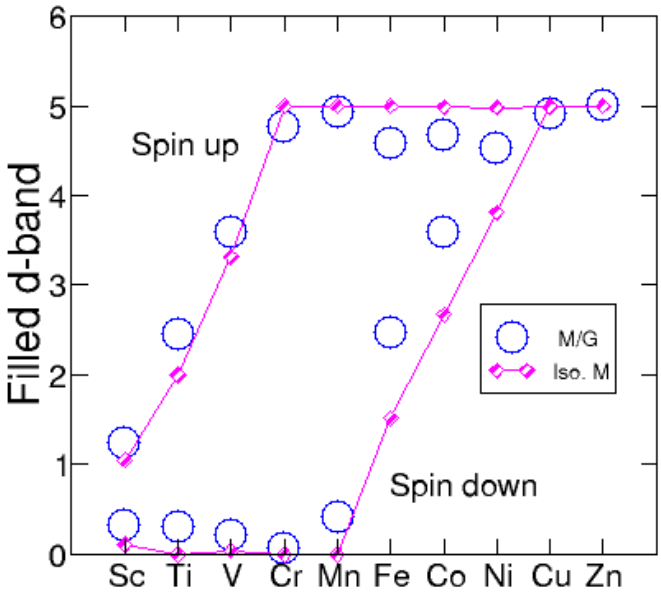

Figure 37: d-band filling for isolated metal atoms (diamonds) and metal atom adsorbed graphene sheet (circles).

In case of Cr, spin up are totally filled on the cost of reducing one electron from 4s-orbital. It makes both the sub-shells (3d and 4s) half filled which is more preferable rather than when it were having four electrons at d and 2 electrons at s orbitals. Spin down are empty up to Mn. After Mn, spin up orbitals are always totally filled and filling of spin down orbitals increase by unity according to the Hund's rule. The metal atoms after their adsorption on graphene show some changes on d-band filling. For Fe, Co and Ni, d-band filling of up-spin decreases on the cost of increasing down-spin orbitals. For Ti and V, however, both the occupancies at d-band increases. There is almost no change of d-band filling in case of weakly bound atoms (Cr, Mn, Cu and Zn).

Figure 38 shows the side-view and top-view of charge density difference plots in between metal adatom-graphene and its constituent systems (metal atom and graphene), by using Bader method of analysis. The charge density differences are plotted for the fixed isosurface, and the size of the lobes reflect the amount of charge transfer from metal atom towards the graphene. The green lobes are charge depleted regions and the red lobes are charge accumulated regions. The plots clearly show the rearrangement and polarization of charge densities. Although the nature of charge density redistribution changes from atom to atom, we see large green lobes at the outer part of the metal atom and red lobes near to graphene surface, in case of some of

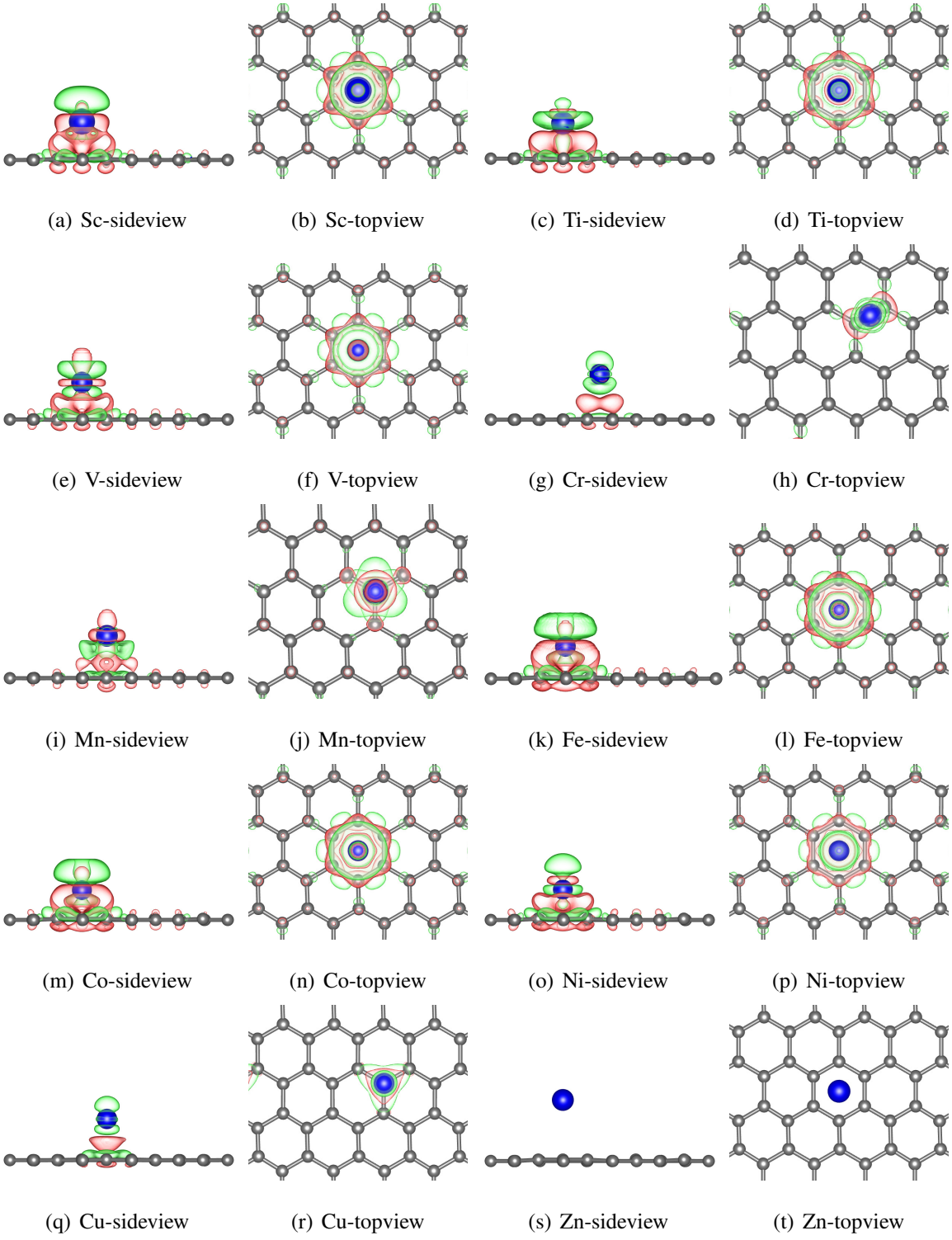

(a) Sc-sideview (b) Sc-topview (c) Ti-sideview (d) Ti-topview

(e) V-sideview (f) V-topview (g) Cr-sideview (h) Cr-topview

(i) Mn-sideview (j) Mn-topview (k) Fe-sideview (l) Fe-topview

(m) Co-sideview (n) Co-topview (o) Ni-sideview (p) Ni-topview

(q) Cu-sideview (r) Cu-topview (s) Zn-sideview (t) Zn-topview

Figure 38: Side-view and top-view of charge density difference with isosurface 0.0025 electrons/Bohr^3 between the M/G andcits constituent systems (graphene and isolated atoms). The green and red lobes represent the charge depleted and accumulated regions after the adsorption of metal atoms. Since the charge density differences are plotted for the fixed value of isosurface, larger the lobes represent higher the rearrangement of electronic charge.

the strongly bound atoms (Sc, Fe, and Co) . The green lobes in Ni is somehow smaller than these three metal atoms, however, the nature of charge lobes are similar. The fundamental information displayed from the plots can be inferred that there is the formation of vertical dipole around the metal atom due to transfer and rearrangement of electronic charge. As we mentioned that the charge density differences are plotted for the fixed isosurface, the larger lobes in Sc, Fe and Co meant for the largest amount of charge transfer from metal atom towards the graphene. Ti and V (Figure 38 (c, d, e, f)), however display multiple charge lobes around them. It implies the complicated and multipolar distribution of electronic charge density. Also the nature of d-band filling in Figure 37 shows different property of Ti and V. Their spin up filling increases without decreasing spin down filling. Spin polarized charge density calculations may give the further information regarding these peculiar properties. Weakly bound Cr (Figure 38 (g, h)) and Mn (Figure 38 (i, j)) show significant rearrangement in charge density in spite of natural expectation of small changes in electronic structure because of their weak binding. This property is consistent with the magnitude of charge transfer, where they have significant transfer of charge in spite of low binding energy. This could be due to small energy difference in between nearby orbitals. Copper (Figure 38 (r, s)) shows green lobes at its both the sides (up and down) with large red lobe nearby graphne, and Zn (Figure 38 (s, t)) shows no effect at this level of isosurface.

Density of States (DOS)

Density of states is defined as the number of available electronic states per unit energy range. In computational physics/chemistry, it is a way to represent electronic eigenstates in energy space of a molecule, where it counts the number of energy states nearby a given energy value (say E). If Ψ_i and E_i represent the normalized eigenfunctions and eigenvalues respectively, the total density of states (TDOS) can be defined as (Kittel, 2005),

$$D(E) = \sum_i \delta(E - E_i) \tag{4.2}$$

where $D(E)$ represents the density-of-states, and its integral $\int D(E)dE$ in between the energies E_1 and E_2 gives the number of states within the specified energy range (Grosso & Parravicini, 2005). The density of states projected over any arbitrary state (say $|f_0\rangle$, under the condition that it is normalized to unity) is defined as projected density of states (PDOS). It can be expressed as

$$n_0(E) = \sum_i |\langle f_0|\Psi_i\rangle|^2 \delta(E - E_i) \tag{4.3}$$

with $\int n_0(E)\,\mathrm{dE} = 1$, due to the normalization condition of chosen orbital $|f_0\rangle$. When plotted, PDOS gives the relative contributions to total DOS (TDOS) and hence helps to analyze the relative contributions of each atom or molecule in the larger systems. In the present work, we discuss density of states of M/G and metal atom contributions in such total DOS.

Figure [39] shows metal atom contributions on total density of states (DOS) of metal-adatom-graphene. The contributions are calculated by using the method of projected density of states (PDOS). In absence of impurity atom(s), DOS of graphene shows symmetrical cones at the Fermi level for up and down-spin contributions (Pantha, Belbase, & Adhikari, 2015). The cones are called Dirac cones, and the point where the Dirac cones meet is called Dirac point. Since up-spin and down-spin occupations are equal, pure graphene is non-magnetic. In presence of impurities: like transition atoms, however, actual cone-like structure disappears and Fermi level moves up with reference to the initial position due to additional donor level (Pantha, Khaniya, & Adhikari, 2015). The electronic occupation also changes due to hybridization of C-atom-orbitals with the metal orbitals, and the density of states may also break its symmetry (K. T. Chan et al., 2008). The difference in up- and down-spin fillings can be observed at PDOS plots and the same information reveals, at least qualitatively, the origin of magnetism of the new species. In Figure (39, black lines show total DOS (TDOS) of adatom-graphene and red dashed lines show PDOS of metal atom contributions. The increase in magnetic moment of M/G while going through Sc to Cr is reflected through the increasing asymmetry in their PDOS. There are increasing peaks of metal atoms for up-spins whereas no peaks for down spins, except a small filling in Ti and V (Figure [39 (b, c)]). This small filling in down-spin for Ti and V is also shown in Figure 37. Down spin peaks start from Fe (Figure 39 (f)) and asymmetry decreases from Fe to Ni. For Ni Figure 39 (h), PDOS is totally symmetric showing the equal contributions from up and down spin electrons. This approves the decreasing magnetic moment of M/G going from Fe to Ni. PDOS of Zn (Figure 37(j)) is also symmetric showing no magnetic moment, and half of the peak within the Fermi level of Cu (smaller peak at Fermi level) contributes magnetism for Cu (Figure 37(i)). In summary, present work is consistent with the spin-asymmetry theory for the origin of magnetism, where it is understood that higher the net difference in electronic occupancy in between up and down spins, higher the magnetic moment.

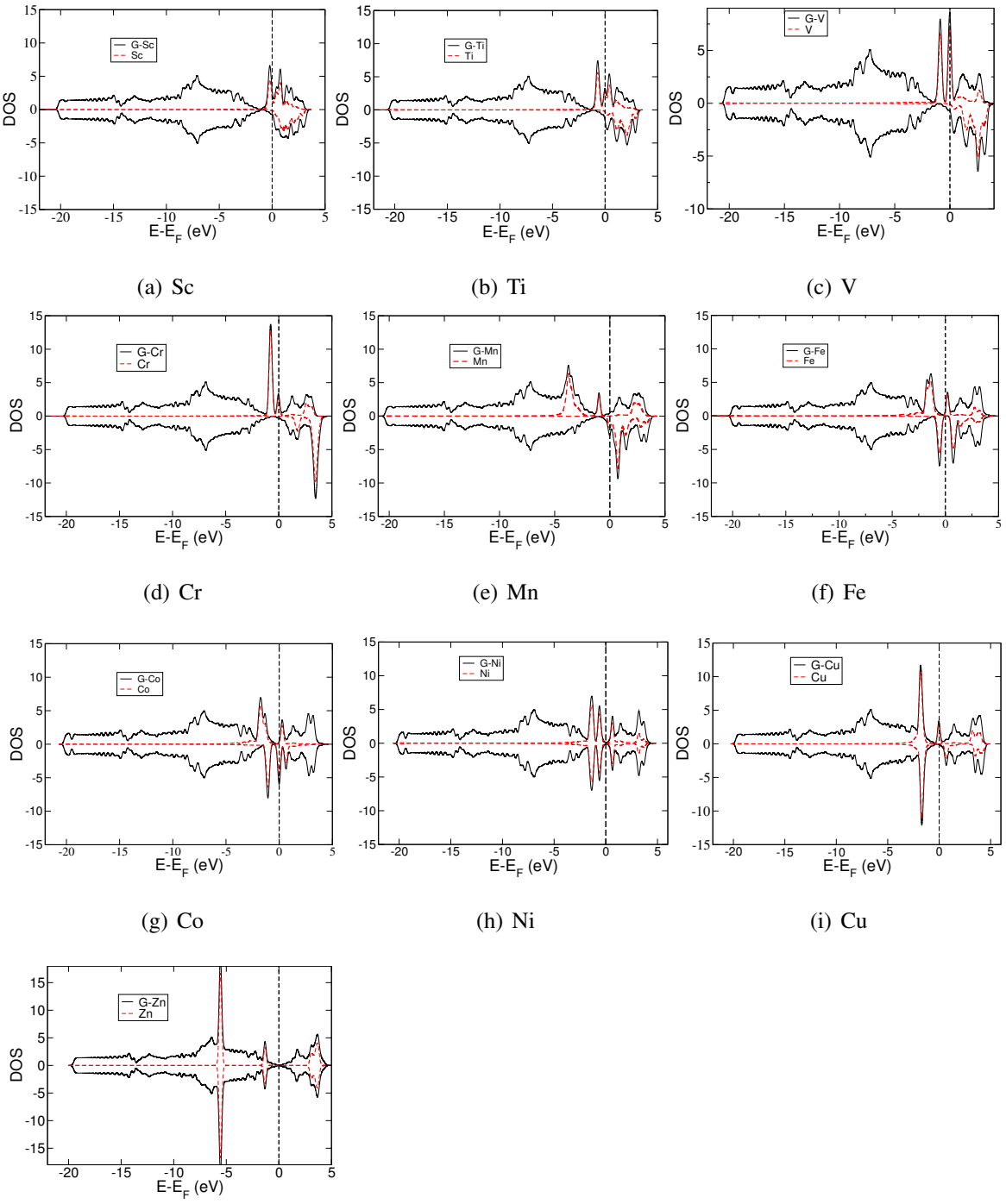

(a) Sc (b) Ti (c) V

(d) Cr (e) Mn (f) Fe

(g) Co (h) Ni (i) Cu

(j) Zn

Figure 39: Total density of states (TDOS) of M/G (black lines) and the corresponding metal atom contributions (dashed red lines) from PDOS calculations. Metal atoms Sc-Zn, are plotted in order.

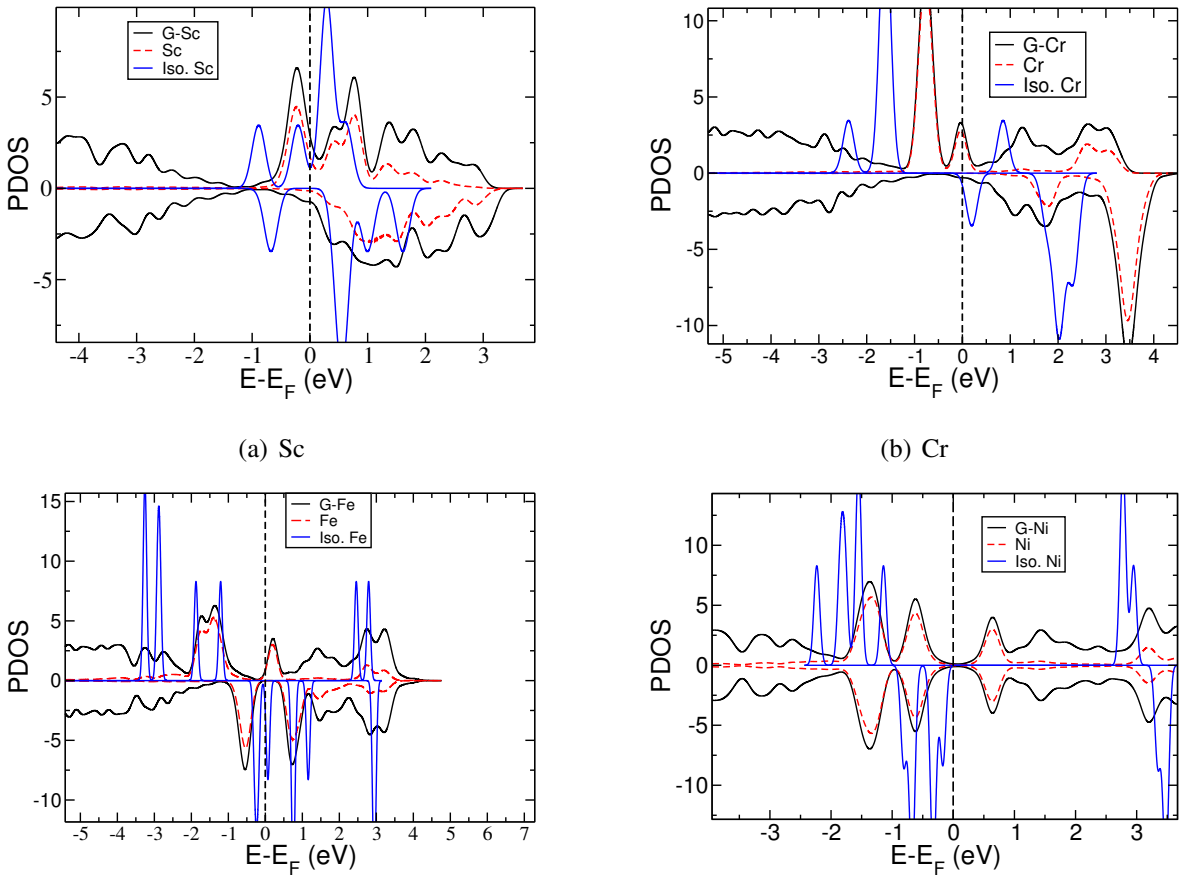

(a) Sc

(b) Cr

(c) Fe

(d) Ni

Figure 40: Total density of states (black lines), metal atom contributions (dashed red lines) of M/G, and projected density of states (PDOS) of corresponding isolated metal atoms (blue lines) for Sc, Cr, Fe and Ni from PDOS calculations. The atoms are taken as samples to represent atoms in 3d series.

As we discussed before, the magnetic moment of adatom-graphene changes with respect to the corresponding isolated metal atoms. This is because of change in electronic occupancy of electronic orbitals during the hybridization in between atomic orbitals. To get more insights of metal orbital contributions and their modification in M/G, we compare PDOS of isolated metal atoms and when they are adsorbed in graphene (Figure 40). The magnetic moment of isolated metal atoms from Sc to Mn increases by unity due to unpaired 3d electrons. In PDOS plots, we see them as up-spin peaks which obviously increases from left to right in the atomic row. Down-spin peak(s) in this case is due to one of the 4s electrons (Sc, Figure 40(a)), if semi-core (3p) electrons are not considered as valence electrons in pseudopotential. In case of metal atoms in graphene, down-spin of 4s electron in strongly bound atoms (Sc, Ti and V) transfers towards graphene and metal d-orbitals which are yet to be singly filled. The consequence of this rearrangement of charge shows no down-spin peaks in metal adatom-graphene. In case

of Cr and Mn, net quantity of polarization does not altered and thus no magnetic moment is changed. For isolated Fe onwards, 3d orbitals are at least singly filled. Hence the peaks for up-spin, in addition to down-spin peak of 4s electron are clearly visible (Fe and Ni, Figure 40(c, d)). The number of down-spin peaks increases while moving towards the higher atomic numbers and the asymmetry in up and down-spin peaks decreases resulting decrease in magnetic moment on moving towards right in the atomic row. Upon their adsorption on graphene, on the other hands, the sharpness and the number of peaks decreases due to transfer of up-spin electrons towards the down-spin orbitals and graphene layer. This decreases the net difference in electronic charge at up- and down-spin orbitals and causes decrease in magnetic moment.

The properties of metal adatom adsorbed graphene are crucial for using them as substrate to adsorb the energy carrying gases like methane. We study the adsorption properties of methane on these modified graphene structures in the following section.

4.3.2 Adsorption of methane

In spite of being a widely available energy resource, methane has limitations for its practical applications due to shortage of safe and effective storage. Adsorption of methane in solid materials like porous carbons (Menon & Komarneni, 1998) and carbon nanomaterials (Lozano-Castello et al., 2002; Adisa et al., 2011; Kaiser et al., 2013) are some of the potential sectors. We study its adsorption on pristine garphene and M/G to see if the adsorption of metal atom advances the purpose of optimal storage properties of methane (Bhatia & Myers, 2006) in solid structures.

Adsorption of methane on monolayer graphene

The adsorption properties of energy carrying gases including methane in garphene and other two dimensional materials have been widely studied areas (Yang et al., 2006; Ricca & Bauschlicher, 2006; Albesa et al., 2008; Thierfelder et al., 2011; Zhao & Meng, 2013; Man-Chao & Jian, 2013; Rao et al., 2015). Methane is tetrahedral and non-polar molecule. Also its adsorption on graphene is direction dependent. To understand the effect of methane-orientation in its binding properties, we consider three most symmetric configurations of methane [namely straddle (S), tripod-towards (TT) and tripod-away (TA)] on graphene and functionalized-graphene as described in “Computational method (Section 3.11.2)” and shown in Figure 41. We also consider only highly symmetric points of graphene, named as hollow

(H), bridge (B) and top (T) as mentioned in Section 3.11.2 and Figure 17. The adsorption energy of methane is calculated by using equation 4.1 with the proper replacement of substrate and adsorbents.

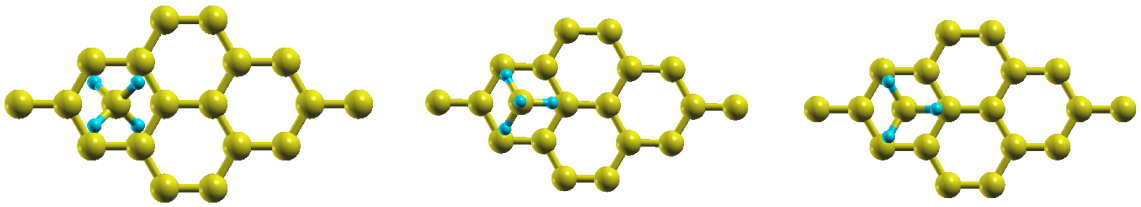

(a) Straddle (b) Tripod-towards (c) Tripod-away

Figure 41: Top-view of three different configurations (S, TT and TA) of methane at the hollow site of pristine graphene.

Table 4: The adsorption energy (E_{ad}) and dispersion contributions ($E_{dis.}$) on adsorption energy of methane molecule of three different configurations (S, TT and TA) at possible adsorption sites (H, B and T) of pristine graphene. The highest values are boxed to get them noticed.

Adsorption Site	E_{ad} (eV)			$E_{dis.}$ (eV)		
	S	TT	TA	S	TT	TA
H	0.134	0.139	0.124	0.171	0.164	0.182
B	0.132	0.134	0.112	0.171	0.154	0.143
T	0.133	0.134	0.109	0.171	0.154	0.140

Table 4 shows the adsorption energy of methane on pristine graphene. The energy lies in the order of hundreds of meV within the variation of a few dozens of meV with respect to the adsorption sites and methane configurations. Among the tested occupation sites, H site is seen favorable over the other sites by few meVs. Methane with TT configuration on the graphene plane is more stable, and it is followed by S and TA configurations, respectively. The highest adsorption energy is tabulated as 0.139 eV (~ 0.14 eV) for TT configuration at hollow site which is larger by 0.005 eV (5 meV) comparing to corresponding B and T sites. The value of this most stable structure agrees with the previous studies performed via simulation by using LDA, 0.12 eV (Wood et al., 2012), with van der waals interactions, 0.15 eV (Thierfelder et al., 2011), and experiment on graphite, 0.14 eV (Vidali et al., 1991).

Non-polar gaseous molecules are generally bound by weak van der Waals interactions in pure two dimensional materials (Wood et al., 2012). As a non-polar and tetrahedrally symmetric inert gas, methane is chemically inert towards graphene and other carbon nanostructures.

Table 4 reveals the London dispersion contributions, one of the major contributors of the van der Waals forces for the adsorption of methane in pure graphene. The values of dispersion contributions in binding are observed higher than the corresponding adsorption energies themselves. For an example, dispersion contributions for TT configurations of methane have been found 0.164 eV, 0.154 eV and 0.154 eV at H, B and T sites respectively comparing to corresponding adsorption energy values 0.139 eV, 0.134 eV and 0.134 eV. It infers that the methane molecule would not be bound in graphene if the van der Waals interactions were absent in the calculations. As similar to the adsorption energy values, dispersion energies are site and configuration dependent.

The adsorption energy values of molecular methane in graphene, as shown in Table 4, are too small for the purpose of energy (methane) storage in solids (Bhatia & Myers, 2006). Previous studies have noted that functionalized carbon nanomaterials enhance the adsorption energy of gaseous molecules (Ulman et al., 2014; Wood et al., 2012). This situation has motivated us to study metal elements as foreign atoms for such a purpose.

Adsorption of methane on metal adatom-graphene (M/G)

Metal atom changes the properties of graphene up on its adsorption. We have discussed changes in geometrical, electronic and magnetic properties of functionalized graphene (by metal atoms) in the previous sections. From the discussion we saw that the metal atom increases polarity of the substrate (M/G) and makes the adsorption of gaseous particles easier. In the following sections, we show three configurations of methane molecules on Fe adatom graphene (side view) to show their geometries and relative stability (Figure 42).

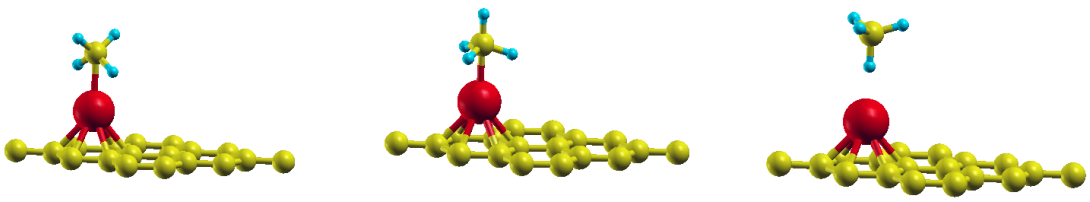

(a) E_{ad} = 0.656 eV (b) E_{ad} = 0.655 eV (c) E_{ad} = 0.276 eV

Figure 42: Side-view geometries of methane configurations (S, TT and TA) at the hollow site of Fe adatom adsorbed graphene (Fe/G).

Figure 42 shows side view geometries of methane adsorbed Fe-functinalized graphene. The

adsorption energy values reveal that adsorption energy of methane is enhanced from its maximum value 0.139 eV in pristine graphene to 0.656 eV when graphene is functionalized with Fe. We will show the details in Table 5, however, in case of Fe, adsorption energy of S and TT configurations of methane are almost equal to each other with magnitudes 0.656 eV and 0.655 eV, respectively, whereas that of TA configuration (0.276 eV) is smaller by less than half.

The individual transition metal elements of 3d series, Sc to Zn, are first adsorbed on most stable site of graphene to construct the properly functionalized graphene structures (M/G). Note that the stable site of graphene for metal atom differs from one atom to another (discussed in previous sections). Three different configurations of methane (S, TT and TA) are then allowed to be adsorbed in most stable structures (M/G). The adsorption energy values of methane are listed in Table 5 and the highest values are boxed to get them noticed.

Table 5: The adsorption site of metal atom (M) on graphene, the binding energy of metal atoms at their most favorable structures (E_b) and the adsorption energy of methane molecule in S, TT and TA configurations (E_{ad} (S), E_{ad} (TT) and E_{ad} (TA)) on most stable M/G are listed. The higher adsorption energy of methane among the configurations are boxed to highlight them. The energies are measured in electron volts (eV).

Adatom (M)	Adsorption site (M)	E_b	E_{ad} (S)	E_{ad} (TT)	E_{ad} (TA)
Sc	H	1.695	0.227	0.369	0.033
Ti	H	2.002	0.287	0.469	0.019
V	H	1.864	0.531	0.428	0.183
Cr	B	0.488	0.013	0.015	0.024
Mn	T	0.298	0.021	0.024	0.029
Fe	H	0.870	0.656	0.655	0.276
Co	H	1.254	0.872	0.642	0.360
Ni	H	1.753	0.911	0.630	0.442
Cu	T	0.570	0.069	0.070	0.063
Zn	H	0.179	0.043	0.048	0.045

Our calculations show that TA configuration of methane is less preferable (except for Cr and Mn) than S and TT configurations (Table 5). So methane always prefers to be adsorbed in either S or/and TT configurations. For Cr and Mn, the adsorption energy of S, TT and TA are comparable and are lower than the adsorption energy of methane in pristine graphene. It makes clear that TA configurations are either least stable or not relevant for the purpose of reversible storage of methane. In the following sections, therefore, we only consider

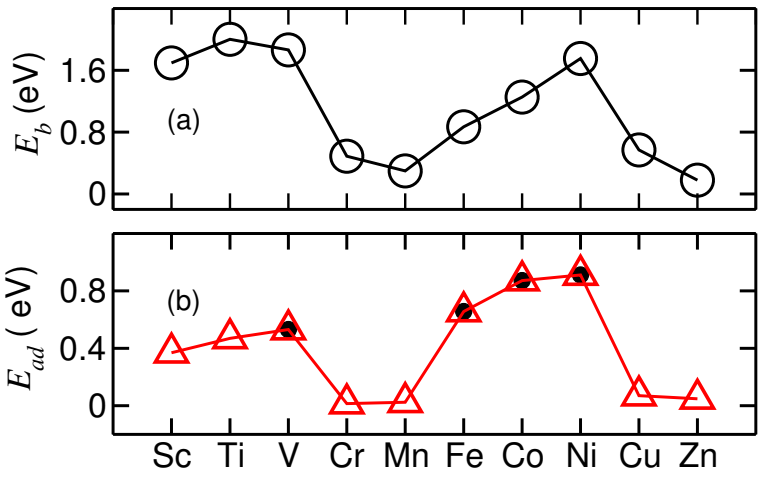

Figure 43: (a) Binding energy of metal adatom on graphene, (b) Adsorption energy of methane on M/G (black circles inside the triangles note that the straddle configuration is favorable). The values are taken for the most stable geometries of M/G and methane@M/G.

adsorption of S or/and TT configurations. The geometries of most stable configurations with their charge densities are shown in Figure 55.

Figure [43] shows the correlation in between the binding energy of metal atom on pure graphene and the adsorption energy of methane on the most stable geometries of metal on graphene (M/G). The figure refers that the larger the binding energy of the metal atom the larger the adsorption energy of methane on the corresponding metal-substrate (M/G). We have already discussed the conditions for the stronger binding of metal atom on graphene, which is directly related to the (electronic) charge transfer and change in magnetism during the adsorption of metal atom. The charge density difference plots for M/G (Figure 38) have also displayed that there is larger rearrangement of electronic charge around the strongly bound metal atoms and the same condition favors to induce dipole, quadrapole and multiple polarities. These functinalized graphene geometries are more polarized and reactive towards the non-polar gaseous particles like methane. This enhances the binding strength of M/G substrate towards the methane molecule(s).

Table 5 shows the magnitudes of binding energy of metal atoms at their most favorable graphene site, in addition to the adsorption energy values of methane at S, TT and TA configurations. The binding energy of Sc, Ti, V, Co and Ni are greater than 1.2 eV, and that for Fe is greater than 0.8 eV. For rest of the adatoms (Cr, Mn, Cu and Zn), the values are less than 0.6 eV. We have treated the former six adatoms (including Fe) as chemically bound whereas later four atoms as physically bound mostly via van der Waals interactions. The adsorption energy of methane has also been seen directly related to the nature of the metal atom by which

the graphene is functionalized. The methane molecule in both the configurations (S and TT) is more strongly bound (E_{ad} > 0.2 eV) on M/G when M is chemically bound. On the other hand, methane is very weakly bound (E_{ad} < 0.1 eV) on M/G, when M is physisorbed. This magnitude of E_{ad} of methane in weakly bound M/G systems is less than that in pure graphene (Table 4). It seems that physisorbed metal atoms are neither reactive towards graphene surface nor towards the methane molecule. They rather isolate the methane molecules with graphene surface, which would provide large surface/contact area nearby methane in absence of metal atoms. From these facts, it can be understood that the physisorbed metal atoms play negative role for the purpose of adsorption of methane in energy storing devices. The optimal adsorption energy implies the useful adsorption energy of methane for on-board applications. The value depends on the operating condition at which the stored energy is to be extracted for practical applications. Bhatia et al. (Bhatia & Myers, 2006) have noted that the adsorption energy of methane is around 0.18 eV (18 kJ/mol) as right strength for on-board vehicular applications. In this sense E_{ad} of methane on M/G, with M chemically bound, overcomes its optimal value.

When a methane molecule is adsorbed above the surface of functinalized graphene, the initial structure of methane gets deformed. In the present work, we include change in bond length, and bond-angles of methane, upon its adsorption with reference to their initial tetrahedral parameters. The correlations of structural deformations and other properties of methane and substrate are also discussed.

Figure 44 shows the schematic picture of S and TT configurations over the metal atom. Upon adsorption of methane, its tetrahedral geometry and the electronic structure of the system changes. The bond-angles (like value of $\angle$ M-H-C) are metal atom dependent, and reversely the change in geometric parameters can be taken as indicators of the metal atom properties. Because of the different orientations of methane in two different configurations, change in their geometric parameters (like C-H bond pointing towards metal atom, M-H-C angles etc) are also configuration dependent. In tetrahedral methane, H-C-H angle is equal to 109.472°. From the structure, it is clear that angle α_1 (at S configuration) is half of the H-C-H angle = 109.472/2 = 54.736° and whereas α_2 (at TT configurations) is equal to 180 − 109.472 = 70.528°.

Figure 45 represents the variation of angle M-H-C as a function of M-C distance. The symbols in the figure are defined as, $f_S(x) = 90 - \alpha_1 + \theta$ and $f_{TT}(x) = 90 - \alpha_2 + \theta$, with $\alpha_1 = 54.736°$,

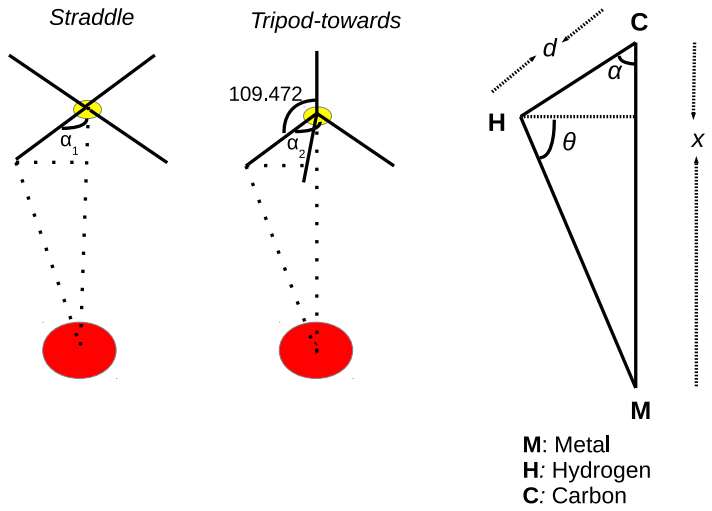

Figure 44: Schematic diagram of (undistorted) tetrahedral methane in straddle (S) and tripod-towards (TT) configurations over the metal atoms. The angles α_1 and α_2 represent the angle between hydrogen, carbon and the metal atoms (H-C-M) in S and TT configurations, respectively. The distance x represents the distance of C (of CH_4) from the metal atom, and d represents C-H bond length. Angle M-H-C, could be an indicator of deformation of methane while being adsorbed and can be expressed as a function of known parameters like d, α and x.

$\alpha_2 = 70.528°$ and $\theta = \tan^{-1}(\frac{x - d\cos\alpha}{d\sin\alpha})$. Further, x is the distance of C (of CH_4) from the metal atom, and d is C-H bond length. The dashed lines show the trends how do they look like for undistorted methane of S and TT configurations. The circles and squares are the values obtained from our calculations. The figure shows that the systems with metal atoms Cr, Mn, Cu and Zn, follow the trend lines as they do not affect the geometry of the methane molecule(s). In case of strongly bound adatoms, however, methane molecule gets distorted while being adsorbed. The level of distortion is reflected on the magnitudes of deviation from the trend lines. Geometrical distance of methane (M-C distance) and M-H-C bond angles are smaller for higher adsorption energy.

Figure 46 shows the variation of adsorption energy of methane as a function of carbon to hydrogen (C-H) bond pointing towards the metal atoms. The C-H bond length does not alter the positions of hydrogens pointing away from the metal atoms (not shown in figure). When a methane molecule is strongly attracted by M/G, the hydrogens lying nearby the metal atoms are greatly affected. They try to move downwards with respect to the position of carbon (of

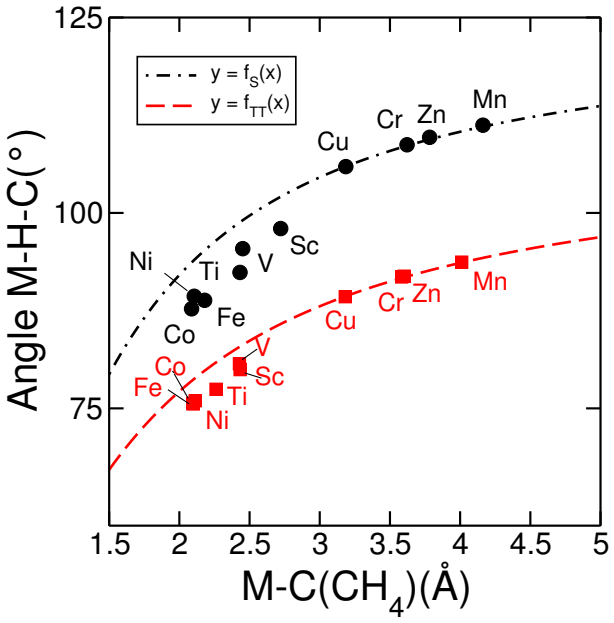

Figure 45: Angle M-H-C (metal-hydrogen-carbon) changes as a function of metal to carbon (M-C) distance. The dashed lines show the trends how do they look like for undistorted methane of S and TT configurations. The circles and squares are the values obtained from our calculations. Note that systems with metal atoms Cr, Mn, Cu and Zn, follow the trend lines whereas systems with other adatoms (in such cases the methane gets distorted while being adsorbed) deviate from the trend-lines. (Symbols, $f_S(x) = 90 - \alpha_1 + \theta$ and $f_{TT}(x) = 90 - \alpha_2 + \theta$, as defined by Figure 44.)

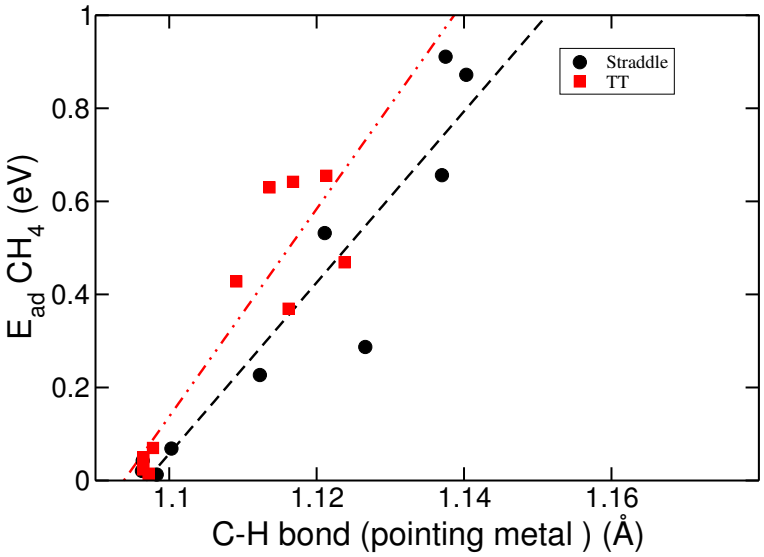

Figure 46: Adsorption energy of methane as a function of C-H (carbon-hydrogen of methane pointing towards the metal atom) bond length. The circles and squares represent the values for Straddle and Tripod-towards configurations respectively. The dashed lines are the linear fit for corresponding values in both the configurations.

methane) and other hydrogens. Figure 46 reiterates this concept, where C-H bond is higher for the higher adsorption energy of the methane. The dotted lines represent the linear fits for the corresponding values. In the figure, the average C-H bond is higher for S-configuration

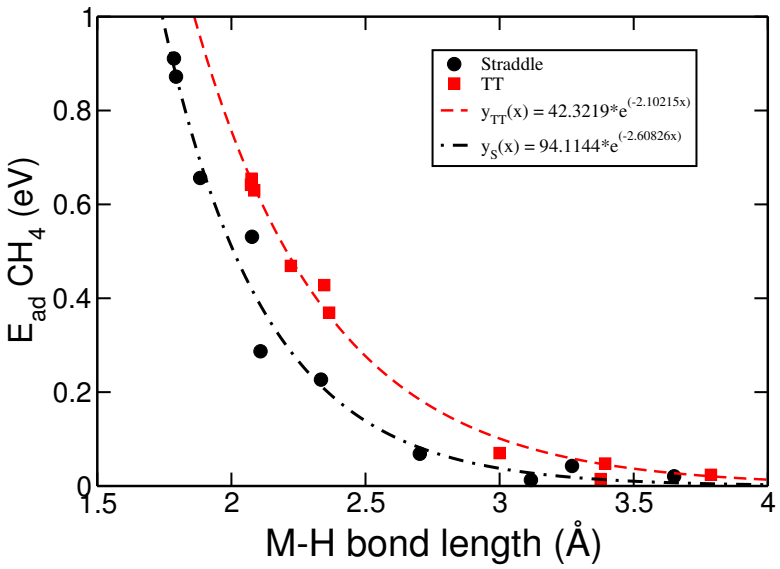

Figure 47: Adsorption energy of methane (on M/G) as a function of M-H (Metal to Hydrogen of methane pointing towards the metal atom) bond length. The circles and squares represent the adsorption energy values for S and TT configurations of methane. The dashed lines are the linear fit for corresponding values in both the configurations.

than that for TT-configuration for the same level of adsorption energy. Since S- and TT-configurations are having two and three C-H bonds towards the metal atom respectively, it is logical to assume higher strength of attraction per C-H bond and longer bond length in case of S-configurations.

Figure 47 shows the variation of adsorption energy of methane as a function of average distance of H with reference to the metal atom. The parameter is assumed to reflect the relative position of methane and its hydrogens. Consistent with the natural expectation, the figure shows that the adsorption energy of methane decreases on increasing its distance. The dashed lines represent the exponential fits of such values and indicate that adsorption energy decreases exponentially with the distance. The regular and broken dashed lines show two different trend lines which implies that average distance of H from the metal atom (for the same adsorption energy) is higher for TT configurations. It might be related to their (TT configurations) smaller average C-H distance. Since H lies in between C and metal atoms, smaller C-H may compensate higher M-H distance, even if metal to carbon distance is constant in both the cases.

Figure 48 shows the variation of adsorption energy of methane as a function of distance between metal atom and carbon (of methane, M-C) for both (S and TT) configurations. This property properly locates the distance of methane molecule from the metal atoms. The

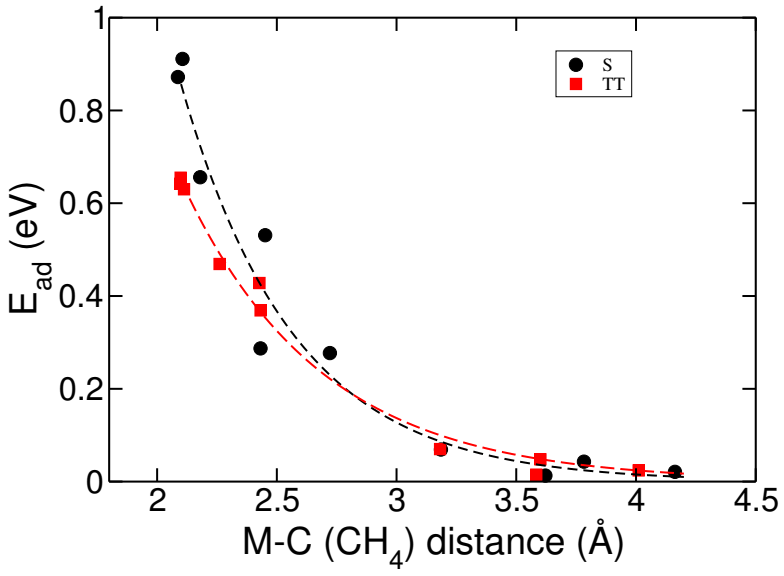

Figure 48: Adsorption energy of methane (on M/G) as a function of M-C (Metal to Carbon of methane) distance. The circles and squares represent the adsorption energy values for S and TT configurations of methane. The dashed lines are the linear fit for corresponding values in both the configurations.

adsorption energy of methane seems to vary exponentially with the distance of methane as similar to M-H distance. However, dissimilar to the relation of E_{ad} with M-H distance, there is no distinction in the trend lines of S and TT configurations for M-C distance. It means that the general relation can be referred for the most stable geometries of methane, independent to their S or TT configurations.

Figure 49 shows the relationship of the adsorption energy of methane with its geometrical distortion in terms of C-H bond length and metal to methane (taking C as reference for methane) distance, for the most favorable configuration of methane. As discussed in the previous sections, the adsorption energy is linearly related to the extension of C-H bond length (Figure 49(a). On the other hand, it decreases exponentially on increasing metal to methane distance (Figure 49(b)).

Figure 50 shows the adsorption energy of methane at relaxed and unrelaxed configurations. The relaxed configurations represent the optimized structures of methane-adsorbed M/G, where the methane molecule gets distorted from its initial tetrahedral symmetry. On the other hand, unrelaxed structure of methane represents the tetrahedral methane fixed at the relaxed position of C (of CH_4) keeping hydrogens intact, without caring their possible variations in rotational configurations. Since these calculations are motivated to observe the effect of deformation of methane molecule in functionalized graphene structures, the adatoms for which the methane does not get significantly deformed are not considered. For the purpose

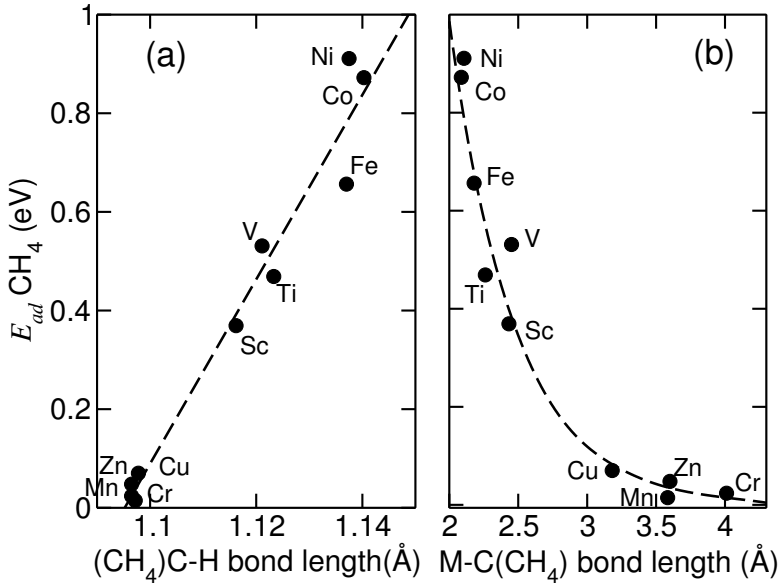

Figure 49: Adsorption energy of methane in favorable configuration as a function of (a) C-H (carbon-hydrogen of methane pointing towards the metal atom) bond length. The circles represent the calculated values and the dashed line represents the linear fit. (b) M-C (metal-carbon of CH_4) distance. The circles represent the calculated values and the dashed line represents the exponential fit for the observed values.

Table 6: The table represents the adsorption energy values of single methane molecule when it is relaxed (distorted from the initial symmetry) and unrelaxed (undistorted) on metal-adatom-graphene. The case of weakly bound metal atoms where the methane molecule does not get deformed in the structures are not considered for this type of calculations.

Metal	Relaxed CH_4 (eV)		Unrelaxed CH_4 (eV)		Difference (eV)	
	S	TT	S	TT	S	TT
Sc	0.227	0.369	0.182	0.329	0.045	0.040
Ti	0.287	0.469	0.168	0.408	0.119	0.061
V	0.531	0.428	0.485	0.408	0.123	0.020
Cr	0.013	0.014				
Mn	0.02	0.024				
Fe	0.656	0.655	0.522	0.598	0.134	0.057
Co	0.872	0.642	0.741	0.598	0.131	0.044
Ni	0.911	0.630	0.815	0.593	0.096	0.037
Cu	0.069	0.070				
Zn	0.043	0.048				

of adsorption energy calculations, we consider relaxed constituents like methane and metal adatom-graphenes. By using the information of adsorption energy of methane in both the conditions, it is seen that the methane at relaxed geometry is consistently more strongly bound comparing to that of unrelaxed one. During the geometrical optimization of the system, C-H bonds of methane pointing towards the metal atom get extended on the cost of weakening these bonds. Since the polarity is induced in relaxed methane, due to breaking of its symmetry, the molecule is more reactive towards the metal atoms. In other words, the unrelaxed methane is not allowed to go its ground state because of fixed position, and total energy is higher comparing to the relaxed ones. This gives less adsorption energy of methane when it is not relaxed. Table 6 shows the quantities by which the adsorption energy of relaxed methane changes with respect to that if it were unrelaxed. The difference is in the order of 0.1 eV (except for Sc) for S configuration, and that is remarkably low (in between 0.020 eV to 0.061 eV) for TT configuration of methane. This seems to be related to the higher geometrical deformation of S configurations than TT configurations of methane in their respective relaxed structures. For an example, the average C-H bond-length pointing towards the metal atom is lower for TT configuration at the similar level of adsorption energy (Figure 46).

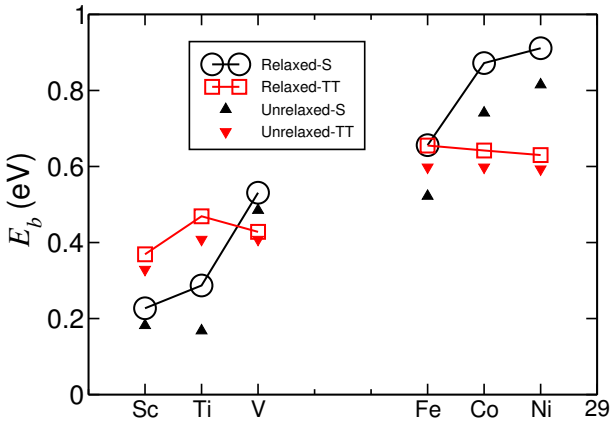

Figure 50: Adsorption energy for relaxed and unrelaxed methane at S and TT configurations. Symbols: circles (relaxed, S configuration), squares (relaxed, TT configuration), up-triangles (unrelaxed, S configuration), down-triangles (unrelaxed, TT configuration).

Charge transfer

Charge transfer in between two interacting particles is an ambiguous quantity and no unique definition is there for its measurement (Liu et al., 2012). Further, the relevancy of the charge transfer depends on the nature of bonding between the particles. For an example, it is more practical for ionic bonding than that for covalent bonding (K. T. Chan et al., 2008). A number of approaches have been used to quantify the charge transfer. Chan et al. (K. T. Chan et al.,

2008) have used two different approaches to calculate the charge transfer. They rely on the information of (i) shifting of Fermi-level at density of states and (ii) charge density difference to calculate the charge transfer from metal adatoms to graphene. The results thus obtained from the method of shifting Fermi level are more than double comparing to the values from the method of charge density difference. On the other hand, Valencia et al. (Valencia et al., 2010) have used Bader charge decomposition method (Bader, 1990) to calculate the charge transfer from the metal adatom to the graphitic surfaces. In the present work, we checked two different techniques (i) Bader's analysis method and (ii) planer average charge density method, to calculate charge transfer from methane towards the metal adatom-graphene. The values obtained from both the methods were similar and we mention only the Bader's method in this document.

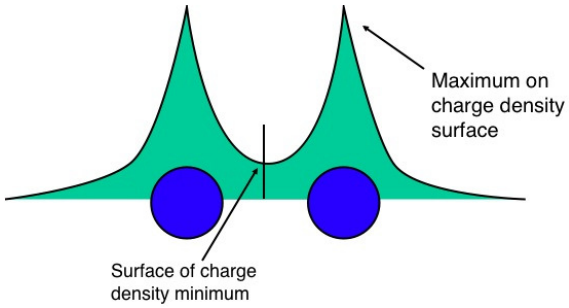

Figure 51: Schematic diagram to define the surface of charge density minimum in Bader method of analysis (Tang et al., 2009).

Bader method isolates the electronic charge density of atoms in molecules. (Henkelman et al., 2006; Bader, 1990) The boundary of atoms are separated by assuming minimum value of charge density surface (Figure 51). A minimum charge density surface, also called as zero flux surface, has no component of gradient of electronic charge density along its perpendicular direction. Once the minimum charge density surface is defined, the regions for substrate and adsorbent could be isolated, and the integration over such volumes finds the total electronic charge within the interacting particles. Finally, the difference of total charge in between isolated atoms/molecules and upon their combination quantify the charge transfer from one system to another.

In Figure 52, we show charge transfer from methane (in both the configurations) to the functionalized graphene by using Bader's method of analysis. For weakly bound atoms, the charge transfer is independent of methane configuration. For strongly bound atoms, however, it is correlated with the adsorption energy of methane. Among S and TT configurations, adsorption of favorable configuration of methane shows the higher charge transfer. In case

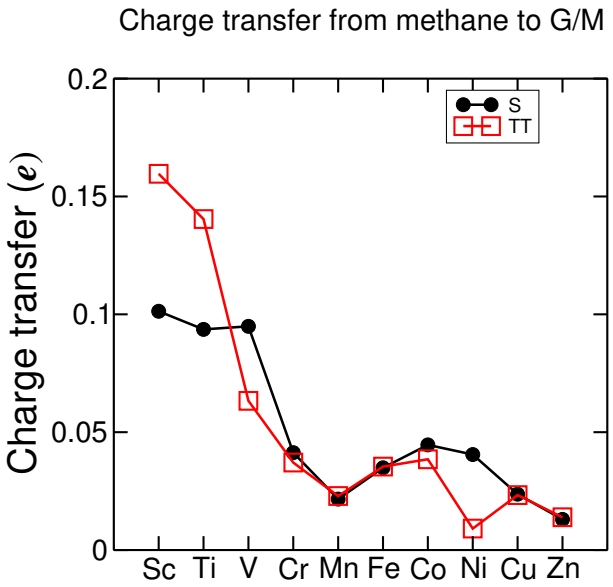

Figure 52: Charge transfer from methane molecule towards the substrate by the Bader's method of analysis. The black line with circles and red line with squares represent S and TT configurations of methane.

of Sc and Ti, charge transfer is higher for TT configuration, and for the remaining strongly bound metal atoms V, Fe, Co and Ni (where the S-configuration of methane is more favorable) it is higher for S configuration. Adsorption energy is nearly equal for both the configurations in Fe, and thus charge transfer is also equal for them.

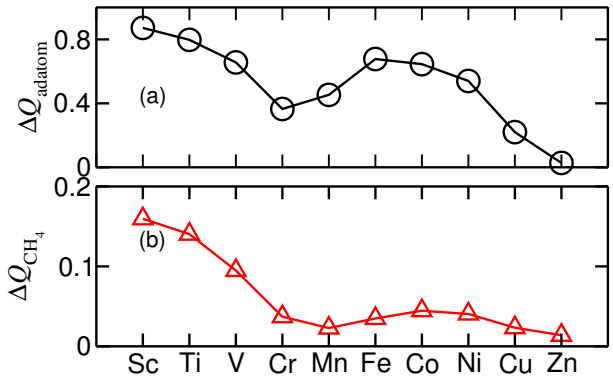

Figure 53: Charge transfer calculated by using Bader's method of analysis, (a) metal to graphene and (b) methane to metal adatom-graphene.

Figure 53 shows the relationship between the charge transfer from metal to graphene at M/G and methane to metal-adatom graphene for the favorable methane structures. It reveals that the higher the charge transfer from metal to graphene the higher the charge transfer from methane to metal adatom-graphene. In addition to the binding strength of the metal atoms on graphene and methane on adatom-graphene, charge transfer seems to be correlated to the electro-positivity of the metal atoms. It is higher for the more electro-positive metal atoms, lying left to Cr/Mn, comparing to the metal atoms with low electro-positivity (towards right

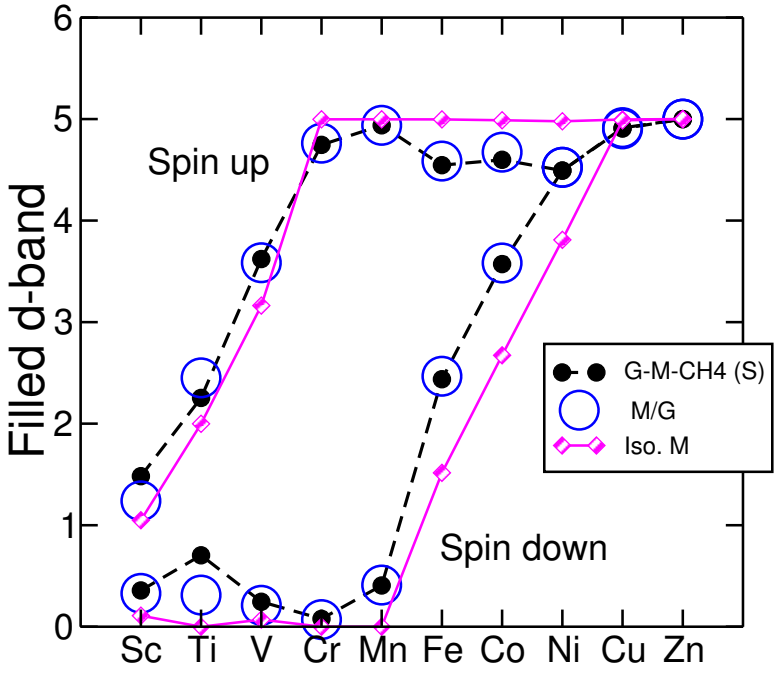

Figure 54: d-band filling for isolated metal atoms (diamonds), metal adatom-graphene sheet (circles) and methane adsorbed metal adatom-graphene (dark spheres).

hand side in the row). This rule of charge transfer is more pronounced for methanes than the metal atoms themselves. The relationship of charge transfer in between metal to graphene and methane to M/G is understandable. When the higher deficiency of electronic charge at M/G is created because of higher transfer of charge from metal to graphene, it can attract more electronic charge from its adsorbent (methane).

Comparative study of d-band filling of the materials containing transition metal atoms as impurities reveals the major causes of change in electronic structure. The nature of partially filled d-orbitals of the atoms affect on binding energy, charge transfer and magnetic moments. Figure 54 shows the comparative study of d-band filling of isolated metal atoms (diamonds), metal atoms at M/G (circles) and metal atoms at methane adsorbed M/G graphene (dark spheres). The changes and correlations of d-band filling in between isolated metal atom and the metal atom at M/G has already been shown in Figure 37. Here we see no change in d-band filling of metal atoms before and after adsorption of methane except for Ti. This observation is true for both the configurations of methane (not shown). In case of Ti, we see increasing d-band filling at spin down orbitals without much changes in spin-up arrangement. This seems to be the cause of changing its magnetism due to adsorption of methane, and may open the possibility of magnetic sensors for methane detection.

Figure 55 displays the side-views of charge density differences between the methane adsorbed

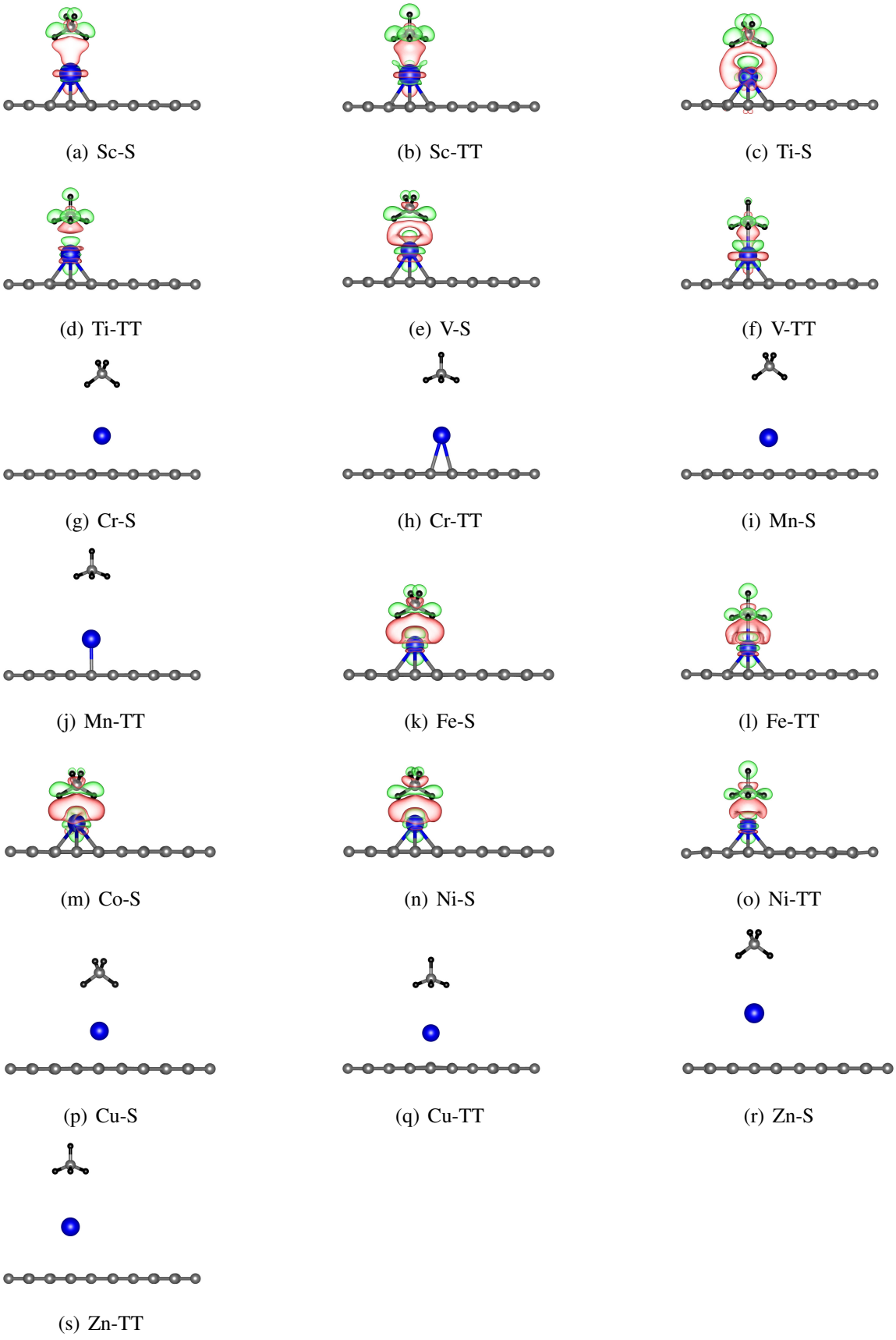

(a) Sc-S (b) Sc-TT (c) Ti-S

(d) Ti-TT (e) V-S (f) V-TT

(g) Cr-S (h) Cr-TT (i) Mn-S

(j) Mn-TT (k) Fe-S (l) Fe-TT

(m) Co-S (n) Ni-S (o) Ni-TT

(p) Cu-S (q) Cu-TT (r) Zn-S

(s) Zn-TT

Figure 55: Side-view of charge density difference between the methane adsorbed M/G and its constituent systems (M/G and methane in both the configurations) for the fixed isosurface 0.0015 electrons/Bohr^3.

adatom-graphene and its constituents. The green lobes represent the depletion of electronic charge density and the red lobes represent their accumulation. Since the charge density differences are plotted for a fixed value of isosurface, the size of the charge lobes are meaningful for the observation of rearrangement of electronic charges. The weakly bound atoms (Cr, Mn, Cu and Zn), for example, do not show any lobes indicating that there is no rearrangement of electronic charge at this level. The general trend of the plots for strongly bound atoms, on the other hand, show that the green lobes are located far from the metal atoms and the red lobes lie nearby them indicating a polarization of electronic charge density, whose magnitude however depend upon the nature of the adatoms. Hydrogens and carbon of the methane are surrounded by the green lobes, and small red lobes respectively. The inconsistent type of red lobes in between methane and metal atoms shows varying nature of redistribution of electronic charge density with respect to metal atoms. In case of Sc, Fe, Co and Ni, the space is almost occupied by the red lobes, and the distribution is more complicated in case of Ti and V. The overall scenario says that the polarization is mainly dipolar with minor contributions from the higher order polarity.

We show PDOS plots of methane (of configuration S) adsorbed functinalized-graphene structures in Figure 56. In the plots, black lines, red dotted lines and green lines respectively represent the total DOS (TDOS), and PDOS plots of metal contributions and methane contributions, respectively, within the same level of calculations. For the weakly bound atoms (Cr, Mn, Cu and Zn) there are clearly separated peaks for methane and metal atoms, and no hybridization occurs between them. Methane contributes two peaks, first peak in between -5.0 eV to -6.0 eV and second peak in between -12.5 eV to -13.5 eV, below the Fermi level. The peaks are similar for all these four atoms. The peaks of metal atom, on the other hand, vary according to their electronic occupancy, and can be easily defined by the general rule of electronic configuration as similar to metal adatom-graphene (MAG). In case of strongly bound atoms (Sc-V, Fe-Ni), however, first peak of methane splits into two peaks. The splitted peaks lie in between -7.0 eV to 8.75 eV. The sharpness of the peaks vary with the metal atoms. It can thus be expected that splitting of methane peak might be due to the electric field created by dipoles/multipoles of metal atom graphene rather than hybridization of methane with the substrate. The second (lower energy) peak seems intact with respect to its isolated methane case in between -14.5 eV to -16.5 eV.

Figure 57 shows the PDOS for TT configuration of methane adsorbed on adatom-graphene. From the figures, dissimilar to S-configuration, it is understood that methane peaks remain

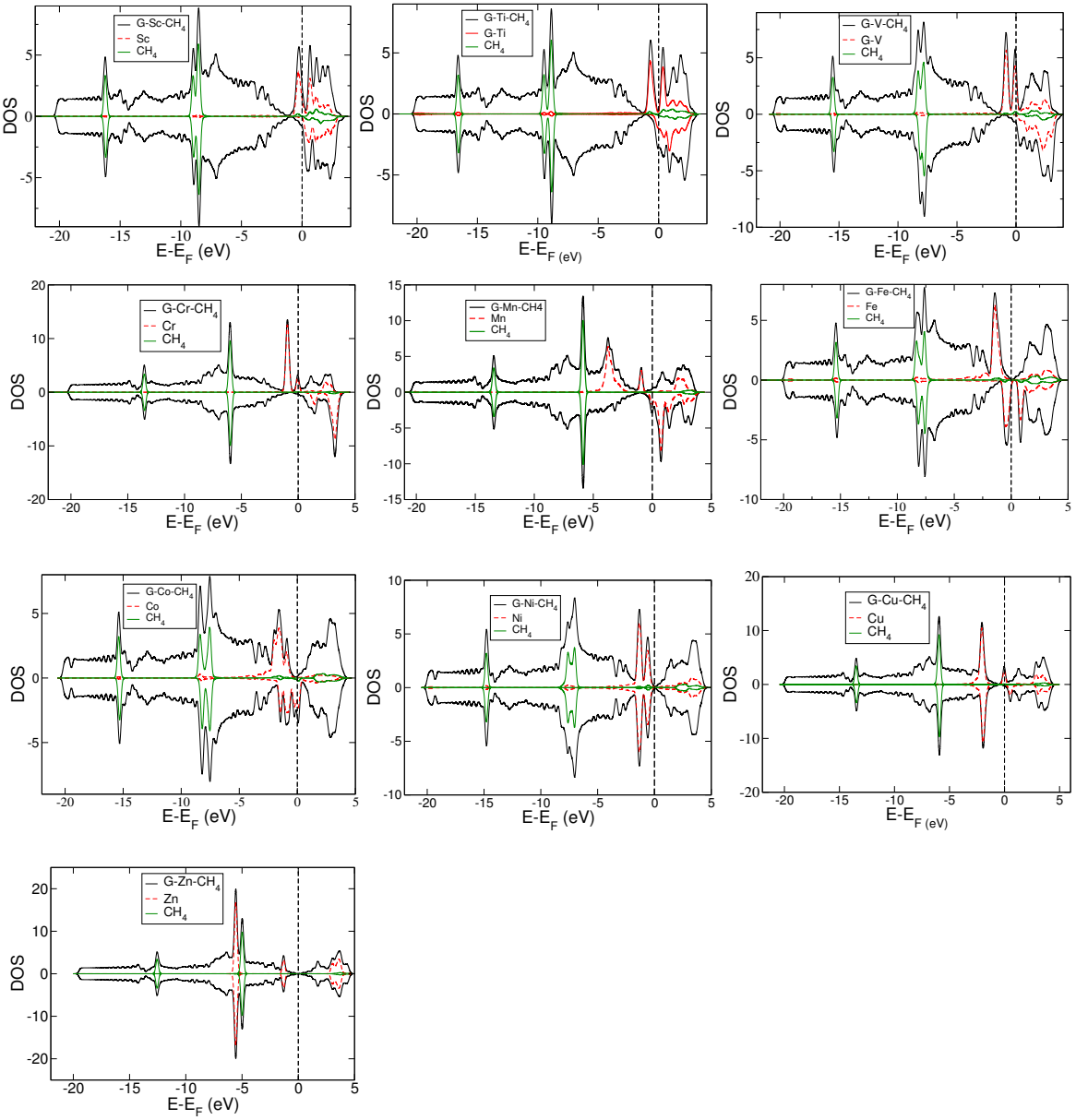

Figure 56: Density of states of methane adsorbed M/G (black lines). Red dotted lines and the green lines represent the metal atom and CH_4 (in S configuration) contributions in total PDOS calculations.

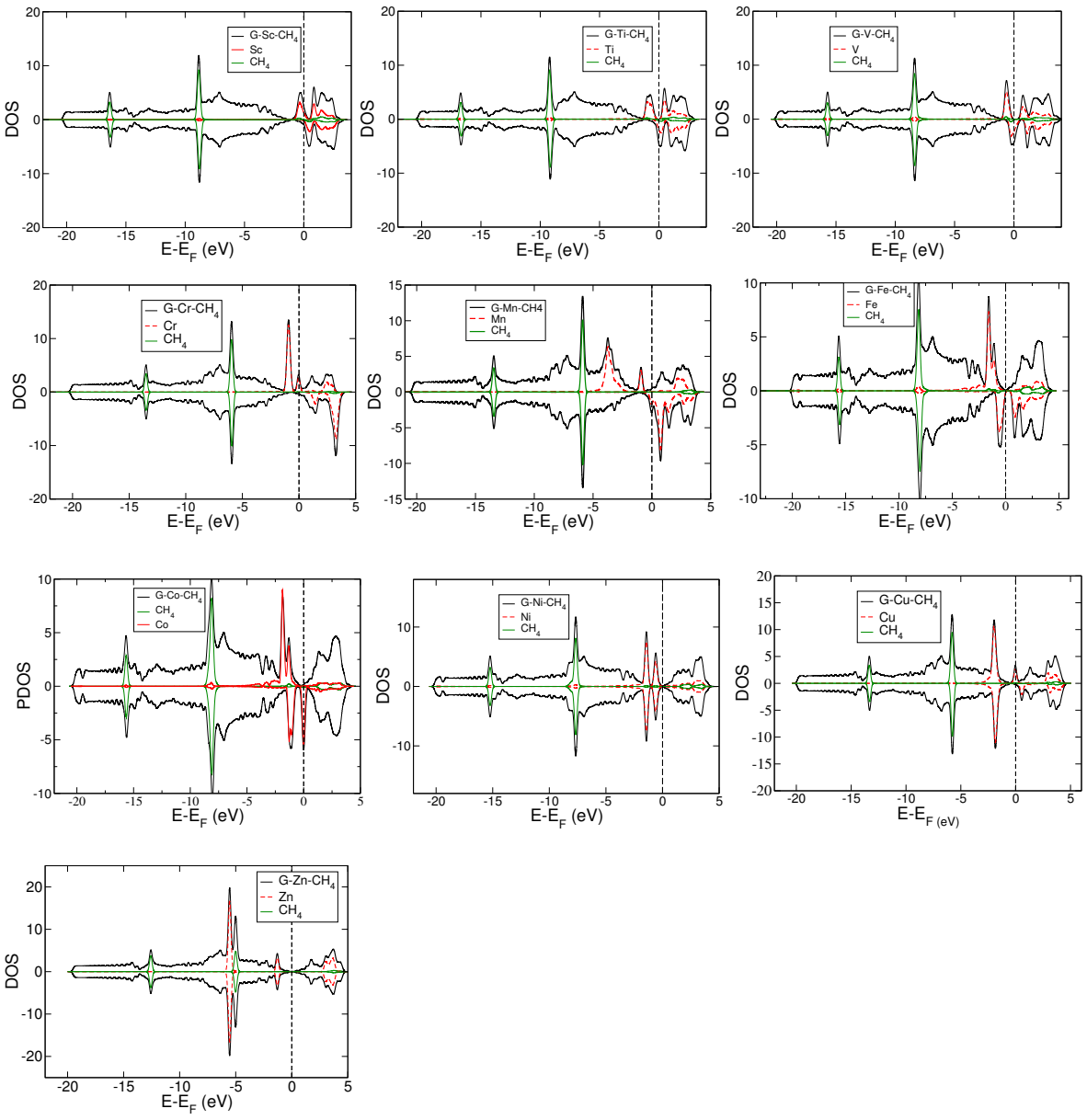

Figure 57: Density of states of methane adsorbed M/G (black lines). Red dotted lines and the green lines represent the metal atom and CH_4 (in TT configuration) contributions from the same PDOS calculations.

intact for both the type of atoms (weakly and strongly bound atoms). In case of weakly bound atoms, methane-peaks are consistent in nature and positions with respect to the corresponding peaks of S configuration. For the strongly bound adatoms, however, one peak splits into two in case of S-configuration of methane which is not the case in TT configuration.

Atoms in molecules (Bader's method of analysis)

The information of bonding between atoms in molecules can reveal energy, geometry, reactivity and other fundamental physical/chemical properties of the system of interest (Bader, 1990). The Bader's method of *atoms in molecules* (AIM) is one of the powerful approaches, which assumes topology of electron density as a basis to study the nature of bonding, including other meaningful chemical properties of the system (Lein, 2009; Popelier & Logothetis, 1998). Because of its superiority like; independence to the model of algorithm, type of basis function and molecular orbitals, the method has been widely used to study charge transfer and nature of bonding (Scherer & McGrady, 2004; Lein, 2009).

The bonding in a diatomic system can be easily predicted with the analysis of minimum energy distance (finite) between them. In other words the bonding can be ensured if it is possible to locate an inter-atomic distance at which the energy is minimum. In polyatomic systems, however, it is complicated to find whether any two atoms are bonded or not. AIM method relies on charge density gradient path, which is obtained with the summation of infinitesimal gradient vectors. The extrema in the gradient path (where $\nabla\rho(\mathbf{r}) = 0$), also known as saddle point, is called critical point (CP). Two atoms get bonded if a gradient curve which passes through the critical point, joins the atoms. The path is called bond path (BP) and the critical point is called bond-critical point (BCP). One can try to find a saddle point at the charge density gradient path to study the nature of bonding between the atoms. Popelier and Logothetis (Popelier & Logothetis, 1998) have used this method to study the inter-atomic interactions in between carbon-hydrogen groups and transition metal centers.

The magnitude of charge density at the bond critical points (BCPs) is an important parameter to study the nature and strength of bonding (Koch & Popelier, 1995; Popelier & Logothetis, 1998). In the present work, we try to find the saddle points in between the atoms of interest, and we draw charge density surfaces so that they just meet at the saddle points. The charge densities of iso-surfaces, in this case, are the charge densities ($\rho_{(\mathbf{r})}$) at BCP. Since very weak adsorption of methane in metal adatom-graphene is out of relevancy for the purpose of methane storage, we consider charge density analysis for the adsorption of methane in

strongly bound atoms (Sc-V and Fe-Ni).

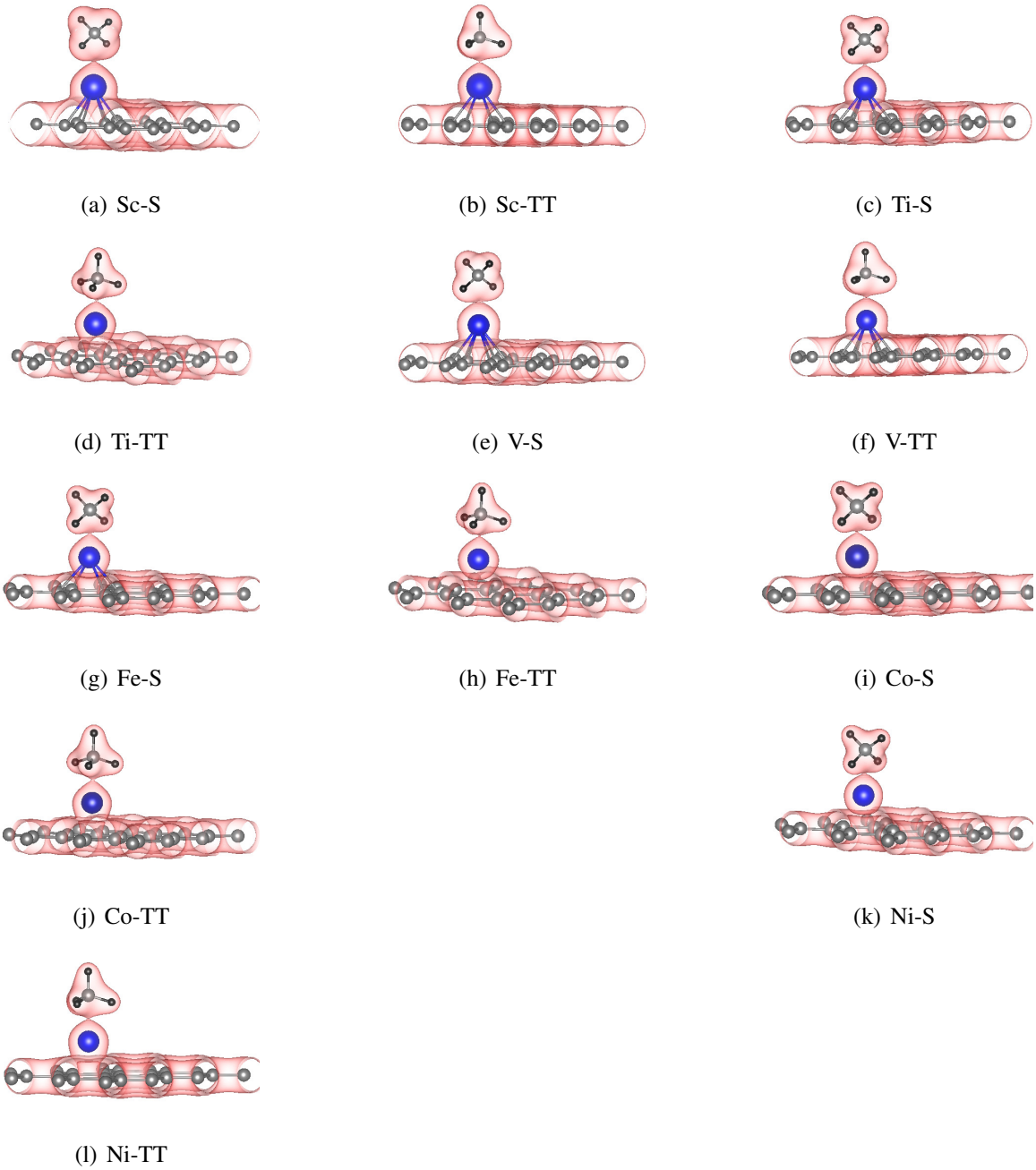

(a) Sc-S (b) Sc-TT (c) Ti-S

(d) Ti-TT (e) V-S (f) V-TT

(g) Fe-S (h) Fe-TT (i) Co-S

(j) Co-TT (k) Ni-S

(l) Ni-TT

Figure 58: Charge density isosurfaces of methane molecule and the metal atom of M/G. Figures show S and TT configurations of methane on different adatom systems. The value of electron density isosurface at which the charge density surfaces of two regions just touch to each other define the charge density at bond critical point (BCP).

We show charge density isosurfaces of methane-adsorbed M/G such that they meet at the saddle points (Figure 58). The magnitudes of charge densities of these isosurfaces are their values at BCP. Charge density at BCP is a useful information to analyze the nature of interactions in between the metal atom and atoms in methane molecule. The observation of the charge density plots in the figures shows that BCPs lie in between metal atoms and carbon

of methane. This implies that there is some bonding (most probably covalent) in between C of methane and metal atoms, instead of '*agostic interactions*' which is usually present in between carbon-hydrogen group and metal centers with non-zero d-electrons (Brookhart et al., 1988, 2007). Agostic interactions is described by a three-center two-electron bond in between carbon, hydrogen and metal center, which has been widely available in organometallic compounds (Scherer & McGrady, 2004). However, some effects of metal atoms on hydrogens (facing towards the metal atoms) is obvious, since carbon to hydrogens (C-H) bond-lengths have been increased due to presence of the metal atoms. This effect is higher when a metal atom has unsaturated d-orbitals (say unsaturated metal atom). The interactions in between the unsaturated metal atoms and molecular hydrogens has been discussed in previous studies, (Kubas et al., 1984; A. K. Singh et al., 2010; N. Singh et al., 2013) and explained that this is due to the exchange (donation and back-donation) of electronic charge in between the interacting atoms. We have observed the higher reduction of electronic charge at hydrogens (of methane) facing towards metal atoms comparing to the hydrogens facing away. This implies some exchange of electronic charge with the metal atoms, in addition to that with carbon of methane. This phenomenon, however, is different from Kubas interactions as discussed in the references (Kubas et al., 1984) which requires η^2 coordination of H_2 with the metallic center (coordination of molecular-hydrogen with the metal center). In the present case, dominant interaction is observed in between metal center and carbon of methane.

The charge densities at the BCPs are plotted in Figure 59. The circles and squares (with trend lines) represent their values for S and TT configurations of methane. The general trend of the plots says: the larger the charge densities at BCPs, the stronger the binding of methane. There seems to be a linear relationship in between charge density and binding strengths. However, the slopes for S and TT configurations are different with a tendency of steeper line and greater fluctuations in S configuration. Because of less number of hydrogens in between metal center and the methane molecule in straddle structure, its binding strength is more sensitive with the variation of charge density.

As mentioned in Table 5, among the chemically bound six metal adatoms, E_{ad} for methane on Sc, Ti and V ranges in the order of 0.35 eV to 0.5 eV whereas that value for Fe, Co and Ni is greater than 0.6 eV. This energy (E_{ad}) is more than double for the requirement of the optimal binding of methane for on-board applications (Bhatia & Myers, 2006; Chouhan et al., 2015). Very strong binding is also counter effective due to the requirement of higher desorption energy. Also the content of methane is important in the context of gravimetric

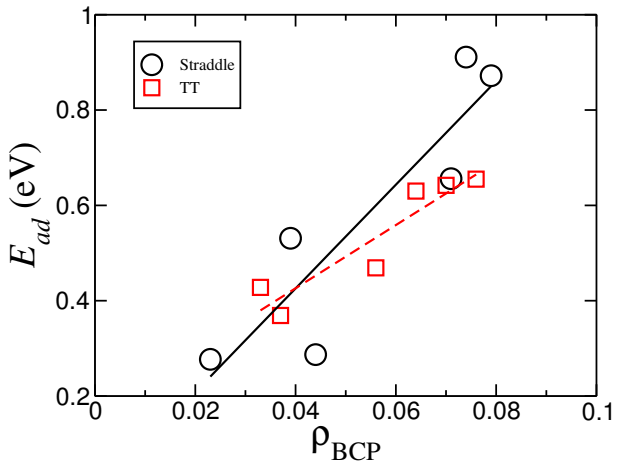

Figure 59: Variation of adsorption energy of methane with charge density at bond critical point (BCP). The circles and squares represent the values for S (straddle) and TT (tripod-towards) configurations of methane. The dashed and solid lines are the linear trend lines.

requirement of methane for economically viable storage. In the present work, we purpose to increase in concentration of adsorbed methane expecting to reduce over-binding of methane and increase the methane storage capacity of the substrate.

4.3.3 Adsorption of methane-dimer on metal adatom-graphene

Among the wide range of adsorption energy of methane (in between 0.05 eV to 0.91 eV), weakly bound methane systems (below 0.1 eV) are out of relevancy for the purpose of present study. We therefore exclude the discussion for the adsorption of methane in loosely held metal systems where E_{ad} (for methane) is less than 0.1 eV. In case of strongly bound methane systems, we increase the number of methanes from one to two, and increase the surface area of the substrate from 3×3 to 4×4 supercells with single metal adatoms. We have considered five different combinations of two methane molecules on chemisorbed metal adatoms (Sc-V and Fe-Ni) at 4×4 supercell of graphene. The initial configurations of these systems are shown in Figure 19.

The converged geometries of two methane molecules (say methane-dimer) on functinalized graphene with charge density distribution are shown in Figure 65. By using the information of total energies of the optimized geometries of methane-dimer adsorbed 4×4 M/G ($E_{2CH_4@M/G}$), corresponding M/G ($E_{M/G}$), and single methane molecule (E_{CH_4}), we calculate the adsorption energy and adsorption energy per methane with the help of equation,

$$E_{ad}(2CH_4) = 2 \times E_{CH_4} + E_{M/G} - E_{(2CH_4@M/G)}. \tag{4.4}$$

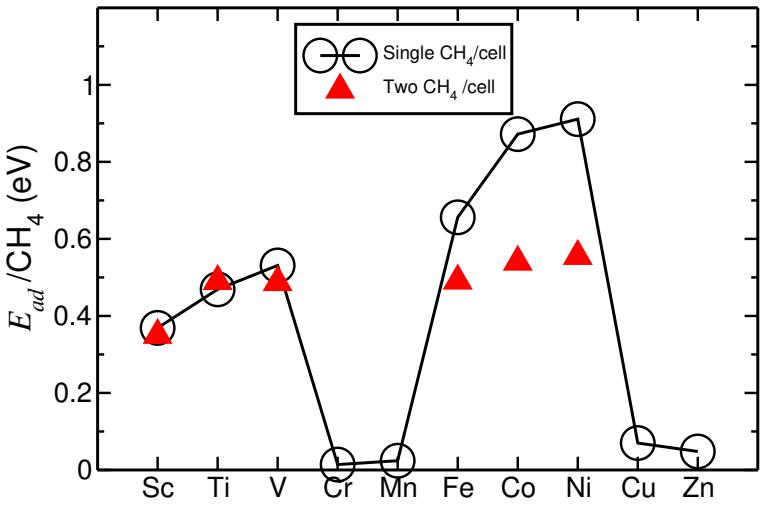

Figure 60: Adsorption energy per methane when single methane (solid line hollow circles) and two methane molecules (up-triangles) are adsorbed in M/G. There is no significant change in adsorption energy per methane on increasing methane concentration in case of initial three atoms (Sc-V) of 3d series, however, it decreases remarkably in the later adatoms (Fe-Ni).

The half of the adsorption energy of methane-dimer ($E_{ad}(2CH_4)/2$) is referred as average adsorption energy of methane-dimer (E_{ad}(ave)). The adsorption energy of single methane and average adsorption energy of methane-dimer are shown in Figure 60 and Table 7. From the values, it can be inferred that there is no significant change in adsorption energy per methane on increasing methane concentration in case of initial three atoms (Sc-V) of 3d series, however, it decreases remarkably (almost by half) in the later adatoms (Fe-Ni). We can correlate this property with the number of vacant d-orbitals, where it is larger for Sc, Ti and V due to the fact that the orbitals are yet to be singly filled. The larger number of vacant d-orbitals might have the capacity of holding larger number of methanes without much reducing in binding strength. On the other hand, for Fe, Co and Ni, half of the orbitals are already occupied and few number of 3d orbitals are vacant. The number of vacant orbitals decreases on moving from Fe towards Ni. Also the average adsorption energy per methane E_{ad}(ave) decreases with higher proportion with respect to E_{ad} for single methane on moving from Fe towards Ni. It might be due to the lack of enough number of vacant orbitals once the metal atoms hold methane molecule. Valencia et al. (Valencia et al., 2015) in their recent study have reported that adsorption of (saturated) number of hydrogens decreases on the right of 3d series by following 18 electron rule. The core concept is consistent with the present justification. Further increase in concentration of methane may check whether the saturation rule is similar for methane.

From the physical observation of optimized geometries of methane-dimer adsorbed M/G,

Table 7: The table represents adsorption energy values of single methane molecule E_{ad}(single), average adsorption energy of methane-dimer E_{ad} (ave) and adsorption energy of individual methanes of methane dimer [E_{ad} (CH_4(1)) and E_{ad} (CH_4(2))] respectively. We freeze CH_4(1) and remove CH_4(2) to calculate the adsorption energy of CH_4(1) and vice-versa. The adsorption energies are measured in electron vlots (eV).

Metal	E_{ad} (Single)	E_{ad} (ave.)	E_{ad} (CH_4(1))	E_{ad} (CH_4(2))
Sc	0.369	0.350	0.290	0.399
Ti	0.469	0.490	0.401	0.402
V	0.531	0.487	0.492	0.499
Fe	0.656	0.491	0.596	0.616
Co	0.872	0.540	0.730	0.534
Ni	0.911	0.555	0.149	0.908

one can notice that every methane is not held by an equal energy. It could be understood that methane nearby the metal atom is more strongly bound than the methane at distance. To quantify their individual adsorption energy, without accounting methane-methane interactions, we performed their separate self-consistent field (scf) calculations at optimized geometries of methane-dimer. For the purpose of their recognition, we define them as CH_4(1) and CH_4(2) in such a way that CH_4(1) and CH_4(2) remain at right and left, respectively, with respect to each other (Figure 61). We freeze CH_4(1) and remove CH_4(2) to calculate the adsorption energy of CH_4(1) and vice-versa.

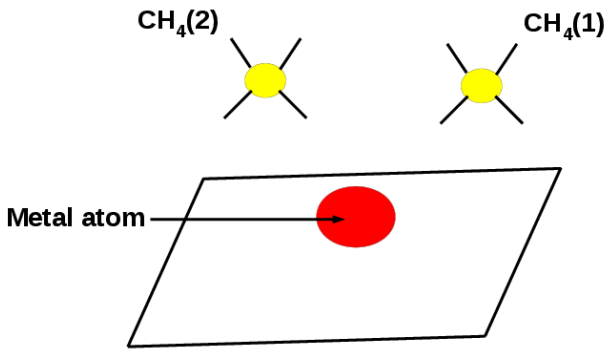

Figure 61: Schematic diagram of the relative positions of CH_4(1) and CH_4(2) above the functinalized-graphene. We define methane-dimer in such a way that CH_4(1) and CH_4(2) remain at right and left respectively with respect to each other.

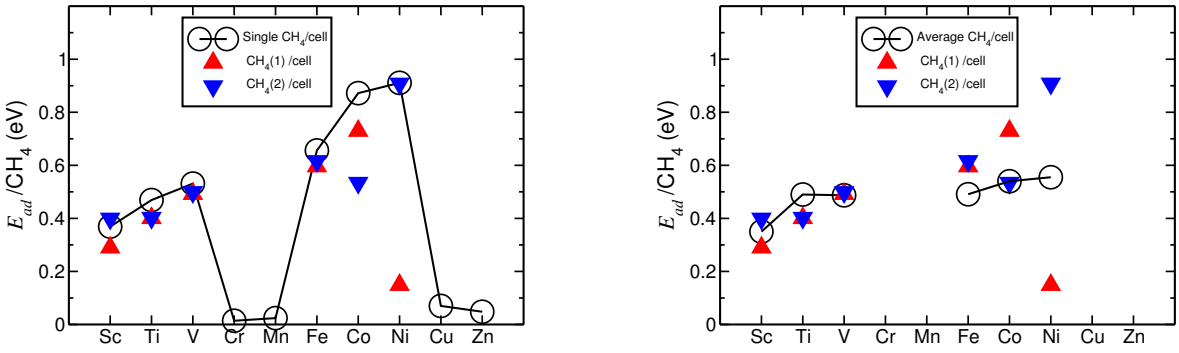

Figure 62: (a) Adsorption energy of single methane of favorable configuration on M/G (hollow circles), and individual adsorption energies of methanes when they are separately calculated (up-triangles and down-triangles). (b) Average adsorption energy (per methane) of methane-dimer (hollow circles). The up-triangles and down-triangles represent the adsorption energy of $CH_4(1)$ and $CH_4(2)$, when they are separately freezed at their relaxed positions (of methane-dimer).

Figure 62 and Table 7 show adsorption energies of one methane molecule from methane-dimer, single methane in favorable configuration and average adsorption energy (per methane). In Figure 62(a), we see that both the methanes ($CH_4(1)$ and $CH_4(2)$) are held with nearly equal energies for Sc, Ti, V and Fe. The individual adsorption energy is also nearly equal to the adsorption energy of single methane, where the atoms are at the left of the 3d series with enough vacant 3d orbitals. However, noticeable asymmetry in adsorption energy of individual methane is seen for Co and this is very high for Ni. It implies that tendency of attracting the second methane decreases on decreasing the number of vacant d-orbitals in metal atoms. Caution should be taken that both the methanes were put together and it is not clear what happens when the second methane is put at the optimized geometry of the first methane @ M/G. Figure 62(b) compares the average adsorption energy of methane-dimer with the individual methanes. In the Figure 62, we see that average adsorption energy of methane-dimer, in general, is different than adsorption energy of individual methanes, and therefore different with the average of individual adsorption energies, $(E_{ad}CH_4(1) + E_{ad}CH_4(2))/2$. For Sc and Ti, average energy seems to be higher than the average of individual adsorption energies. For V, the quantities are equal, and average adsorption energy seems to be smaller in case of the metal atoms on the right side of the 3d series. The difference in between two quantities (the average adsorption energy and average of individual adsorption energies) could be understood in terms of methane-methane interactions which is not accounted when separate methane calculations were performed.

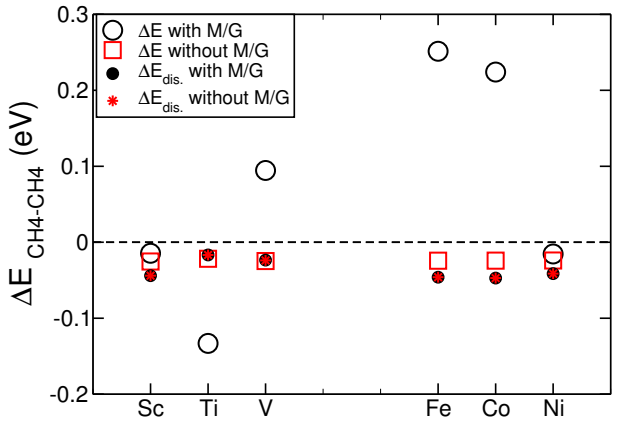

Figure 63: Methane-methane interactions in presence and absence of substrate (metal adatom-graphene). The hollow circles represent two-methane interactions in presence of substrate whereas hollow squares represent the values in absence of substrate. The solid circles and stars (not seen) respectively, are the dispersion contributions on interaction energy.

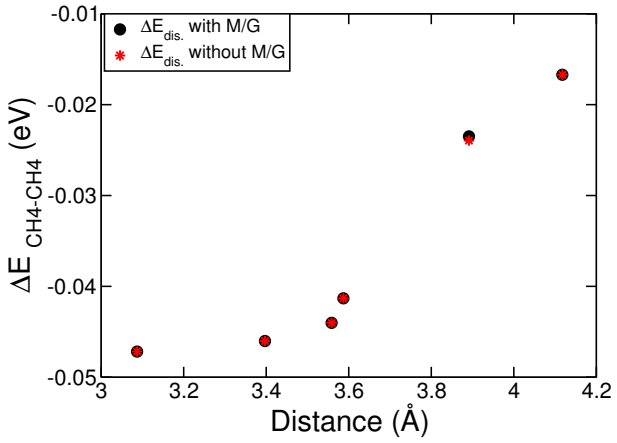

Figure 64: London dispersion contributions in methane-methane interactions. The solid spheres and stars represent the values in presence and absence of substrate.

Figure 63 shows the methane-methane interaction energy in absence and presence of substrate (functinalized-graphene). They are represented by the hollow squares and circles respectively. In addition, the dispersion contributions on the interaction energy are shown. The negative sign in the magnitudes represents the attractive interactions, and the positive sign represents the repulsive ones. In presence of substrate, the nature of methane-methane interactions is metal atom dependent, attractive for Sc, Ti, Ni, and repulsive for V, Fe, Co. On the other hand, the interaction energy is always attractive and comparative to the dispersion contributions in absence of substrate. The dispersion contributions are always equal in both the cases, which is consistent with the fundamental definition of London interactions. It implies that only the London dispersion interactions is present in between the methane dimer when the substrate is absent. In presence of self-polarized substrate (functinalized-graphene), it is understood

that the substrate has a significant role on producing induced dipoles on methanes, which causes the electrostatic interactions in between the constituents in addition to the London dispersion interactions. Since the electrostatic interactions are distance and charge dependent, methane-methane interactions have distinct nature for different metals. The methane-methane attraction is the strongest in case of Ti, where two methanes are separated by distance (4.12 Å). The net interactions in between the methanes is repulsive when they are relatively near (V, Co (3.3 Å) and Fe (3.0 Å)). On the other hand, the magnitude of dispersion contributions are inversely related to distance (smaller the distance stronger the interaction) irrespective to the nature of substrate. Figure 64 shows the dispersion contributions of methane-methane interactions in presence (black circles) and absence of substrate, as a function of distance between them. The figure explains the distance dependent dispersion contributions which could be explained by Grimme's model of van der Waals interactions (Grimme, 2006).

Figure 65 shows the side-view of charge density differences in between optimized geometries of methane-dimer adsorbed functionalized graphene and its constituent systems for fixed isosurface. In the figures, the green lobes and the red lobes represent the regions where the charge density is depleted and accumulated, respectively. Since the isosurfaces are taken for the fixed values, the size of the lobes give qualitative information of rearrangement of electronic charge with respect to their constituent compounds. As similar to the single methane adsorption, green lobes are appeared around the hydrogens lying far from the metal atoms. Red lobes, on the other hand, appear either nearby carbons (of methane) or in between metal atom and carbons. In this sense, hydrogens generally donate the electronic density which is received by carbon (of methane) and metal atoms. The transfer of charge is neither identical for all the metal-atoms nor for two methanes in the same system. For example, green lobes around both the methanes are comparable in case of Ti, and they differ significantly around the methanes in case of Ni. In case of Ni-adatom graphene, one of the methanes is nearby the metal atom, with larger green and red lobes, whereas the second methane lies far way. This implies that no electrostatic interactions seems to be acting in between Ni and far-methane. The differences in rearrangement of electronic charge in between two methanes is moderate for other metal-atoms.

The Agostic Interactions

The interactions in between the carbon-hydrogen groups and the transition metal centers in organometallic compounds are defined by 'Agostic interactions ' (Brookhart & Green,

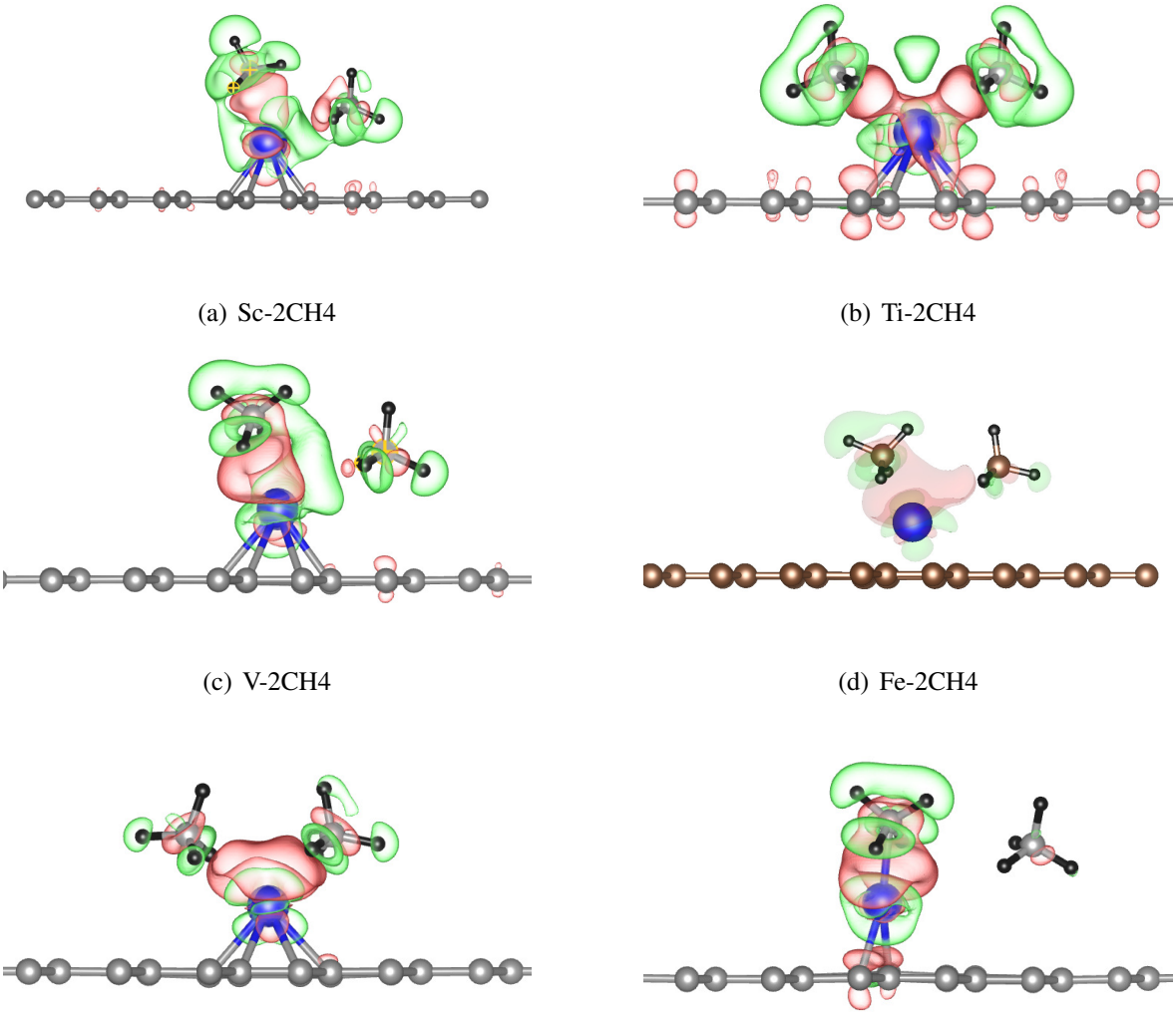

(a) Sc-2CH4 (b) Ti-2CH4

(c) V-2CH4 (d) Fe-2CH4

(e) Co-2CH4 (f) Ni-2CH4

Figure 65: Side-view of the charge density differences in between optimized geometries of two-methane (methane-dimer) adsorbed adatom-graphene and its constituent systems for fixed isosurfaces (metal-adatom graphene and methane-dimers). The green and red lobes represent (electronic) charge depleted and accumulated regions respectively. Methane molecules are defined as $CH_4(1)$ and $CH_4(2)$ as shown in Figure 61.

1983; Brookhart et al., 2007). In agostic interactions, hydrogen atom is bonded to both the carbon and unsaturated-transition metal atom, and results two electrons involved three-center (C-H-M) bonding. Agostic bonding is a special type of covalent bonding and is denoted by half arrow in between metal and hydrogen ($\rightharpoonup$). The bonding strength is intermediate of physisorption and chemisorption with change in enthalpy (ΔH) in the order of 10-15 Kcal/mol. Carbon to hydrogen (C-H) bond distances are 5-10 % longer than expected non-bridging C-H bonds of hydrocarbons. Metal to hydrogen bond distance of the agostic group appear to be longer by 15-20 % than normal M-H bond, and lies in the order of 1.8 Å-2.3 Å. Metal-

hydrogen-carbon M-H-C angle falls in the range of 90 - 140° (Brookhart & Green, 1983). The interaction can be identified as α-, β-, or γ- agostic bonding, and so on, on the basis of carbon that links the hydrogen atom located close to the metal atom (Vidal et al., 2006).

Agostic interactions attracted a great attention of many research groups (Eisenstein & Jean, 1985; Scherer & McGrady, 2004; Brookhart et al., 2007; Lein, 2009) after the publication of two review papers (Brookhart & Green, 1983; Brookhart et al., 1988). Neither only the 3-center 2-electron interactions nor only C-H-M interactions confirm the agostic interactions. Rather some geometric and electronic structure properties should be verified to define an agostic interaction. There are some electronic density and molecular spectroscopy based methods to identify the agostic type of interactions. The information of electronic densities are useful in computational methods like: Atoms In Molecules (AIM), Natural Bonding Orbitals (NBO) and Electron Localization Function (ELF). On the other hand, molecular spectroscopy are more relevant in experiments (Vidal et al., 2006). We follow the Bader's technique based on AIM to study the inter-atomic bonding in between the CH-group and metal centers.

Electronic properties and agostic interactions

We have discussed AIM (atoms in molecules) method to study the interactions in between CH-group and metal centers in section [4.3.2]. Here we discuss the charge density isosurfaces for the total systems where the isosurfaces of substrates and methanes meet at the saddle point. With the help of physical observation and information of charge densities at these saddle points, we predict the nature of bonding between the interacting particles.

Figure 66 shows charge density surfaces of methane-dimer adsorbed functinalized-graphene structures. We show two different surfaces (visible in case of Sc and Ni) to recognize saddle points in between methane-dimer and metal centers. The difference is not vissible in the plot for Co, however, can be observed in Table 8. In case of Ti, V and Fe, charge densities of two surfaces for both the methanes are almost equal. This seems to be correlated with their equal individual adsorption energy [for $CH_4(1)$) and ($CH_4(2)$, Figure 62]. For Sc and Ni, two surfaces are clearly seen and reflect the difference in strength of their binding. The figures also display the saddle points in between the methanes and metal centers. In most of the cases, saddle point lies in between the metal atoms and carbon of methane which might be causing the covalent bond in between them. In case of Sc ($CH_4(1)$) and Co ($CH_4(2)$), however, saddle point lies in between metal atoms and hydrogens. This reflects the possibility

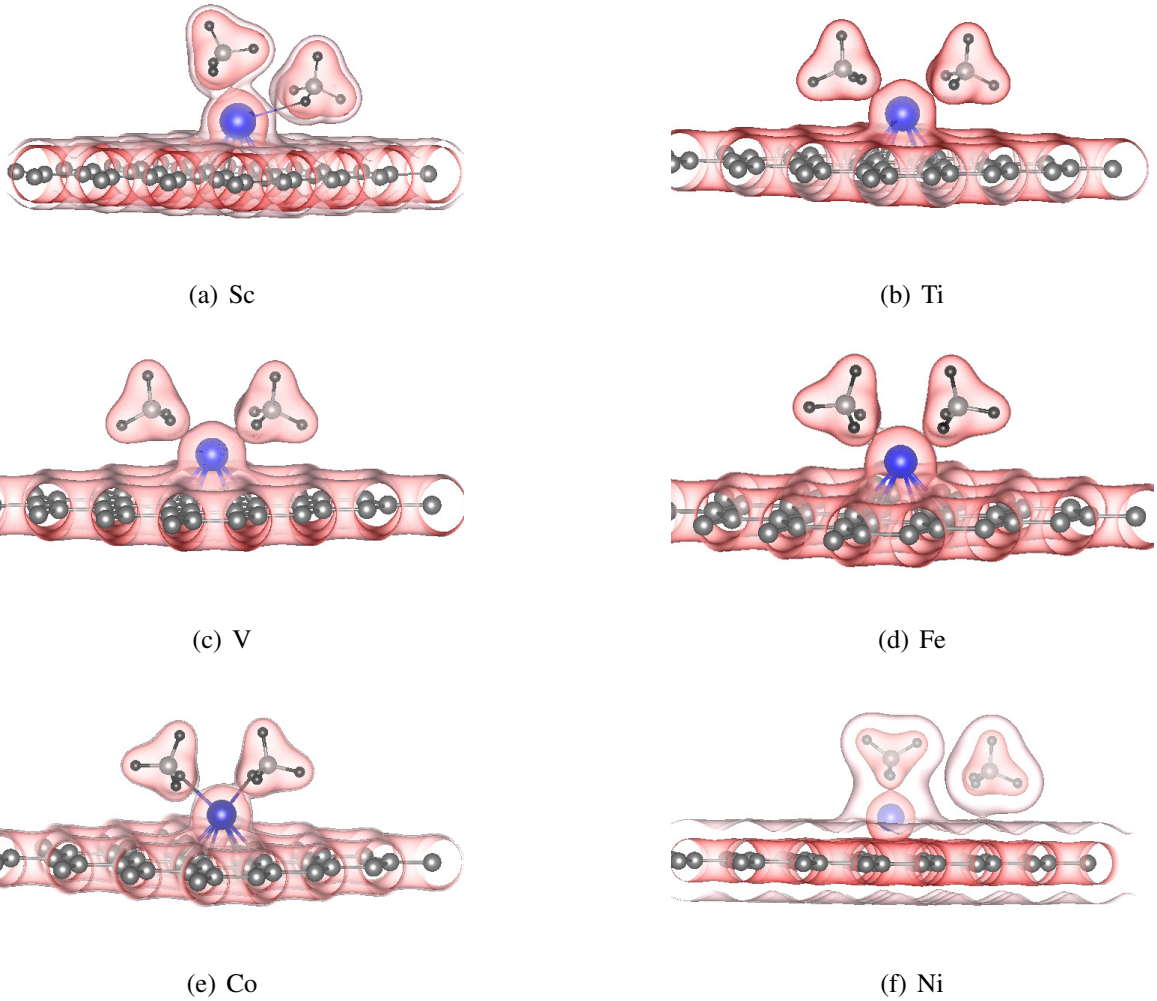

(a) Sc (b) Ti

(c) V (d) Fe

(e) Co (f) Ni

Figure 66: Charge density surfaces of methane molecules and the metal atom graphene. The point/s at which the electronic charge density isosurfaces of two regions just touch to each other are the bond critical point (BCP), and the corresponding isosurfaces define charge densities at BCP. Each of the figures shows two isosurfaces and implies that the charge densities at bond critical point are different for two methanes.

of agostic interactions (interactions in between carbon, hydrogens and metal centers). We do not have calculated separate bonding strength in between CH group of methane and metal atoms, and are the subject of future work for the proper analysis of other properties of agostic interactions.

The optimized geometries of methane-dimer and also the charge density difference plots have been shown in Figure 66. It further displays that most of the geometries of adsorbed methanes follow straddle-like configurations (except $CH_4(2)$ of Sc). In Sc-added graphene, $CH_4(2)$ seems to be near to TT configuration rather than straddle one. To get more information about the geometries, electronic charge density at BCP and binding energy of methanes, we show the relationship in between adsorption energy of single methanes in S, and TT configurations

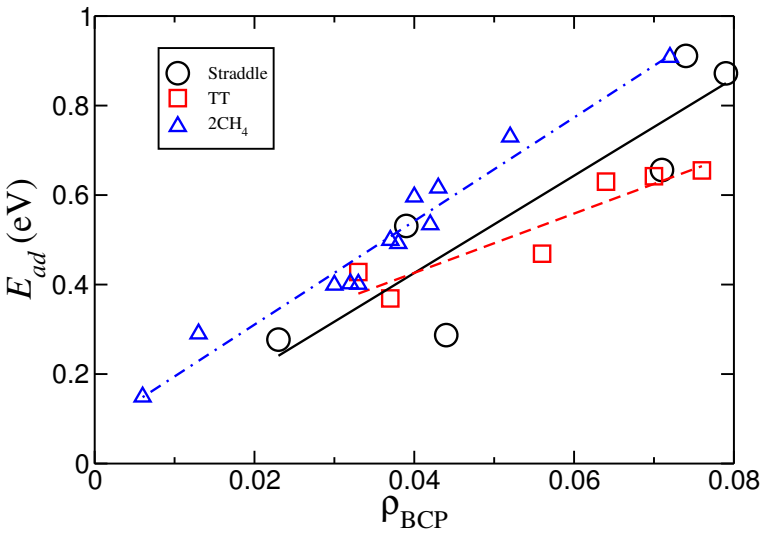

Figure 67: Variation of adsorption energy of methane with charge density at bond critical point (BCP). The blue triangles represent individual adsorption energy of methane molecule in methane-dimer. The circles and squares, on the other hand, represent the relationship of adsorption energy of methane in S and TT configurations when only one molecule of methane is adsorbed.

separately and also E_{ad} (CH_4(1)) and E_{ad} (CH_4(2)) from methane-dimer (Figure 67).

Table 8: Table represents adsorption energy values of single methane molecule E_{ad} in S and TT configurations, adsorption energies of individual methanes of methane-dimer [E_{ad} (CH_4(1)) and E_{ad} (CH_4(2))] and their corresponding charge densities at bond critical points ($\rho_{(BCP)}$). The adsorption energies are measured in eV.

Metal	E_{ad} (S)	$\rho_{(BCP)}$	E_{ad} (TT)	$\rho_{(BCP)}$	E_{ad} (CH_4(1))	$\rho_{(BCP)}$	E_{ad} (CH_4(2))	$\rho_{(BCP)}$
Sc	0.277	0.023	0.369	0.037	0.290	0.013	0.399	0.030
Ti	0.287	0.044	0.469	0.056	0.401	0.033	0.402	0.032
V	0.531	0.039	0.428	0.033	0.492	0.038	0.499	0.037
Fe	0.656	0.071	0.655	0.076	0.596	0.040	0.616	0.043
Co	0.872	0.079	0.642	0.070	0.730	0.052	0.534	0.042
Ni	0.911	0.074	0.630	0.064	0.149	0.006	0.908	0.072

Figure 67 shows the variation of adsorption energies of methane as a function of charge densities at BCPs. The figure includes individual adsorption energy of methane-dimer, and adsorption energies of single methane in both the configurations. Single methane case has already been discussed in Figure 59, which are plotted here for the purpose of comparison with methane-dimer. The trend lines of methane-dimer and single methane at S configuration seems to be parallel to each other. This is consistent with the optimized geometries where we see every methane in methane-dimer at Straddle configuration (except for CH_4(2)). The exceptional methane (CH_4(2) in Sc) lies at the boundary region of S and TT trend lines, and also near to the trend line of methane-dimer as well.

4.4 Methane-dimer in liquid environment

Hydrophobic interactions in between non-polar solutes on liquid media represents the model system for protein folding and its denaturation in living creatures. Different solutes and solvents have differences in their molecular size and structural arrangement which affect the nature of interactions in between solute particles (Sobolewski et al., 2007). We have considered the interactions between two methane molecules in presence of water, methanol and acetonitrile as solvent media, which basically follows the method of pair-wise addition of interaction energies in terms of potential of mean force (PMF) (J. Wu & Prausnitz, 2008) and/or potential of mean effective force (PMEF). The physical meaning of PMF and PMEF, and their mathematical relations are discussed in upcoming paragraphs.

The system size of water, methanol and acetonitrile in the cubic boxes of size 25 Å, 35 Å and 35 Å contain 507, 669 and 396 number of solvent molecules, respectively. The method of classical molecular dynamics simulations with umbrella sampling in GROMACS has been performed to study their atomistic level of interactions. The inbuilt force-field parameters available in GROMACS (GROMOS) have basically been used as potentials acting in between interacting particles. Methane positions are fixed at certain separations by using biasing (harmonic) potential, which have been discussed in section 3.11.3.

We have estimated the PMEF, volume-entropy corrections and PMF, separately for the systems that have discussed before. PMEF defines the effective potential, W(r), in between the solute molecules which incorporates the effect of solvent environment in addition to the solute-solute interactions. The potential is related to the mean effective force by the relation,

$$\mathrm{f}(\bar{r}) = -\frac{\mathrm{d}}{\mathrm{d}r}\mathrm{W}(r) = -\frac{\mathrm{d}}{\mathrm{d}r}\mathrm{F}(r, T, V, N) \tag{4.5}$$

where F(r, T, V, N) is the Helmholtz free energy. Helmholz free energy, in general, is the function of temperature (T), volume (V), and number of particles (N) (F(T, V, N)). Here **r** represents the separation between the solutes particles. It plays an important role in determining PMF and becomes a parameter of free energy. The bar sign at $\mathrm{f}(\bar{r})$ is to represent mean effective force (value). When the solute particles (methanes in our case) are constrained or restrained within certain distances in solvent environment, free volume of spherical shell to solutes changes. This causes entropic contributions which is not being incorporated in PMEF. This could be corrected by using more usual term, potential of mean force (PMF), w(r), which

relates probability of finding two interacting solutes at given separation (J.-L. Li et al., 2007),

$$w(r) = -k_B T \ln g(r). \tag{4.6}$$

The symbol $g(r)$ represents the radial distribution function of solute molecules. Furthermore, the average effective force and PMF are related by,

$$f(\bar{r}) = -\frac{d}{dr} w(r) + \frac{2k_B T}{r}. \tag{4.7}$$

with $2k_B T/r$ as volume-entropy correction. By solving equations (4.5 and 4.7), we obtain the relation for PMF which includes PMEF in addition to the volume-entropy corrections,

$$w(r) = W(r) + 2k_B T \ln(r). \tag{4.8}$$

Figure 68 shows the potential of mean effective force $W(r)$ (PMEF) in between two methane molecules in water against the reaction co-ordinates simulated by means of umbrella sampling in GROMACS. In the present work, reaction co-ordinbates define the separation between two methane molecules, which changes from minimum distance (around 0.4 nm) to nearby half of the simulating box-size (around 1.0 nm). The system was first simulated in NPT ensemble (keeping N, P and T fixed) to check the density of corresponding solvents before going through the production run in NVT ensemble. In the Figure, W(r) is plotted with reference to its value at contact minimum (will be discussed in the following paragraphs). Three lines in Figure (68) show the PMEF values simulated for different time-durations, that is first 5 ns (dotted line), 5 ns to 10 ns (dashed line) and total length (10 ns) of the simulation (solid line) in NVT ensemble. Very good agreement in between the curves (lines) until 1 nm implies that the system has been equilibrated, where the system properties are time-independent.

PMEFs remain constant (and positive) at small values of reaction co-ordinates, up to 0.31 ns (Figure 68). These sections (straight lines) of the curves represent repulsive regions where the distance between the methane molecules is smaller than the sum of their vdW radii. Methane molecules are assumed as the hard spheres in the present simulations and thus overlapping of their molecular cores is excluded. Also the curves show their minima at around 0.38 nm, which could be understood as the minimum energy distance (equilibrium distance) in between the molecules when the liquid environment is absent. The minimum energy position of PMEF is defined as *contact minimum* where two methane molecules are supposed to be in physical contact with each other. The position (of minimum) is also consistent with the minimum of Lennard-Jones potential (Figure 9) and the sum of van der Waals radii of methane molecules

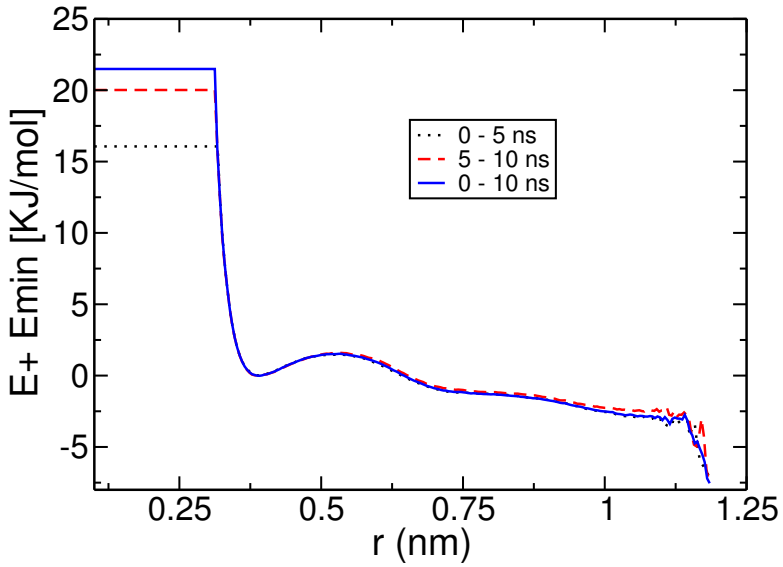

Figure 68: The potential of mean effective force W(r) calculated by means of umbrella sampling in GROMACS. The plot shows firs-half, second-half and total length (10 ns) of the md simulation.

estimated via calculations (0.42 nm) and experiments (0.41 nm). The calculations were performed by using the concept of spherical surfaces enclosing most of its *electron-density* and experiment was done for crystalline structure (Kammeyer & Whitman, 1972).

In Figure 68, we see a hump after contact minimum which resists the system to sample at these regions and beyond. The height of the hump defines *desolvation barrier*, the quantity by which the system is opposed to move in larger solute separations. Beyond the hump, there is a second minimum which however is not clear due to decreasing PMEF against the reaction co-ordinates. This implies that the system is unstable at larger separations. It is due to exclusion of volume-entropy contributions in PMEF.

Inclusion of volume-entropy corrections in addition to PMEF in the same figure reveals their separate contributions on PMF. Figure 69 shows PMEF (dashed line), volume-entropy corrections (dotted line) and PMF (solid line) of methane-methane interactions in water. The curves in the figure represent the results simulated for 10 ns in NVT ensemble. PMEF in Figure 69 is identical with the curves shown in Figure 68 and discussed in the paragraphs above. The contact minimum is observed at around 0.38 nm with the hump (desolvation barrier) just towards the right hand side. The decreasing slope beyond the barrier (desolvation barrier) implies that methane-dimer does not remain stable except at its equilibrium separation. Previous studies have shown that apolar molecular-dimers are stable also at larger distance which are supposed to be equivalent to the distance between methanes when they are separated by the single layer of solvent molecules.

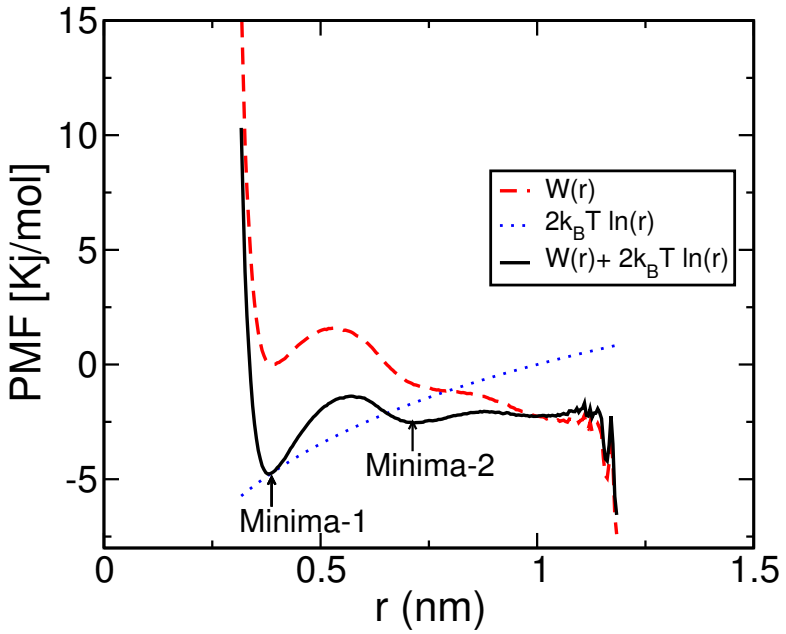

Figure 69: Potential of mean effective force (W(r), dashed line), volume-entropy correction (dotted line) and potential of mean force (w(r), solid line) of methane dimer against their separation in water. Minima-1 and Minima-2 represent the contact minimum and solvent-separated minimum respectively.

The dotted line in Figure 69 represents the volume-entropy correction in free-energy calculations. The term, $2k_BT\ \ln(r)$, is the function of methane-methane separation (r), and increases on increasing the value of r. The sum of PMEF (dashed line) and the volume-entropy correction gives PMF (Equation 4.8) which is represented by the solid line in Figure 69. The solid line shows a depression (at around 0.73 nm) beyond the barrier. This depression is the *second minimum* (Minima-2) in the curve and is observed only in presence of solvent environment. The presence of second minimum defines the stability of methane dimer at larger separation in addition to the equilibrium state (condition of contact minimum). The position of second minimum is equivalent to the methane-methane separation when a molecular layer of solvent (water) is sandwiched in between them. Because of the nature of molecular arrangement, the condition is also named as solvent-separated minimum.

Figure 70 (a) shows a cartoon picture of spherical solutes (solid spheres) and solvent molecules (hollow circles) around them. At contact minimum, solute particles touch to each other and the spherical shell of solvent molecules surround the remaining sides. At the separation of desolvation barrier, neither the solute molecules touch to each other nor the solvent molecules penetrate between them. At solvent-separated minimum, however, monolayer of solvent molecules penetrate in between solutes.

The cartoon picture (Figure 70) is consistent with the situation of methane-methane and

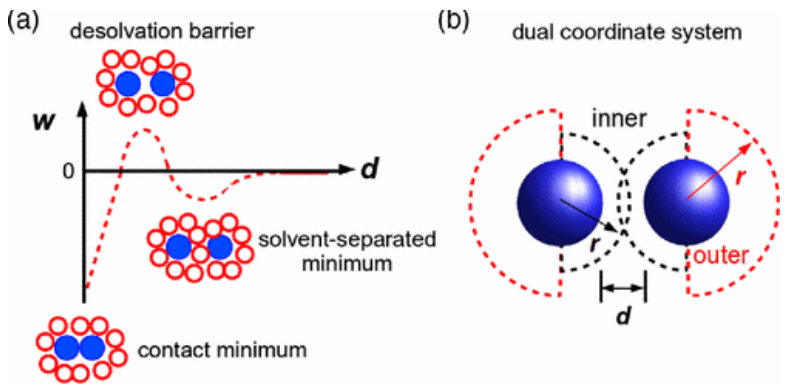

Figure 70: (a) Cartoon picture of contact minimum, desolvation barrier, solvent-separated minimum, and corresponding free-energy profiles in between two non polar molecules in aqueous solution. (b) Inner and outer hydration semi-shells around the hydrophobic solutes (Godec et al., 2013).

methane-water interactions of the present study. As described in paragraphs before, contact minimum (0.38 nm) is comparable to the sum of vdW radii of two methanes (0.42 nm (Kammeyer & Whitman, 1972). The slight discrepancy with vdW radii could be understood in terms of method of calculations where certain percentage of electron density is taken as reference for molecular size. The effect of solvent environment is insignificant in case of contact minimum. The condition of desolvation barrier, however, is mainly influenced by solvent molecules around the solutes. In the present case, water molecules are partially inserted in between methane molecules, although the condition is thermodynamically unfavorable. In spite of absence of any direct (effective) attractive forces in between two methane molecules beyond 0.45 nm, we observe second minimum at around 0.73 nm. This could be understood as the effect of solvent environment. Consistent with the literal meaning and previous studies (Hummer et al., 1998), the situation is supposed to be methane-dimer separated by single layer of water molecules. With the assumption of spherical water molecules of diameter in the order of 0.3 nm, the sum of vdW radii of methane dimer (0.42 nm) and single water molecule meet the condition (separation) for solvent-separated minimum (Godec et al., 2013). Molecular reorientation due to fluctuations of water molecules may also cause for differences in between the values. Figure 70 (b) shows the assumption of inner and outer hydration semi-shells, which have many body effects in structural order and fluctuations during the formation and breaking of hydrogen bonds.

The solubility of solutes in aqueous solution and hence the depth of PMF at its minima depends mainly upon two contrasting factors. Insertion of solutes from gaseous phase to solvent-environment has to create vacuum in the solvent which is accounted in the form of volume-entropy corrections. The change in energy is larger for larger solutes, and discourages

the solubility. On the other hand, van der Waals (vdW) interactions in between solute and solvents, and also formation of induced dipoles of solvent molecules usually help to enhance the solubility. The stronger solute-water interactions, for a pair of hydrophobic solutes, decreases the depth of PMF and enhances the solubility (Sobolewski et al., 2007). In the present work, the depth of first and second minima, and desolvation barrier of PMF (Figure 69) of methane-dimer in water have been estimated. The estimated values are 2.54 kJ/mol, 0.314 kJ/mol and 3.4 kJ/mol respectively (Table 9), which are in good agreement with the results reported by a previous study (Dang, 1994). In the reference, the depth of contact minimum and desolvation barrier are reported as 2.65 kJ/mol and 3.78 kJ/mol (at the same temperature of the present study, 300 K). The discrepancy (4.15 % and 10.05 % in the depth of contact minima and desolvation barrier, respectively) might be due to difference in model-systems considered for methanes. In contrast to the all atom model assumed in the previous work ((Dang, 1994)), we have taken united atom model for methanes.

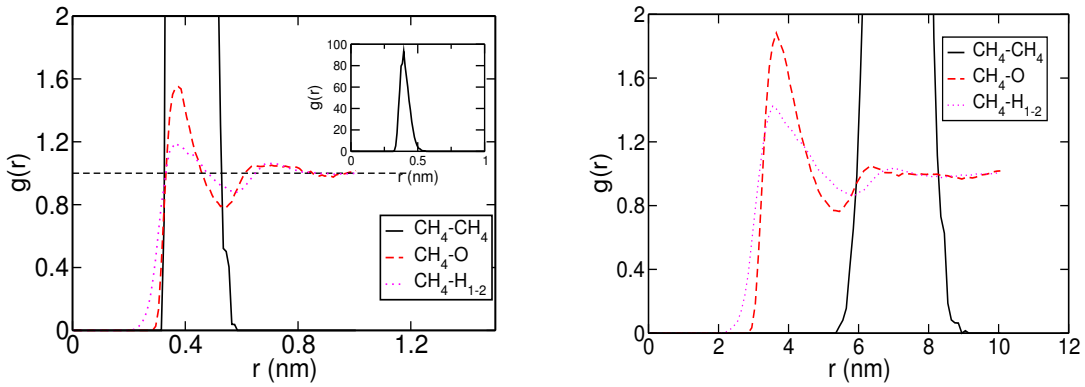

Figure 71: Radial distribution functions of methane with methane (solid lines), oxygen (dashed lines) and hydrogens (dotted lines, named H_{1-2}) of water, when methane-methane separation is constrained at (a) 0.4 nm (b) at 0.7 nm. Methane-methane peaks are cut to show the meaningful values of other molecules. Inset at (a) gives an idea of maximum value of g(r), when methane-methane separation is confined at the fixed distance.

Radial distribution function implies the composition and distribution of constituent particles with reference to anyone of them. Figure 71 shows the radial distribution functions in between methane and methane, methane and oxygen of water and methane and hydrogens of water by solid lines, dashed lines and dotted lines respectively, when methane-methane separation is constrained (a) at 0.4 nm and (b) at 0.7 nm. In Figure 71, radial distribution function g(r) is related to the probability of finding an another molecule by methane at specified distances. Since the methane-methane separation is confined at fixed distances (0.4 nm and 0.7 nm), it is expected that g(r) for methane and methane is infinite at those separations and zero elsewhere.

The figures also display that peak values of g(r) for methane-oxygen and methane-hydrogens remain at around the similar distance. This is the consequence of first hydration shell around the methane molecules, which are in contact with methane molecules themselves. The exclusive regions up to 0.28 nm for methane-oxygen and 0.22 nm for methane-hydrogens is consistent with the larger core for oxygen than that of the hydrogens. In spite of being smaller in size, the first peak positions of g(r) for hydrogens are comparable to that for oxygens. Also the peaks of hydrogens are wider. Water molecules are polar and thus oxygen and hydrogens could be considered at the different poles of a dipole. Figure 71 thus infers that oxygens either directly or in some orientation might be pointing towards the methane molecules.

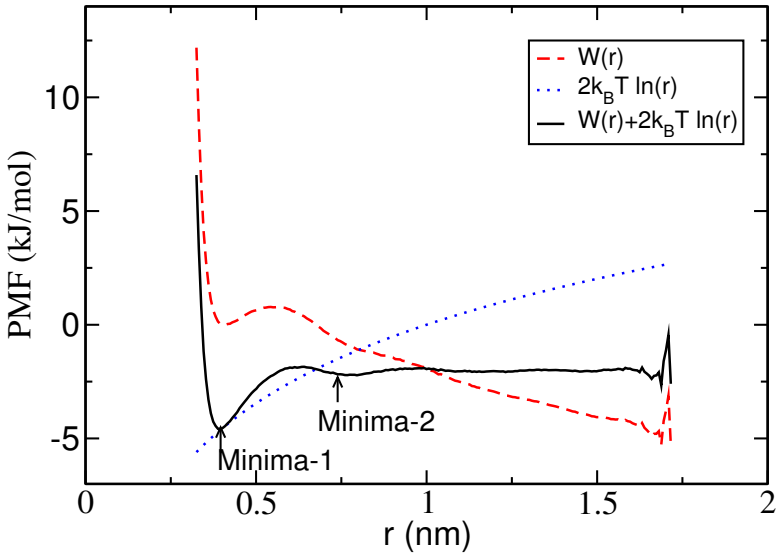

Figure 72: The potential of mean effective force (W(r), dashed line), volume-entropy correction (dotted line) and potential of mean force (w(r), solid line) of methane dimer against their separation (r) in methanol are shown. The values are plotted with reference to PMEF-minimum (contact-minimum).

To get more insight of the effect of solvent molecules in solute-solute interactions, we performed the similar calculations in methanol. Figure 72 shows the potential of mean effective force (W(r), dashed line), volume-entropy correction (dotted line) and potential of mean force (w(r), solid line) of methane-dimer against their separation in methanol. The values are plotted with reference to PMEF-minimum to compare different contributions in PMF. The overall trend of PMF in methanol, sum of PMEF and volume-entropy term, seems to be identical with that of methane-dimer in water. The contact minimum of methane-dimer in methanol lies at 0.40 nm, slightly larger than that in water (0.38 nm). The disolvation barrier and solvent-separated minimum, however, lie at noticeably larger separations, 0.64 nm and 0.77 nm comparing to 0.57 nm and 0.72 nm in water (Table 9). Methanol (CH_3OH), composed of methyl group and hydroxide, contains a hydrophobic methyl group which may

compete with the non-polar methane molecules of methane-dimer and weaken methane-methane interactions. Hence the position of contact minimum might have been affected. In addition to the competing methyl group, methanol is larger in size than that of water and pushes methane-dimer in larger apart for disolvation barrier and solvent-separated minimum. The comparison of energy depths in PMF curves are being shown in Figure 74 and discussed in upcoming paragraphs.

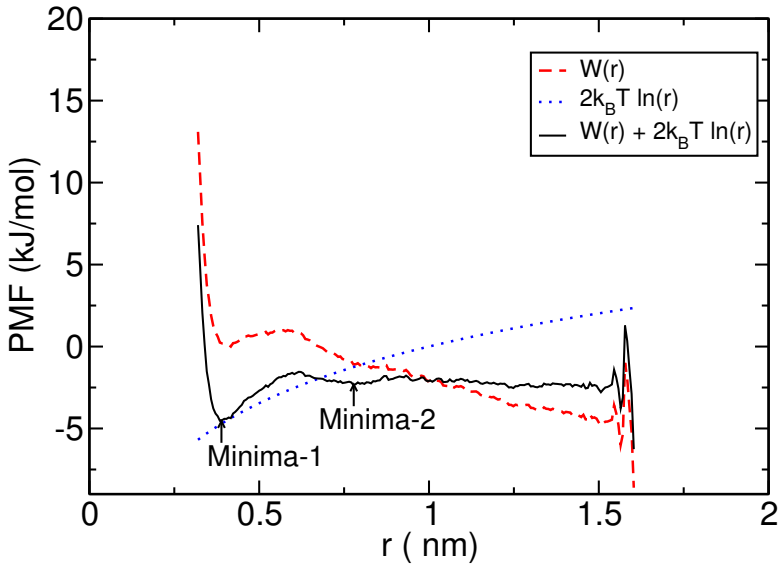

Figure 73: The potential of mean effective force (W(r), dashed line), volume-entropy correction (dotted line) and potential of mean force (w(r), solid line) in between methane dimer in acetonitrile are shown. The values are plotted with reference to PMEF-minimum.

Acetonitrile has also been considered as solvent media to see its effect in methane-methane interactions. Figure 73 shows the potential of mean effective force (W(r), dashed line), volume-entropy correction (dotted line) and potential of mean force (w(r), solid line) of methane-dimer against their separation in acetonitrile. The values are plotted with reference to PMEF-minimum to compare the contributions from each of the components. The overall trend of PMF of methane-dimer in acetonitrile seems to be similar as in the case of water and methanol. The positions of contact minimum, desolvation barrier, and solvent-separated minimum in acetonitrile are calculated as 0.39 nm, 0.62 nm and 0.78 nm respectively (Table 9). There is no remarkable change in positions of contact minimum in all the solvent environments. The positions of desolvation barrier and solvent-separated minimum, on the other hand, are larger for methanol and acetonitrile than that of water and comparable within themselves. The similarity in between methanol (CH_3OH) and acetonitrile (CH_3CN) solvent environments might be because of common methyl group in both the cases. The small discrepancy in the values might be because of the replacement of OH group in methanol by CN group in

Table 9: Table shows the positions of contact minimum (Minima-1), desolvation barrier (DB), solvent-separated minimum (Minima-2) and their depths with respect to PMF at infinite methane-methane separations (zero level) in different solvent environments. The depths for desolvation barrier, contact minimum and solvent-separated minimum in the table are represented by DB, Eb-1 and Eb-2 respectively. The values in the bracket are taken from references, (a) (Hummer et al., 1998) and (b) (Dang, 1994), for the purpose of comparison.

System	Minima-1 (nm)	Maximum (nm)	Minima-2 (nm)	DB (kJ/mol)	Eb-1 (kJ/mol)	Eb-2 (kJ/mol)
CH4 in water	0.38 (0.39, a)	0.57	0.72 (0.73, a)	3.40 (3.78, b)	2.54 (2.65, b)	0.31
CH4 in methanol	0.40	0.64	0.77	2.75	2.67	0.29
CH4 in acetonitrile	0.39	0.62	0.78	2.98	2.46	0.28

acetonitrile. The error bar in the calculations could also have affected the results. Further comparison and differences in between the effect of solvent media on methane-methane interactions have been discussed below.

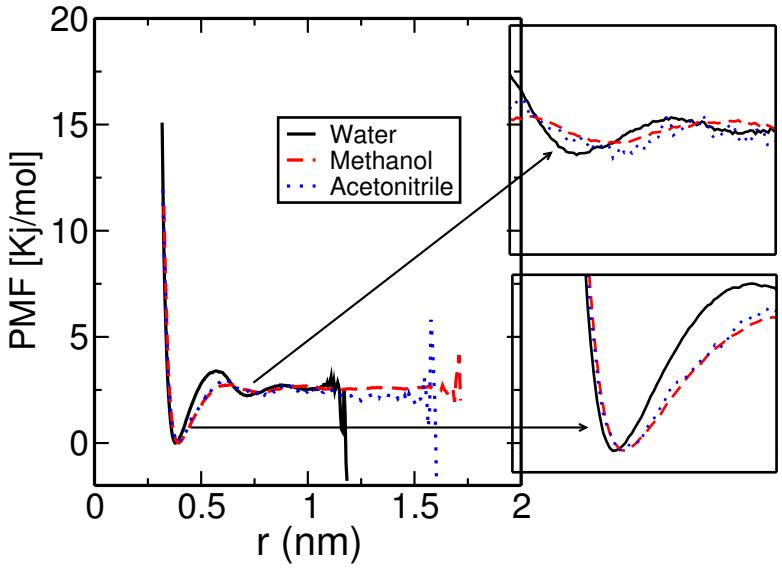

Figure 74: The potential of mean force of methane dimer in water (solid line), methanol (dashed line) and acetonitrile (dotted line). The values are being plotted with reference to contact minimum. The insets in the figure aim to highlight the PMF values at contact minimum and solvent separated minimum.

Figure 74 and Table 9 show the comparison of PMF of methane-dimer in the environment of water, methanol and acetonitrile. The depths for desolvation barrier, contact minimum and solvent-separated minimum are represented by DB, Eb-1 and Eb-2 respectively (table 9). In Figure 74, the curves at contact minimum and solvent separated minimum are highlighted to notice their closer view. The values are calculated with reference to the contact-minimum (Minima-1). The values of desolvation barrier are thus heights of the humps (beyond contact minimum) with reference to Minima-1. The depths of minima (Eb-1 and Eb-2), however,

measure binding energies of methane-dimer at the given positions with respect to the values at infinite methane-methane separation. Comparing the nature of curves in Figure 74, we see that contact minimum in water is deeper and narrower than that in methanol and acetonitrile. It means hydrophobic interactions in between two methane molecules is stronger and stiffer in water, and the fluctuations are larger in methanol/acetonitrile. As discussed in above paragraphs, it might be due to presence of methyl (hydrophobic) group in methanol and acetonitrile. The methyl groups in solvents surround the methane molecules and compete with the neighboring methane to interact. Hence the hydrophobicity in between methanes becomes weaker. The degree of polarization of solvent molecules around the solutes might be playing a significant role, which is the subject of further research. The positions of contact-minimum could be understood similar in all the cases. Also the depths of second minimum are shallower (comparing to first minimum) and comparable for all the liquid media. The positions of desolvation barrier and second minimum for methanol and acetonitrile have been found to be shifted towards right hand side (comparing that of water) due to their molecular size in addition to their hydrophobic competition. The larger molecules of solvents for methanol and acetonitrile (Marenich et al., 2009) are partially or completely inserted in between methane-dimer at the conditions of desolvation barrier and solvent-separated minimum, respectively. These situations obviously increase the methane-methane separation.

The nature of PMF in vacuum should be identical to Lennard-Jones potential as described in Figure 9. This is also verified with the previous calculations for potential minimum of methane dimer (in vacuum) via first-principles calculations (Tsuzuki et al., 1998). The reported values for Linnard-Jones minimum, through a number of methods, lie within the range of 0.38 nm to 0.43 nm with their depth 1.39 kJ/mol to 1.93 kJ/mol, which are consistent with the contact-minimum of present calculations. The discrepancy is because of the different basis sets used in calculations (Tsuzuki et al., 1998).

CHAPTER 5

CONCLUSIONS AND RECOMMENDATIONS

The interactions of methane molecule(s) with other like and unlike molecules have been studied by using density functional theory based first-principles method and classical molecular dynamics method of calculations. Methanes in three different environments (methane hydrate clathrate, functionalized carbon nanomaterials and varying solvent media) have been considered to see their nature of interactions, and more importantly to explore its multidimensional applications.

Methane hydrates are ice like compounds where the ice cages/channels encapsulate methane as guest molecules. They are considered to be one of the major components at the interior of the giant icy planets. In the earth they are available at the continental slopes of the ocean and permafrost regions showing abundant potential for the source of energy. The structure and stability are the matter of interest in many sectors including planetary science and alternative source of energy, and have been searched by both the computational methods and experiments. By using density-functional theory based first-principles calculations, we show methane hydrate (MH-III) unstable against its decomposition into ice and methane above a pressure of a few GPa (4 GPa) which agrees with a recent experiment. The experiment shows that methane hydrate decomposes above 3 GPa. In the context of disagreement with some of other studies, where they claim methane hydrates stable compounds until high pressure (86 GPa) and temperature (1000 K) (S.-i. Machida et al., 2006), we remark that the authors might have conducted their research in the regime of metastability (Pantha, Adhikari, & Scandolo, 2015). Slow kinetics of decomposition and large energy barriers could be the cause for preventing methane hydrate from decomposition. Further, we find transformation of MH-III into new structure (within the regime of metastability) above 180 GPa which is called HP (High Pressure) structure. The structure is characterized by quasi-one-dimensional crystal along *b* axis and remarkably short carbon-carbon distance (2.33 Å at 180 GPa) along *c* axis.

We caution however that our search for high pressure structures was limited to a structural optimization of the MH-III structure at constant pressure and zero temperature.

The structural properties like the compression of MH III are also observed under the elevated pressure. Consistent with the previous studies, we find compression of the compound largely anisotropic with respect to crystal directions due to structural variations. MH III compresses faster along the shorter diameter (along c axis) of the larger channel which runs along a axis. Because of the anisotropic compression of the compound, the separation in between both the like and unlike molecules decreases differently. The rate of compression in between oxygen-oxygen atoms of water channel has been found faster in MH III comparing to that in pure ice. Hence the symmetrization of H-bond where H atom comes in between two nearest oxygens occurs at lower pressure (around (65-70) GPa) than that in pure ice (100 GPa). In the regime of MH III structure, the clathrate compound is found always less denser (higher volume) than its constituents. van der Waals (vdW) interactions influence on the rate of compression of methane hydrate at lower pressures. The effect is also observed on the decomposition pressure of MH-III, where we report the values as above 12 GPa and 4 GPa respectively for without and with vdW interactions. At the higher pressure, shorter intermolecular separation causes repulsive interaction, and the vdW becomes less important. We find effect of vdW on the structural properties of MH III negligible above 65 GPa.

In spite of abundant presence of methane hydrate on the Earth, potential applications of methane as an alternative resource of energy is hindered by technical limitations. Extraction of methane from those resources, its safe and economic storage, and transportation for practical applications are a series of works which need detail analysis. The search of effective storage of methane and other energy carrying gases has been conducted with different combinations of carbon nanomaterials. We use modified graphenes (by single metal atom adsorption) to study the adsorption energy of methane on the way of searching proper combinations of metals and organic compounds. The binding stabilities of individual metal atoms of 3d series in monolayer graphene has been studied within DFT-D2 level of approximations where London dispersion interactions are inclusive. From the calculations, the most stable geometries are picked to check the adsorption strength of single methane and methane-dimer on them. The results which are consistent with the previous study show that six adatoms (Sc, Ti, V, Fe, Co and Ni) are strongly adsorbed (chemisorped) in graphene layer. On the other hand, four remaining metal atoms on the series whose 3d shell is either totally occupied or half-filled (say only up-spins), are weakly bound (physisorbed). We also notice that the magnetic properties

of metal atoms are modified differently on graphene according to their binding strength.

The single methane molecule in their two most relevant configurations (S and TT) are adsorbed in the most stable metal adatom-graphenes. The methane molecules seems to be physisorbed, with the adsorption energy less than 0.1 eV, in weakly bound metal atoms (Cr, Mn, Cu and Zn). On the other hand, methanes are more tightly held in strongly bound metal atoms which motivate us to see what happens on increasing methane molecules from one to two (so called methane-dimer). From the values of adsorption energy per methane, and other electronic properties, it is observed that the adsorption energy of methane ranges in useful order for the reversible storage of methane (within 0.4 eV in most of the cases), which can be targeted for on-board vehicular applications. Most of the methanes seems to have covalent bonds, and the few others have agostic type of interactions (interactions of CH group with unsaturated metal atoms). Since both the methane are symmetrically held in case of Ti, V and Fe, they could be considered as the best elements in organometallic compounds for the storage of energy carrying natural gases, like methane. In the present work, the average adsorption energy per methane in case of Ti, V and Fe has been noted as 0.49 eV.

The magnetic properties of methane adsorbed Ti adatom graphene have been observed interesting. The properties show the possibility of developing methane sensors, and opens the huge applications in industrial sectors and academia. We reveal the primary information of binding strength in between metal-adatom graphene and methanes, and believe that there is an enough space for in-depth study of the nature and stability of bonding. Further increase in number of methanes for their adsorption on metal-adatom graphene can predict the optimum concentration of methane for its reversible storage in carbon nanomaterials as discussed in previous studies (Bhatia & Myers, 2006) .

Methane-methane interactions in different solvent environments can be a model research for the hydrophobic interactions in biological molecules. The solvent environment around the hydrophobic groups affect the strength and nature of interactions which may reveal the conditions for protein folding and their denaturation. We consider water, methanol and acetonitrile as solvents to study their effect on methane-methane interaction. From the results of our calculations, we notice that presence of solvent molecules around the methane molecules causes mimima-2 (second minima) at PMF, called solvent separated minima, in addition to the deeper one (potential minima) at equilibrium separation. The position of deeper minimum, also known as contact minimum, is usually independent (in between 0.38 nm to

0.40 nm) to the nature of solvent media. The solvent separated minimum on the other hand changes with liquid environment (at 0.72 nm in water, 0.77 nm in methanol and 0.78 nm in acetonitrile). The PMF between two methane molecules in water agree well with the previously reported values. Our results show that methane-methane interactions in methanol and acetonitrile are softer and long-ranged comparing to that in water. The PMFs in between methanes molecules are wider and shallower in methanol and acetonitrile showing their larger fluctuations in these solvents.

It is well-known that liquid water form their network around the hydrophobic groups. The microscopic understanding of probability of forming networks with different size and nature helps to predict many biological and chemical processes. Previous studies have used ring statistics (formation of water rings) around the hydrophobic molecules for such purpose (Hassanali et al., 2013). Such an analysis to see the nature of water rings around the methane molecules, and also the interactions between the methyl, OH and CN groups with methane, in methanol and acetonitrile can be the next level of work to understand the solvent perturbation in hydrophobic interactions.

CHAPTER 6

SUMMARY

We have studied the interactions of methane molecule(s) with other methane(s) and/or other substances by using electronic structure and atomistic model of calculations. Methanes are encapsulated inside the ice-like channels in methane hydrates (MH) clathrates. The clathrate structures of methane hydrates are usually found at high pressure which are consistent with the ocean floor and the interior of the permafrost regions in the Earth. By using methane hydrate III (MH-III) as the initial structure of methane hydrate at 10 GPa, we performed density-functional theory (DFT) based calculations to study its geometrical and electronic properties as a function of elevated pressure (up to 300 GPa). Similar level of calculations have been performed for ice VIII-X structures and solid methane to determine the relative (thermodynamic) stability of MH-III against its constituents. Our calculations have shown that MH-III is unstable against its constituents above 4 GPa of pressure. Within the metastable regime of MH-III, the structure changes to high pressure (HP) structure above 180 GPa.

Methane in natural resources (usually in clathrates) has been considered as one of the alternative sources of energy. In addition to the extraction of methane from natural resources, its proper storage and transportation at operating conditions are the crucial factors for their exploitation in daily use like for vehicular transportation. Previous studies have found that adsorption of methane in porous medium like metal-organic frameworks (MOFs) is one of the proper ways for such a purpose. We have used single metal atoms from 3d series (transition metal atoms) in periodic table as impurity atoms to functionalize monolayer graphene sheet. Our DFT based first-principles calculations have shown that adsorption energy per methane increases remarkably from 0.139 eV in pure graphene to in the order of 0.35 eV - 0.50 eV in the case of metal-adatom graphene (when two methane molecules are adsorbed). The later case lies with in the range of target set by department of energy (DOE), United States (US).

Methane is the simplest alkane molecule and can be considered a model system to study hydrophobicity in biological systems. Methane-methane interactions in different liquid environments represent the role of liquid molecules in the hydrophobicity of hydrophobic particles. We have considered water, methanol and acetonitrile as solvents to study their effect on methane-methane interactions. The classical molecular dynamics simulations at room temperature and atmospheric pressure have been performed to calculate the potential of mean force (PMF) in between two methanes in different solvent environments. These atomistic level of simulations have shown that methane-methane interactions is stiffer and stronger in water comparing to that of methanol and acetonitrile. The screening effect of competitive methyl group has been assumed to be responsible for the weaker and shallower type of interactions in methanol and acetonitrile.

REFERENCES

Abergel, D., Russell, A., & Fal'ko, V. I. (2007). Visibility of graphene flakes on a dielectric substrate. *Applied Physics Letters*, *91*(6), 063125–1–3.

Abkevich, V., Gutin, A., & Shakhnovich, E. (1995). Impact of local and non-local interactions on thermodynamics and kinetics of protein folding. *Journal of Molecular Biology*, *252*(4), 460–471.

Adamo, C., & Barone, V. (1999). Toward reliable density functional methods without adjustable parameters: The PBE0 model. *The Journal of Chemical Physics*, *110*(13), 6158–6170.

Adisa, O. O., Cox, B. J., & Hill, J. M. (2011). Modelling the surface adsorption of methane on carbon nanostructures. *Carbon*, *49*(10), 3212–3218.

Alberts, B., Johnson, A., Lewis, J., Raff, M., Roberts, K., & Walter, P. (2002). Molecular biology of the cell. new york: Garland science; 2002. *Classic textbook now in its 5th Edition*.

Albesa, A. G., Llanos, J. L., & Vicente, J. L. (2008). Comparative study of methane adsorption on graphite. *Langmuir*, *24*(8), 3836–3840.

Alder, B., & Wainwright, T. (1957). Phase transition for a hard sphere system. *The Journal of Chemical Physics*, *27*(5), 1208–1209.

Alibert, Y., Baraffe, I., Benz, W., Chabrier, G., Mordasini, C., Lovis, C., ... others (2006). Formation and structure of the three neptune-mass planets system around HD 69830. *Astronomy & Astrophysics*, *455*(2), L25–L28.

Allen, M. P., & Tildesley, D. J. (1989). *Computer simulation of liquids*. Oxford University press.

Andersen, H. C. (1980). Molecular dynamics simulations at constant pressure and/or temperature. *The Journal of Chemical Physics*, *72*(4), 2384–2393.

Anufrieva, E., Birshtein, T., Nekrasova, T., Ptitsyn, O., & Sheveleva, T. (1967). The models of the denaturation of globular proteins. ii. hydrophobic interactions and conformational transition in polymethacrylic acid. In *Journal of polymer science: Polymer symposia* (Vol. 16, pp. 3519–3531).

Arora, A., & Cameotra, S. S. (2015). Techniques for exploitation of gas hydrate (clathrates) an untapped resource of methane gas. *Journal of Microbial & Biochemical Technology*, *7*(02), 108–111.

Ataca, C., Aktürk, E., Ciraci, S., & Ustunel, H. (2008). High-capacity hydrogen storage by metallized graphene. *Applied Physics Letters*, *93*(4), 043123–1–3.

Bader, R. F. (1990). *Atoms in molecules*. Wiley Online Library.

Balbuena, P., & Seminario, J. M. (1999). *Molecular dynamics: from classical to quantum methods* (Vol. 7). Elsevier.

Barnett, R. N., & Landman, U. (1993). Born-oppenheimer molecular-dynamics simulations of finite systems: Structure and dynamics of $(H_2O)_2$. *Physical Review B*, *48*(4), 2081–2097.

Basu, S., & Bhattacharyya, P. (2012). Recent developments on graphene and graphene oxide based solid state gas sensors. *Sensors and Actuators B: Chemical*, *173*, 1–21.

Becke, A. D. (1988). Density-functional exchange-energy approximation with correct asymptotic behavior. *Physical Review A*, *38*(6), 3098–3100.

Becke, A. D. (1993). A new mixing of Hartree–Fock and local density-functional theories. *The Journal of Chemical Physics*, *98*(2), 1372–1377.

Belosludov, V. R., Inerbaev, T. M., Belosludov, R. V., Kudoh, J.-i., & Kawazoe, Y. (2002). Absolute stability boundaries of clathrate hydrates of cubic structure ii. *Journal of Supramolecular Chemistry*, *2*(4), 377–383.

Benoit, M., Romero, A. H., & Marx, D. (2002). Reassigning hydrogen-bond centering in dense ice. *Physical Review Letters*, *89*(14), 145501–1–4.

Berendsen, H. J., Postma, J. v., van Gunsteren, W. F., DiNola, A., & Haak, J. (1984). Molecular dynamics with coupling to an external bath. *The Journal of Chemical Physics*, *81*(8), 3684–3690.

Bergethon, P. R. (1998). *The physical basis of biochemistry: The foundations of molecular biophysics*. Springer Science & Business Media.

Bhatia, S. K., & Myers, A. L. (2006). Optimum conditions for adsorptive storage. *Langmuir*, *22*(4), 1688–1700.

Black, J., et al. (2010). Cost and performance baseline for fossil energy plants volume 1: bituminous coal and natural gas to electricity. *Final report (2nd ed.) National Energy Technology Laboratory (2010 Nov) Report no.: DOE20101397*.

Booth, J. S., Rowe, M. M., Fischer, K. M., et al. (1996). *Offshore gas hydrate sample database: with an overview and preliminary analysis*. Citeseer.

Bora, P. L., & Singh, A. K. (2013). New insights into designing metallacarborane based room temperature hydrogen storage media. *The Journal of Chemical Physics*, *139*(16), 164319–1–6.

Born, M., & Oppenheimer, R. (1927). Zur quantentheorie der molekeln. *Annalen der Physik*, *389*(20), 457–484.

Brewer, P., Charter, R., Holder, G., Holdtitch, S., Johnson, A., Kastner, M., ... Parrish, W. (2002). *Report of the hydrate advisory committee on methane hydrate issues and opportunities including assessment of uncertainty of the impact of methane hydrate on global climate changes. Report for US congress.*

Brookhart, M., & Green, M. L. (1983). Carbon - hydrogen-transition metal bonds. *Journal of Organometallic Chemistry*, *250*(1), 395–408.

Brookhart, M., Green, M. L., & Parkin, G. (2007). Agostic interactions in transition metal compounds. *Proceedings of the National Academy of Sciences of the United States of America*, *104*(17), 6908–6914.

Brookhart, M., Green, M. L., & Wong, L.-L. (1988). Carbon-hydrogen-transition metal bonds. *Progress in Inorganic Chemistry, Volume 36*, 1–124.

Bull, H. B. (2009). Protein structure. *Advances in Enzymology and Related Areas of Molecular Biology*, *1*, 1–42.

Burchell, T., & Rogers, M. (2000). *Low pressure storage of natural gas for vehicular applications* (Tech. Rep.). SAE Technical Paper.

Cao, C., Wu, M., Jiang, J., & Cheng, H.-P. (2010). Transition metal adatom and dimer adsorbed on graphene: Induced magnetization and electronic structures. *Physical Review B*, *81*(20), 205424–1–9.

Car, R., & Parrinello, M. (1985). Unified approach for molecular dynamics and density-functional theory. *Physical Review Letters*, *55*(22), 2471–2474.

Carrillo, I., Rangel, E., & Magaña, L. (2009). Adsorption of carbon dioxide and methane on graphene with a high titanium coverage. *Carbon*, *47*(11), 2758–2760.

Casco, M. E., Martínez-Escandell, M., Gadea-Ramos, E., Kaneko, K., Silvestre-Albero, J., & Rodríguez-Reinoso, F. (2015). High-pressure methane storage in porous materials: are carbon materials in the pole position? *Chemistry of Materials*, *27*(3), 959–964.

Ceperley, D. M., & Alder, B. (1980). Ground state of the electron gas by a stochastic method. *Physical Review Letters*, *45*(7), 566–569.

Chai, J.-D., & Head-Gordon, M. (2008). Long-range corrected hybrid density functionals with damped atom–atom dispersion corrections. *Physical Chemistry Chemical Physics*, *10*(44), 6615–6620.

Chan, H. S., & Dill, K. A. (1991). Polymer principles in protein structure and stability. *Annual Review of Biophysics and Biophysical Chemistry*, *20*(1), 447–490.

Chan, K. T., Neaton, J., & Cohen, M. L. (2008). First-principles study of metal adatom adsorption on graphene. *Physical Review B*, *77*(23), 235430–1–12.

Chatti, I., Delahaye, A., Fournaison, L., & Petitet, J.-P. (2005). Benefits and drawbacks of clathrate hydrates: a review of their areas of interest. *Energy Conversion and Management*, *46*(9), 1333–1343.

Chen, P., Wu, X., Lin, J., & Tan, K. (1999). High H2 uptake by alkali-doped carbon nanotubes under ambient pressure and moderate temperatures. *Science*, *285*(5424), 91–93.

Chong, Z. R., Yang, S. H. B., Babu, P., Linga, P., & Li, X.-S. (2016). Review of natural gas hydrates as an energy resource: Prospects and challenges. *Applied Energy*, *162*, 1633–1652.

Chou, I.-M., Sharma, A., Burruss, R. C., Shu, J., Mao, H.-k., Hemley, R. J., ... Kirby, S. H. (2000). Transformations in methane hydrates. *Proceedings of the National Academy of Sciences*, *97*(25), 13484–13487.

Chouhan, R. K., Ulman, K., & Narasimhan, S. (2015). Graphene oxide as an optimal candidate material for methane storage. *The Journal of Chemical Physics*, *143*(4), 044704–1–6.

Ci, L., Song, L., Jin, C., Jariwala, D., Wu, D., Li, Y., ... others (2010). Atomic layers of hybridized boron nitride and graphene domains. *Nature Materials*, *9*(5), 430–435.

Cole, L. A., & Perdew, J. (1982). Calculated electron affinities of the elements. *Physical Review A*, *25*(3), 1265–1271.

Crovetto, R., Fernández-Prini, R., & Japas, M. L. (1982). Solubilities of inert gases and methane in h2o and in d2o in the temperature range of 300 to 600 k. *The Journal of Chemical Physics*, *76*(2), 1077–1086.

Dai, L., Chang, D. W., Baek, J.-B., & Lu, W. (2012). Carbon nanomaterials for advanced energy conversion and storage. *Small*, *8*(8), 1130–1166.

Daimaru, T., Yamasaki, A., & Yanagisawa, Y. (2007). Effect of surfactant carbon chain length on hydrate formation kinetics. *Journal of Petroleum Science and Engineering*, *56*(1), 89–96.

Dang, L. X. (1994). Potential of mean force for the methane–methane pair in water. *The Journal of Chemical Physics*, *100*(12), 9032–9034.

Davidson, D., Leaist, D., & Hesse, R. (1983). Oxygen-18 enrichment in the water of a clathrate hydrate. *Geochimica et Cosmochimica Acta*, *47*(12), 2293–2295.

Davy, H. (1811). The bakerian lecture: On some of the combinations of oxymuriatic gas and oxygene, and on the chemical relations of these principles, to inflammable bodies. *Philosophical Transactions of the Royal Society of London*, *101*, 1–35.

Dickens, G. R., O'Neil, J. R., Rea, D. K., & Owen, R. M. (1995). Dissociation of oceanic methane hydrate as a cause of the carbon isotope excursion at the end of the paleocene. *Paleoceanography*, *10*(6), 965–971.

Dill, K. A. (1990). Dominant forces in protein folding. *Biochemistry*, *29*(31), 7133–7155.

Ding, J., Qiao, Z., Feng, W., Yao, Y., & Niu, Q. (2011). Engineering quantum anomalous/valley hall states in graphene via metal-atom adsorption: An ab-initio study. *Physical Review B*, *84*(19), 195444–1–9.

Ding, Y., Hassanali, A. A., & Parrinello, M. (2014). Anomalous water diffusion in salt solutions. *Proceedings of the National Academy of Sciences*, *111*(9), 3310–3315.

Dirac, P. A. (1930). Note on exchange phenomena in the thomas atom. In *Mathematical proceedings of the cambridge philosophical society* (Vol. 26, pp. 376–385).

Djikaev, Y., & Ruckenstein, E. (2016). Recent developments in the theoretical, simulational, and experimental studies of the role of water hydrogen bonding in hydrophobic phenomena. *Advances in Colloid and Interface Science*, *235*, 23–45.

Duffy, D., & Blackman, J. (1998). Magnetism of 3 d transition-metal adatoms and dimers on graphite. *Physical Review B*, *58*(11), 7443–7449.

Düren, T., Sarkisov, L., Yaghi, O. M., & Snurr, R. Q. (2004). Design of new materials for methane storage. *Langmuir*, *20*(7), 2683–2689.

Durgun, E., Dag, S., Ciraci, S., & Gülseren, O. (2004). Energetics and electronic structures of individual atoms adsorbed on carbon nanotubes. *The Journal of Physical Chemistry B*, *108*(2), 575–582.

Dyadin, Y. A., Aladko, E. Y., & Larionov, E. G. (1997). Decomposition of methane hydrates up to 15 kbar. *Mendeleev Communications*, *7*(1), 34–35.

Eddaoudi, M., Kim, J., Rosi, N., Vodak, D., Wachter, J., O'keeffe, M., & Yaghi, O. M. (2002). Systematic design of pore size and functionality in isoreticular mofs and their application in methane storage. *Science*, *295*(5554), 469–472.

Eisenstein, O., & Jean, Y. (1985). Factors favoring an m... hc interaction in metal-methyl complexes. an mo analysis. *Journal of the American Chemical Society*, *107*(5), 1177–1186.

Ercolessi, F. (1997). A molecular dynamics primer. *Spring college in computational physics, ICTP, Trieste*, *19*.

Eslamimanesh, A., Mohammadi, A. H., Richon, D., Naidoo, P., & Ramjugernath, D. (2012). Application of gas hydrate formation in separation processes: a review of experimental studies. *The Journal of Chemical Thermodynamics*, *46*, 62–71.

Esquinazi, P., Spemann, D., Höhne, R., Setzer, A., Han, K.-H., & Butz, T. (2003). Induced magnetic ordering by proton irradiation in graphite. *Physical Review Letters*, *91*(22), 227201–1–4.

Fair, K., Cui, X., Li, L., Shieh, C., Zheng, R., Liu, Z., ... Stampfl, C. (2013). Hydrogen adsorption capacity of adatoms on double carbon vacancies of graphene: a trend study from first principles. *Physical Review B*, *87*(1), 014102–1–7.

Fermi, E. (1928). A statistical method for determining some properties of the atoms and its application to the theory of the periodic table of elements. *Z. Phys*, *48*, 73–79.

Feynman, R. P. (1939). Forces in molecules. *Physical Review*, *56*(4), 340–343.

Fock, V. (1930). Bemerkung zum virialsatz. *Zeitschrift für Physik*, *63*(11-12), 855–858.

Frank, H. S., & Evans, M. W. (1945). Free volume and entropy in condensed systems iii. entropy in binary liquid mixtures; partial molal entropy in dilute solutions; structure and thermodynamics in aqueous electrolytes. *The Journal of Chemical Physics*, *13*(11), 507–532.

Franks, F. (1966). Solute–water interactions and the solubility behaviour of long-chain paraffin hydrocarbons. *Nature*, *210*(5031), 87–88.

Frenkel, D., & Smit, B. (2002). *Understanding molecular simulations: from algorithms to applications* (Tech. Rep.). Academic Press.

Frisch, M., Trucks, G., Schlegel, H. B., Scuseria, G., Robb, M., Cheeseman, J., ... others (2004). Gaussian 03; gaussian, inc. *Wallingford, CT*, *6492*.

Ganji, H., Manteghian, M., Omidkhah, M., Mofrad, H. R., et al. (2007). Effect of different surfactants on methane hydrate formation rate, stability and storage capacity. *Fuel*, *86*(3), 434–441.

Gao, G., Oganov, A. R., Ma, Y., Wang, H., Li, P., Li, Y., ... Zou, G. (2010). Dissociation of methane under high pressure. *The Journal of Chemical Physics*, *133*(14), 144508–1–5.

Geim, A. K. (2009). Graphene: status and prospects. *Science*, *324*(5934), 1530–1534.

Geim, A. K. (2011). Nobel lecture: Random walk to graphene. *Reviews of Modern Physics*, *83*(3), 851–862.

Geim, A. K., & Novoselov, K. S. (2007). The rise of graphene. *Nature Materials*, *6*(3), 183–191.

Gekko, K., Ohmae, E., Kameyama, K., & Takagi, T. (1998). Acetonitrile-protein interactions: amino acid solubility and preferential solvation. *Biochimica et Biophysica Acta (BBA)-Protein Structure and Molecular Enzymology*, *1387*(1), 195–205.

Giannozzi, P., Baroni, S., Bonini, N., Calandra, M., Car, R., Cavazzoni, C., ... others (2009). Quantum espresso: a modular and open-source software project for quantum simulations of materials. *Journal of Physics: Condensed Matter*, *21*(39), 395502–1–19.

Gitlin, I., Carbeck, J. D., & Whitesides, G. M. (2006). Why are proteins charged? networks of charge–charge interactions in proteins measured by charge ladders and capillary electrophoresis. *Angewandte Chemie International Edition*, *45*(19), 3022–3060.

Go, N., & Taketomi, H. (1978). Respective roles of short-and long-range interactions in protein folding. *Proceedings of the National Academy of Sciences*, *75*(2), 559–563.

Go, N., & Taketomi, H. (1979). Studies on protein folding, unfolding and fluctuations by computer simulation iii. effect of short-range interactions. *Chemical Biology & Drug Design*, *13*(3), 235–252.

Godec, A., Smith, J. C., & Merzel, F. (2013). Soft collective fluctuations governing hydrophobic association. *Physical Review Letters*, *111*(12), 127801–1–5.

Goncharov, A., Struzhkin, V., Somayazulu, M., Hemley, R., & Mao, H. (1996). Compression of ice to 210 gigapascals: Infrared evidence for a symmetric hydrogen-bonded phase. *Science*, *273*(5272), 218–220.

Grimme, S. (2004). Accurate description of van der waals complexes by density functional theory including empirical corrections. *Journal of Computational Chemistry*, *25*(12), 1463–1473.

Grimme, S. (2006). Semiempirical gga-type density functional constructed with a long-range dispersion correction. *Journal of Computational Chemistry*, *27*(15), 1787–1799.

Grosso, G., & Parravicini, G. P. (2005). *Solid state physics*. Academic Press.

Guillot, B., & Guissani, Y. (1993). A computer simulation study of the temperature dependence of the hydrophobic hydration. *The Journal of Chemical Physics*, *99*(10), 8075–8094.

Guo, Z., Wu, H., Srinivas, G., Zhou, Y., Xiang, S., Chen, Z., ... Chen, B. (2011). A metal–organic framework with optimized open metal sites and pore spaces for high methane

storage at room temperature. *Angewandte Chemie International Edition*, *50*(14), 3178–3181.

Haile, J. (1992). *Molecular dynamics simulation* (Vol. 18). Wiley, New York.

Hamann, D., Schlüter, M., & Chiang, C. (1979). Norm-conserving pseudopotentials. *Physical Review Letters*, *43*(20), 1494–1497.

Hammerschmidt, E. (1934). Formation of gas hydrates in natural gas transmission lines. *Industrial & Engineering Chemistry*, *26*(8), 851–855.

Han, S.-J., Garcia, A. V., Oida, S., Jenkins, K. A., & Haensch, W. (2014). Graphene radio frequency receiver integrated circuit. *Nature Communications*, *5*, 3086–1–6.

Hansen, J.-P., & McDonald, I. (2006). *Theory of simple liquids*. Academic Press.

Harp, G., & Berne, B. (1970). Time-correlation functions, memory functions, and molecular dynamics. *Physical Review A*, *2*(3), 975–996.

Harp, G., & Berne, B. J. (1968). Linear-and angular-momentum autocorrelation functions in diatomic liquids. *The Journal of Chemical Physics*, *49*(3), 1249–1254.

Hartree, D. R. (1928). The wave mechanics of an atom with a non-coulomb central field. part ii. some results and discussion. In *Mathematical proceedings of the cambridge philosophical society* (Vol. 24, pp. 111–132).

Hassanali, A., Giberti, F., Cuny, J., Kühne, T. D., & Parrinello, M. (2013). Proton transfer through the water gossamer. *Proceedings of the National Academy of Sciences*, *110*(34), 13723–13728.

Hellmann, H. (1939). Einführung in die quantenchemie (deuticke, leipzig, 1937); rp feynman. *Phys. Rev*, *56*(4), 340.

Henkelman, G., Arnaldsson, A., & Jónsson, H. (2006). A fast and robust algorithm for bader decomposition of charge density. *Computational Materials Science*, *36*(3), 354–360.

Hester, R. E., & Harrison, R. M. (2010). *Carbon capture: sequestration and storage* (Vol. 29). Royal Society of Chemistry.

Hill, T. L. (1960). *An introduction to statistical thermodynamics*. Courier Corporation.

Hirai, H., Tanaka, T., Kawamura, T., Yamamoto, Y., & Yagi, T. (2003). Retention of filled ice structure of methane hydrate up to 42 GPa. *Physical Review B*, *68*(17), 172102–1–4.

Hirai, H., Tanaka, T., Kawamura, T., Yamamoto, Y., & Yagi, T. (2004). Structural changes in gas hydrates and existence of a filled ice structure of methane hydrate above 40GPa. *Journal of Physics and Chemistry of Solids*, *65*(8), 1555–1559.

Hirai, H., Uchihara, Y., Fujihisa, H., Sakashita, M., Katoh, E., Aoki, K., ... Yagi, T. (2001). High-pressure structures of methane hydrate observed up to 8 GPa at room temperature. *The Journal of Chemical Physics*, *115*(15), 7066–7070.

Hohenberg, P., & Kohn, W. (1964). Inhomogeneous electron gas. *Physical Review*, *136*(3B), B864–B871.

Hoover, W. G. (1985). Canonical dynamics: equilibrium phase-space distributions. *Physical Review A*, *31*(3), 1695–1697.

Hotta, T., Kimura, A., & Sasai, M. (2005). Fluctuating hydration structure around nanometer-size hydrophobic solutes. i. caging and drying around C60 and C60H60 spheres. *The Journal of Physical Chemistry B*, *109*(39), 18600–18608.

Hu, T., Hashmi, A., & Hong, J. (2014). Transparent half metallic g-C4N3 nanotubes: potential multifunctional applications for spintronics and optical devices. *Scientific Reports*, *4*, 6059–1–7.

Hummer, G., Garde, S., Garcia, A. E., Paulaitis, M. E., & Pratt, L. R. (1998). The pressure dependence of hydrophobic interactions is consistent with the observed pressure denaturation of proteins. *Proceedings of the National Academy of Sciences*, *95*(4), 1552–1555.

Hwang, S., Shao, Q., Williams, H., Hilty, C., & Gao, Y. Q. (2011). Methanol strengthens hydrogen bonds and weakens hydrophobic interactions in proteins–a combined molecular dynamics and nmr study. *The Journal of Physical Chemistry B*, *115*(20), 6653–6660.

Iitaka, T., & Ebisuzaki, T. (2003). Methane hydrate under high pressure. *Physical Review B*, *68*(17), 172105–1–5.

Jeffrey, G. (1996). Hydrate inclusion compounds. *Comprehensive Supramolecular Chemistry*, *6*, 757–788.

Joshi, N., & Ghosh, P. (2013). Substrate-induced changes in the magnetic and electronic properties of hexagonal boron nitride. *Physical Review B*, *87*(23), 235440–1–8.

Kaiser, A., Zöttl, S., Bartl, P., Leidlmair, C., Mauracher, A., Probst, M., ... Scheier, P. (2013). Methane adsorption on aggregates of fullerenes: Site-selective storage capacities and adsorption energies. *ChemSusChem*, *6*(7), 1235–1244.

Kaloni, T., Joshi, R., Adhikari, N., & Schwingenschlögl, U. (2014). Band gap tunning in bn-doped graphene systems with high carrier mobility. *Applied Physics Letters*, *104*(7), 073116–1–5.

Kaloni, T. P., Cheng, Y., & Schwingenschlögl, U. (2012). Fluorinated monovacancies in graphene: Even-odd effect. *EPL (Europhysics Letters)*, *100*(3), 37003–1–6.

Kaloni, T. P., Kahaly, M. U., & Schwingenschlögl, U. (2011). Induced magnetism in transition metal intercalated graphitic systems. *Journal of Materials Chemistry*, *21*(46), 18681–18685.

Kammeyer, C. W., & Whitman, D. R. (1972). Quantum mechanical calculation of molecular radii. i. hydrides of elements of periodic groups iv through vii. *The Journal of Chemical Physics*, *56*(9), 4419–4421.

Kandagal, V. S., Pathak, A., Ayappa, K., & Punnathanam, S. N. (2012). Adsorption on edge-functionalized bilayer graphene nanoribbons: assessing the role of functional groups in methane uptake. *The Journal of Physical Chemistry C*, *116*(44), 23394–23403.

Kang, S.-P., & Lee, H. (2000). Recovery of CO_2 from flue gas using gas hydrate: thermodynamic verification through phase equilibrium measurements. *Environmental Science & Technology*, *34*(20), 4397–4400.

Kästner, J. (2011). Umbrella sampling. *Wiley Interdisciplinary Reviews: Computational Molecular Science*, *1*(6), 932–942.

Katz, D. L., et al. (1945). Prediction of conditions for hydrate formation in natural gases. *Transactions of the AIME*, *160*(01), 140–149.

Kauzmann, W. (1959). Some factors in the interpretation of protein denaturation. *Advances in Protein Chemistry*, *14*, 1–63.

Kittel, C. (2005). *Introduction to solid state physics*. John Wiley & Sons.

Klimeš, J., & Michaelides, A. (2012). Perspective: Advances and challenges in treating van der waals dispersion forces in density functional theory. *The Journal of Chemical Physics*, *137*(12), 120901–1–12.

Koch, U., & Popelier, P. (1995). Characterization of cho hydrogen bonds on the basis of the charge density. *The Journal of Physical Chemistry*, *99*(24), 9747–9754.

Koh, C. A., Savidge, J. L., & Tang, C. C. (1996). Time-resolved in-situ experiments on the crystallization of natural gas hydrates. *The Journal of Physical Chemistry*, *100*(16), 6412–6414.

Kohn, W., & Sham, L. J. (1965). Self-consistent equations including exchange and correlation effects. *Physical Review*, *140*(4A), A1133–A1138.

Kremer, K. (2003). Computer simulations for macromolecular science. *Macromolecular Chemistry and Physics*, *204*(2), 257–264.

Kroto, H. W., Heath, J. R., O'Brien, S. C., Curl, R. F., Smalley, R. E., et al. (1985). C 60: buckminsterfullerene. *Nature*, *318*(6042), 162–163.

Kubas, G. J., Ryan, R., Swanson, B., Vergamini, P., & Wasserman, H. (1984). Characterization of the first examples of isolable molecular hydrogen complexes, M(CO)3(PR3)2(H2)(M= molybdenum or tungsten; R= Cy or isopropyl). evidence for a side-on bonded dihydrogen ligand. *Journal of the American Chemical Society*, *106*(2), 451–452.

Kuhs, W., Chazallon, B., Radaelli, P., & Pauer, F. (1997). Cage occupancy and compressibility of deuterated n2-clathrate hydrate by neutron diffraction. *Journal of Inclusion Phenomena and Molecular Recognition in Chemistry*, *29*(1), 65–77.

Kumar, S., Rosenberg, J. M., Bouzida, D., Swendsen, R. H., & Kollman, P. A. (1992). The weighted histogram analysis method for free-energy calculations on biomolecules. i. the method. *Journal of Computational Chemistry*, *13*(8), 1011–1021.

Kvenvolden, K. A. (1988). Methane hydrate—a major reservoir of carbon in the shallow geosphere? *Chemical Geology*, *71*(1-3), 41–51.

Kvenvolden, K. A. (1993). Gas hydrates-geological perspective and global change. *Reviews of Geophysics*, *31*, 173–189.

Lamichhane, S., Lage, P., Khatri, G., Pantha, N., Adhikari, N., & Sanyal, B. (2016). First-principles study of adsorption of halogen molecules on graphene-MoS2 bilayer hetero-system. In *Journal of physics: Conference series* (Vol. 765, pp. 012011–1–10).

Lamichhane, S., Pantha, N., & Adhikari, N. (2014). Hydrogen storage on platinum decorated graphene: a first-principles study. *Bibechana*, *11*, 113–122.

Langmuir, I. (1917). The constitution and fundamental properties of solids and liquids. ii. liquids. 1. *Journal of the American Chemical Society*, *39*(9), 1848–1906.

Lazaridis, T., & Karplus, M. (2000). Effective energy functions for protein structure prediction. *Current Opinion in Structural Biology*, *10*(2), 139–145.

Leach, A. R. (2001). *Molecular modelling: principles and applications*. Pearson education.

Lee, B. (1985). The physical origin of the low solubility of nonpolar solutes in water. *Biopolymers*, *24*(5), 813–823.

Lee, C., & Scott, H. (1980). The surface tension of water: A monte carlo calculation using an umbrella sampling algorithm. *The Journal of Chemical Physics*, *73*(9), 4591–4596.

Lee, C., Yang, W., & Parr, R. G. (1988). Development of the colle-salvetti correlation-energy formula into a functional of the electron density. *Physical Review B*, *37*(2), 785–789.

Lee, J. Y., Ryu, B. J., Yun, T. S., Lee, J., & Cho, G.-C. (2011). Review on the gas hydrate development and production as a new energy resource. *KSCE Journal of Civil Engineering*, *15*(4), 689–696.

Lein, M. (2009). Characterization of agostic interactions in theory and computation. *Coordination Chemistry Reviews*, *253*(5), 625–634.

Levine, I. N., Busch, D. H., & Shull, H. (2009). *Quantum chemistry* (Vol. 6). Pearson Prentice Hall Upper Saddle River, NJ.

Li, J.-L., Car, R., Tang, C., & Wingreen, N. S. (2007). Hydrophobic interaction and hydrogen-bond network for a methane pair in liquid water. *Proceedings of the National Academy of Sciences*, *104*(8), 2626–2630.

Li, X., Wang, X., Zhang, L., Lee, S., & Dai, H. (2008). Chemically derived, ultrasmooth graphene nanoribbon semiconductors. *Science*, *319*(5867), 1229–1232.

Lindahl, E., Hess, A., Buuren, R. v., Apol, E., Meulenhoff, P., Tieleman, D., ... Berendsen, H. (2010). Gromacs user manual, version 4.5. 6., 2010.

Liu, X., Wang, C., Yao, Y., Lu, W., Hupalo, M., Tringides, M., & Ho, K. (2011). Bonding and charge transfer by metal adatom adsorption on graphene. *Physical Review B*, *83*(23), 235411–1–12.

Liu, X., Wang, C.-Z., Hupalo, M., Lin, H.-Q., Ho, K.-M., & Tringides, M. C. (2013). Metals on graphene: interactions, growth morphology, and thermal stability. *Crystals*, *3*(1), 79–111.

Liu, X., Wang, C.-Z., Hupalo, M., Lu, W., Tringides, M. C., Yao, Y., & Ho, K.-M. (2012). Metals on graphene: correlation between adatom adsorption behavior and growth morphology. *Physical Chemistry Chemical Physics*, *14*(25), 9157–9166.

Longo, R., Carrete, J., & Gallego, L. (2011). Ab initio study of 3 d, 4 d, and 5 d transition metal adatoms and dimers adsorbed on hydrogen-passivated zigzag graphene nanoribbons. *Physical Review B*, *83*(23), 235415–1–9.

Loubeyre, P., LeToullec, R., Wolanin, E., Hanfland, M., & Hausermann, D. (1999). Modulated phases and proton centring in ice observed by x-ray diffraction up to 170 GPa. *Nature*, *397*(6719), 503–506.

Loucks, T., & Slater, J. C. (1967). Augmented plane wave method: a guide to performing electronic structure calculations. *Physics Today*, *20*(11), 92–93.

Loveday, J., & Nelmes, R. (2008). High-pressure gas hydrates. *Physical Chemistry Chemical Physics*, *10*(7), 937–950.

Loveday, J., Nelmes, R., Guthrie, M., Belmonte, S., Allan, D., Klug, D., ... Handa, Y. (2001). Stable methane hydrate above 2 GPa and the source of titan's atmospheric methane. *Nature*, *410*(6829), 661–663.

Loveday, J., Nelmes, R., Guthrie, M., Klug, D., & Tse, J. (2001). Transition from cage clathrate to filled ice: the structure of methane hydrate iii. *Physical Review Letters*, *87*(21), 215501–1–4.

Lozano-Castello, D., Alcaniz-Monge, J., De la Casa-Lillo, M., Cazorla-Amorós, D., & Linares-Solano, A. (2002). Advances in the study of methane storage in porous carbonaceous materials. *Fuel*, *81*(14), 1777–1803.

Lucas, M. (1976). Size effect in transfer of nonpolar solutes from gas or solvent to another solvent with a view on hydrophobic behavior. *The Journal of Physical Chemistry*, *80*(4), 359–362.

Ma, S., Sun, D., Simmons, J. M., Collier, C. D., Yuan, D., & Zhou, H.-C. (2008). Metal-organic framework from an anthracene derivative containing nanoscopic cages exhibiting high methane uptake. *Journal of the American Chemical Society*, *130*(3), 1012–1016.

Ma, S., & Zhou, H.-C. (2010). Gas storage in porous metal–organic frameworks for clean energy applications. *Chemical Communications*, *46*(1), 44–53.

Machida, S.-i., Hirai, H., Kawamura, T., Yamamoto, Y., & Yagi, T. (2006). A new high-pressure structure of methane hydrate surviving to 86gpa and its implications for the interiors of giant icy planets. *Physics of the Earth and Planetary Interiors*, *155*(1), 170–176.

Machida, S.-I., Hirai, H., Kawamura, T., Yamamoto, Y., & Yagi, T. (2007). Raman spectra of methane hydrate up to 86 gpa. *Physics and Chemistry of Minerals*, *34*(1), 31–35.

Mahajan, D., & Mansoori, G. A. (2007). An introduction to natural gas hydrate/clathrate: The major organic carbon reserve of the earth. *Journal of Petroleum Science and Engineering*, *56*(1), 1–8.

Mak, T. C., & McMullan, R. K. (1965). Polyhedral clathrate hydrates. X. structure of the double hydrate of tetrahydrofuran and hydrogen sulfide. *The Journal of Chemical Physics*, *42*(8), 2732–2737.

Makal, T. A., Li, J.-R., Lu, W., & Zhou, H.-C. (2012). Methane storage in advanced porous materials. *Chemical Society Reviews*, *41*(23), 7761–7779.

Makogon, Y., Holditch, S., & Makogon, T. (2007). Natural gas-hydrates—a potential energy source for the 21st century. *Journal of Petroleum Science and Engineering*, *56*(1), 14–31.

Makowski, M., Czaplewski, C., Liwo, A., & Scheraga, H. A. (2009). Potential of mean force of association of large hydrophobic particles: Toward the nanoscale limit. *The Journal of Physical Chemistry B*, *114*(2), 993–1003.

Man-Chao, H., & Jian, Z. (2013). Methane adsorption on graphite (0001) films: A first-principles study. *Chinese Physics B*, *22*(1), 016802–1–5.

Marenich, A. V., Cramer, C. J., & Truhlar, D. G. (2009). Universal solvation model based on solute electron density and on a continuum model of the solvent defined by the bulk dielectric constant and atomic surface tensions. *The Journal of Physical Chemistry B*, *113*(18), 6378–6396.

Martin, R. M. (2004). *Electronic structure: basic theory and practical methods*. Cambridge university press.

Marx, D., & Hutter, J. (2009). *Ab initio molecular dynamics.* Cambridge University Press,.

Mason, J. A., Oktawiec, J., Taylor, M. K., Hudson, M. R., Rodriguez, J., Bachman, J. E., ... others (2015). Methane storage in flexible metal–organic frameworks with intrinsic thermal management. *Nature*, *527*(7578), 357–361.

McAuliffe, C. (1963). Solubility in water of C1–C9 hydrocarbons. *Nature*, *200*(4911), 1092–1093.

McClure, J. (1957). Band structure of graphite and de haas-van alphen effect. *Physical Review*, *108*(3), 612–618.

McClure, J. (1958). Analysis of multicarrier galvanomagnetic data for graphite. *Physical Review*, *112*(3), 715–721.

McMullan, R. K., & Jeffrey, G. (1965). Polyhedral clathrate hydrates. ix. structure of ethylene oxide hydrate. *The Journal of Chemical Physics*, *42*(8), 2725–2732.

McNaught, A., & Wilkinson, A. (1997). *Compendium of chemical terminology, the gold book, 2. izdanje.* Blackwell Science, New York.

Melchionna, S., Ciccotti, G., & Lee Holian, B. (1993). Hoover npt dynamics for systems varying in shape and size. *Molecular Physics*, *78*(3), 533–544.

Menon, V., & Komarneni, S. (1998). Porous adsorbents for vehicular natural gas storage: a review. *Journal of Porous Materials*, *5*(1), 43–58.

Mukherjee, S., & Kaloni, T. (2012). Electronic properties of boron-and nitrogen-doped graphene: a first principles study. *Journal of Nanoparticle Research*, *14*(8), 1059–1–5.

Nakanishi, E., & Reid, R. C. (1971). Liquid natural gas-water reactions. *Chemical Engineering Progress*, *67*(12).

Nerheim, A. R., Svartaas, T. M., Samuelsen, E. J., et al. (1994). Laser light scattering studies of gas hydrate formation kinetics. In *The fourth international offshore and polar engineering conference.*

Neto, A. C., Guinea, F., Peres, N. M., Novoselov, K. S., & Geim, A. K. (2009). The electronic properties of graphene. *Reviews of Modern Physics*, *81*(1), 109–162.

Norrby, E. (2010). *Nobel prizes and life sciences*. World Scientific.

Nosé, S. (1984). A molecular dynamics method for simulations in the canonical ensemble. *Molecular Physics*, *52*(2), 255–268.

Novoselov, K. S., Geim, A. K., Morozov, S., Jiang, D., Katsnelson, M., Grigorieva, I., ... Firsov, A. (2005). Two-dimensional gas of massless dirac fermions in graphene. *Nature*, *438*(7065), 197–200.

Novoselov, K. S., Geim, A. K., Morozov, S. V., Jiang, D., Zhang, Y., Dubonos, S. V., ... Firsov, A. A. (2004). Electric field effect in atomically thin carbon films. *Science*, *306*(5696), 666–669.

O'Brien, E. P., Dima, R. I., Brooks, B., & Thirumalai, D. (2007). Interactions between hydrophobic and ionic solutes in aqueous guanidinium chloride and urea solutions: lessons for protein denaturation mechanism. *Journal of the American Chemical Society*, *129*(23), 7346–7353.

Orimo, S.-i., Nakamori, Y., Eliseo, J. R., Züttel, A., & Jensen, C. M. (2007). Complex hydrides for hydrogen storage. *Chemical Reviews*, *107*(10), 4111–4132.

Pakin, S., & Lang, M. (2013). Energy modeling of supercomputers and large-scale scientific applications. In *Green computing conference (IGCC), 2013 international* (pp. 1–6).

Palacios, J., Fernández-Rossier, J., & Brey, L. (2008). Vacancy-induced magnetism in graphene and graphene ribbons. *Physical Review B*, *77*(19), 195428–1–16.

Pantha, N., Acharya, J., & Adhikari, N. P. (2014). First-principles study of solid methane at high pressure. *Bibechana*, *12*, 70–79.

Pantha, N., & Adhikari, N. P. (2015). Structure and symmetrization of hydrogen bonding in ices viii and x at high pressure: A density functional theory approach. *Journal of Institute of Science and Technology*, *19*(2), 14–18.

Pantha, N., Adhikari, N. P., & Scandolo, S. (2015). Decomposition of methane hydrates at high pressure: a density-fuctional theory study. *High Pressure Research*, *35*(3), 231–238.

Pantha, N., Belbase, K., & Adhikari, N. P. (2015). First-principles study of the interaction of hydrogen molecular on na-adsorbed graphene. *Applied Nanoscience*, *5*(4), 393–402.

Pantha, N., Khaniya, A., & Adhikari, N. P. (2015). Hydrogen storage on palladium adsorbed graphene: A density functional theory study. *International Journal of Modern Physics B*, *29*(20), 1550143–1–14.

Parac, M., Etinski, M., Peric, M., & Grimme, S. (2005). A theoretical investigation of the geometries and binding energies of molecular tweezer and clip host- guest systems. *Journal of Chemical Theory and Computation*, *1*(6), 1110–1118.

Park, C.-H., & Louie, S. G. (2010). Tunable excitons in biased bilayer graphene. *Nano Letters*, *10*(2), 426–431.

Parker, F. S. (1963). Attenuated total reflectance spectra of glycyl-l-alanine in aqueous solutions. *Nature*, *200*(4911), 1093–1094.

Parr, R. G., & Weitao, Y. (1994). *Density-functional theory of atoms and molecules* (Vol. 16). Oxford university press.

Parrinello, M., & Rahman, A. (1981). Polymorphic transitions in single crystals: A new molecular dynamics method. *Journal of Applied Physics*, *52*(12), 7182–7190.

Parry, M., Canziani, O. F., Palutikof, J. P., van der Linden, P. J., Hanson, C. E., et al. (2007). *Climate change 2007: impacts, adaptation and vulnerability* (Vol. 4). Cambridge University Press Cambridge.

Pathria, R. (1996). *Slarislical mechanics.* Pergamon, Oxford.

Paudel, B. P., Pantha, N., & Adhikari, N. P. (2016). First-principles study of electronic and magnetic properties of manganese decorated graphene. *Journal of Nepal Physical Society*, *3*(1), 24–34.

Paudyal, H., Pantha, N., & Adhikari, N. P. (2015). First-principles study of a molecular adsorption of fluorine on monolayer MoS2. *Bibechana*, *13*, 50–59.

Pauling, L. (1960). *The nature of the chemical bond and the structure of molecules and crystals: an introduction to modern structural chemistry* (Vol. 18). Cornell university press.

Perdew, J. P. (1986). Density-functional approximation for the correlation energy of the inhomogeneous electron gas. *Physical Review B*, *33*(12), 8822–8824.

Perdew, J. P., Burke, K., & Ernzerhof, M. (1996). Generalized gradient approximation made simple. *Physical Review Letters*, *77*(18), 3865–3868.

Perdew, J. P., & Wang, Y. (1992). Accurate and simple analytic representation of the electron-gas correlation energy. *Physical Review B*, *45*(23), 13244–13249.

Perdew, J. P., & Zunger, A. (1981). Self-interaction correction to density-functional approximations for many-electron systems. *Physical Review B*, *23*(10), 5048–5079.

Petrenko, V. F., & Whitworth, R. W. (1999). *Physics of ice*. OUP Oxford.

Petroski, H. (1992). *The pencil: A history of design and circumstance*. Alfred a Knopf Incorporated.

Piacenza, M., & Grimme, S. (2005). Van der waals interactions in aromatic systems: structure and energetics of dimers and trimers of pyridine. *ChemPhysChem*, *6*(8), 1554–1558.

Pokharel, S., Pantha, N., & Adhikari, N. (2016). Diffusion coefficients of nitric oxide in water: A molecular dynamics study. *International Journal of Modern Physics B*, *30*(27), 1650205–1–20.

Popelier, P., & Logothetis, G. (1998). Characterization of an agostic bond on the basis of the electron density. *Journal of Organometallic Chemistry*, *555*(1), 101–111.

Poudyal, I., & Adhikari, N. P. (2014). Temperature dependence of diffusion coefficient of carbon monoxide in water: A molecular dynamics study. *Journal of Molecular Liquids*, *194*, 77–84.

Pratt, L. R., & Chandler, D. (1980). Effects of solute–solvent attractive forces on hydrophobic correlations. *The Journal of Chemical Physics*, *73*(7), 3434–3441.

Privalov, P. L., & Gill, S. J. (1988). Stability of protein structure and hydrophobic interaction. *Advances in Protein Chemistry*, *39*, 191–234.

Pumera, M. (2011). Graphene-based nanomaterials for energy storage. *Energy & Environmental Science*, *4*(3), 668–674.

Rackley, S. (2009). *Carbon capture and storage*. Gulf Professional Publishing.

Radosavljević, M., Appenzeller, J., Avouris, P., & Knoch, J. (2004). High performance of potassium n-doped carbon nanotube field-effect transistors. *Applied Physics Letters*, *84*(18), 3693–3695.

Rahman, A. (1964). Correlations in the motion of atoms in liquid argon. *Physical Review*, *136*(2A), A405–A411.

Ramos-Castillo, C., Reveles, J., Zope, R., & De Coss, R. (2015). Palladium clusters supported on graphene monovacancies for hydrogen storage. *The Journal of Physical Chemistry C*, *119*(15), 8402–8409.

Rao, C., Gopalakrishnan, K., & Maitra, U. (2015). Comparative study of potential applications of graphene, mos2, and other two-dimensional materials in energy devices, sensors, and related areas. *ACS Applied Materials & Interfaces*, *7*(15), 7809–7832.

Rao, C., Sood, A., Subrahmanyam, K., & Govindaraj, A. (2009). Graphene: the new two-dimensional nanomaterial. *Angewandte Chemie International Edition*, *48*(42), 7752–7777.

Rapoport, D. (1997). *The art of molecular dynamics simulations.* New York: Cambridge University Press.

Raschke, T. M., Tsai, J., & Levitt, M. (2001). Quantification of the hydrophobic interaction by simulations of the aggregation of small hydrophobic solutes in water. *Proceedings of the National Academy of Sciences*, *98*(11), 5965–5969.

Restrepo, O. D., Krymowski, K. E., Goldberger, J., & Windl, W. (2014). A first principles method to simulate electron mobilities in 2d materials. *New Journal of Physics*, *16*(10), 105009–1–12.

Reynolds, J. A., Gilbert, D. B., & Tanford, C. (1974). Empirical correlation between hydrophobic free energy and aqueous cavity surface area. *Proceedings of the National Academy of Sciences*, *71*(8), 2925–2927.

Ricca, A., & Bauschlicher, C. W. (2006). The physisorption of ch 4 on graphite and on a (9, 0) carbon nanotube. *Chemical Physics*, *324*(2), 455–458.

Ripmeester, J. A., John, S. T., Ratcliffe, C. I., & Powell, B. M. (1987). A new clathrate hydrate structure. *Nature*, *325*(6100), 135–136.

Rogers, R., Zhang, G., Dearman, J., & Woods, C. (2007). Investigations into surfactant/gas hydrate relationship. *Journal of Petroleum Science and Engineering*, *56*(1), 82–88.

Rydberg, H., Dion, M., Jacobson, N., Schröder, E., Hyldgaard, P., Simak, S., ... Lundqvist, B. I. (2003). Van der waals density functional for layered structures. *Physical Review Letters*, *91*(12), 126402–1–4.

Saha, S. K., Chandrakanth, R. C., Krishnamurthy, H., & Waghmare, U. (2009). Mechanisms of molecular doping of graphene: A first-principles study. *Physical Review B*, *80*(15), 155414–1–6.

Sanchez-Portal, D., Artacho, E., & Soler, J. M. (1995). Projection of plane-wave calculations into atomic orbitals. *Solid State Communications*, *95*(10), 685–690.

Santra, B., Klimeš, J., Alfè, D., Tkatchenko, A., Slater, B., Michaelides, A., ... Scheffler, M. (2011). Hydrogen bonds and van der waals forces in ice at ambient and high pressures. *Physical Review Letters*, *107*(18), 185701–1–5.

Scandolo, S., Giannozzi, P., Cavazzoni, C., de Gironcoli, S., Pasquarello, A., & Baroni, S. (2005). First-principles codes for computational crystallography in the quantum-espresso package. *Zeitschrift für Kristallographie-Crystalline Materials*, *220*(5/6), 574–579.

Schedin, F., Geim, A., Morozov, S., Hill, E., Blake, P., Katsnelson, M., & Novoselov, K. (2007). Detection of individual gas molecules adsorbed on graphene. *Nature Materials*, *6*(9), 652–655.

Scheraga, H. A. (1998). Theory of hydrophobic interactions. *Journal of Biomolecular Structure and Dynamics*, *16*(2), 447–460.

Scherer, W., & McGrady, G. S. (2004). Agostic interactions in d0 metal alkyl complexes. *Angewandte Chemie International Edition*, *43*(14), 1782–1806.

Scott, R., & Hildebrand, R. (1950). The solubility of nonelectrolytes. *New York, Reinhold Publish-ing Corp*, *374*.

Sharp, K. A., Nicholls, A., Friedman, R., & Honig, B. (1991). Extracting hydrophobic free energies from experimental data: relationship to protein folding and theoretical models. *Biochemistry*, *30*(40), 9686–9697.

Shimizu, H., Kumazaki, T., Kume, T., & Sasaki, S. (2002). In situ observations of high-pressure phase transformations in a synthetic methane hydrate. *The Journal of Physical Chemistry B*, *106*(1), 30–33.

Shing, K., & Gubbins, K. (1981). The chemical potential from computer simulation: Test particle method with umbrella sampling. *Molecular Physics*, *43*(3), 717–721.

Shu, J., Chen, X., Chou, I.-M., Yang, W., Hu, J., Hemley, R. J., & Mao, H.-k. (2011). Structural stability of methane hydrate at high pressures. *Geoscience Frontiers*, *2*(1), 93–100.

Simpson, L., & Director, H. (2009). US department of energy office of energy efficiency and renewable energy fuel cell technologies program hydrogen sorption center of excellence (HSCoE) materials go/no-go recommendation document.

Singh, A. K., Sadrzadeh, A., & Yakobson, B. I. (2010). Metallacarboranes: toward promising hydrogen storage metal organic frameworks. *Journal of the American Chemical Society*, *132*(40), 14126–14129.

Singh, N., Kaloni, T. P., & Schwingenschlögl, U. (2013). A first-principles investigation of the optical spectra of oxidized graphene. *Applied Physics Letters*, *102*(2), 023101–1–4.

Slater, J. (1937). Wave functions in a periodic potential. *Physical Review*, *51*(10), 846–851.

Sloan, E. D. (2003). Clathrate hydrate measurements: microscopic, mesoscopic, and macroscopic. *The Journal of Chemical Thermodynamics*, *35*(1), 41–53.

Sloan, E. D. (2004). Introductory overview: Hydrate knowledge development. *American Mineralogist*, *89*(8-9), 1155–1161.

Sloan, E. D., Subramanian, S., Matthews, P., Lederhos, J., & Khokhar, A. (1998). Quantifying hydrate formation and kinetic inhibition. *Industrial & engineering chemistry research*, *37*(8), 3124–3132.

Sloan Jr, E. D., & Koh, C. (2007). *Clathrate hydrates of natural gases*. CRC press.

Slonczewski, J., & Weiss, P. (1958). Band structure of graphite. *Physical Review*, *109*(2), 272–279.

Sobolewski, E., Makowski, M., Czaplewski, C., Liwo, A., Oℓdziej, S., & Scheraga, H. A. (2007). Potential of mean force of hydrophobic association: dependence on solute size. *The Journal of Physical Chemistry B*, *111*(36), 10765–10774.

Soler, J. M., Artacho, E., Gale, J. D., García, A., Junquera, J., Ordejón, P., & Sánchez-Portal, D. (2002). The SIESTA method for ab initio order-N materials simulation. *Journal of Physics: Condensed Matter*, *14*(11), 2745–2779.

Southall, N. T., Dill, K. A., & Haymet, A. (2002). *A view of the hydrophobic effect.* ACS Publications.

Stackelberg, M. v., & Müller, H. (1951). On the structure of gas hydrates. *The Journal of Chemical Physics*, *19*(10), 1319–1320.

Staykova, D. K., Kuhs, W. F., Salamatin, A. N., & Hansen, T. (2003). Formation of porous gas hydrates from ice powders: Diffraction experiments and multistage model. *The Journal of Physical Chemistry B*, *107*(37), 10299–10311.

Stokes, H. T., & Hatch, D. M. (2005). Findsym: program for identifying the space-group symmetry of a crystal. *Journal of Applied Crystallography*, *38*(1), 237–238.

Stone, A. (1996). *The theory of intermolecular forces*.

Sugimura, E., Iitaka, T., Hirose, K., Kawamura, K., Sata, N., & Ohishi, Y. (2008). Compression of H2O ice to 126 GPa and implications for hydrogen-bond symmetrization: Synchrotron x-ray diffraction measurements and density-functional calculations. *Physical Review B*, *77*(21), 214103–1–6.

Sum, A. K., Burruss, R. C., & Sloan, E. D. (1997). Measurement of clathrate hydrates via raman spectroscopy. *The Journal of Physical Chemistry B*, *101*(38), 7371–7377.

Sun, L., Yi, W., Wang, L., Shu, J., Sinogeikin, S., Meng, Y., ... others (2009). X-ray diffraction studies and equation of state of methane at 202GPa. *Chemical Physics Letters*, *473*(1), 72–74.

Tanaka, T., Hirai, H., Matsuoka, T., Ohishi, Y., Yagi, T., Ohtake, M., ... Irifune, T. (2013). Phase changes of filled ice ih methane hydrate under low temperature and high pressure. *The Journal of Chemical Physics*, *139*(10), 104701–1–8.

Tanford, C. (1997). How protein chemists learned about the hydrophobic factor. *Protein science*, *6*(6), 1358–1366.

Tanford, C. (2004). *Ben franklin stilled the waves: An informal history of pouring oil on water with reflections on the ups and downs of scientific life in general*. OUP Oxford.

Tanford, C., et al. (1961). *Physical chemistry of macromolecules*. Wiley.

Tang, W., Sanville, E., & Henkelman, G. (2009). A grid-based bader analysis algorithm without lattice bias. *Journal of Physics: Condensed Matter*, *21*(8), 084204–1–7.

Thapa, R., Sen, D., Mitra, M., & Chattopadhyay, K. (2011). Palladium atoms and its dimers adsorbed on graphene: first-principles study. *Physica B: Condensed Matter*, *406*(3), 368–373.

Thapa, S., & Adhikari, N. (2013). a molecular dynamics study of oxygen gas in water at different temperatures. *International Journal of Modern Physics B*, *27*(08), 1350023–1–18.

Thierfelder, C., Witte, M., Blankenburg, S., Rauls, E., & Schmidt, W. (2011). Methane adsorption on graphene from first principles including dispersion interaction. *Surface Science*, *605*(7), 746–749.

Thomas, L. H. (1927). The calculation of atomic fields. In *Mathematical proceedings of the cambridge philosophical society* (Vol. 23, pp. 542–548).

Thomas, S., & Dawe, R. A. (2003). Review of ways to transport natural gas energy from countries which do not need the gas for domestic use. *Energy*, *28*(14), 1461–1477.

Torrie, G., & Valleau, J. (1977). Monte carlo study of a phase-separating liquid mixture by umbrella sampling. *The Journal of Chemical Physics*, *66*(4), 1402–1408.

Torrie, G. M., & Valleau, J. P. (1977). Nonphysical sampling distributions in monte carlo free-energy estimation: Umbrella sampling. *Journal of Computational Physics*, *23*(2), 187–199.

Tsuzuki, S., Uchimaru, T., & Tanabe, K. (1998). Intermolecular interaction potentials of methane and ethylene dimers calculated with the møller–plesset, coupled cluster and density functional methods. *Chemical Physics Letters*, *287*(1), 202–208.

Tulk, C. A., Klug, D. D., dos Santos, A. M., Karotis, G., Guthrie, M., Molaison, J. J., & Pradhan, N. (2012). Cage occupancies in the high pressure structure h methane hydrate: A neutron diffraction study. *The Journal of Chemical Physics*, *136*(5), 054502–1–6.

Udachin, K. A., Ratcliffe, C. I., & Ripmeester, J. A. (2001). Structure, composition, and thermal expansion of co2 hydrate from single crystal x-ray diffraction measurements. *The Journal of Physical Chemistry B*, *105*(19), 4200–4204.

Ugeda, M. M., Brihuega, I., Guinea, F., & Gómez-Rodríguez, J. M. (2010). Missing atom as a source of carbon magnetism. *Physical Review Letters*, *104*(9), 096804–1–4.

Ulman, K., Bhaumik, D., Wood, B. C., & Narasimhan, S. (2014). Physical origins of weak h2 binding on carbon nanostructures: Insight from ab initio studies of chemically

functionalized graphene nanoribbons. *The Journal of Chemical Physics*, *140*(17), 174708–1–12.

Valencia, H., Gil, A., & Frapper, G. (2010). Trends in the adsorption of 3d transition metal atoms onto graphene and nanotube surfaces: a dft study and molecular orbital analysis. *The Journal of Physical Chemistry C*, *114*(33), 14141–14153.

Valencia, H., Gil, A., & Frapper, G. (2015). Trends in the hydrogen activation and storage by adsorbed 3d transition metal atoms onto graphene and nanotube surfaces: A dft study and molecular orbital analysis. *The Journal of Physical Chemistry C*, *119*(10), 5506–5522.

Vanderbilt, D. (1990). Soft self-consistent pseudopotentials in a generalized eigenvalue formalism. *Physical Review B*, *41*(11), 7892–7895.

Vidal, I., Melchor, S., Alkorta, I., Elguero, J., Sundberg, M. R., & Dobado, J. A. (2006). On the existence of α-agostic bonds: bonding analyses of titanium alkyl complexes. *Organometallics*, *25*(23), 5638–5647.

Vidali, G., Ihm, G., Kim, H.-Y., & Cole, M. W. (1991). Potentials of physical adsorption. *Surface Science Reports*, *12*(4), 135–181.

Vosko, S. H., Wilk, L., & Nusair, M. (1980). Accurate spin-dependent electron liquid correlation energies for local spin density calculations: a critical analysis. *Canadian Journal of Physics*, *58*(8), 1200–1211.

Wallace, P. R. (1947). The band theory of graphite. *Physical Review*, *71*(9), 622–634.

Wilcox, W. I., Carson, D., & Katz, D. (1941). Natural gas hydrates. *Industrial & Engineering Chemistry*, *33*(5), 662–665.

Wolanin, E., Pruzan, P., Chervin, J., Canny, B., Gauthier, M., Häusermann, D., & Hanfland, M. (1997). Equation of state of ice vii up to 106 gpa. *Physical Review B*, *56*(10), 5781–5785.

Wood, B. C., Bhide, S. Y., Dutta, D., Kandagal, V. S., Pathak, A. D., Punnathanam, S. N., ... Narasimhan, S. (2012). Methane and carbon dioxide adsorption on edge-functionalized graphene: a comparative dft study. *The Journal of Chemical Physics*, *137*(5), 054702–1–11.

Wu, H., Zhou, W., & Yildirim, T. (2009). High-capacity methane storage in metal- organic frameworks m2 (dhtp): the important role of open metal sites. *Journal of the American Chemical Society*, *131*(13), 4995–5000.

Wu, J., & Prausnitz, J. M. (2008). Pairwise-additive hydrophobic effect for alkanes in water. *Proceedings of the National Academy of Sciences*, *105*(28), 9512–9515.

Wu, M., Liu, E.-Z., Ge, M., & Jiang, J. (2009). Stability, electronic, and magnetic behaviors of cu adsorbed graphene: A first-principles study. *Applied Physics Letters*, *94*(10), 102505–1–3.

Yagi, Y., Briere, T. M., Sluiter, M. H., Kumar, V., Farajian, A. A., & Kawazoe, Y. (2004). Stable geometries and magnetic properties of single-walled carbon nanotubes doped with 3 d transition metals: A first-principles study. *Physical Review B*, *69*(7), 075414–1–9.

Yamawaki, H., Fujihisa, H., Sakashita, M., Nakayama, A., & Aoki, K. (2004). Powder x-ray diffraction study of the volume change of ice viii under high pressure. *Physica B: Condensed Matter*, *344*(1), 260–264.

Yang, S., Ouyang, L., Phillips, J. M., & Ching, W. (2006). Density-functional calculation of methane adsorption on graphite (0001). *Physical Review B*, *73*(16), 165407–165417.

Yevi, G., Rogers, R., et al. (1996). Storage of fuel in hydrates for natural gas vehicles (ngvs). *Journal of Energy Resources Technology. Transactions of the ASME*, *118*(3), 209–213.

Zhao, W., & Meng, Q. Y. (2013). Adsorption of methane on pristine and al-doped graphene: a comparative study via first-principles calculation. In *Advanced materials research* (Vol. 602, pp. 870–873).

Zhou, M., Lu, Y., Zhang, C., & Feng, Y. P. (2010). Strain effects on hydrogen storage capability of metal-decorated graphene: a first-principles study. *Applied Physics Letters*, *97*(10), 103109–1–3.

PUBLICATIONS

International Peer-reviewed Journal

1. **Decomposition of methane hydrates: a density-functional theory study,** N. Pantha, N. P. Adhikari, and S. Scandolo, High Presuure Research **85**, 231-238 (2015).

2. **First-principles study of the interaction of hydrogen molecular on Na-adsorbed graphene,** N. Pantha, K. Belbase, and N. P. Adhikari, Appl. Nanosci **5**, 393-402 (2015).

3. **Hydrogen storage on palladium adsorbed graphene: a density functional theory study,** N. Pantha, A. Khaniya, and N. P. Adhikari, Int. J. Mod. Phys. B **29(20)**, 1550143-1-14 (2015).

4. **Diffusion coefficients of Nitric Oxide in water: a molecular dynamics study.** S. Pokhrel, N. Pantha and N. P. Adhikari, Int. J. Mod. Phys. B **30**, 1650205-1-20 (2016).

International Conference Proceeding

1. **First-Principles Study of Adsorption of Halogen Molecules on Graphene-MoS2 Bilayer Hetero-system.** S. Lamichhane, P. Lage, G. B. Khatri, N. Pantha, N. P. Adhikari, and B. Sanyal. J. Phys.: Conf. Ser., **765(1)**, 012011-1-10 (2016).

National Peer-reviewed Journal

1. **First-principles study of solid methane at high pressure,** N. Pantha, J. Acharya and N. P. Adhikari, Bibechana **12**, 70-79 (2014).

2. **Structure and Symmetrization of Hydrogen bonding in Ices VIII-X at high pressure** N. Pantha, and N. P. Adhikari, JIST **19(2)**, 14-19 (2015).

3. **Hydrogen storage on Platinum decorated Graphene,** S. Lamichhane, N. Pantha, and N. P. Adhikari, Bibechana **11(1)**, 107-117 (2015).

4. **First-principles Study of Electronic and Magnetic Properties of Manganese Decorated Graphene,** B. P. Paudel, N. Pantha, and N. P. Adhikari, JNPS **2(1)**, 33-43

(2015).

5. **First-principles study of a molecular adsorption of fluorine on monolayer MoS_2,** H. Paudyal, N. Pantha, and N. P. Adhikari, Bibechana **13**, 50-59 (2016).

Manuscript submitted/under preparation.

1. **First-principles study of molecular adsorption of hydrogen(s) on Co-adatom graphene.** S. Thapa, N. Pantha and N. P. Adhikari, submitted to J. CDPTU.
2. **Functionalizing graphene for enhanced bonding of methane by decorating with metal adatoms**
3. **Methane-methane interactions in different solvent environments.**